



## Durham E-Theses

---

### *NMH studies of porous silicate gels and related materials: both in the solid and solution-state*

Pritchard, Timothy Neil

#### How to cite:

---

Pritchard, Timothy Neil (1989) *NMH studies of porous silicate gels and related materials: both in the solid and solution-state*, Durham theses, Durham University. Available at Durham E-Theses Online: <http://etheses.dur.ac.uk/6461/>

#### Use policy

---

The full-text may be used and/or reproduced, and given to third parties in any format or medium, without prior permission or charge, for personal research or study, educational, or not-for-profit purposes provided that:

- a full bibliographic reference is made to the original source
- a [link](#) is made to the metadata record in Durham E-Theses
- the full-text is not changed in any way

The full-text must not be sold in any format or medium without the formal permission of the copyright holders.

Please consult the [full Durham E-Theses policy](#) for further details.

NMR STUDIES OF POROUS SILICATE GELS AND RELATED MATERIALS:  
BOTH IN THE SOLID AND SOLUTION-STATE

BY

TIMOTHY NEIL PRITCHARD

A thesis submitted for the degree of Doctor of Philosophy  
of the University of Durham 1989

## Acknowledgements

During the course of my three years at Durham University I have become indebted to many individuals whom I wish to thank.

Firstly, I wish to thank my supervisor Professor R. K. Harris for his encouragement and advice throughout the three years and in the grim business of writing up. Thanks also to Dr.'s Edd Smith and Alan Miniham of Unilever Research for many useful discussions and suggestions, and Dr.'s B.J. Say, A. Sebald, P. Jackson, P. Wilkes, R. Matthews and L.H. Merwin for help with NMR equipment, Dr.'s P. Gillespie, G. Hardgrove and A.R. Grimmer for interesting comments and Professor L.S. Dent-Glasser for letting me borrow some samples. Thanks also to Matt, Xio Ping, Anita, Youseff, and Rob (who still owes everyone a pint!) for numerous discussions, sometimes philosophical, often humorous.....never dull.

I am especially grateful to Shirley Stewart who typed this thesis, and also Mr. and Mrs. Palmer, who made a "home from home" for me during my visits to Portsunlight.

I acknowledge and thank the Science and Engineering Research Council and Crosfield Chemicals Ltd. for financial support through an SERC CASE award.

Finally, and certainly not least, I wish to thank my parents for their continued love and support, and Chris, Alan, Jez, Joy and Jacqui. Thank you for being there.

MEMORANDUM

The research work presented in this thesis has been carried out in the Department of Chemistry, at the University of Durham between October 1985 and September 1988. It is the original work of the author unless stated otherwise. None of this work has been submitted for any other degree.

TO MUM AND DAD

19 DOWN

"IT SOUNDS FOOLISH TO STUDY THIS ELEMENT"

"THE TIMES" CROSSWORD PUZZLE N<sup>o</sup>. 13321

NMR STUDIES OF POROUS SILICATE GELS AND RELATED MATERIALS:  
BOTH IN THE SOLID AND SOLUTION-STATE

BY

TIMOTHY NEIL PRITCHARD

ABSTRACT

The purpose of this thesis is to describe research, using both solid and solution-state NMR techniques, to investigate the properties of a wide variety of silicon-containing materials.

One solid-state  $^{29}\text{Si}$  NMR technique ( $^{29}\text{Si}$ - $^1\text{H}$  cross-polarisation), and the experimental aspects important when using it, has been discussed in detail, and later used together with single pulse  $^{29}\text{Si}$  NMR techniques, to obtain information concerning geometry and local site symmetry of silicon sites in organosilicon compounds and silicate minerals. These techniques, together with a range of  $^1\text{H}$  CRAMPS experiments have also proved to be powerful tools for investigating the structure and properties of porous silicate gels (i.e. xerogels).

$^{29}\text{Si}$  and  $^{23}\text{Na}$  NMR measurements have been used to acquire evidence for the relaxation mechanisms of silicate species present in aqueous alkaline silicate solutions, and a technique for investigating the properties of sodium ions in colloidal silica solutions is tentatively proposed.

Conclusions are drawn from the results obtained, demonstrating that where structural information can be obtained from these systems using other techniques (e.g. X-ray diffraction) NMR proves to be a valuable adjunct. However, in situations where this information is unknown or difficult to obtain using other techniques, NMR may yield new insights into the structural properties of the materials.

The following abbreviations and symbols have been used:

AQ	= Acquisition time
$B_0$	= Static magnetic field
$B_1$	= Applied magnetic field
CP	= Cross-polarisation
CRAMPS	= Combined Rotation And Multiple Pulse Sequences
EFG	= Electric Field Gradient
FID	= Free Induction Decay
FT	= Fourier Transform
$\hbar$	= Plancks constant/ $2\pi$
$\mathcal{H}$	= Hamiltonian operator
MAS	= Magic Angle Spinning
NS	= Number of transients
$N_\alpha, N_\beta$	= Spin populations in $\alpha$ and $\beta$ spin states
NMR	= Nuclear Magnetic Resonance
RD	= Recycle Delay
$\bar{\delta}$	= Anisotropy
$\delta/\text{ppm}$	= Isotropic Chemical Shifts (in parts per million)
SW	= <del>SPECTRAL</del> Width
RF	= Radio Frequency
$\omega_r$	= Rotation rate
$\omega_0$	= Resonance frequency (radians $\text{sec}^{-1}$ ).

## CONTENTS

	PAGE
1.0 CHAPTER ONE	
INTRODUCTION	1
2.0 CHAPTER TWO	
THEORY	3
2.1 INTRODUCTION	
2.2 GENERAL THEORY	3
2.3 THE CLASSICAL PICTURE	3
2.3.1 THE ROTATING FRAME OF REFERENCE AND RELAXATION	6
2.4 THE QUANTUM MECHANICAL PICTURE	8
2.4.1 THE EXTERNAL HAMILTONIAN	9
2.4.2 THE INTERNAL HAMILTONIAN	11
2.5 RELAXATION	17
2.5.1 RELAXATION IN THE ROTATING FRAME OF REFERENCE	17
2.5.2 RELAXATION MECHANISMS	20
2.5.3 THE NUCLEAR OVERHAUSER EFFECT	20
2.6 SELECTIVE AVERAGING TECHNIQUES	21
2.6.1 MAGIC ANGLE SPINNING	21
2.6.2 HIGH POWER PROTON DECOUPLING	23
2.6.3 HOMONUCLEAR SPIN DECOUPLING	23
2.6.4 CARR-PURCELL-MERIBOOM-GILL $T_2$ MEASUREMENTS	25
2.6.5 CROSS-POLARIZATION	26
2.7 QUADRUPOLEAR NUCLEI	33
2.8 NOMENCLATURE	35
3.0 CHAPTER THREE	36
EXPERIMENTAL	
3.1 THE BRUKER CXP200 NMR SPECTROMETER	36
3.1.1 PROBES USED FOR SOLID-STATE NMR STUDIES	36
3.1.2 SHIMMING AND $^1\text{H}$ PULSE CALIBRATION	37
3.1.3 SETTING THE ANGLE	37
3.1.4 $^{29}\text{Si}$ REFERENCING AND PULSE CALIBRATION	37

3.2	$^1\text{H}$ CRAMPS	38
3.3	RELAXATION TIME MEASUREMENTS	40
3.3.1	SOLID STATE WORK	40
3.3.2	SOLUTION STATE WORK	41
3.4	MATERIALS STUDIED	41
3.4.1	CHAPTER FOUR	41
3.4.2	CHAPTER FIVE	41
3.4.3	CHAPTER SIX	42
3.4.4	CHAPTER SEVEN	42
3.5	THE BRUKER AC250 NMR SPECTROMETER	42
3.6	CHARACTERISATION OF SAMPLES STUDIED	43
3.6.1	SURFACE AREA MEASUREMENTS	43
3.6.2	PORE CHARACTERISATION	45
3.6.3	CHEMICAL ANALYSIS OF SILICA XEROGELS	46
3.6.4	CHEMICAL ANALYSIS OF AQUEOUS ALKALINE SOLUTIONS	46
4.0	CHAPTER FOUR	48
	$^{29}\text{Si}$ CROSS POLARISATION (CP) AND REFERENCE STANDARDS	
4.1	INTRODUCTION	48
4.2	EXPERIMENTAL	49
4.3	RESULTS AND DISCUSSION	52
4.4	DETERMINING S SPIN $T_1$ VALUES VIA CP	69
4.5	CONCLUSIONS	73
5.0	CHAPTER FIVE	76
	$^{29}\text{Si}$ NMR STUDIES OF CRYSTALLINE INORGANIC AND ORGANIC SILICON CONTAINING MATERIALS	
5.1	INTRODUCTION	76
5.2	THEORETICAL INTERPRETATION OF $^{29}\text{Si}$ ISOTROPIC CHEMICAL SHIFTS	78
5.3	$^{29}\text{Si}$ SHIELDING TENSORS	82
5.4	EXPERIMENTAL	89
	THE DETERMINATION OF THE PRINCIPAL COMPONENTS OF $^{29}\text{Si}$ SHIELDING TENSORS	
5.4.1	THE MOMENTS ANALYSIS METHOD	90
5.5	COMPUTER SIMULATION OF THE SPECTRA	92
5.6	RESULTS AND DISCUSSION	96
5.6.1	THE DIHYDROGEN SILICATE HYDRATES	96

5.6.2	DATOLITE	103
5.6.3	TILLEYLITE AND THORTVEITITE	103
5.6.4	MINERALS CONTAINING $Q^3$ UNITS	109
5.6.4.1	XONOTLITE	110
5.6.4.2	APOPHYLLITE	112
5.6.4.3	$[N(Me)_4]_8Si_8O_{20} \cdot 69H_2O$	112
5.6.4.4	OCTOSILICATE AND KANEMITE	116
5.6.5	ORGANOSILICON COMPOUNDS	119
5.6.5.1	1,1,1-TETRAMETHYLTRIPHENYL- DISILANE	120
5.6.5.2	HEXAPHENYLDISILANE	123
5.6.5.3	OCTAPHENYLDISILANE	125
5.6.5.4	HEXAPHENYLDISILOXANE	125
5.6.5.5	TRIPHENYLSILANE AND TRIBENZYLSILANE	126
5.6.5.6	TMS SALT	130
5.7	CONCLUSIONS	133
6.0	CHAPTER SIX	134
	SOLID-STATE NMR STUDIES OF SILICA XEROGELS	
6.1	INTRODUCTION	134
6.2	THE FORMATION OF SILICA XEROGELS	135
6.3	THE SURFACE STRUCTURE OF SILICA XEROGELS	136
6.3.1	SURFACE MODELS	139
6.3.2	THE ADSORPTION OF WATER	140
6.4	HYDROTHERMAL AGING	143
6.5	NMR STUDIES OF SILICA XEROGELS	148
6.6	EXPERIMENTAL	149
6.6.1	SILICA XEROGEL PREPARATION	149
6.7	RESULTS AND DISCUSSION	151
6.7.1.1	$T_1(^{29}Si)$ MEASUREMENTS	153
6.7.1.2	INTENSITY MEASUREMENTS	155
6.7.2	STRUCTURAL MODELS OF SILICA XEROGELS	158
6.7.2.1	THE RANDOM DISTRIBUTION MODEL	161
6.7.2.2	THE SINGLE DISCRETE PARTICLE MODEL	161
6.7.3	$^{29}Si$ CP MAS NMR TECHNIQUES	163
6.7.4	$^1H$ CRAMPS STUDIES OF SILICA XEROGELS	174

6.7.4.1	$^1\text{H}$ CRAMPS STUDIES OF SILICA XEROGEL S-TYPE(1)	174
6.7.5	TREATMENT OF SILICA XEROGELS	191
6.7.5.1	WASHING AND DRYING	191
6.7.6	HYDROTHERMAL AGING	195
6.7.6.1	SOLID-STATE NMR MEASUREMENTS	201
6.8	CONCLUSIONS	208
7.0	CHAPTER SEVEN	209
	NMR STUDIES OF AQUEOUS ALKALINE SILICATE SOLUTIONS AND COLLOIDAL SILICATE SOLUTIONS	
7.1	INTRODUCTION	209
7.2	EXPERIMENTAL	214
7.3	RESULTS AND DISCUSSION	216
7.3.1	$^{29}\text{Si}$ LONGITUDINAL RELAXATION TIME MEASUREMENTS	216
7.3.2	$^{23}\text{Na}$ NMR STUDIES OF COLLOIDAL SILICA	222
7.4	CONCLUSIONS	227
8.0	CHAPTER EIGHT	229
	CONCLUSIONS AND SUGGESTIONS FOR FURTHER INVESTIGATIONS	229
	REFERENCES	232
	APPENDIX	245

## 1.0 CHAPTER ONE

### INTRODUCTION

There are many spectroscopic techniques which may be employed to investigate the nature of solution and solid-state chemical systems. In particular, NMR has proved useful in gaining information concerning the structure of crystalline and amorphous solid silicon-containing materials, and the structure, distribution and exchange dynamics of species present in aqueous alkaline silicate solutions. In some cases this information is difficult or impossible to obtain using other techniques.

The purpose of this thesis is to describe research where nuclear magnetic resonance techniques have been employed to gain information concerning the structure and NMR properties of a variety of silicon containing systems.

In order to gain an understanding of the nature of NMR experiments and the various interactions that determine the nature of the NMR spectrum, a brief over-view of NMR theory is given in Chapter Two. It is seen that while solution-state NMR spectra are generally characterised by narrow peaks, in the solid-state, there are a number of anisotropic interactions which nuclei experience, causing solid-state NMR spectra to be generally broad and featureless. However, with the aid of various experimental techniques it is possible to take advantage of these interactions to improve the sensitivity of the NMR experiment and/or eliminate these interactions, so that "solution-like" NMR spectra of solid-samples can be obtained. These techniques are also discussed in Chapter Two.

Chapter Three gives details of the equipment, hardware and software employed for the investigations performed during the course of this research. This chapter also includes a list of the chemical systems studied, and physical/chemical techniques employed to



characterise silica xerogels and aqueous alkaline silicate solutions.

Chapters Four, Five and Six are concerned with the application of solid-state NMR techniques to study silicate minerals, organosilicon compounds and porous silica gels. One solid-state NMR technique which takes advantage of certain interactions to improve the sensitivity of the NMR experiment is discussed in Chapter Four. Details concerning the choice of standard chemical systems and experimental conditions required to set up this experiment for  $^{29}\text{Si}$  solid-state NMR investigations are given. Chapter Five, deals with the use of experimental techniques to take advantage of certain interactions to obtain information about the geometry and bonding of silicon sites in a variety of silicate minerals and organosilicon compounds. Chapter Six is concerned with the application of various solid-state NMR techniques (including  $^1\text{H}$  CRAMPS) to study silica xerogels, and structural changes that occur as xerogels are prepared or treated in different ways.

In Chapter Seven  $^{29}\text{Si}$  and  $^{23}\text{Na}$  NMR techniques are employed to investigate the relaxation properties of species present in aqueous alkaline silicate solutions and colloidal silicas.

Finally, general conclusions are drawn from the results described in this thesis, and in the light of data published here, suggestions for future investigations are made.

## 2.0 CHAPTER TWO

### THEORY

#### 2.1 INTRODUCTION

In this chapter the basic theory of nuclear magnetic resonance, which is applicable to solution and solid-state NMR, will be briefly discussed. The aim is to provide a basic knowledge of the physical effects that determine the form of the NMR spectrum. The main differences between the two forms of NMR are discussed. In particular, attention will be paid to the broadening mechanisms in solid-state NMR, and various techniques which may be employed to selectively average these interactions.

#### 2.2 GENERAL THEORY

All nuclei with odd atomic mass or odd atomic numbers have spin angular momentum and (as a consequence of the motion of the charged particle,) a nuclear magnetic moment co-linear with the axis of spin.<sup>(1)</sup> The nuclear magnetic moment ( $\mu$ ) is usually expressed in terms of the magnetogyric ratio ( $\gamma$ ).<sup>(2)</sup>

$$(2.1) \quad \mu = \gamma \hbar [I(I+1)]^{\frac{1}{2}}$$

where  $I$  is the nuclear spin quantum number. For most of this chapter we will restrict ourselves to the discussion of nuclei where  $I = \frac{1}{2}$ . Quadrupolar nuclei (i.e. nuclei where  $I > \frac{1}{2}$ ) will be discussed in section 2.7.

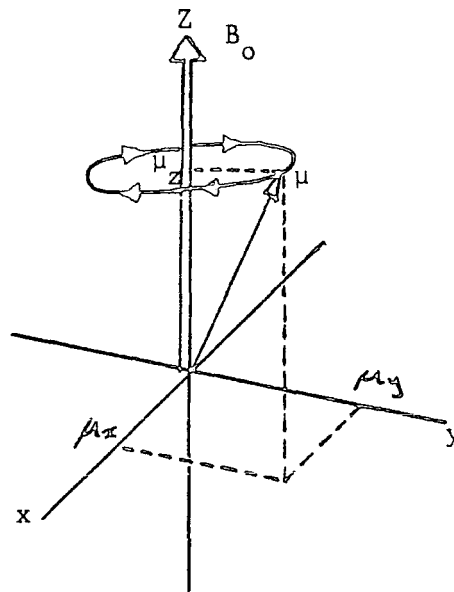
#### 2.3 THE CLASSICAL PICTURE<sup>(2,3)</sup>

In the classical picture, when a nucleus of spin  $I = \frac{1}{2}$  is placed in a static magnetic field  $B_0$ , the magnetic field exerts a torque upon the magnetic moment causing it to precess about  $B_0$ . This motion is described by equation 2.2.

$$(2.2) \quad \frac{d\mu}{dt} = +\gamma \cdot \mu \cdot B_0$$

Considering the static magnetic field to be directed along the Z axis in the laboratory frame of reference, the magnetic moment  $\mu$  can be resolved into three components as shown in Figure 2.1.

FIGURE 2.1



At equilibrium in the absence of any exciting radio frequency (RF) field the Z component of  $\mu$  will remain constant.

$$(2.3) \quad \frac{d\mu_z}{dt} = 0$$

The magnitudes of  $\mu_x$  and  $\mu_y$  will vary as  $\mu$  precesses about  $B_0$ . It may be seen that these components are  $90^\circ$  out of phase with each other.

This situation is represented by equations 2.4 and 2.5 respectively.

$$(2.4) \quad \frac{d\mu_x}{dt} = +\gamma\mu_y B_0$$

$$(2.5) \quad \frac{d\mu_y}{dt} = -\gamma\mu_x B_0$$

Equation 2.3 indicates that  $\mu_z$  is not coupled to the other components and has the integral result

$$(2.6) \quad \mu_z(0) = \mu_z(t)$$

The  $\mu_x$  and  $\mu_y$  components, however, are coupled. Using the definitions

$$(2.7) \quad \frac{d\mu_{\pm}}{dt} = \frac{d\mu_x}{dt} \pm i \frac{d\mu_y}{dt} = \pm i\mu_{\pm}\gamma B_0$$

$$(2.8) \quad \mu_{\pm}(t) = \mu_{\pm}(0) \exp(\pm i\gamma B_0 t)$$

This yields

$$(2.9a) \quad \mu_x(t) = \mu_x(0) \cos \gamma B_0 t - \mu_y(0) \sin \gamma B_0 t$$

$$(2.9b) \quad \mu_y(t) = \mu_x(0) \sin \gamma B_0 t + \mu_y(0) \cos \gamma B_0 t$$

In a constant field, therefore, the component of the magnetic moment along the field is time independent. However, those components perpendicular to the field oscillate in such a way, that the magnitude of the transverse component remains constant.

$$(2.9c) \quad \mu_x(t)^2 + \mu_y(t)^2 = \mu_x(0)^2 + \mu_y(0)^2$$

These equations suggest a picture in which the magnetic moment  $\mu$  is precessing about  $B_0$  with a rotation frequency  $\omega_0$ . This angular frequency is known as the Larmor frequency.

$$(2.10) \quad \omega_0 = -\gamma B_0$$

The discussion so far has been restricted to considering the motions of one magnetic moment. In most experimental situations, however, there is an ensemble of magnetic moments, and hence an equation of motion that describes the motions of roughly  $10^{23}$  spins, with a net magnetic moment  $M$ . is required.

$$(2.11) \quad M = \sum_i \mu_i$$

Considering the fields produced by the individual magnetic moments upon each other are negligible compared to  $B_0$ , and the moments are identical, the equation of motion for the net magnetic moment in the field is

$$(2.12) \quad \frac{dM}{dt} = \sum_i \frac{d\mu_i}{dt} = \sum_i +\gamma \mu_i B_0 = +\gamma M B_0$$

Equation 2.12 is entirely analogous to that for a single moment (equation 2.2), provided all the moments start out at time zero with exactly the same orientation. In reality, however, for an unperturbed system there is a random distribution of initial orientations. Under

these conditions (i.e. a random orientation of the x-y components of the magnetic moments), the only observable net moment is directed along the field. The other components are zero.

### 2.3.1 THE ROTATING FRAME OF REFERENCE AND RELAXATION

In the classical picture, the absorption of energy by a nucleus may be visualised by a resonance phenomenon. The nuclei precessing about  $B_0$  at the Larmor frequency are perturbed from equilibrium when a small magnetic field  $B_1$  rotating perpendicular to  $B_0$  is applied, this  $B_1$  field rotating at the Larmor frequency and in the same sense as the nuclear magnetic moments. Resonance will then occur, and energy is absorbed from the exciting field.

In the discussion so far, the description of the NMR experiment has been outlined in terms of a cartesian coordinate system fixed with respect to the laboratory. It is often convenient, however, to consider the complex behaviour of nuclear spins in terms of a coordinate systems where the z axis is still aligned along the field, but the x,y axes rotate about the z axis at the Larmor frequency. This is called the rotating frame of reference.<sup>(4)</sup>

In the rotating frame of reference nuclei precess about the effective field  $B_{\text{eff}}$ , just as they precess about  $B_0$  in the laboratory frame where

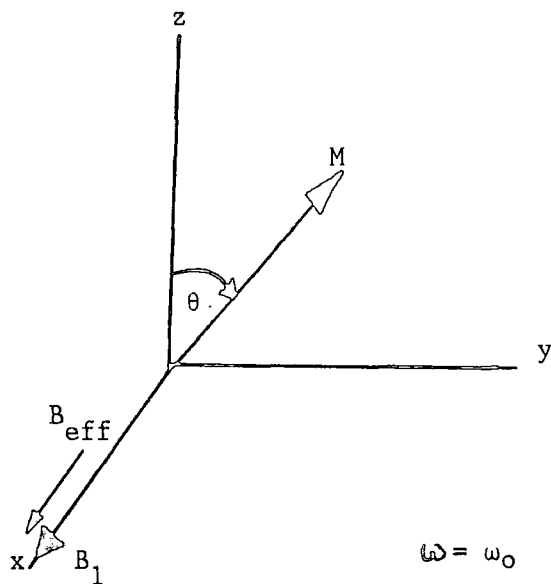
$$(2.13) \quad B_{\text{eff}} = \left[ \left[ B_0 - \frac{\omega}{\gamma} \right]^2 + B_1^2 \right]^{\frac{1}{2}}$$

$$\text{When } \omega = \omega_0 \text{ then } \left[ B_0 - \frac{\omega}{\gamma} \right] = 0, \quad B_{\text{eff}} = B_1$$

and the nuclear spins precess about the  $B_1$  field, the effect of an RF pulse applied at a frequency  $\omega_0$  along the x axis of the rotating frame, results in the rotation of the net magnetic moment from the z axis, through an angle  $\theta$  in the y-z plane (Figure 2.2)

$$(2.14) \quad \theta = \gamma B_1 t$$

FIGURE 2.2



where  $t$  is the length of time the  $B_1$  field is applied for. When  $\theta = \frac{\pi}{2}$  a so called  $90^\circ$  pulse results, which flips the magnetisations into the  $x, y$  plane. It is this rotation property of RF pulses that is utilised in NMR experiments.

Following perturbation of the spin systems by (for example) a  $90^\circ$  pulse two types of relaxation processes occur in order to return the spin systems to equilibrium. These must be contended with if meaningful data are to be acquired.

The first type of relaxation, spin-lattice (or longitudinal relaxation), is characterised by the time constant  $T_1$ . This governs the rate at which the spins repolarize in the external magnetic field (equation 2.15).

The second type of relaxation, spin-spin (or transverse relaxation) is characterised by the time constant  $T_2$ . This governs the rate at which the individual spin isochromats dephase in the rotating frame of reference, as a consequence of interactions between the spins and other magnetic fields, (equations 2.16 and 2.17

respectively). The linewidths observed in any NMR experiment are of the order of  $(\pi T_2)^{-1}$ .

$$(2.15) \quad \frac{dM_z}{dt} = -\frac{[M_z - M_{eqm}]}{T_1}$$

$$(2.16) \quad \frac{dM_x}{dt} = -\frac{M_x}{T_2}$$

$$(2.17) \quad \frac{dM_y}{dt} = -\frac{M_y}{T_2}$$

#### 2.4 THE QUANTUM MECHANICAL PICTURE<sup>(3,5)</sup>

In the previous discussion, it has been stated that in any NMR experiment the resolution observed is determined by  $T_2$ , which in turn is dependent upon the extent to which the individual spins interact with magnetic fields other than  $B_0$ . The rate at which experiments may be repeated is governed by  $T_1$ , which is also dependent upon these interactions. In order to more fully understand the nature of these interactions, which influence  $T_1$  and  $T_2$  values it is necessary to turn to quantum mechanics.

In quantum mechanics, the various physically different interactions that determine the state of the system are expressed in terms of the nuclear spin Hamiltonian  $\mathcal{H}_T$ . This Hamiltonian, in diamagnetic non-conducting substances for spin  $I = \frac{1}{2}$  nuclei is expressed in equation 2.18 (in terms of energy units).

$$(2.18) \quad \mathcal{H}_T = \mathcal{H}_{int} + \mathcal{H}_{ext}$$

where

$$(2.18a) \quad \mathcal{H}_{ext} = \mathcal{H}_Z + \mathcal{H}_{RF}$$

and

$$(2.18b) \quad \mathcal{H}_{int} = \mathcal{H}_{D_{II}} + \mathcal{H}_{D_{IS}} + \mathcal{H}_{CS} + \mathcal{H}_J + \mathcal{H}_{SR}$$

The term  $\mathcal{H}_{ext}$  is referred to as the external Hamiltonian, since the terms that form this Hamiltonian depend (apart from specific nuclear

properties i.e.  $\gamma$ ) on external parameters which may be experimentally controlled. The term  $\mathcal{H}_{\text{int}}$  is referred to as the internal Hamiltonian, since the terms that form it supply information of chemical interest. Each of the terms that make up the nuclear spin Hamiltonians will be discussed in turn.

#### 2.4.1 THE EXTERNAL HAMILTONIAN $\mathcal{H}_{\text{ext}}$

The external Hamiltonian ( $\mathcal{H}_{\text{ext}}$ ) is the sum of the Zeeman and radio frequency terms (equation 2.18a).

The Zeeman Hamiltonian ( $\mathcal{H}_Z$ ) describes the interaction of the nuclear spins with the external static magnetic field  $B_0$ , it may be written as

$$(2.19) \quad \mathcal{H}_Z = \hbar B_0 \sum_j I_{Z_j} \gamma_j$$

where  $I_{Z_j}$  is the spin operator for the  $j^{\text{th}}$  nucleus with a magnetogyric ratio  $\gamma_j$ .

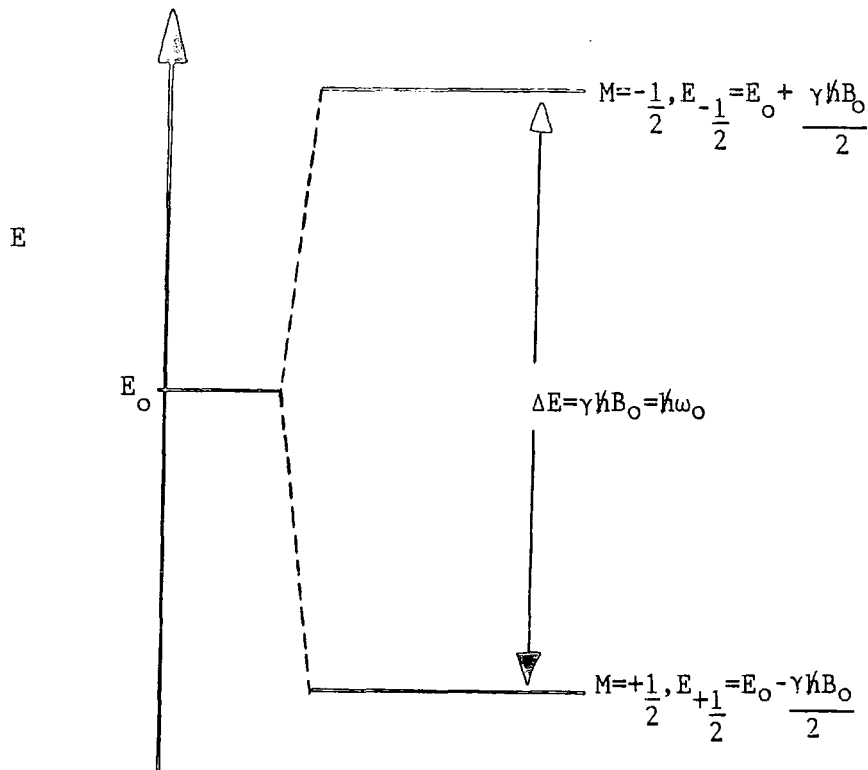
Quantum mechanics requires that the orientation of a magnetic moment with respect to  $B_0$  is quantised.  $2I+1$  different orientations are possible, each of which is described by the quantum number  $m$  and corresponds to a different energy  $E_m$

$$(2.20) \quad E_m = -\gamma \hbar m B_0$$

where  $m = I, I-1, \dots, -I$

For a spin  $I = \frac{1}{2}$  nuclei with a positive  $\gamma$ , two possible orientations of the nuclear spin define a high ( $\beta$ ) and a low ( $\alpha$ ) energy state. The energy level diagram is shown in Figure 2.3

FIGURE 2.3



At thermal equilibrium with the lattice, the population distribution between the two states can be described by a Boltzmann distribution.

$$(2.21) \quad \frac{N_\beta}{N_\alpha} = \exp\left[\frac{-\gamma \hbar B_0}{kT}\right] \approx 1 - \frac{\gamma \hbar B_0}{kT}$$

Since  $1 \gg (\gamma \hbar B_0 / kT)$ ,  $N_\alpha > N_\beta$ , so net absorption can occur at the resonance condition producing the NMR signal. The net magnetisation of a sample containing  $N$  nuclei of spin  $I = \frac{1}{2}$  is given by the Curie Law.

$$(2.22a) \quad M_0 = \frac{N \gamma^2 \hbar^2 B_0^2}{4kT} = C B_0^2 \beta_L$$

The energy of the spin system is given as

$$(2.22b) \quad E = \frac{N \gamma^2 \hbar^2 B_0^2}{4kT} = C B_0^2 \beta_L$$

where  $C = \frac{N \gamma^2 \hbar^2}{4}$  and  $\beta_L = 1/kT_L$ , where  $T_L$  is the temperature of the lattice.

The radio frequency Hamiltonian ( $\mathcal{H}_{RF}$ )

The Hamiltonian describing the interaction of nuclei with the

perturbing radio frequency field, which is usually assumed to be aligned parallel to the x axis, may be written as

$$(2.23) \quad \mathcal{H}_{\text{RF}} = \hbar \gamma I_x B_1 (\omega_t + \phi)$$

where  $\omega_t$  and  $\phi$  are the frequency and phase of the perturbing field.

#### 2.4.2 THE INTERNAL HAMILTONIAN ( $\mathcal{H}_{\text{int}}$ )

The internal Hamiltonian ( $\mathcal{H}_{\text{int}}$ ), is the sum of the dipolar ( $\mathcal{H}_{\text{D}}$ ) chemical shielding ( $\mathcal{H}_{\text{CS}}$ ) J-coupling ( $\mathcal{H}_{\text{J}}$ ) and spin-rotation ( $\mathcal{H}_{\text{SR}}$ ) Hamiltonian terms (equation 2.18b).

Each of these Hamiltonians describes an anisotropic interaction and has a common structure (equation 2.24). This may be represented by a cartesian tensor linking two vectors,

$$(2.24) \quad \mathcal{H} = k^\lambda I^\lambda \underline{R}^\lambda Y^\lambda$$

where  $k^\lambda$  is a scalar constant,  $I^\lambda$  and  $Y^\lambda$  are row and column matrices respectively, representing vectors, and  $\underline{R}^\lambda$  is a second rank cartesian tensor containing nine components.

$$(2.25) \quad I^\lambda \underline{R}^\lambda Y^\lambda = (I_x I_y I_z) \begin{bmatrix} R_{XX} & R_{XY} & R_{XZ} \\ R_{YX} & R_{YY} & R_{YZ} \\ R_{ZX} & R_{ZY} & R_{ZZ} \end{bmatrix} \begin{bmatrix} Y_X \\ Y_Y \\ Y_Z \end{bmatrix}$$

All these tensors are molecular properties, and therefore, are best described in a molecule fixed axis system. This coordinate system is called the principal axis system (PAS). In this, the tensors are diagonalised.

$$(2.26) \quad R^\lambda = \begin{bmatrix} R_{XX} & R_{XY} & R_{XZ} \\ R_{YX} & R_{YY} & R_{YZ} \\ R_{ZX} & R_{ZY} & R_{ZZ} \end{bmatrix} \xrightarrow{\text{"DIAGONALISATION"}} \begin{bmatrix} R_{XX} & 0 & 0 \\ 0 & R_{YY} & 0 \\ 0 & 0 & R_{ZZ} \end{bmatrix}$$

LAB FRAME PAS

$R_{XX}$ ,  $R_{YY}$  and  $R_{ZZ}$  are the diagonal elements of the tensor in the PAS, these are referred to as the principal components. The following convention is used to label the components

$$(2.27) \quad [R_{ZZ} - R_{\text{iso}}] \geq [R_{XX} - R_{\text{iso}}] \geq [R_{YY} - R_{\text{iso}}]$$

where

$$(2.28) \quad R_{\text{iso}} = \frac{1}{3} \text{Tr} \underline{R}(\text{PAS}) = \frac{1}{3} (R_{XX} + R_{YY} + R_{ZZ})$$

In addition, two other parameters may be defined to describe the tensor. The anisotropy ( $\bar{\delta}$ ) and the asymmetry ( $\eta$ ).

$$(2.29) \quad \bar{\delta} = R_{ZZ} - R_{\text{iso}}$$

$$(2.30) \quad \eta = \frac{(R_{YY} - R_{XX})}{(R_{ZZ} - R_{\text{iso}})}$$

Using these parameters the tensor in the PAS may be re-expressed as

$$(2.31) \quad \underline{R}(\text{PAS}) = \begin{bmatrix} R_{XX} & 0 & 0 \\ 0 & R_{YY} & 0 \\ 0 & 0 & R_{ZZ} \end{bmatrix} = R_{\text{iso}} + \bar{\delta} \begin{bmatrix} -\frac{1}{2}(1+\eta) & 0 & 0 \\ 0 & -\frac{1}{2}(1-\eta) & 0 \\ 0 & 0 & 1 \end{bmatrix}$$

The asymmetry ( $\eta$ ) has a value between 0 and 1. If  $\eta = 0$ , the tensor  $\underline{R}$  is axially symmetric, where  $R_{xx} = R_{yy} = R_{\perp}$  and  $R_{zz} = R_{\parallel}$ .

The values of  $k^{\lambda}$ ,  $R^{\lambda}$ , and  $Y^{\lambda}$  for each interaction which determines the internal Hamiltonian for spin  $I = \frac{1}{2}$  nuclei are listed in table 2.1.

TABLE 2.1

HAMILTONIAN TERM ( $\mathcal{H}$ )	$K^{\lambda}$	$R^{\lambda}$	$Y^{\lambda}$	UNITS OF $\underline{R}^{\lambda}$
$\mathcal{H}_D$	$\left[ \frac{\mu_0}{4\pi} \right] \frac{\gamma_i \gamma_j \hbar}{r_{ij}^3}$	D	$I^k$	NONE
$\mathcal{H}_{CS}$	$\gamma$	$\sigma$	$B_0$	NONE
$\mathcal{H}_J$	$2\pi$	J	$I^k$	Hz
$\mathcal{H}_{SR}$	1	C	$J^m$	NONE

(A) THE SPIN ROTATION HAMILTONIAN ( $\mathcal{H}_{SR}$ )

The spin rotation Hamiltonian ( $\mathcal{H}_{SR}$ ), describes the coupling of nuclear spins (I) with magnetic moments associated with the molecular

angular momentum ( $J^m$ ) of a molecule M, it may be written as

$$(2.32) \quad \mathcal{H}_{SR} = \sum_{\vec{z}} \sum_{\vec{m}} \sum_{\vec{I}} \vec{c}^{\vec{z}, \vec{m}, \vec{I}}$$

### (B) THE DIPOLAR HAMILTONIAN ( $\mathcal{H}_D$ )

The dipolar interaction between two nuclear spins may be described by the classical expression for the energy of the interaction between magnets separated by a distance  $r_{IS}$ .

$$(2.33) \quad U = \left[ \frac{\mu_0}{4\pi} \right] \left[ \frac{\mu_S \mu_I}{r_{IS}^3} - 3 \frac{[\mu_S r_{IS}][\mu_I r_{IS}]}{r_{IS}^5} \right]$$

The classical expression can be converted into its quantum mechanical counterpart by using the operators  $\hat{\mu}_I$  and  $\hat{\mu}_S$ , where

$$(2.34) \quad \hat{\mu}_I = \gamma_I \hbar \hat{I}_I$$

Equation 2.33 then becomes

$$(2.35) \quad \mathcal{H}_D = \left[ \frac{\mu_0}{4\pi} \right] \frac{\gamma_I \gamma_S \hbar}{r_{IS}^3} \left[ \hat{I}_I \cdot \hat{I}_S - 3 \frac{[\hat{I}_I r_{IS}][\hat{I}_S r_{IS}]}{r_{IS}^2} \right]$$

This equation may be rewritten in matrix form by expanding the various products of  $\hat{I}_I \cdot \hat{I}_S$ ,  $\hat{I}_I r_{IS}$  and  $\hat{I}_S r_{IS}$ .

(2.36)

$$\mathcal{H}_D = \left[ \frac{\mu_0}{4\pi} \right] \gamma_I \gamma_S \hbar \begin{bmatrix} I_{IX} & I_{IY} & I_{IZ} \end{bmatrix} \begin{bmatrix} (r^2 - 3x^2)/r^5 & -3xy/r^5 & -3xz/r^5 \\ -3yx/r^5 & (r^2 - 3y^2)/r^5 & -3yz/r^5 \\ -3zx/r^5 & -3zy/r^5 & (r^2 - 3z^2)/r^5 \end{bmatrix} \begin{bmatrix} I_{SX} \\ I_{SY} \\ I_{SZ} \end{bmatrix}$$

If the orientation of  $r$  (the internuclear vector) is given relative to the  $x, y, z$  axes of the Laboratory frame of reference then the tensor is not diagonalised. If, however, one chooses a coordinate system, the principal axis system, where  $r$  is parallel to the  $Z$  axis, then equation 2.36 becomes

$$(2.37) \quad \mathcal{H}_D = \left[ \frac{\mu_0}{4\pi} \right] \frac{\gamma_I \gamma_S \hbar}{r_{IS}^3} \begin{bmatrix} I_{Ix} & I_{Iy} & I_{Iz} \end{bmatrix} \begin{bmatrix} 1 & 0 & 0 \\ 0 & 1 & 0 \\ 0 & 0 & -2 \end{bmatrix} \begin{bmatrix} I_{Sx} \\ I_{Sy} \\ I_{Sz} \end{bmatrix}$$

$$\text{i.e. } \mathcal{H}_D = k^{\lambda} \mathbf{I}_I \mathbf{D} \mathbf{I}_S$$

where  $\mathbf{D}$  is the dipolar tensor

The dipolar interaction may then be described in terms of polar coordinates, which define the orientation of the principal axis system to the laboratory frame of reference, where the Euler angles  $\alpha$  and  $\beta$  describe the position of the internuclear vector  $r_{IS}$  in the laboratory frame of reference. When this is done, the dipolar Hamiltonian is given as

$$(2.38) \quad \mathcal{H}_D = K^D [A+B+C+D+E+F] \quad (6)$$

where

$$(2.38a) \quad K^D = \left[ \frac{\mu_0}{4\pi} \right] \frac{\gamma_I \gamma_S \hbar}{r_{IS}^3}$$

$$(2.38b) \quad A = \hat{I}_{IZ} \cdot \hat{I}_{SZ} (1 - 3\cos^2\beta)$$

$$(2.38c) \quad B = -\frac{1}{4} [\hat{I}_{I+} \cdot \hat{I}_{S-} + \hat{I}_{I-} \cdot \hat{I}_{S+}] (1 - 3\cos^2\beta)$$

$$(2.38d) \quad C = -\frac{3}{2} [\hat{I}_{IZ} \cdot \hat{I}_{S-} + \hat{I}_{I+} \cdot \hat{I}_{SZ}] \sin\beta \cos\beta \exp(-i\alpha)$$

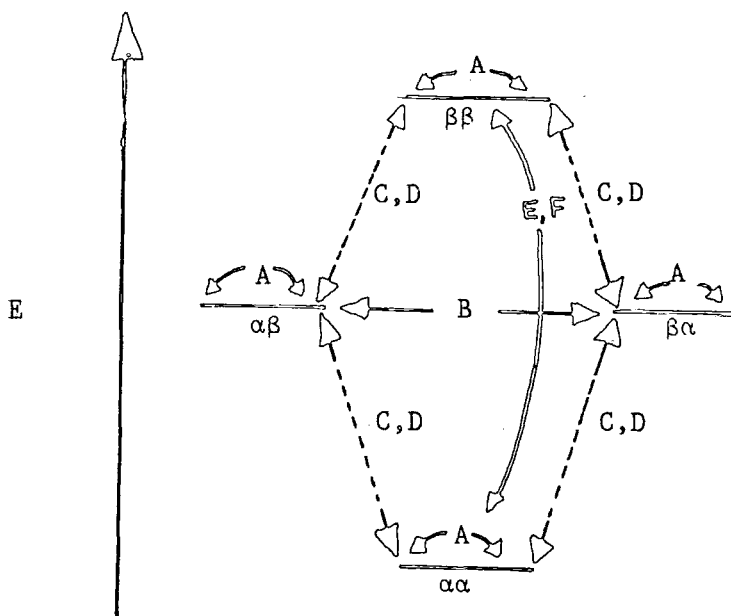
$$(2.38e) \quad D = -\frac{3}{2} [\hat{I}_{IZ} \cdot \hat{I}_{S+} + \hat{I}_{I-} \cdot \hat{I}_{SZ}] \sin\beta \cos\beta \exp(-i\alpha)$$

$$(2.38f) \quad E = -\frac{3}{4} \hat{I}_{I+} \cdot \hat{I}_{S+} \sin^2\beta \exp(\approx 2i\alpha)$$

$$(2.38g) \quad F = -\frac{3}{4} \hat{I}_{I-} \cdot \hat{I}_{S+} \sin^2\beta \exp(2i\alpha)$$

These terms A to F describe all possible links between the Zeeman energy levels for a spin pair as shown in Figure 2.4.

Figure 2.4



The terms C,D,E and F in reality make a negligible contribution to the observed NMR signal, since these terms link spin states differing in energy and are, therefore, disregarded. The Hamiltonian for the dipolar interaction is, therefore, truncated. For homonuclear spins the Hamiltonian ( $\mathcal{H}_{D_{II}}$ ) may be written as

$$(2.39) \quad \mathcal{H}_{D_{II}} = \left[ \frac{\mu_0}{4\pi} \right] \frac{\gamma_I^2 \hbar^2}{2r_{ij}^3} (1-3\cos^2\beta) (3I_{iz}I_{jz} - I_i \cdot I_j)$$

For heteronuclear spins, however, since the  $\alpha\beta$  and  $\beta\alpha$  states differ in energy, the B term may be disregarded and the Hamiltonian ( $\mathcal{H}_{D_{IS}}$ ) becomes

$$(2.40) \quad \mathcal{H}_{D_{IS}} = \left[ \frac{\mu_0}{4\pi} \right] \frac{\gamma_I \gamma_S \hbar^2}{2r_{IS}^3} (1-3\cos^2\beta) I_{IZ} \cdot I_{SZ}$$

### (C) THE SHIELDING HAMILTONIAN ( $\mathcal{H}_{CS}$ )

The Hamiltonian describing the shielding of an individual spin may be written as

$$(2.41) \quad \mathcal{H}_{CS} = \hbar \gamma I \sigma B_0$$

where  $\underline{g}$  is the shielding tensor in the principal axis system

$$(2.42) \quad \underline{g}(\text{PAS}) = \begin{bmatrix} \sigma_{xx} & 0 & 0 \\ 0 & \sigma_{yy} & 0 \\ 0 & 0 & \sigma_{zz} \end{bmatrix}$$

Using the definitions given by equations 2.27 to 2.31, equation 2.41 may be written as

$$(2.42) \quad \mathcal{H}_{\text{CS}} = \gamma I_Z \left[ \sigma_{\text{iso}} + \delta \begin{bmatrix} -\frac{1}{2}(1+\eta) & 0 & 0 \\ 0 & -\frac{1}{2}(1-\eta) & 0 \\ 0 & 0 & 1 \end{bmatrix} \right] B_0$$

Again, it is convenient to consider the form of this Hamiltonian when polar coordinates are employed to define the orientation of the PAS in the laboratory frame of reference. When this is done, the Hamiltonian takes on the form given in equation 2.43

$$(2.43) \quad \mathcal{H}_{\text{CS}} = \gamma I_Z \left[ \sigma_{\text{iso}} + \delta \left[ \frac{(3\cos^2\beta - 1) + \eta \sin^2\beta \cos^2\alpha}{2} \right] \right]$$

#### (D) THE INDIRECT SPIN-SPIN COUPLING TERM ( $\mathcal{H}_J$ )

The indirect spin-spin coupling term ( $\mathcal{H}_J$ ) describes the coupling of nuclear spins  $i$  and  $k$  via electron spins, this may be written as

$$(2.44) \quad \mathcal{H}_J = 2\pi I^i \cdot \tilde{J} \cdot I^k$$

The significance of this interaction is discussed elsewhere in this thesis.

### 2.5 RELAXATION

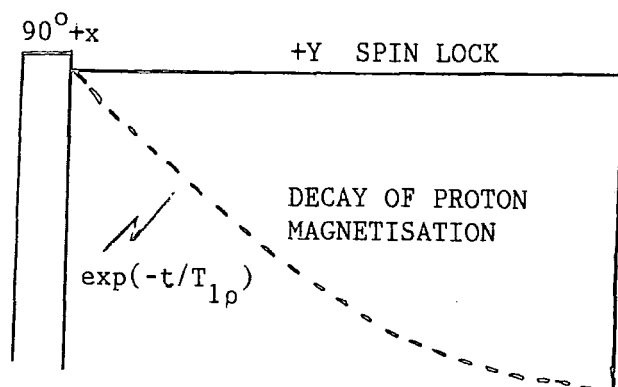
The general requirement for relaxation is that local fields should be present which fluctuate with time, and at an appropriate frequency so as to induce transitions between different energy levels. These local fields arise as a consequence of the interactions described in Section 2.4 and molecular motion<sup>(4)</sup>.

In this work we will be considering three types of relaxation, spin-lattice relaxation, spin-spin relaxation and spin-lattice relaxation in the rotating frame of reference. The first two types of relaxation have already been described briefly in Section 2.3.1.

#### 2.5.1 RELAXATION IN THE ROTATING FRAME OF REFERENCE

As discussed in Section 2.3.1, a  $90^\circ$  +x pulse of RF, on resonance, is followed by spin-spin relaxation. If the RF field following the pulse is not switched off, however, but is phase-adjusted by  $90^\circ$  a different situation occurs (see Figure 2.5). In this situation, the magnetisation becomes aligned with the RF field, which is the only effective field in the rotating frame of reference. The magnetisation undergoes no precession and is said to be spin-locked. The energy difference between the two energy levels becomes equal to  $\gamma\hbar B_1$ . The magnitude of the magnetisation is, however, far larger than can be maintained by  $B_1$ , as it was developed in  $B_0$ . As a result the  $M_y$  magnetisation will decay to its equilibrium value at a rate governed by the exponential time constant  $T_{1\rho}$ .

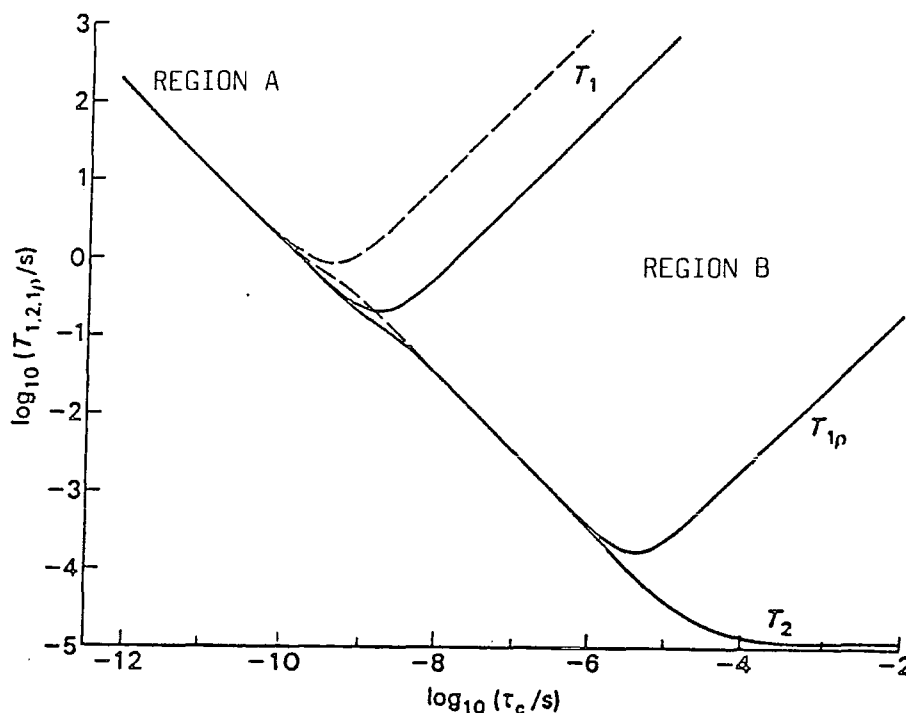
FIGURE 2.5



The difference between these three relaxation parameters occurs as a consequence of the frequency of the local field fluctuations required to cause transitions between energy levels. This is governed by the rate of molecular reorientation, which may be described by the correlation time  $\tau_c$ . This corresponds to the average time taken for a molecule to progress through one radian.

It is of interest to consider how these relaxation times change as  $\tau_c$  changes, This is illustrated in Figure 2.6.

FIGURE 2.6

THE EFFECT OF MOLECULAR MOTION ON RELAXATION

In situations where  $\tau_c$  is very short, rapid isotropic molecular motion causes averaging of the anisotropic interactions described in Section 2.4, to such a degree that  $T_1 = T_{1\rho} = T_2$  (the extreme narrowing limit). As a consequence of this motion, only the isotropic chemical shifts (and sometimes the isotropic value of the Hamiltonian  $\mathcal{H}_J$ ) is observed in the NMR spectrum. As  $\tau_c$  decreases, these interactions are further averaged, resulting in an increase in  $T_1$  (region A, Figure 2.6).

As  $\tau_c$  increases, however, the extent to which these anisotropic interactions are averaged decreases. As a result the amplitudes of the local fields produced by these interactions increase, however, the rate at which these fields fluctuate also decreases. As a result there are fewer local fields that fluctuate at a frequency sufficient to induce transitions between the  $\beta$  and  $\alpha$  energy states in the

laboratory or rotating frame of reference. As a result  $T_1$  increases with increasing  $\tau_c$ . This situation corresponds to region B.

Since  $T_2$  is governed by spin-spin flip-flop transitions which are energy conserving,  $T_2$  decreases as  $\tau_c$  increases.

The NMR spectra of solids are, therefore, dominated by short  $T_2$ 's, as a result of these anisotropic interactions, giving very broad NMR signals which obscure valuable chemical information.

### 2.5.2 RELAXATION MECHANISMS

For  $^{29}\text{Si}$  the commonest mechanisms for relaxation occur as a result of

- (i) DIPOLAR INTERACTIONS
  - (II) SHIELDING ANISOTROPY
  - (III) SPIN ROTATION
- and (IV) SCALAR COUPLING, where the fluctuating local field is produced from modulation of the I-S scalar coupling as a result of fast relaxation or rapid exchange.

### 2.5.3 THE NUCLEAR OVERHAUSER EFFECT

The Nuclear Overhauser Effect (NOE) describes the effect upon the intensity of S spins (e.g.  $^{29}\text{Si}$ ,  $^{13}\text{C}$  etc.) when the resonances of other spins (e.g.  $^1\text{H}$ ) which interact with the S spins through relaxation, are saturated by means of a decoupling field, as a result of the redistribution of spin populations.

The NOE may be measured from the ratio of the intensity of the decoupled resonance ( $I_d$ ) to the coupled resonance ( $I_c$ ), and is defined by the parameter  $\eta_{oe}$ .

$$(2.45) \quad \frac{I_d}{I_c} = 1 + \eta_{oe}$$

The observed NOE effect ( $\eta_{oe}^{obs}$ ) is proportional to the percentage of dipolar relaxation

$$(2.46) \quad \frac{T_{1\text{obs}}}{T_{1\text{DD}}} = \eta_{\text{oe}}^{\text{obs}} \frac{2\gamma_{\text{S}}}{\gamma_{\text{I}}} = \frac{\eta_{\text{oe}}^{\text{obs}}}{\eta_{\text{oe}}^{\text{max}}}$$

It is important to note that for silicon, since  $\eta_{\text{oe}}^{\text{max}} = -2.52$ , the value of  $\eta_{\text{oe}}$  is negative, as a result of the negative magnetogyric ratio for silicon. In solution-state spectroscopy, in conditions where the ( $^{29}\text{Si}$ - $^1\text{H}$ ) dipolar relaxation mechanism dominates, negative or null signals may result.

## 2.6 SELECTIVE AVERAGING TECHNIQUES

In summary, so far it has been stated that in solution-state NMR high resolution NMR spectra are generally observed. Rapid random molecular motion ensures that the anisotropic spin interactions described in Section 2.4 are effectively averaged out. In the solid state, however, these interactions result in broad lines which obscure valuable chemical information. The lineshapes observed in the solid-state are of two types.

### (A) HOMOGENEOUS

These types of lineshapes result from the dipolar interactions between abundant spins, where each spin is effectively coupled to every other spin.

### (B) INHOMOGENEOUS

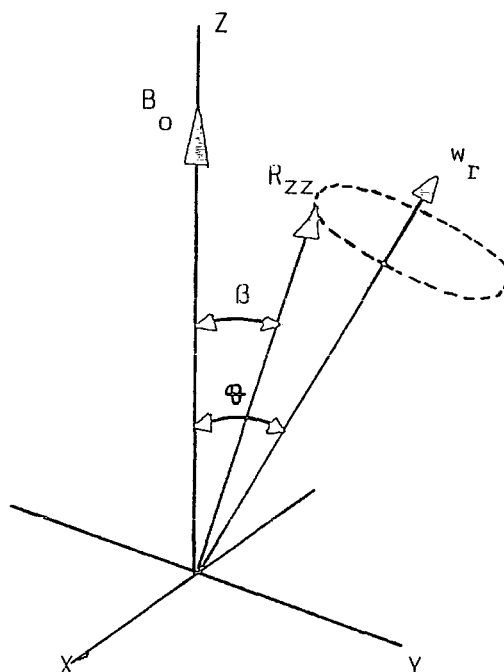
These types of lineshapes result from the dipolar interactions between abundant and rare spins and shielding anisotropy. The resonance frequency for a particular spin is dependent upon the orientation of the PAS with respect to  $B_0$ . Thus in powdered systems, where all orientations are possible, the lineshape results from the superposition of many narrow lines.

Several techniques have been developed, however, which allow the interactions described in Section 2.4 to be selectively averaged, so that the "solution-state" type of spectra may be obtained for solids.

### 2.6.1 MAGIC ANGLE SPINNING

The effects of the direct dipolar interactions and shielding anisotropy in solids can be dramatically reduced using a technique known as magic angle spinning (MAS), in which the sample is rotated at an angle  $\theta$  with respect to  $B_0$  (Figure 2.7) at a rate  $\omega_r$ .

FIGURE 2.7



Inspection of the equations for the Hamiltonians  $\mathcal{H}_D$  and  $\mathcal{H}_{CS}$  (equations 2.39 , 2.40 and 2.43 respectively) reveals they contain a common term  $(1-3\cos^2\beta)$ . The angle  $\beta$  describes the orientations of the PAS of these interactions with respect to  $B_0$ . For these orientation-dependent interactions,<sup>(8)</sup> rotation of the sample at an angle  $\theta$  which is fixed relative to  $B_0$  imposes a time dependence. Provided that the rate of sample rotation is greater than the width of the static interaction, then the average angle of  $\beta$  is such that

$$(2.47) \quad \langle 1-3\cos^2\beta \rangle = \frac{1}{2}(1-3\cos^2\theta)(1-3\cos^2\phi)$$

The powder spectrum is scaled by a factor  $\frac{1}{2}(1-3\cos^2\theta)$  since all values of  $\phi$  are possible. When  $\theta = 54.7^\circ$  is chosen then  $\langle 1-3\cos^2\beta \rangle = 0$  and

averaging of these interactions is accomplished. In situations, however, when the rate of rotation is less than the static linewidth of the particular interaction to be averaged, the static lineshape breaks up to form a series of spinning sidebands located at integral multiples of the spinning frequency either side of the isotropic chemical shift. Analysis of the intensity distribution of these spinning sidebands can then provide information about this partially averaged interaction. This sort of experiment will be discussed further in Chapter 5.

### 2.6.2 HIGH-POWER PROTON DECOUPLING

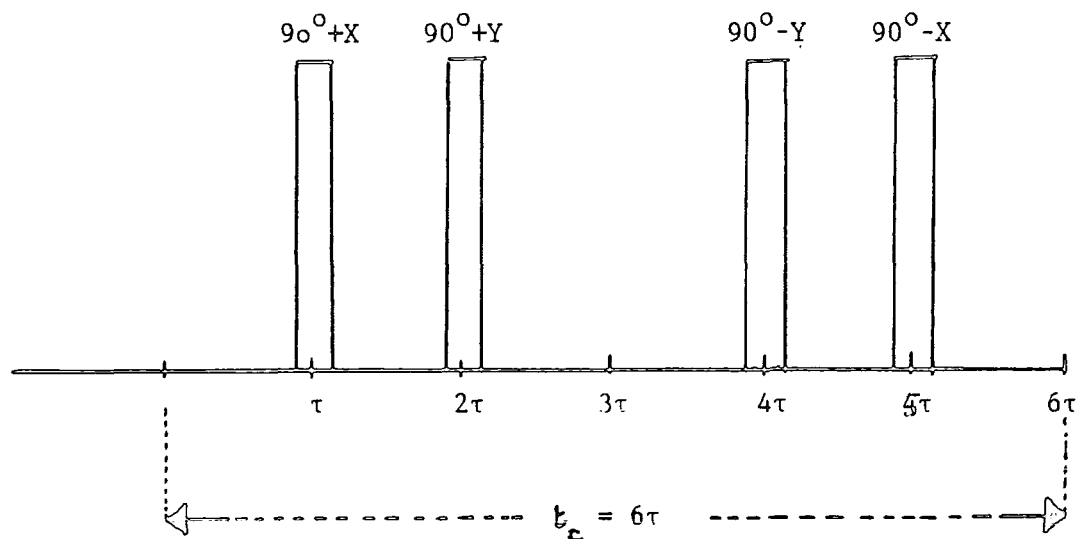
This technique is employed when observing the NMR signal from isotopically or spatially dilute ( $S$ ), <sup>spins</sup> in the presence of strong heteronuclear dipolar interactions with the abundant spins ( $I$ ). These interactions may be so large that they cannot be removed completely by MAS.

The abundant ( $I$ ) spins are effectively decoupled from the rare spins by the application of a strong continuous radio-frequency field on resonance. This technique is exactly analogous to that of heteronuclear decoupling used in solution-state NMR to remove J-coupling. However, since  $|H_{D_{IS}}|$  is very much greater in the solid state than in solution, much larger power levels are required.

### 2.6.3 HOMONUCLEAR SPIN DECOUPLING

A number of multiple pulse techniques have been developed<sup>(10-12)</sup> which are designed to remove homonuclear dipolar interactions between the abundant spins, via manipulation of the spin systems using a sequence of RF pulses. The simplest of these is the WAHUHA sequence<sup>(10)</sup> seen in Figure 2.8.

FIGURE 2.8



The effect of this pulse sequence is to cause the magnetisation to spend equal amounts of time directed along the three axes of the rotating frame of reference. Thus, under conditions where the cycle time for the pulse sequence ( $t_c$ ) is such that  $t_c^{-1} \gg |\kappa \mathcal{H}_{D_{II}}|$ , the magnetisation may be considered to be orientated along the  $-(111)$  direction, (at the magic angle with respect to  $B_0$ ). This situation implies that the effective precession of the magnetisation is about a field  $B_{111}$  directed along this axis, resulting in the suppression of homonuclear dipolar interactions. The chemical shift observed under the WAHUA sequence will be scaled by a factor  $(3)^{-\frac{1}{2}}$ , when the  $90^\circ$  pulse lengths are infinitely small ( $P_\omega = 0$ ).

In this thesis, multiple pulse work has been performed using an eight-pulse sequence known as M-REV8.<sup>(11)</sup> This is designed to suppress errors in the adjustment of pulse phases and lengths. The principle upon which this pulse sequence works is the same as that of

the WAHUHA pulse sequence. However, chemical shifts are scaled by a different factor  $S$ , where

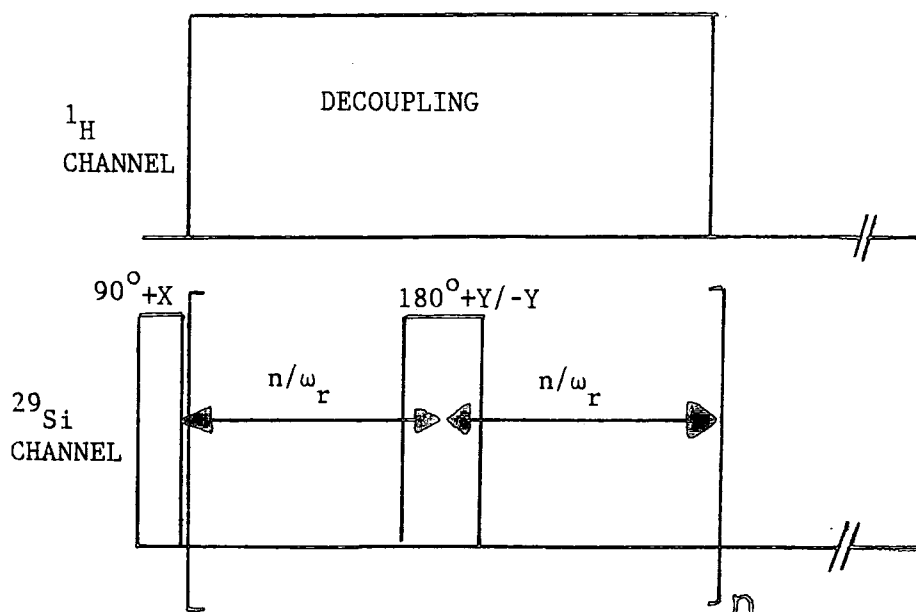
$$(2.48) \quad S = \sqrt{\frac{2}{3}} \left[ 1 + \left[ \frac{6P\omega}{t_c} \right] \left[ \frac{4}{\pi} - 1 \right] \right]$$

This equation takes into account the effects of finite pulse lengths. For a more detailed description of multiple-pulse sequences the reader is referred to References 3 and 5. When MAS is combined with these multiple pulse techniques further narrowing is produced, this results from the averaging of interactions such as shielding anisotropy (scalar coupling is retained). This method is known as Combined Rotation and Multiple-Pulse Spectroscopy or CRAMPS.

#### 2.6.4 CARR-PURCELL-MERIBOOM-GILL $T_2$ MEASUREMENTS (6,6a)

The objective of this experiment is to measure the natural linewidth of a resonance in the absence of any  $B_0$  field inhomogeneity effects. For solid-state experiments, the pulse sequence employed is shown in Figure 2.9.

FIGURE 2.9



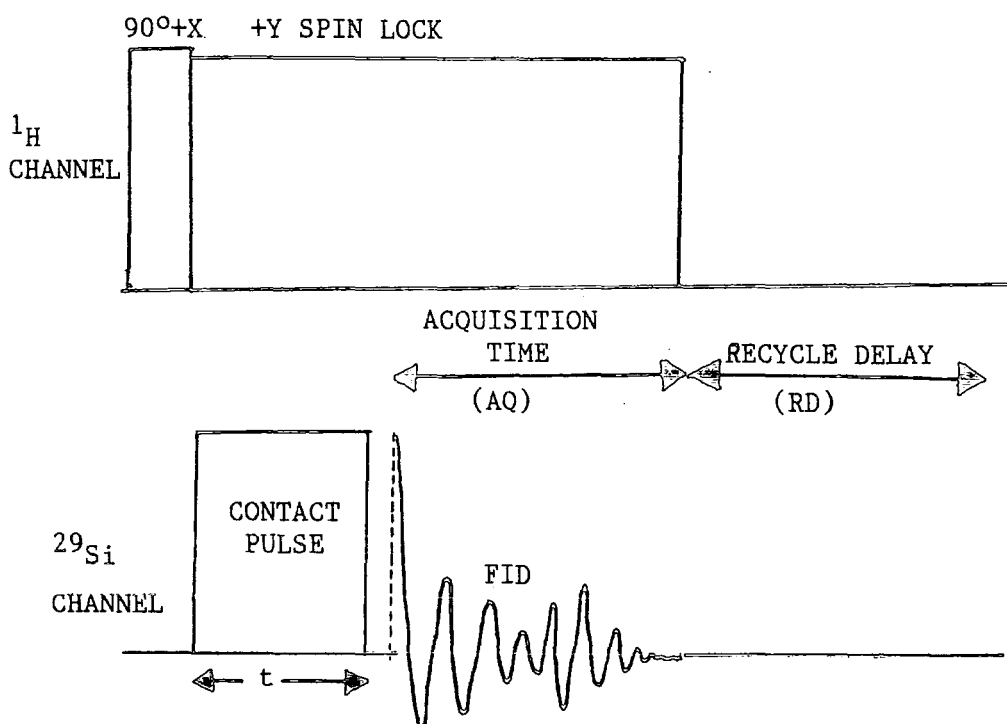
In this experiment, the initial  $\pi/2$  pulse rotates the silicon

magnetisation into the x,y plane (or  $^{29}\text{Si}$  magnetisation is derived by cross-polarisation). The  $^{29}\text{Si}$  spin isochromats then dephase during the time interval  $\tau$ . Following the application of a  $\pi$  pulse, they refocus after a time period of  $2\tau$  to produce an echo. The intensity of the echo peak is then sampled, the delay incremented and the process repeated. The decay of the intensity of the echo peaks with  $\tau$  is exponential and characterised by the natural  $T_2$ , in the absence of inhomogeneous interactions and  $B_0$  field inhomogeneity effects. In order to perform this experiment in the solid state, it is important that the refocusing pulses are rotation synchronised, that is the delay periods  $\tau$  should be equal to integral multiples of the rotation periods ( $\tau = n/\omega$ ). The phase of the refocusing pulse is alternated so as to avoid accumulative errors in the  $\pi$  or  $180^\circ$  pulses.

#### 2.6.5 CROSS-POLARISATION

One of the most important factors of any NMR experiment is the sensitivity of the nucleus under observation. This is dependent upon the natural abundance of the particular isotope, and the population distribution between the various energy levels, resulting from the interaction of its nuclear magnetic moment with a static magnetic field  $B_0$ . For isotopically rare spins (e.g.  $^{29}\text{Si}$ ) or spatially dilute spins (S), there is an intrinsically weak NMR signal compared to that observed for abundant spins (I). In addition, the spin-lattice relaxation times of the rare spins (S) can be very long in comparison with those of the abundant spins (e.g. protons). This factor can severely limit the rate at which experiments may be repeated, and makes it sensible to generate the rare S spin magnetisation from the abundant I spins. This can be achieved using a technique known as cross-polarisation. A simplified pulse sequence to carry out this process is shown in Figure 2.10.

FIGURE 2.10



From equation 2.22, the equilibrium magnetisation for the abundant I spins in the  $B_0$  field is given as

$$(2.49) \quad M_I(0) = C_I B_0 \beta_L$$

At the start of the experiment the abundant spin (I) magnetisation is rotated to lie along the y axis in the rotating frame of reference by a  $90^\circ + x$  pulse. The magnetisation is then spin-locked. In this situation, the abundant spin magnetisation is no longer at thermal equilibrium, since there is more spin order than can be justified for the strength of the spin-locking field  $B_{1I}$ . This situation may be described by saying that the spins have effectively been cooled.

$$(2.50) \quad M_I(0) = C_I B_0 \beta_L = C_I B_{1I} \beta_I$$

where

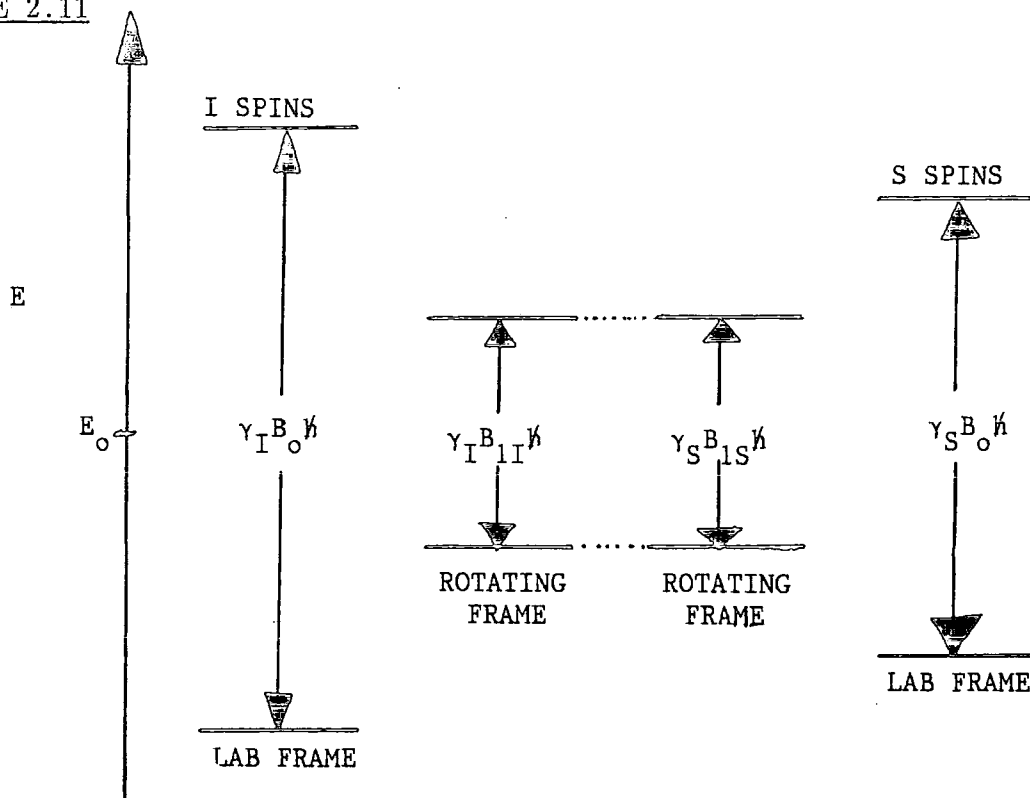
$$(2.51) \quad \frac{1}{kT_I} = \beta_I = \frac{B_0}{B_{1I}} \beta_L$$

At this point the RF in the S spin channel is switched on, and the amplitude of the magnetic field  $B_{1I}$  is adjusted to establish the Hartmann-Hahn matching condition. <sup>(15)</sup>

$$(2.52) \quad \gamma_I B_{1I} = \gamma_S B_{1S}$$

This condition ensures that in their respective rotating frames of reference, the I and S spins precess at the same rate and with equal energies (Figure 2.11).

FIGURE 2.11



This condition then allows the transfer of energy between the two spin systems as a result of energy-conserving flip-flop transitions, induced by the heteronuclear dipolar interaction.

At this point the magnetisation of the S spins in the xy plane of the rotating frame is considered to be zero, and this situation may be described in terms of the S spins, effectively, having an infinite spin temperature (i.e.  $\beta_S \approx 0$ ). When the Hartmann-Hahn matching condition is established spin temperature averaging (or cross-relaxation) will occur as spin energy is redistributed between the two spin systems to give a common spin temperature ( $\beta_f$ ).

Assuming energy conservation in the rotating frame, one may write

$$(2.53) \quad \beta_I C_I B_{1I}^2 + \beta_S C_S B_{1S}^2 = \beta_f [C_I B_{1I}^2 + C_S B_{1S}^2]$$

with  $\beta_S = 0$  equation 2.53 may be written as

$$(2.54) \quad \frac{\beta_f}{\beta_I} = \frac{1}{1+\epsilon\alpha^2}$$

where

$$\epsilon = \frac{N_S}{N_I} \quad \text{and} \quad \alpha = \frac{\gamma_S B_{1S}}{\gamma_I B_{1I}}$$

The S spin magnetisation following cross-polarisation is

$$(2.55) \quad M_S = \frac{M_S(o) \cdot \beta_f B_{1S}}{\beta_L \cdot B_o} = \frac{\gamma_I}{\gamma_S} \frac{\alpha M_S(o)}{1+\epsilon\alpha^2}$$

The intensity of the S spin magnetisation has been enhanced provided  $(\gamma_I/\gamma_S) > 1$ .  $M_S(o)$  corresponds to the intensity of the S spin magnetisation observed in a normal single-pulse experiment.

### CROSS-POLARISATION DYNAMICS

In this discussion so far we have neglected to discuss the various types of relaxation which influence the observed S spin signal intensity at a particular contact time.

For the abundant I spins, three types of relaxation may occur during the course of the cross-polarisation experiment. (16)

- (1) (17) The cross-polarisation experiment begins with a  $90^\circ$  +x preparation pulse which transfers the I spin magnetisation to the y axis, in the rotating frame. In situations where  $T_2^*$  for the I spins is comparable to the  $90^\circ$  pulse duration ( $\rho_\omega$ ) significant spin-spin relaxation can occur during this time period, leading to a reduction in the amount of I spin magnetisation transferred.
- (2) Following spin-locking of the I spin magnetisation, the magnetisation decays at a rate governed by the exponential time constant  $T_{1\rho_I}$
- (3) Loss of I spin magnetisation occurs as a consequence of cross-relaxation with the S spins. The rate at which cross-relaxation occurs is governed by the exponential

time constant  $T_{IS}$ .

For the rare S spins, two types of relaxation occur during the course of the cross-polarisation experiment

- (1) Loss of S spin magnetisation occurs as a result of relaxation in the rotating frame of reference. The rate of decay is governed by the exponential time constant  $T_{1\rho_S}$ .
- (2) Growth of the S spin magnetisation occurs as a consequence of cross-relaxation with the I spins. The rate at which this process occurs is governed by the exponential time constant  $T_{IS}$ .

In the following discussion, it is assumed that  $T_2^* \ll \rho_\omega$  and that  $T_{1\rho_S}^{-1} \approx 0$ . Invoking energy conservation in the rotating frame one may write

$$(2.56) \quad \frac{d\beta_I}{dt} + \epsilon\alpha^2 \frac{d\beta_S}{dt} = 0$$

The variation of the inverse spin temperature with contact time for the S spins is given as

$$(2.57) \quad \frac{d\beta_S}{dt} = \frac{(\beta_I - \beta_S)}{T_{IS}}$$

The variation of the inverse spin temperature with contact time for the I spins is given as

$$(2.58) \quad \frac{d\beta_I}{dt} = -\epsilon\alpha^2 \frac{(\beta_I - \beta_S)}{T_{IS}} - \frac{\beta_I}{T_{1\rho_S}}$$

These coupled differential equations have been solved, under the initial condition  $\beta_S(0)=0$ . The solution for  $\beta_S(t)$  is given as

$$(2.59a) \quad \beta_S(t) = \beta_I(0) \left[ \frac{1}{a_+ + a_-} \right] \left\{ \text{EXP}(-a_- t/T_{IS}) - \text{EXP}(-a_+ t/T_{IS}) \right\}$$

where

$$a_{\pm} = \frac{1}{2} \left[ \frac{1 + \epsilon \alpha^2 + T_{IS}}{T_{1\rho}} \right] \left[ 1 \pm \left[ \frac{4T_{IS}/T_{1\rho}}{1 + \epsilon \alpha^2 + T_{IS}/T_{1\rho}} \right] \right]$$

$$T_{1\rho} \equiv T_{1\rho_I}$$

The variation in the S spin magnetisation with contact time may then be calculated

$$(2.59b) \quad \frac{M_S(t)}{M_S(0)} = \frac{\beta_S(t) \gamma_I \cdot \alpha}{\beta_I(0) \gamma_S}$$

Following the development of the S spin magnetisation, spin-locking of the I spins is continued, in order to provide heteronuclear decoupling whilst the S spins are observed during the acquisition time (AQ).

This technique offers the added advantage that because the S spin magnetisation is derived from the I spins, the recycle delay time (RD) between experiments is governed by the  $T_1$  of the I spins, and not the S spins, which often have considerably longer  $T_1$  values. Combining this technique with MAS allows the observation of isotropic chemical shifts. However, MAS will also influence cross-polarisation dynamics.<sup>(18)</sup> This subject will be discussed in more detail in Chapter 4.

The previous discussion has been concerned with the theoretical aspects of a so-called "single-contact" cross-polarisation experiment. This pulse sequence has been used in this thesis. However two modifications have been incorporated into this pulse sequence, known as spin-temperature inversion<sup>(19)</sup> and flip-back.<sup>(20)</sup>

- (1) The first type of modification (spin-temperature inversion) is required since cross-polarisation experiments are susceptible to two different artifacts. These arise as a result of the long RF-pulse on the S spins. The first of these arises from phase irregularities (glitches), which results in some of the S

spin magnetisation present at the start of the experiment, being rotated by the glitch so that it becomes spin-locked along the RF field. It cannot be distinguished from the S spin magnetisation derived by cross-polarisation. The second type of artifact arises from transients generated by eddy currents in the aluminium probe housing. Both these types of artifacts are determined solely by the characteristics of that pulse, and may be effectively removed by this technique.

- (2) The second type of modification is designed to improve the efficiency with which spectra are acquired using this cross-polarisation technique. In a normal single-contact experiment, the signal to noise ratio (S/N) observed in the spectrum is dependent upon the length of time between experiments (RD) during which time repolarisation of the I spins occurs.

$$(2.60) \quad \left[ \frac{S}{N} \right] \propto n^{1/2} (1-B)$$

where  $n$  = the number of transients acquired and

$$B = \exp \left[ \frac{-RD}{T_{1I}} \right]$$

When  $T_{1I} > T_{1\rho I} > A Q$  repolarisation of the I spins may be induced by rotating the I spin magnetisation back to be aligned along the field direction  $B_0$  following acquisition, thereby improving the efficiency of the experiment. Under these conditions

$$(2.61) \quad \left[ \frac{S}{N} \right] \propto n^{1/2} \frac{(1-B)}{(1-AB)}$$

where  $A = \exp \left[ \frac{-A Q}{T_{1\rho I}} \right]$

## 2.7 QUADRUPOLEAR NUCLEI

In the preceding discussion we have been concerned with nuclei with a spin quantum number  $I = \frac{1}{2}$ . However, for nuclei where  $I > \frac{1}{2}$ , the nuclei not only possess a spin angular momentum but also an electric quadrupole moment. The direction of quantisation, therefore, depends upon the magnitude of  $B_0$  and the quadrupolar interaction. The Hamiltonian describing this quadrupolar interaction may be written in the PAS as

$$(2.62) \quad \mathcal{H}_Q = \frac{\chi h}{4I(2I-1)} \left[ \left[ 3I_Z^2 - I(I+1) \right] + \frac{1}{2}\eta \left[ I_X^2 + I_Y^2 \right] \right]$$

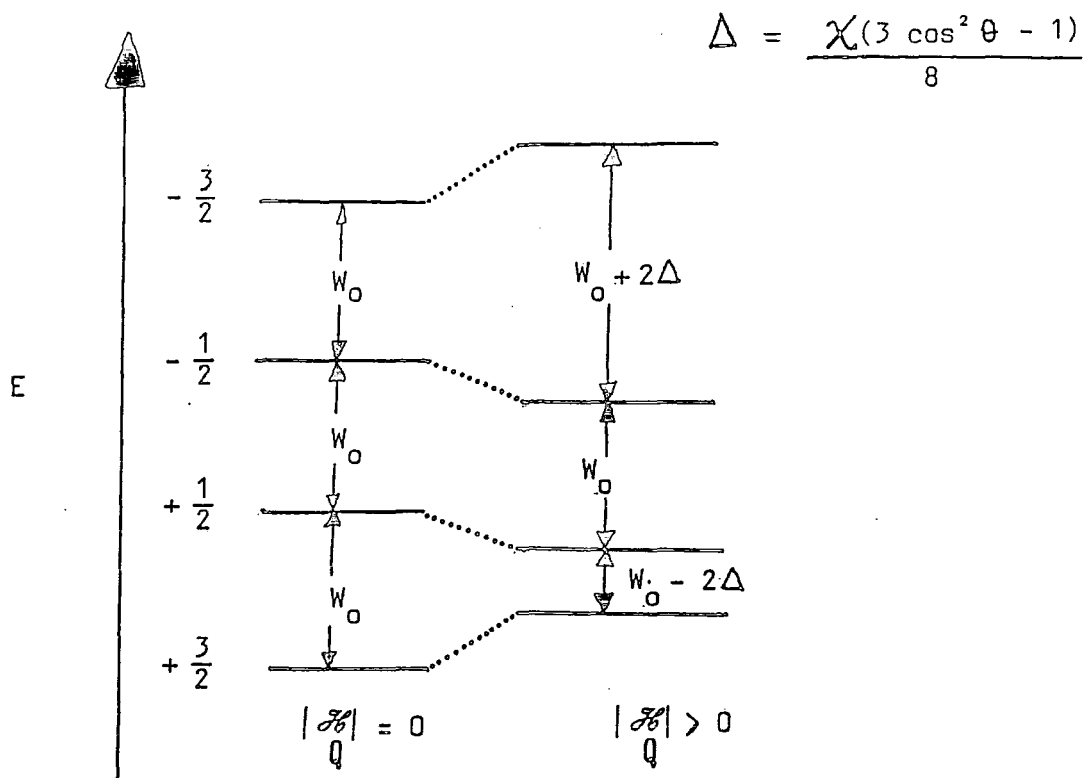
where  $\chi$  is the quadrupolar coupling constant, given in frequency units.

$$(2.63) \quad \chi = \frac{e^2 Q q_{ZZ}}{h}$$

$eQ$  is the electric quadrupole of the nucleus, and  $eq_{ZZ}$  is the electric field gradient (e.f.g) experienced by the nucleus. If the nucleus is in an environment which has perfect spherical, octahedral or tetrahedral symmetry then  $q_{ZZ} = 0$ , otherwise  $q_{ZZ} > 0$ ,  $\eta$  is the asymmetry parameter.

When a nucleus with  $I = \frac{3}{2}$  (e.g.  $^{23}\text{Na}$ ) is placed in a magnetic field there are four possible orientations (or energy levels) possible (Figure 2.12) (it is assumed  $|\mathcal{H}_Z| \gg |\mathcal{H}_Q|$ ).

FIGURE 2.12



From Figure 2.12 it may be seen that in the absence of any efg the energy levels are all degenerate, and transitions between the energy levels occur at the same frequency. However, in the presence of an efg, while the  $(+\frac{1}{2} \leftrightarrow -\frac{1}{2})$  transition remains unaffected by first order quadrupolar interactions, the energy of the  $(+\frac{3}{2} \leftrightarrow +\frac{1}{2})$  and  $(-\frac{3}{2} \leftrightarrow -\frac{1}{2})$  transitions are changed.

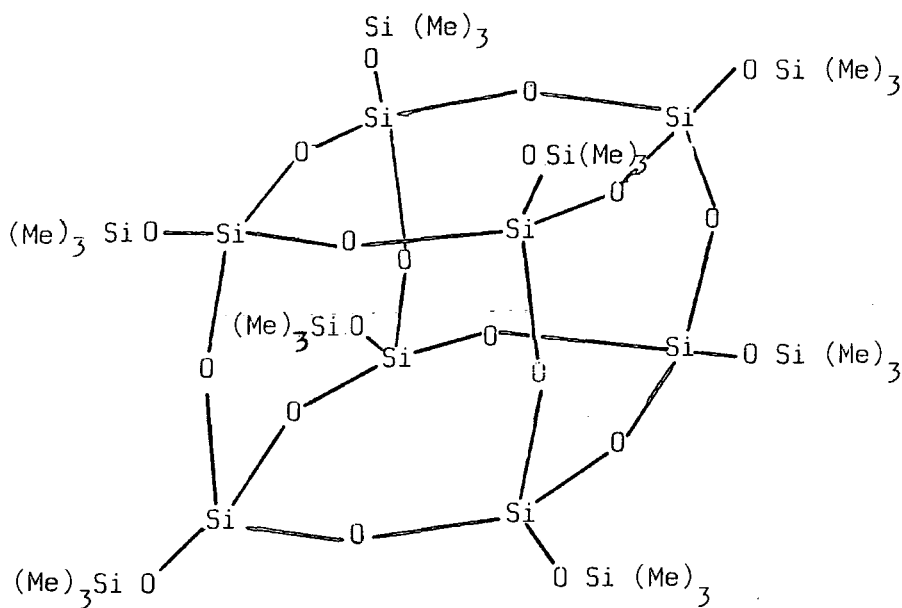
In the solution state, the longitudinal and transverse spin relaxation produced by the quadrupolar interaction will only be simple exponential decays for spin  $I=3/2$  nuclei if the efg's fluctuate more rapidly than the Larmor frequency. If this condition is not satisfied, however, longitudinal and transverse relaxations are the sum of two decaying exponentials. In these circumstances it is sometimes possible to obtain information concerning the magnitude of the quadrupolar coupling constant ( see Chapter 7 ).

## 2.8 NOMENCLATURE

In this thesis, for the presentation of the structure of building units in silicate minerals or silicate anions in solution, the commonly used  $Q_y^n$  notation is adopted. In this notation,  $Q$  represents a silicon atom bonded to four oxygen atoms forming a tetrahedron. The superscript  $n$  denotes the connectivity (i.e. the number of other  $Q$  units attached to the  $SiO_4$  tetrahedron under study (see Figure 5.1). The subscript  $y$  denotes the number of those units of a given type in silicate anions.

The "M" notation refers to  $-OSi(CH_3)_3$  groups. Thus  $Q_8^3M_8$  has the structure shown in Figure 2.13.

FIGURE 2.13



### 3.0 CHAPTER THREE

#### EXPERIMENTAL

##### 3.1 THE BRUKER CXP200 NMR SPECTROMETER

Solid-state NMR spectra shown in this thesis were all acquired using the Bruker CXP200 NMR spectrometer. This instrument is equipped with an Oxford Instruments superconducting solenoid magnet, with an operating field of 4.7 Tesla, producing a resonance frequency of 200.13 MHz and 39.758 MHz for  $^1\text{H}$  and  $^{29}\text{Si}$  respectively.

The CXP is a dual-channel spectrometer, capable of simultaneous irradiation of low frequency nuclei (e.g.  $^{29}\text{Si}$ ) and high frequency nuclei (e.g.  $^1\text{H}$ ). The radio frequency (RF) pulses are controlled by a 16-step pulse programmer that produces  $\pm x, \pm y$  pulses for the low frequency channel, and  $\pm v, \pm w$  pulse commands for the high-frequency channel. The pulses for the two channels are controlled by separate frequency synthesizers. The flexible pulse programmer enables a wide variety of experiments to be undertaken. In addition a microprogram facility allows fully automated experiments to be performed. Data and experimental conditions (with the exception of the spectrometer reference frequency SR) can be stored on hard or floppy discs. Chemical shifts are calculated by the instrument following calibration. For further details of the CXP200, the reader is directed to Reference 1.

##### 3.1.1 PROBES USED FOR SOLID-STATE NMR STUDIES

Three types of probes were routinely used during the course of this work.

- (A) Two wide-bore (84.5 mm) broad-band, dual-channel, high-resolution commercial double-bearing probes covering a frequency range of 20-90 MHz. The double-bearing system with "bullet" shaped rotors allows samples to be rotated at the magic angle, at rates between 100 Hz - 5 kHz.

- (B) One high-power, high-frequency solids probe. This probe is designed for static  $T_1(^1\text{H})$  and  $T_{1\rho}(^1\text{H})$  measurements.
- (C) One home-built probe for proton CRAMPS experiments. The construction of this probe is described in detail elsewhere<sup>(2,3)</sup>.

### 3.1.2 SHIMMING AND $^1\text{H}$ PULSE CALIBRATION

The homogeneity of the magnetic field was maximised by the correct adjustment of the shim gradients, in order to minimise the linewidth of the proton signal observed from a sample of silicone gum. Spectra were acquired using a recycle time of 2 seconds. The linewidth at half height of the resonance observed was typically 6-10 Hz, and the signal occurs at 0.2 ppm with respect to tetramethylsilane (TMS). The proton FID was then set on resonance and the  $90^\circ$  pulse length calibrated by observing the appropriate  $180^\circ$  "null" signal. For the double-bearing probe  $4\mu\text{s}$   $90^\circ$  pulse lengths were used (corresponding to a proton decoupling frequency of 62.5 KHz). For the high-power solids probe  $2\mu\text{s}$   $90^\circ$  pulse lengths were employed.

### 3.1.3 SETTING THE ANGLE

The angle at which the rotor spins, relative to the external magnetic field, was adjusted to the magic angle ( $54.7^\circ$ ) by maximising the number of rotational echoes observed in the  $^{127}\text{I}$  spectra of KI. The sidebands observed result from the spinning modulation of the first-order quadrupolar interaction arising from imperfections in the crystal lattice. This technique has been shown to be accurate to within  $\pm 0.1^\circ$  of the magic angle. The nucleus  $^{127}\text{I}$  has a spin  $I = \frac{5}{2}$ , and a resonance frequency on the CXP200 of 40.047 MHz<sup>(4)</sup>.

### 3.1.4 $^{29}\text{Si}$ REFERENCING AND PULSE CALIBRATION

The  $^{29}\text{Si}$  chemical shifts were routinely obtained using the sodium salt of trimethylsilyl-1-propanesulphonic acid as a reference. This compound exhibits a single isotropic chemical shift of +1.18 ppm with

respect to TMS. The  $^{29}\text{Si}$   $90^\circ$  pulse length was established by careful adjustment of the gain setting on the low frequency amplifier until the Hartmann-Hahn matching condition was established, and cross polarisation observed (see Chapter 4).

### 3.2 $^1\text{H}$ CRAMPS

The rotors used in the  $^1\text{H}$  CRAMPS experiments outlined in this thesis were of the "broom stick" design<sup>(2,3)</sup>. These rotors are made from Kel-F-128<sup>(2)</sup> in order to avoid a  $^1\text{H}$  background signal. The rotors contain a 3 mm spherical sample chamber, so as to improve the homogeneity of the RF pulses across the sample volume. The mass of the sample relative to that of the rotor is small, thereby allowing stable spinning at high rates (ca. 3-5.5 KHz).

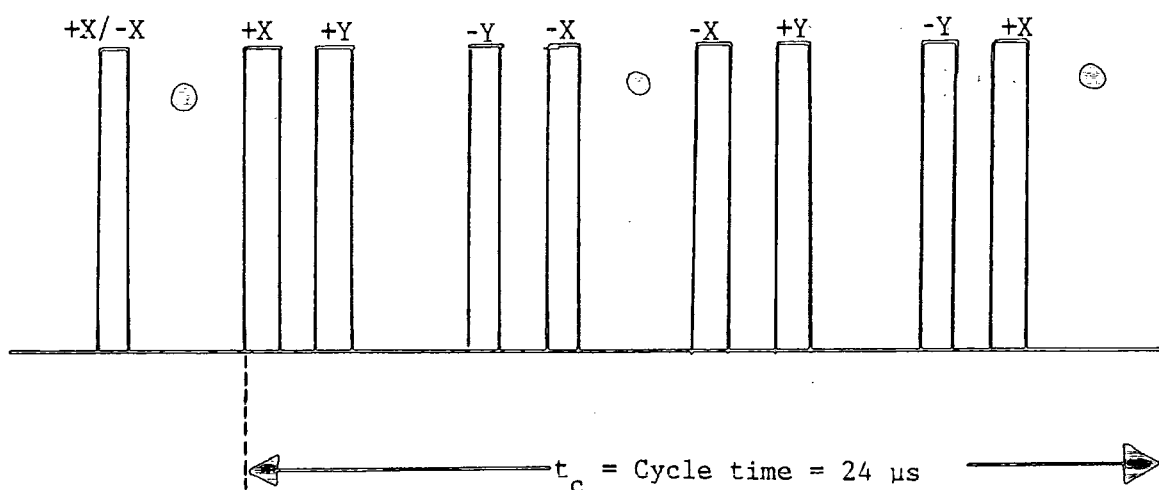
In setting up any  $^1\text{H}$  CRAMPS experiments, a number of factors need to be contended with in order to obtain the best resolution. These are magnetic field inhomogeneity, pulse-amplitude errors, phase glitches, pulse phase errors, dc offset, pulse breakthrough and other spectral artifacts. The magnetic field inhomogeneity is minimised by using flat wire coils, spherical sample chamber rotors, and by careful shimming using either water or silicone gum.

The calibration of pulse amplitudes and phases, and the minimisation of phase glitches is achieved using a number of specially designed pulse sequences. For further details the reader is directed to References 2 and 4. The  $^1\text{H}$  CRAMPS work obtained in this thesis was performed using the M-REV 8 pulse sequence, employing spin-temperature inversion to minimise the effects of pulse breakthrough<sup>(4)</sup> (Figure 3.1). The M-REV 8 pulse sequence was employed rather than other multiple pulse sequences (e.g. WAHUA, Br-24), since this sequence is known to yield the best results at 200 MHz.<sup>(5)</sup>

FIGURE 3.1

MREV-8

○ DATA POINT SAMPLED



The magic angle was adjusted by maximising the length of the FID observed for adamantane under  $^1\text{H}$  CRAMPS conditions,<sup>(5)</sup> or alternatively, by observing the  $^1\text{H}$  CRAMPS spectrum of potassium hydrogen sulphate. This compound exhibits two resonances, and the lineshapes observed are very sensitive to the setting of the magic angle.<sup>(3)</sup>

Chemical shifts for  $^1\text{H}$  CRAMPS spectra shown in this thesis are reported relative to TMS. In practice, a few crystals of adamantane were added to each sample, as an internal chemical shift standard. The  $^1\text{H}$  CRAMPS spectrum of adamantane exhibits a single resonance at 1.74 ppm with respect to TMS, with a linewidth at half height of 0.2 ppm (i.e. 40 Hz at 200 MHz). Scaling factors for the chemical shift scale were determined experimentally by co-adding the FID's of adamantane, acquired at different offset frequencies. Fourier transformation then yielded a spectrum characterised by a series of peaks separated by the difference in the offset frequency. However,

because  $^1\text{H}$  CRAMPS scales the chemical shifts, these peaks appear closer together. The scaling factor was then determined by measuring the ratio of the real and observed frequency separation between the peaks.

### 3.3 RELAXATION TIME MEASUREMENTS

#### 3.3.1 SOLID-STATE WORK

In this thesis, direct measurements of the  $^1\text{H}$  longitudinal relaxation times of solid samples were performed using the saturation recovery technique.<sup>(11)</sup> Direct measurements of  $T_{1\rho}(^1\text{H})$  values were made using the variable spin-locking time technique.<sup>(1)</sup> These are standard techniques, and for further information the reader is directed to References 11 and 1 respectively.

The data obtained from these experiments was then transferred from the CXP200 to a BBC computer, where it could be analysed in terms of theoretical equations and fitted using the Simplex method.<sup>(12)</sup> The program then displayed the relaxation times and percentage composition of each phase in the system. This program was written by B.J. Say.

The variation of the signal intensity observed for the S spins with contact time in CP experiments was fitted to equation 3.1 (see Chapter Four), using a BBC computer program.

$$(3.1) \quad M_S(t) = \frac{M_S(0)\gamma_I \exp(-t/T_{1\rho}) - M_S(0)\gamma_I \cdot \exp(-t/T_{IS})}{\gamma_S(1-\lambda)}$$

where  $\lambda = T_{IS}/T_{1\rho}$

The intensity of the peak of interest, at each given contact time (t) is entered into the program, and a least squares fit of the experimental data to equation 3.1 is performed, from which values of  $T_{1\rho}$  and  $T_{IS}$  may be determined and the optimum contact time (i.e. the contact time at which maximum signal intensity is observed,  $t^{\text{opt}}$ ).

The least squares fit was performed firstly by fitting the experimental data obtained under conditions where  $t \ll t^{\text{opt}}$  to a plot of

$\ln M_G(t)$  against  $t$ , in order to determine  $T_{1S}$ , and then by fitting data obtained under conditions where  $t \gg t^{opt}$ , to a plot of  $\ln M_G(t)$  against  $t$ , in order to determine  $T_{1\rho}$ . The full theoretical curve was then displayed with all the data points, and the "goodness" of the fit determined by the sum of the squares of the error.

### 3.3.2 SOLUTION-STATE WORK

Measurements of  $^{29}\text{Si}$  and  $^{23}\text{Na}$  longitudinal relaxation times were performed using the inversion recovery technique.<sup>(11)</sup> The data obtained from experiments was then analysed in terms of theoretical equations by the Aspect 3000 computer on the AC250,<sup>(6)</sup> via the Simplex method.<sup>(12)</sup>

### 3.4 MATERIALS STUDIED

The chemicals that have been studied in this thesis are listed here, roughly grouped according to the chapters they are discussed in. The author is indebted to Unilever Research, Professor L.S. Dent-Glasser and Dr. A.R. Grimmer, from whom some samples were obtained.

#### 3.4.1 CHAPTER FOUR

SAMPLE	SOURCE
$\text{Na}_2\text{SiO}_3 \cdot 5\text{H}_2\text{O}$	BDH CHEMICALS
1,1,1-TRIMETHYL TRIPHENYLDISILANE	LANCASTER SYNTHESIS
TRIMETHYLSILYL-1-PROPANE SULPHONIC ACID	LANCASTER SYNTHESIS
$\text{Q}_8^3\text{M}_8$	A.R. GRIMMER

#### 3.4.2 CHAPTER FIVE

SAMPLE	SOURCE
$\text{Na}_2\text{SiO}_3 \cdot 9\text{H}_2\text{O}$	LINTON PRODUCTS
DATOLITE	NATURAL (NEW YORK)
THORTVIETITE	NATURAL (A.R. GRIMMER)
TILLEYLITE	NATURAL (A.R. GRIMMER)

XONOTLITE	NATURAL (A.R. GRIMMER)
APOPHYLLITE	NATURAL (ARIZONA)
$[N(Me_4)]_8Si_8O_{20} \cdot 69H_2O$	SYNTHETIC (UNILEVER RESEARCH)
KANEMITE	SYNTHETIC (L.S. DENT-GLASSER)
OCTOSILICATE	SYNTHETIC (L.S. DENT-GLASSER)
HEXAPHENYLDISILANE	LANCASTER SYNTHESIS
HEXAPHENYLDISILOXANE	LANCASTER SYNTHESIS
TRIPHENYLSILANE	PIERCE CHEMICAL COMPANY
OCTAPHENYLCYCLOTETRASILANE	LANCASTER SYNTHESIS
TRIBENZYLSILANE	PIERCE CHEMICAL COMPANY

### 3.4.3 CHAPTER SIX

Silica xerogels studied for this chapter were all obtained or prepared at the Unilever Research laboratories in Port Sunlight, Wirral. Further details are given in Chapter Six.

### 3.4.4 CHAPTER SEVEN

Details concerning the nature of silicate solutions and the colloidal silica studied are given in Chapter Seven.

### 3.5 THE BRUKER AC 250 NMR SPECTROMETER

All solution-state NMR spectra obtained during the period of this research work were acquired using the Bruker AC 250 NMR spectrometer. This instrument is equipped with an Oxford Instruments super-conducting solenoid magnet with an operating field of 7.05 Tesla, producing a resonance frequency of 250.16 MHz, 66.18 MHz and 49.7 MHz for  $^1H$ ,  $^{23}Na$  and  $^{29}Si$  nuclei respectively.

The AC 250 is a dual-channel spectrometer capable of the simultaneous irradiation of both low frequency nuclei (e.g.  $^{23}Na$  and

$^{29}\text{Si}$ ) and the high frequency proton spins. The flexible pulse programmer and microprogram facility allow a range of fully automated experiments to be performed. Data and experimental conditions can be stored on hard or floppy discs. Chemical shifts are calculated by the instrument after calibration. For further details of the AC250, the reader is directed to Reference 6.

### 3.6 CHARACTERISATION OF SAMPLES STUDIED

During the study of silica xerogels and aqueous alkaline silicate solutions, a number of techniques were employed in order to characterise the physical properties and chemical composition of these materials. These techniques will be briefly summarised here.

#### 3.6.1 SURFACE AREA MEASUREMENTS

Measurements of the specific surface area of samples of silica xerogels were made using Sorptly 1750 which works on the static volumetric principle. Prior to surface area measurements all samples were heated in a fan oven at  $140^{\circ}\text{C}$  for 6 hours, to remove physisorbed water. The samples were then heated under vacuum ( $10^{-3}$  Torr) at  $150^{\circ}\text{C}$  for one hour to out gas the sample. The sample was then sealed under vacuum in a vessel of known volume, which was then cooled in liquid nitrogen.

In order to determine the specific surface area of a xerogel, via nitrogen adsorption, one needs to calculate the number of gas molecules required to form a monolayer of adsorbed nitrogen upon the surface. However, a complete monolayer of molecules may also adsorb other molecules, as a consequence of Van der Waals forces, and/or molecules may condense in pores. It is, therefore, often difficult to decide with precision when adsorption of the first monolayer is complete.

In order to overcome this problem, specific surface area measurements were carried out using a technique based upon the theory

of multilayer adsorption developed by Brumauer, Emmet and Teller.<sup>(43)</sup> In this theory, it is considered that the surface of a silica holds fixed adsorption sites for nitrogen molecules, which may be adsorbed in layers. At any given temperature and pressure, the adsorbed molecules are in a state of dynamic equilibrium with molecules in the gaseous phase. It is assumed that at the boiling point of the gas (-196°C for N<sub>2</sub>) the heat of adsorption for all layers beyond the first is equal to the latent heat of condensation (L), and nitrogen molecules condense upon the surface as a liquid, such that, when the vapour pressure (P) reaches the saturated vapour pressure (P<sub>0</sub>) the number of adsorbed layers is infinite. On the basis of these assumptions the BET equation is given as

$$(3.2) \quad \frac{P}{V_a(P_0 - P)} = \frac{1}{V_m C} + \frac{(C-1) \cdot P}{V_m C P_0}$$

where

P = The adsorption equilibrium pressure

P<sub>0</sub> = The saturation pressure

V<sub>m</sub> = The volume of adsorbed gas forming the mono-molecular layer

L = The latent heat of condensation

E<sub>1</sub> = The adsorption energy for the first layer

C = EXP[(E<sub>1</sub>-L)/RT]

For a given silica sample V<sub>m</sub> and C are constant, so that the BET equation may be expressed as

$$(3.3) \quad \frac{P}{V_a(P_0 - P)} = \frac{MP}{P_0} + b$$

where M and b are constants

$$(3.4) \quad M = \frac{(C-1)}{V_m C} \quad b = \frac{1}{V_m C} \approx 0$$

Plotting P/V<sub>a</sub>(P<sub>0</sub>-P) against P/P<sub>0</sub> should yield a straight line graph in the pressure range 0.05 to 0.35 P/P<sub>0</sub>, from which V<sub>m</sub> and C may

be calculated from the slope and intercept. However, the Sorpty 1750 works on a single point measurement and assumes the intercept to be zero (i.e.  $b = 0$ ). It is considered that this assumption gives rise to no more than a 7% error in the surface area measurement.<sup>(8)</sup> The value of  $V_m$  is calculated from a single measurement of  $V_a$  at  $P/P_0 = 0.30$ . The specific area ( $A/m^2 \text{ g}^{-1}$ ) is then given by

$$(3.5) \quad A = \frac{6.023 \times 10^{23} V_m a}{22414 x m}$$

where  $m$  is the mass of the degassed silica sample, and  $a$  is the area of the adsorbed nitrogen molecule ( $a = 0.162 \text{ nm}^2$ ).<sup>(8)</sup>

It is important to note that since the Sorpty 1750 calculates surface areas from the measurement of a single data point, rather than analysis of the full adsorption isotherm, and also assumes that  $E_1$  is constant between all samples and uniform across the sample surface, additional errors are introduced. The actual error in the surface areas measured is considered to be not more than 10%.<sup>(10)</sup>

At the time this work was undertaken, facilities for the more accurate measurement of surface areas were not available to the author.

### 3.6.2 PORE CHARACTERISATION

Pore characterisation of silica samples was performed using the Micrometrics 9220 mercury porosimeter.<sup>(9)</sup>

The pressure ( $P$ ) required to force mercury into a pore of a given diameter is inversely related to the diameter, and volume of mercury in the pores. This pressure is a measure of the number and length of the pores. Hence by measuring the volume of mercury that intrudes into the sample as a function of pressure, information can be gained concerning the pore size distribution and surface area.

The pores are characterised by determining:

- (i) The specific pore area

- (ii) The specific pore volume
- (iii) The average pore diameter (or most abundant pore diameter)
- (iv) The pore size distribution. This is determined by measuring the incremental intrusion volume as a function of pressure or pore diameter.

### 3.6.3 CHEMICAL ANALYSIS OF SILICA XEROGELS

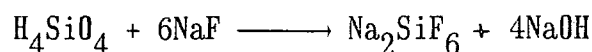
In order to determine the sodium ion concentration within xerogel samples, 0.5 g of the oven-dried sample was weighed into a PTFE bottle and digested in 20 ml of 40% (w/w) HF. The sodium ion concentration present in the solution was then determined via flame photometry and the sodium ion concentration of the gel determined.<sup>(10)</sup> Measurements were made using a Gallenkamp Flame Analyser.

### 3.6.4 CHEMICAL ANALYSIS OF AQUEOUS ALKALINE SILICATE SOLUTIONS

In order to determine the basic metal oxide ( $M_2O$ ) content of a given silicate solution, a known mass of the solution was taken ( $m_1 \approx 2$  g) and diluted with  $100 \text{ cm}^3$  of deionized water. After addition of methyl red indicator, the  $M_2O$  content was determined via direct titration with 1 M solution of HCl. The volume of HCl required to neutralise the solution ( $V_1$ ) was then used to calculate the molality of  $M_2O$  in solution.

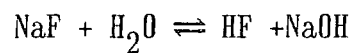
$$(3.6) \quad [M_2O] / \text{MOLALITY} = \frac{MV_1}{2m_1}$$

In order to determine the silica concentration of the solution, 5 g of sodium fluoride was then added to the neutralised silicate solution. The sodium fluoride then reacts with silica in solution



It is assumed that complete depolymerisation of the silicate species in solution occurs. The amount of sodium hydroxide produced by this reaction was then determined by titration with a solution of 1 M HCl.

The volume of acid required to neutralise the solution was recorded ( $V_2$ ). However, since sodium fluoride may also react with water via the reaction



a "blank" titration of a solution of 5 g of NaF in 100 cm<sup>3</sup> of deionized water was also measured ( $V_B$ ). The molality of SiO<sub>2</sub> in solution was then calculated by equation 3.7.

$$(3.7) \quad [\text{SiO}_2]/\text{MOLALITY} = \frac{M(V_2 - V_B)}{4m_1}$$

## 4.0 CHAPTER FOUR

### $^{29}\text{Si}$ CROSS-POLARISATION (CP) AND REFERENCE STANDARDS

#### 4.1 INTRODUCTION

Over the last few decades  $^{29}\text{Si}$  NMR techniques have been employed in the investigation of a wide variety of silicon-containing systems, both in solution and in the solid-state. In the early years of these investigations using solution-state NMR, a number of reference compounds were suggested, including polydimethylsiloxane<sup>(1)</sup>, tetramethoxysilane<sup>(2)</sup>, tetrafluorosilane<sup>(3)</sup> and octamethylcyclotetrasiloxane.<sup>(2)</sup> In spite of these suggestions, however, tetramethylsilane (TMS) has become the most widely accepted internal and external reference standard.

In the solid-state,  $^{29}\text{Si}$  NMR chemical shifts have been reported relative to TMS, the spectrometers being calibrated using either liquid TMS, a replacement liquid organosilicon compound, or a solid silicon-containing compound which exhibits chemical shifts that are known relative to TMS. The choice of a liquid replacement reference compound for  $^{29}\text{Si}$  solid-state NMR work, however, has the disadvantage that it is not possible to carry out cross-polarisation from the proton spins to silicon nuclei, as a consequence of molecular motion averaging dipolar interactions. Therefore it is impossible to establish the Hartmann-Hahn matching condition, and to take advantage of the useful experiments that can be performed using  $^{29}\text{Si}$  -  $^1\text{H}$  cross-polarisation techniques.

In order to establish the conditions necessary for  $^{29}\text{Si}$  -  $^1\text{H}$  CP and to reference the spectrometer, three silicon-containing compounds were examined for use as secondary replacement standards. These compounds were  $\text{Q}_8^3\text{M}_8$ ,<sup>(4)</sup> the sodium salt of trimethylsilyl-1-propane sulphonic acid (TMS salt)<sup>(5)</sup>, and disodium orthosilicate pentahydrate ( $\text{Na}_2\text{SiO}_3 \cdot 5\text{H}_2\text{O}$ ). The TMS salt and  $\text{Q}_8^3\text{M}_8$  have both been used

by other workers as secondary replacement standards, however very little information (if any) exists in the literature concerning either the proton relaxation behaviour and  $^{29}\text{Si}$ - $^1\text{H}$  CP characteristics of these systems or of the best resolution that can be achieved (i.e. the natural linewidths) and the sensitivity of each compound to the Hartmann-Hahn matching condition. All these measurements must be performed before one can evaluate the suitability of each compound, as a secondary replacement standard and for setting the matching condition.

## 4.2 EXPERIMENTAL

Measurements of the proton relaxation times  $T_1$  and  $T_{1\rho}$  were made via the saturation recovery and variable spin-locking time experiments. These are standard techniques, and are described elsewhere.<sup>(6)</sup> The natural linewidths of the  $^{29}\text{Si}$  resonance signals were measured using the rotation synchronised Carr-Purcell -Meriboom-Gill pulse sequence discussed in Chapter Two.

In order to measure the sensitivity of each of these compounds to the Hartmann-Hahn matching condition, it is necessary to consider CP dynamics (see Section 2.6.5). The signal intensity observed at a specific contact time  $t$  is given by equation 2.59 in Chapter Two. Under conditions where  $\alpha = 1.0$  (Hartmann-Hahn match),  $T_{1\rho} \gg T_{\text{IS}}$  and  $N_{\text{I}} \gg N_{\text{S}}$ , equation 2.59 may be simplified to

$$(4.1a) \quad \frac{M_{\text{S}}(t)}{M_{\text{S}}(0)} = \frac{\gamma_{\text{I}}}{\gamma_{\text{S}}(1-\lambda)} \{1 - \text{EXP}(-(1-\lambda)t/T_{\text{IS}})\} \text{EXP}(-t/T_{1\rho})$$

where  $\lambda = T_{\text{IS}}/T_{1\rho}$

Using equation 4.1a<sup>(7)</sup> it is possible to estimate the CP dynamics of each of the compounds by means of a variable contact-time experiment.

In this experiment, the intensity of the signal observed is measured as a function of the contact time and the experimental data are fitted to the equation 4.1, in order to calculate values for  $T_{\text{IS}}$ ,

$T_{1\rho}$  and the % CP efficiency (equation 4.1b), and the contact time at which the maximum signal intensity is observed ( $t^{\text{opt}}$ ).

$$(4.1b) \quad \%CP = \frac{\gamma_S M_S(t^{\text{opt}})}{\gamma_I M_S(0)} \times 100$$

The sensitivity of each of the compounds to the Hartmann-Hahn matching condition, was examined by means of variable  $B_{1S}$  field experiments. In these experiments, the proton spin-locking field was set at 62.5 kHz. Then the magnitude of the  $B_{1S}$  field for the silicon nuclei was adjusted by means of the pulse attenuator helipot on the CXP200. This changes the power output from the transmitter to the probe. A calibration plot was then constructed of the voltage output from the transmitter as a function of the reading on the helipot adjustment (Figure 4.1).

The strength of the silicon  $B_{1S}$  field may be calculated via equation 4.2<sup>(8)</sup>

$$(4.2) \quad B_{1S} = 3 \left[ \frac{PQ}{f_0 V_0} \right]^{\frac{1}{2}}$$

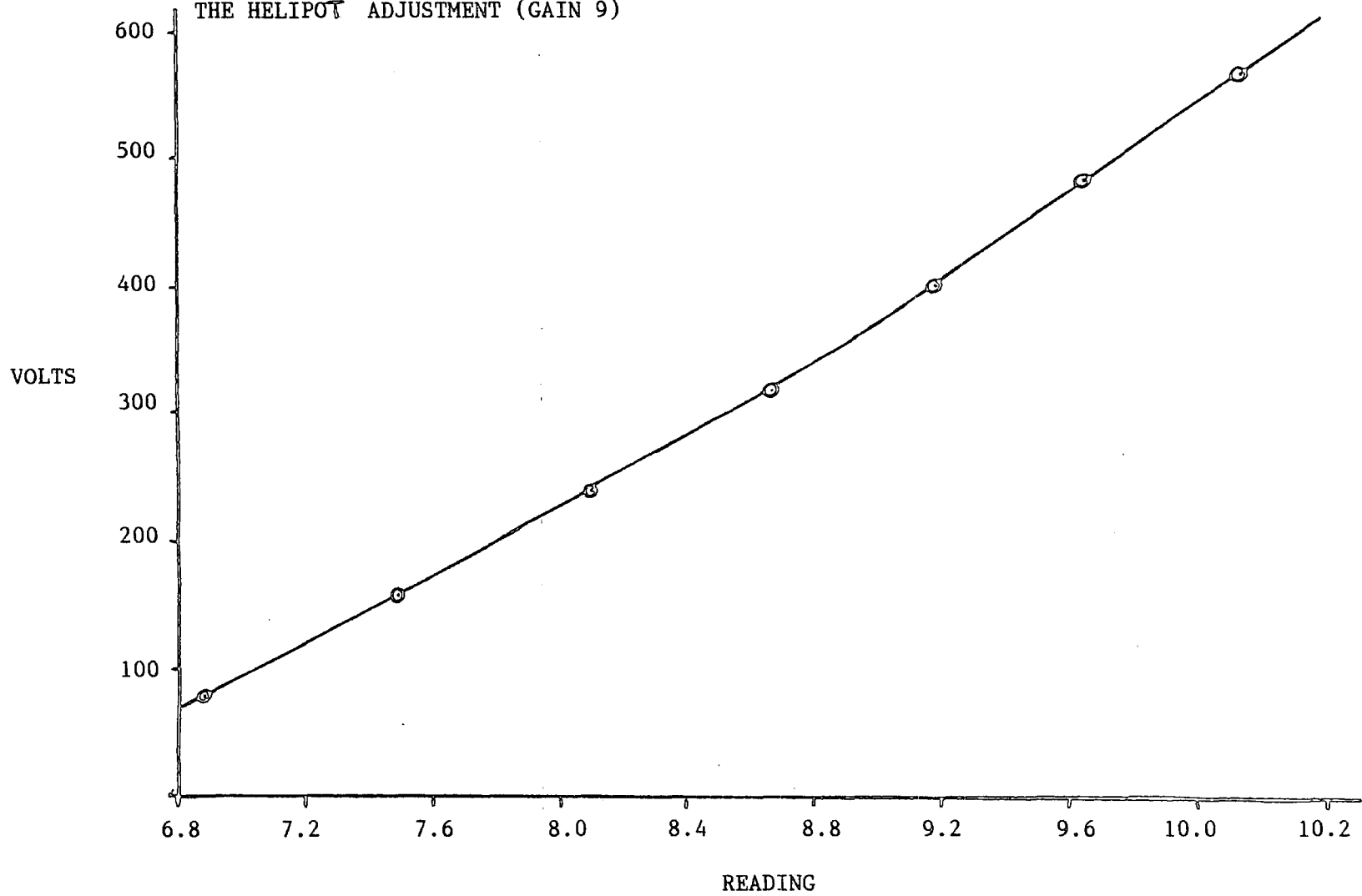
$$\text{where } P = \frac{V^2}{I}$$

$V$ , is the voltage output from the transmitter in volts,  $I$  is the impedance of the probe circuit (50  $\Omega$ ),  $Q$  is the quality factor of the coil,  $f_0$  the frequency in MHz (39.758 MHz) and  $V_0$  is the volume of the coil. Defining the Hartmann-Hahn mismatch parameter as  $\alpha$  by equation 4.3,

$$(4.3) \quad \alpha = \frac{\gamma_{Si} B_{1Si}}{\gamma_H B_{1H}} = \frac{V_{Si}}{V_H} . C$$

FIGURE 4.1

A CALIBRATION PLOT OF VOLTAGE OUTPUT FROM THE LOW FREQUENCY TRANSMITTER AS A FUNCTION OF READING ON THE HELIPOT ADJUSTMENT (GAIN 9)



$$\text{where } C \text{ is a constant} = \frac{\gamma_{\text{Si}}}{\gamma_{\text{H}}} \left[ \frac{Q_{\text{Si}}^f}{Q_{\text{H}}^f} \right]^{\frac{1}{2}}$$

measurement of  $V_{\text{Si}}$  and  $V_{\text{H}}$ , when  $\alpha$  is known to be unity, allows the calculation of the constant  $C$ , and then values of  $\alpha$  may be calculated for different readings of the pulse attenuator helipot adjustment.

The effects of changing the Hartmann-Hahn mismatch parameter ( $\alpha$ ) upon the signal intensity of the resonances, observed at constant contact time, directly reflects the changing rate of CP. Measurements were made at a number of different spinning speeds.

### 4.3 RESULTS AND DISCUSSION

The directly measured proton relaxation characteristics of the compounds studied are summarised in Table 4.1, together with measurements of the natural linewidths of the silicon resonances observed, as measured using the rotation synchronised CPMG pulse sequence

TABLE 4.1

COMPOUND	$T_1(^1\text{H})/\text{s}$	$T_{1\rho}/\text{ms}$	$\Delta\nu_{\frac{1}{2}}^{\text{CPMG}}/\text{Hz}$	$\Delta\nu_{\frac{1}{2}}^{\text{observed}}/\text{Hz}$
$\text{Q}_8^3\text{M}_8^+$	4.06	$>100^\dagger$	*	$\approx 5.0$
TMS SALT	5.70	25	3.5	12.0
$\text{Na}_2\text{SiO}_3 \cdot 5\text{H}_2\text{O}$	69.60(54%) 12.40(46%)	24	5.8	11.0

† In view of the large  $T_{1\rho}$  value it was not possible to follow the decay curve to gain an accurate value

\* This compound exhibits a number of resonances over a wide chemical shift range. As a consequence of limitations imposed by the rotation synchronised CPMG experiment, it was not possible to perform the experiment on this sample

+ Data obtained for the resonance at +11.9 ppm

From  $^{29}\text{Si} - ^1\text{H}$  variable contact time CP experiments, performed

under conditions where  $\alpha = 1.0$ , values of  $T_{IS}$ ,  $T_{1\rho}$  the percentage CP efficiency and the optimum contact time were calculated. These data are summarised in Table 4.2. The experimental variation of the signal intensity as a function of the contact time is shown in Figures 4.2, 4.3 and 4.4, where the experimental data has been fitted to equation 4.1.

TABLE 4.2

COMPOUND	$T_{IS}/\text{ms}$	$T_{1\rho}/\text{ms}$	% CP EFFICIENCY	$\tau^{\text{opt}}/\text{ms}$
$Q_8^3M_8^+$	3.7	108.0	88.7	12.9
TMS SALT	0.7	36.0	92.5	2.8
$Na_2SiO_3 \cdot 5H_2O$	0.6	20.7	89.6	1.9

+ Data obtained for the resonance at + 11.9 ppm

The  $^{29}\text{Si}$  CP MAS NMR spectrum of  $Q_8^3M_8$  is shown in Figure 4.5.

FIGURE 4.2

A GRAPHICAL REPRESENTATION OF CROSS-POLARISATION DATA FOR THE PEAK AT 11.9 ppm IN THE  $^{29}\text{Si}$  CP MAS NMR SPECTRUM OF  $\text{Q}_8^3\text{M}_8$  (SOLID LINE GIVEN BY THEORETICAL EQUATION)

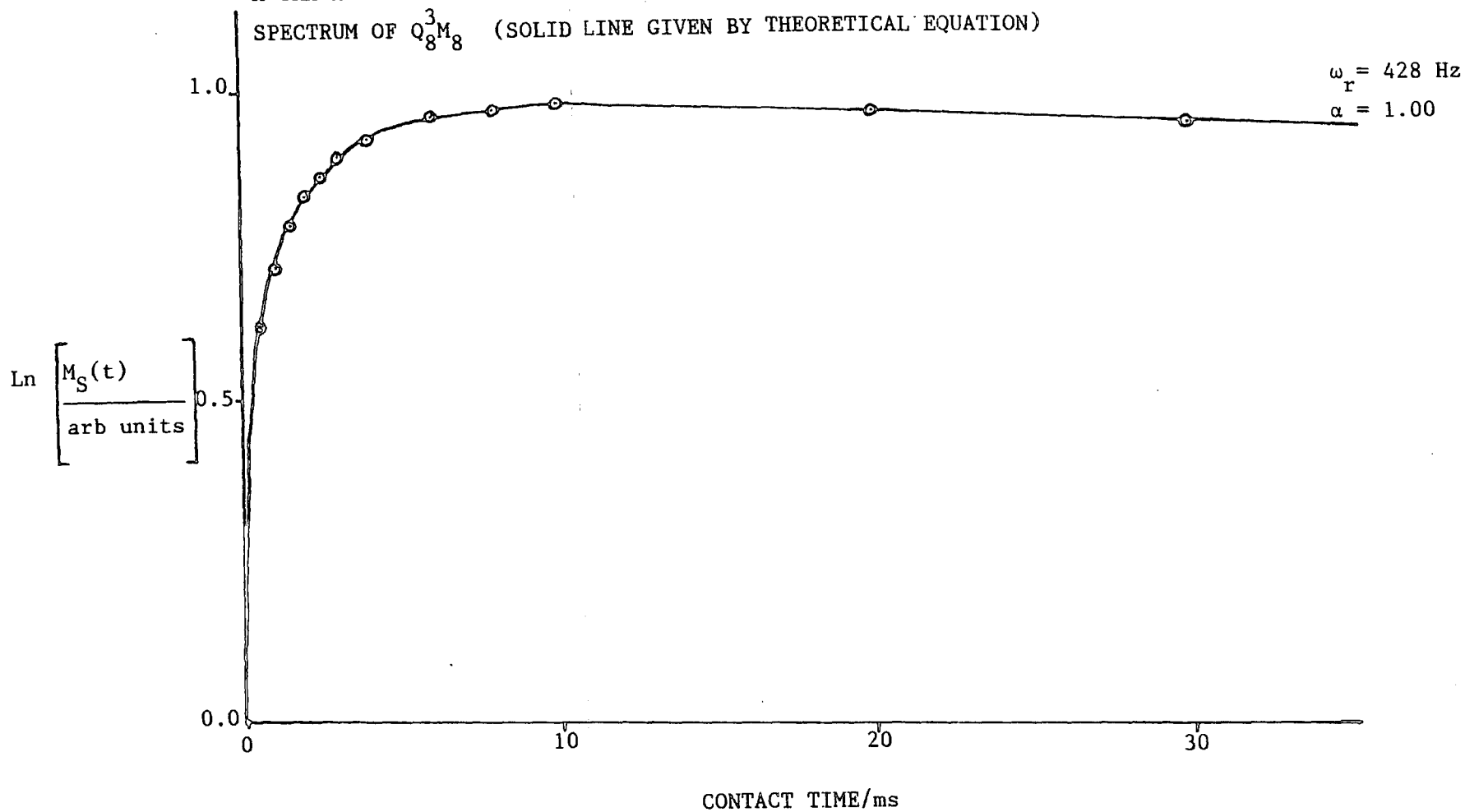


**FIGURE 4.3**

A GRAPHICAL REPRESENTATION OF CROSS-POLARISATION DATA FOR THE SODIUM SALT OF TRIMETHYLSILYL-1-PROPANE SULPHONIC ACID (SOLID LINE GIVEN BY THEORETICAL EQUATION)

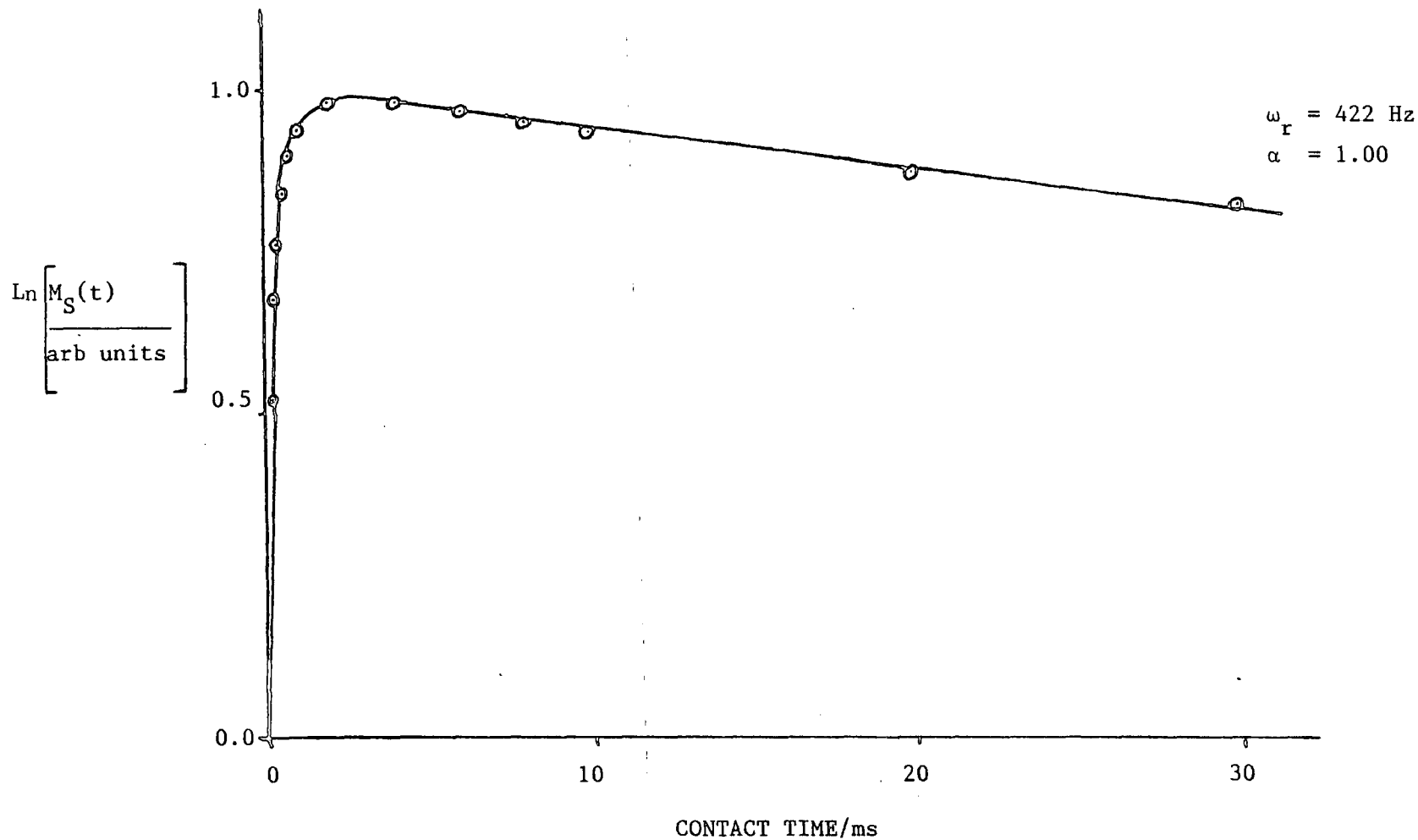
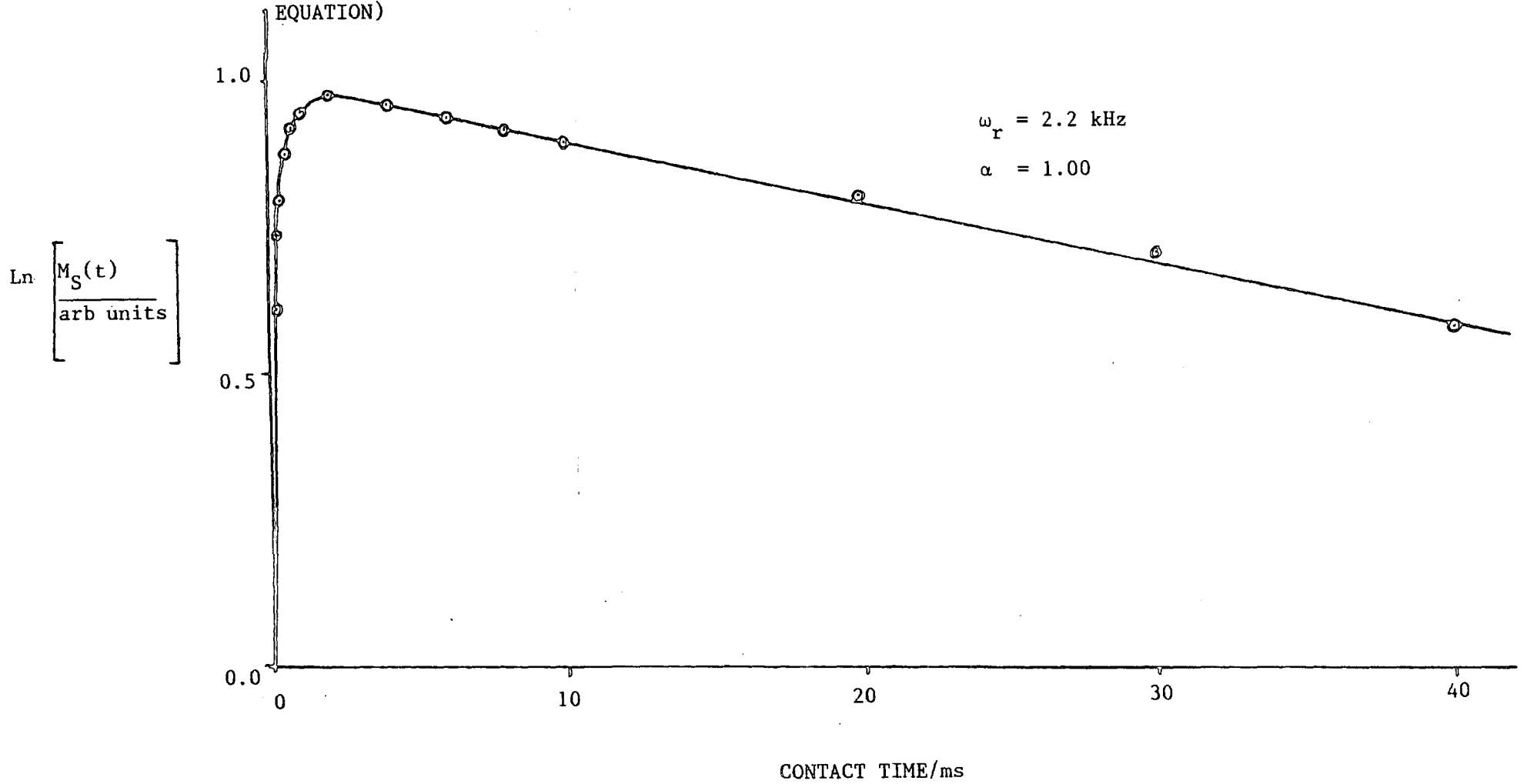


FIGURE 4.4

A GRAPHICAL REPRESENTATION OF CROSS-POLARISATION DATA FOR  $\text{Na}_2\text{SiO}_3 \cdot 5\text{H}_2\text{O}$  (SOLID LINE GIVEN BY THEORETICAL EQUATION)



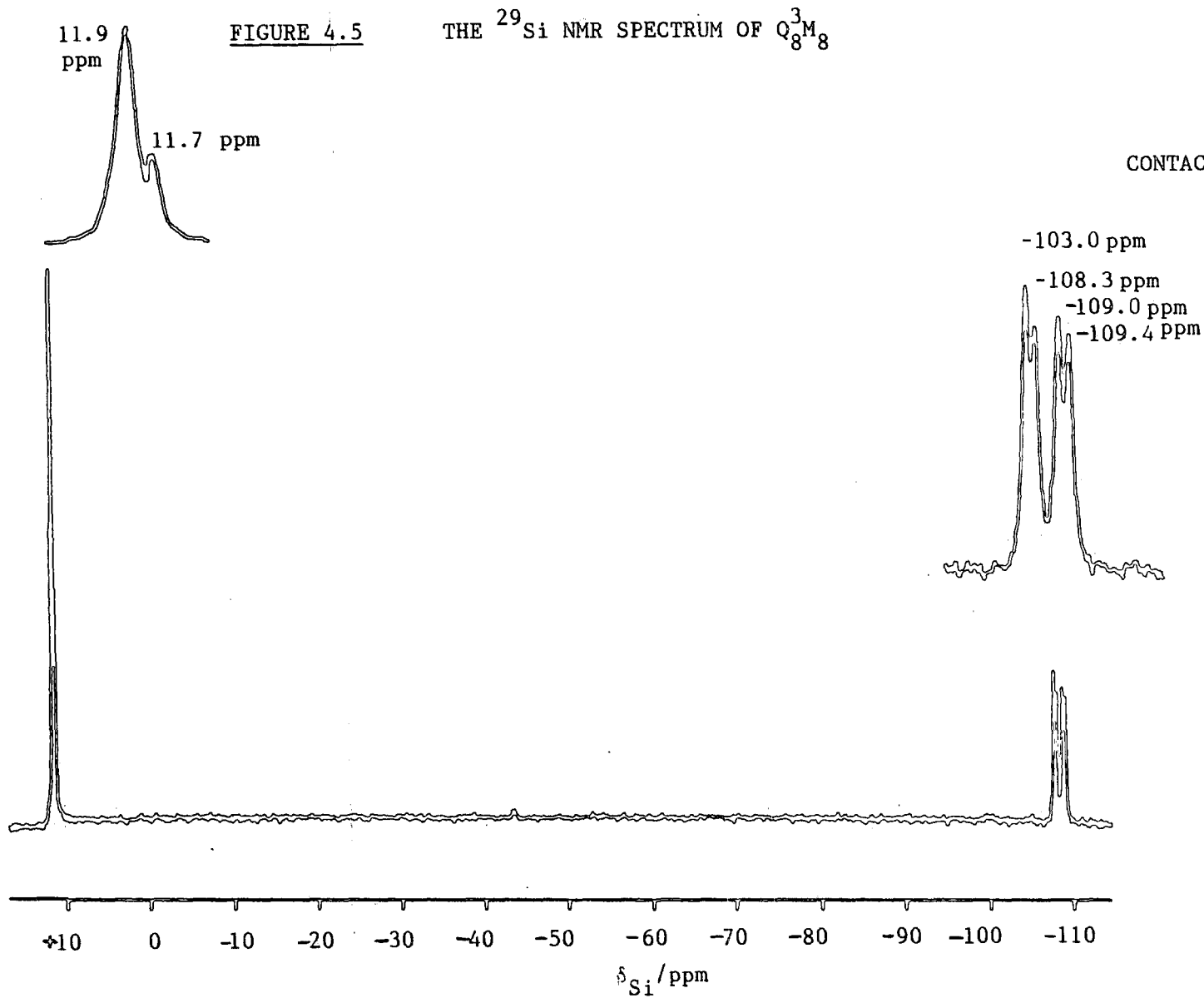
This solid-state spectrum exhibits good resolution, and is similar to the solution-state spectrum, except that the peaks at around +11 ppm and -110 ppm are split, owing to a slight asymmetric deformation of the  $Q_8^3$  cube in the crystal lattice and the asymmetrical fixed orientations of the M groups<sup>(9)</sup>. The results are consistent with the X-ray structure of the solid  $Q_8^3M_8$ <sup>(10)</sup>. The results outlined here also indicate very good CP characteristics, the theoretical CP efficiency being greater than 88% for the peak at +11.9 ppm. The use of this compound also has the advantage that the observation of the splittings in the  $^{29}\text{Si}$  CP MAS NMR spectrum are very sensitive to the setting of the magic angle. The principal disadvantage with the use of this compound, however, is that it is both expensive and difficult to obtain.

In view of the fact that it is possible to quickly and accurately set the magic angle, by maximising the number of rotational echoes in the  $^{79}\text{Br}$  and  $^{127}\text{I}$  MAS NMR spectra of KBr and KI respectively,<sup>(11)</sup> it is convenient to consider the use of other silicon-containing compounds such as the sodium salt of trimethylsilyl-1-propanesulphonic acid (TMS salt) or  $\text{Na}_2\text{SiO}_3 \cdot 5\text{H}_2\text{O}$  as potential replacements for  $Q_8^3M_8$ .

The  $^{29}\text{Si}$  CP MAS NMR spectra of the TMS salt and  $\text{Na}_2\text{SiO}_3 \cdot 5\text{H}_2\text{O}$  both exhibit a single isotropic chemical shift at +1.18 ppm and -68.60 ppm respectively with respect to TMS. The spectra obtained exhibit good resolution and like  $Q_8^3M_8$ , also exhibit very good CP efficiencies (i.e. >88%) at substantially shorter optimum contact times.

The sensitivity of each of these compounds to the Hartmann-Hahn matching condition may be examined by considering Figures 4.6, 4.7, 4.8, 4.9 and 4.10, which show how the rate of CP ( $T_{1S}^{-1}$ ) changes with  $\alpha$  at different spinning speeds.

In the CP experiment, the transfer of magnetisation from the



$\omega_r = 1.4 \text{ KHz}$

CONTACT TIME = 8 ms

NS = 32

$\alpha = 1.00$

RD = 10 s

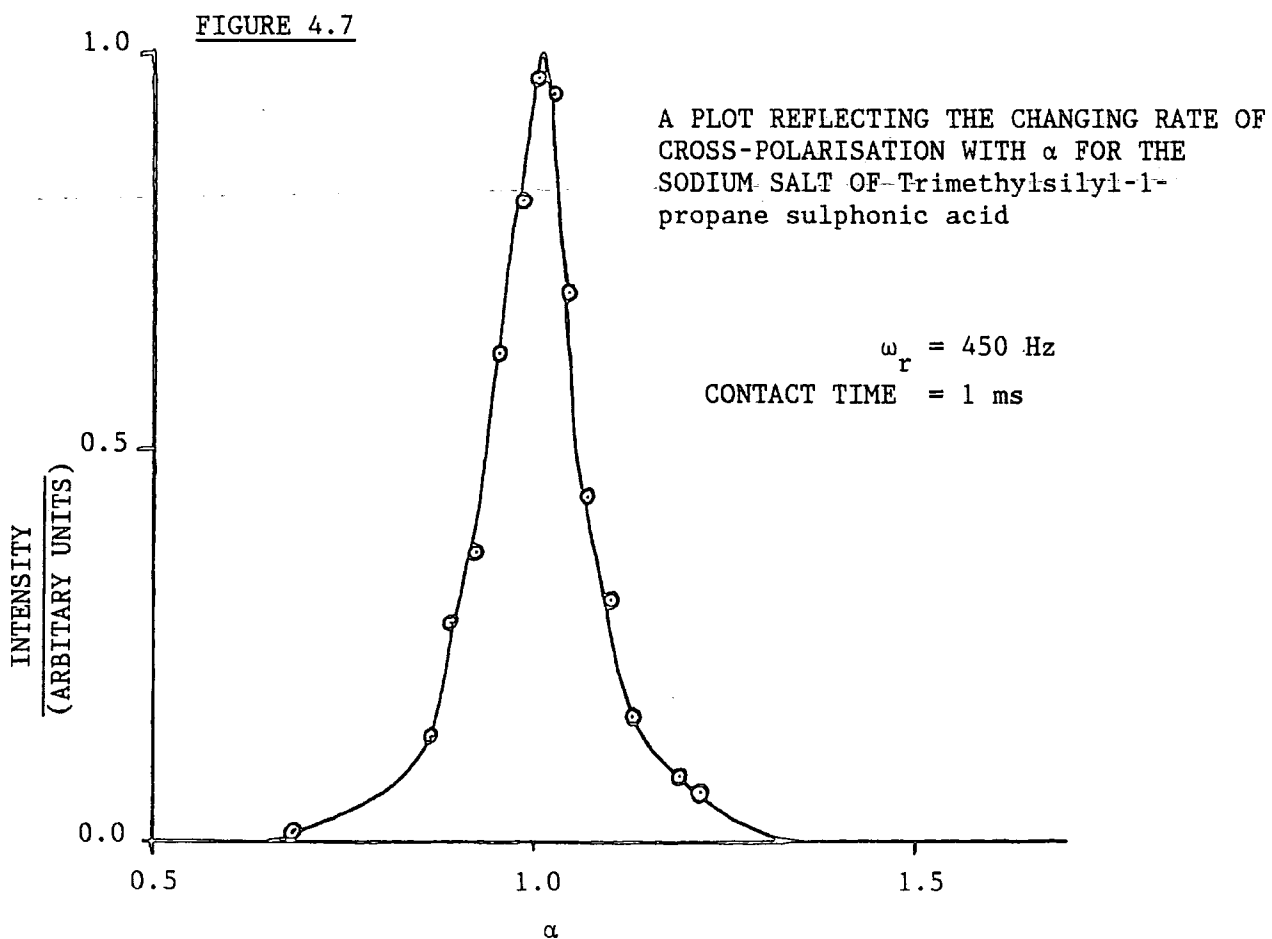
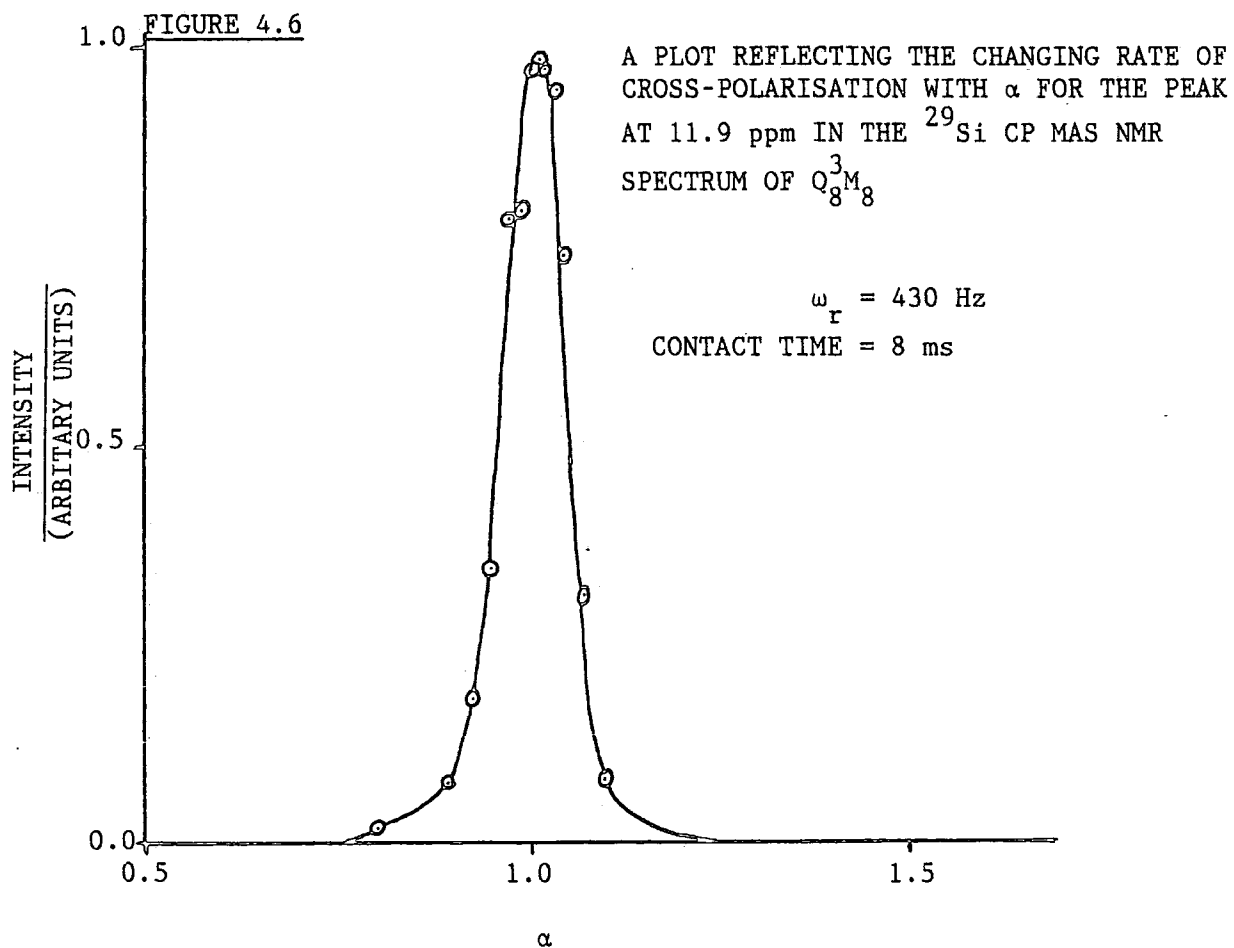


FIGURE 4.8

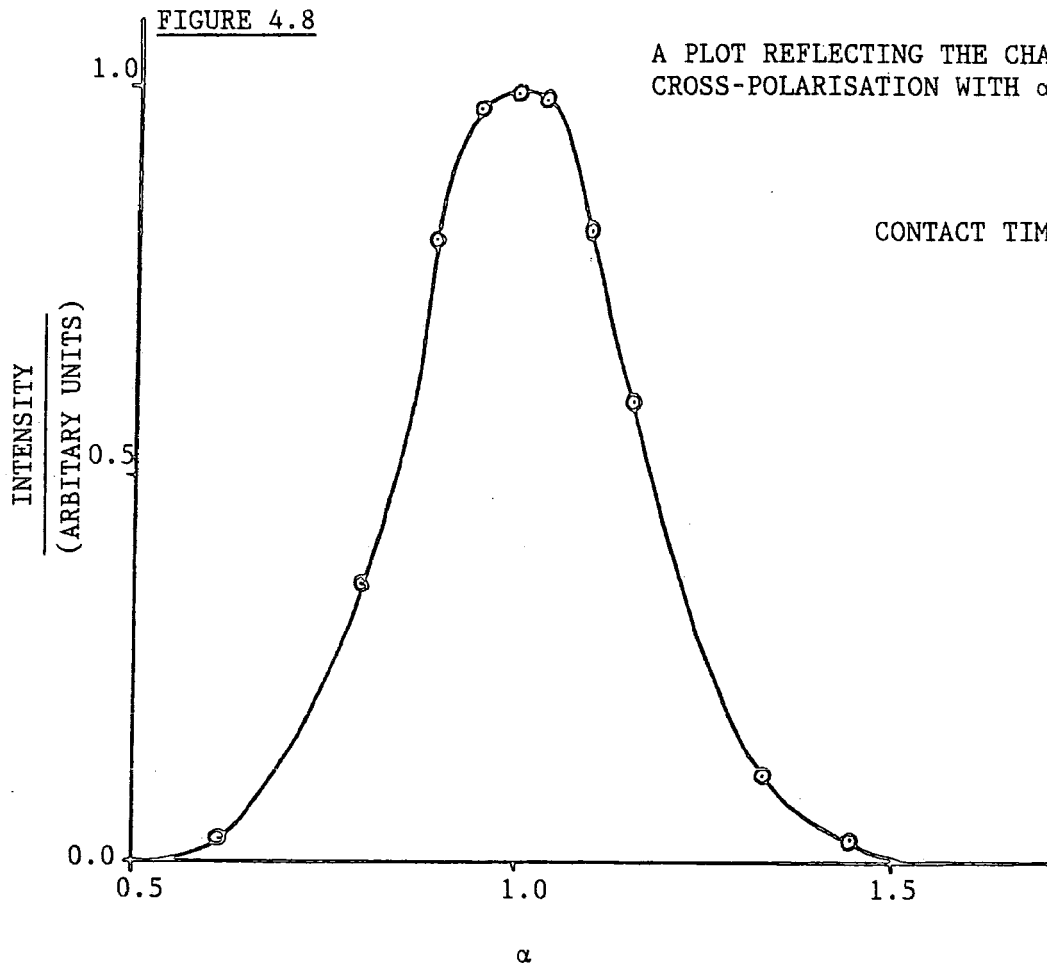


FIGURE 4.9

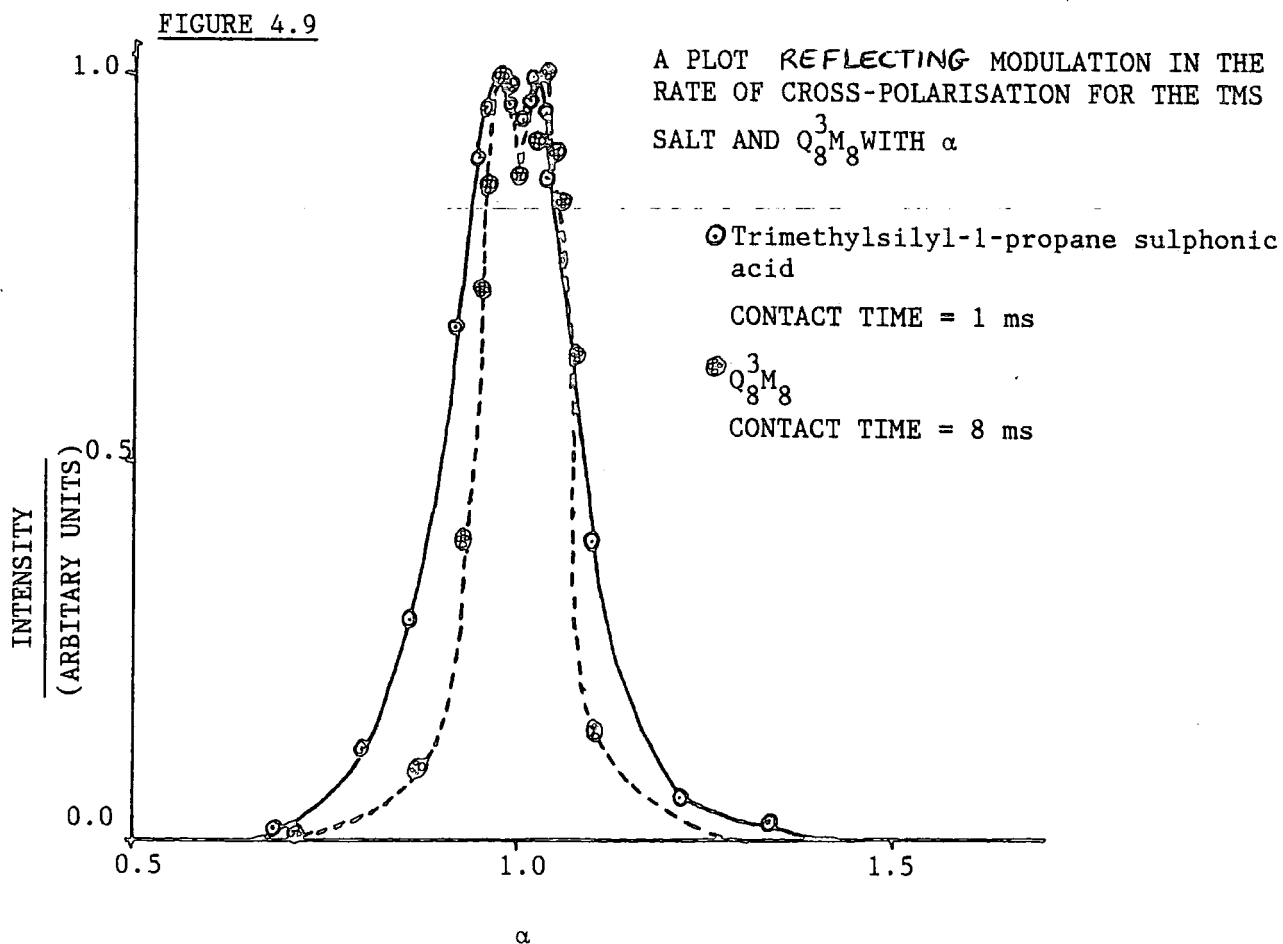
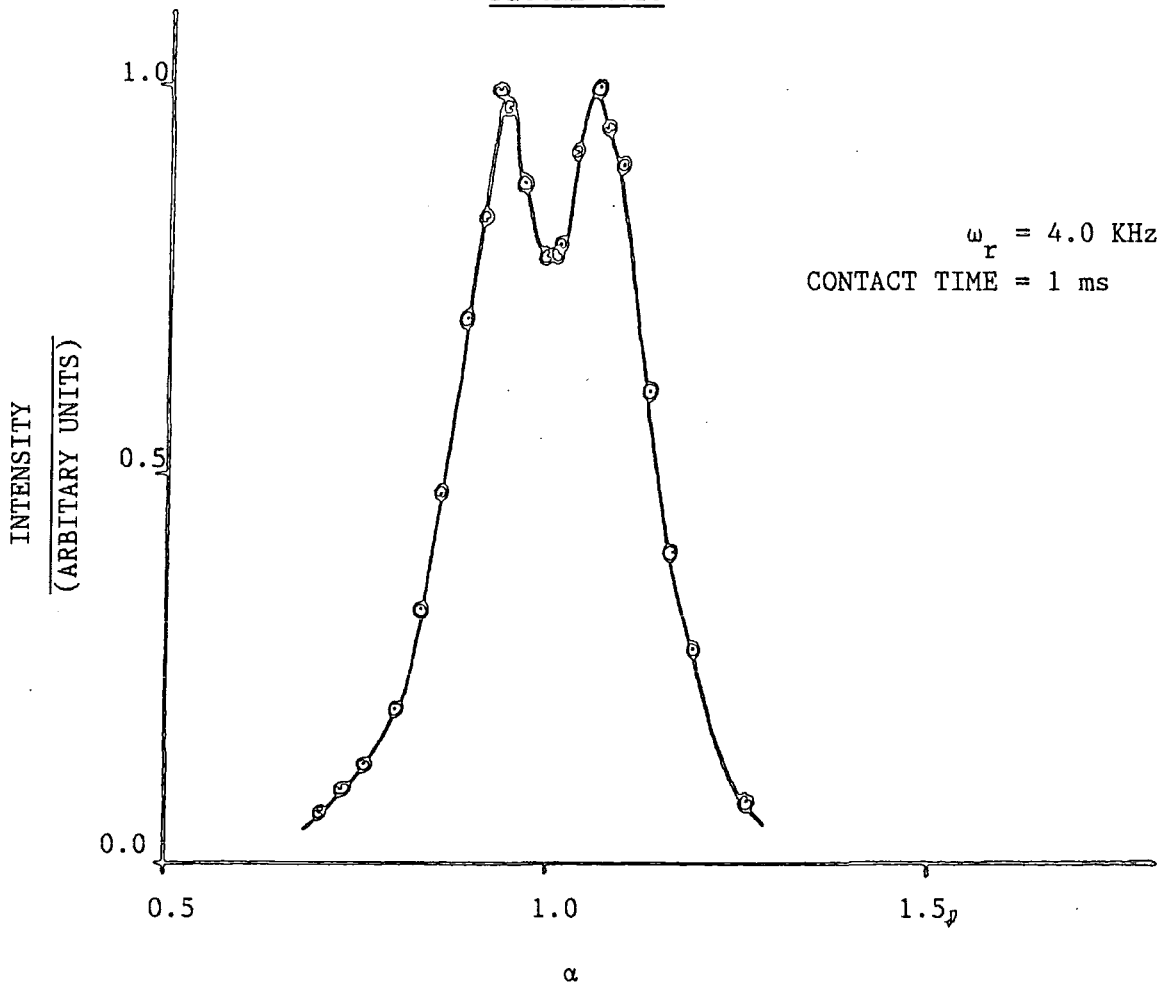


FIGURE 4.10



A PLOT REFLECTING MODULATION IN THE RATE OF CROSS-POLARISATION FOR TMS SALT WITH  $\alpha$

abundant.(I) spins to the rare (S) spins is mediated by dipolar interactions. The rate of CP ( $T_{IS}^{-1}$ ) effectively depends upon the magnitude of the heteronuclear dipolar interaction between the rare and abundant spins ( $|\mathcal{H}_{IS}|$ ). The Hamiltonians for the relevant dipolar interactions for these experiments are given by the following equations. (12)

$$(4.4) \quad \mathcal{H}_{II} = -\frac{1}{2} \sum_{k < l} b_{kl} (I_k \cdot I_l - 3I_{zk} I_{zl})$$

$$(4.5) \quad \mathcal{H}_{IS} = V_{IS}^+ \cos \Delta t + V_{IS}^- \sin \Delta t$$

where

$$(4.6) \quad V_{IS}^{\pm} = -\sum_{\mathbb{H}} \sum_{\mathbb{K}} b_{nk} (I_{xk} S_{xn} \pm I_{yk} I_{yn})$$

$$(4.7) \quad \Delta = \omega_{II} - \omega_{IS} = 2\pi(1 - \alpha)$$

$$(4.8) \quad b_{ij} = \frac{\gamma_i \gamma_j (3 \cos^2 \theta_{ij} - 1)}{r_{ij}^3}$$

The coordinate system for equations 4.4 to 4.8 is the doubly rotating frame of reference, in which the Z axes for both I and S spins are parallel to their respective rotating fields.

Considering the situation where there is an S spin with a single I spin neighbour, equation 4.5 indicates an oscillating behaviour of  $|\mathcal{H}_{IS}|$  with contact time  $t$ , <sup>when  $\Delta \neq 0$ .</sup> The observation of these transient dipolar oscillations can provide important information about the structure and geometry of the S-spin environment (for example the length of Si-H bonds). However, in the situation where each rare spin is coupled to

many I spin neighbours, dipolar oscillations are produced at many different frequencies, and the rate at which cross relaxation occurs, takes on an exponential form, as shown by equation 4.1. Hartmann and Hahn have shown that the rate of cross relaxation governing the rate of CP ( $T_{IS}^{-1}$ ) may be given by equation 4.9.

$$(4.9) \quad T_{IS}^{-1} = \langle \Delta^2 \omega_{IS} \rangle \int_0^{\infty} \cos \Delta t g(t) dt$$

where

$$(4.10) \quad g(t) = \frac{\text{Tr} \left\{ V_{IS} \cdot V_{IS}(t) \right\}}{\text{Tr} \left\{ V_{IS}^+ \cdot V_{IS}^- \right\}}$$

$$(4.11) \quad V_{IS}(t) = \exp\left(\frac{i\mathcal{H}}{II} t\right) \cdot V_{IS} \cdot \exp\left(-\frac{i\mathcal{H}}{II} t\right)$$

$\langle \Delta^2 \omega_{IS} \rangle$  is the second moment of the S spins caused by dipolar interactions with the I spins.

In the absence of MAS, if one considers a situation in which there are no homonuclear dipolar interactions (i.e.  $|\mathcal{H}_{II}|=0$ ), then CP would only occur when  $\Delta=0$  (i.e.  $\alpha=1.0$ ). The effect of the presence of homonuclear dipolar interactions is to cause mutual spin flips with neighbouring spins, and because of the Hartmann-Hahn matching condition, these mutual spin flips also affect the heteronuclear dipolar interaction ( $\mathcal{H}_{IS}$ ). These mutual spin flips that occur between the I and S spins or dipolar fluctuations have the characteristic frequencies  $\omega_{k1}$ . The a factor arises because not all the proton-proton mutual spin flips that take place will affect the heteronuclear dipolar interactions. Cross-polarisation in this

situation will only take place provided the condition  $\Delta \pm ab_{kl} = 0$  is satisfied. In the case of a rare spin interacting with many abundant spins, the result is, that if one plots a graph of the rate of cross-relaxation ( $T_{IS}^{-1}$ ) as a function of the Hartmann-Hahn mismatch parameter  $\alpha$ , a broad peak centred at  $\alpha=1.0$  and having a characteristic width  $ab_{kl}$  <sup>occurs</sup> as illustrated by Figures 4.6, 4.7 and 4.8.

In the presence of MAS, an additional oscillating time dependence to  $\mathcal{H}_{IS}$  and  $\mathcal{H}_{II}$  is introduced via the  $b_{ij}$  term, which for spinning at the magic angle takes on the form given by equation 4.12

(4.12)

$$b_{ij}(t) = \frac{\sqrt{2}\gamma_i\gamma_j\hbar \sin\phi_{ij} \cos\phi_{ij} \cos(\omega_r t - \delta_{ij})}{r_{ij}^3} + \frac{\gamma_i\gamma_j\hbar \sin\phi_{ij} \cos(2\omega_r t - 2\delta_{ij})}{2r_{ij}^3}$$

where  $\phi_{ij}$  is the angle between the spinning axis and the vector  $r_{ij}$ , and  $\delta_{ij}$  is the initial azimuth of  $r_{ij}$  about that axis. The effect of MAS upon  $\mathcal{H}_{IS}$  is to cause modulation of this interaction, so that the static interaction is broken up, and the magnitude of the interaction in the region  $\alpha=1.0$  approaches zero, while it has its maximum magnitude in the regions  $\Delta = \pm\omega_r, \pm 2\omega_r$ . Magic angle spinning also causes modulation of the homonuclear dipolar interactions ( $\mathcal{H}_{II}$ ) and hence modulation of the characteristic frequencies ( $ab_{kl}$ ) with which dipolar fluctuations occur as a consequence of interactions between the I and S spins. This results in each of the peaks at  $\pm\omega_r$  and  $2\omega_r$ , caused by modulation of the  $\mathcal{H}_{IS}$  interaction, being split into frequency modulated sidebands, separated by multiple values of the rotor frequency. The consequence of this process is to restore the possibility of cross-polarisation occurring when  $\Delta=0$  (i.e.  $\alpha=1.0$ ), provided that the rate of rotation is insufficient to average out the homonuclear dipolar interactions. In magic

angle spinning experiments the magnitude of the homonuclear dipolar interaction between the abundant spins has a profound effect upon the cross polarisation characteristics of the sample.

In systems where there are strong homonuclear dipolar interactions, where  $\omega_r \ll \left| \frac{\hbar \mathcal{H}}{II} \right|$  and  $\omega_r \ll ab_{kl}$ , modulation of the  $\frac{\mathcal{H}}{IS}$  interaction produces sidebands which are located entirely within  $ab_{kl}$ , since the homonuclear dipolar interactions are so large, no sidebands of significant intensity are produced outside the width of the peak. These systems reveal cross-polarisation characteristics which are quite insensitive to the Hartmann-Hahn matching condition, since the condition  $\Delta \pm ab_{kl} = 0$  may be satisfied for quite large variations of  $\Delta$  (or  $\alpha$ ).

In systems where there are relatively weak homonuclear dipolar interactions, as a consequence of spin dilution or motional averaging where  $\omega_r > \left| \frac{\hbar \mathcal{H}}{II} \right|$  however, modulation of the rate of cross-relaxation ( $T_{IS}^{-1}$ ) with the Hartmann-Hahn mismatch parameter ( $\alpha$ ) is observed, as MAS causes modulation of the characteristic frequencies  $ab_{kl}$  which  $\frac{\mathcal{H}}{II}$  imposes on  $\frac{\mathcal{H}}{IS}$ . The result is that cross-polarisation will only take place when the conditions  $\Delta \pm 0, \omega_r, 2\omega_r \approx 0$  are satisfied. Examination of the change in the rate of cross-polarisation ( $T_{IS}^{-1}$ ) with  $\alpha$  reveals modulation of the rate of cross-polarisation, a sideband pattern is observed where the peaks are separated by the spinning frequency when the sample is rotated at the magic angle, and separated by twice the spinning frequency if the sample is rotated  $90^\circ$  with respect to  $B_0^{(11)}$ . These systems, therefore, reveal characteristics which are much more sensitive to the Hartmann-Hahn matching condition.

It may be seen from the above discussion, therefore, that the sensitivity of each of the compounds to the Hartmann-Hahn matching condition may be determined by measuring the width of the peaks

observed in the plots of  $T_{IS}^{-1}$  against  $\alpha$  in the absence of MAS. In reality, measurements of the widths of the peaks observed in plots of  $T_{IS}^{-1}$  against  $\alpha$  for the samples of  $Q_8^3M_8$ , the TMS salt and  $Na_2SiO_3 \cdot 5H_2O$  (Figures 4.6, 4.7 and 4.8 respectively) were made while rotating the samples at the magic angle, at speeds just above those required to average out shielding anisotropy. The calculated widths are 3.1 kHz, 4.4 kHz and 11.8 kHz respectively. The results clearly reveal that while  $Na_2SiO_3 \cdot 5H_2O$  exhibits CP characteristics that are relatively insensitive to the Hartmann-Hahn match,  $Q_8^3M_8$  and the TMS salt exhibit a comparable sensitivity, although  $Q_8^3M_8$  is slightly more sensitive.

An alternative method whereby one might assess the sensitivity of a particular compound to the matching condition, might be found from measurements of  $^1H$  longitudinal relaxation rates. For example, in this study it is seen that the ratio  $T_1(^1H)/T_1(^1H)_{Q_8^3M_8}$  for the different compounds, is very similar to the ratio of the band widths observed in Figures 4.6, 4.7 and 4.8 (Table 4.3).

TABLE 4.3

COMPOUND	$\left[ T_1(^1H)/T_1(^1H)_{Q_8^3M_8} \right]$	$\left[ ab_{kl}/ab_{kl}^{Q_8^3M_8} \right]$
$Q_8^3M_8$	1.0	1.0
TMS SALT	1.40	1.42
$Na_2SiO_3 \cdot 5H_2O$	3.05	3.65

The compound  $Na_2SiO_3 \cdot 5H_2O$  exhibits a two component  $T_1(^1H)$ . In Table 4.3 the  $T_1(^1H)$  of the protons that undergo CP to silicon nuclei is taken as 12.4 s. This is confirmed via a CP experiment illustrated

FIGURE 4.11 A PULSE SEQUENCE DESIGNED TO MEASURE  $T_1(^1\text{H})$  VALUES OF PROTONS THAT CROSS-POLARISE TO SILICON SITES

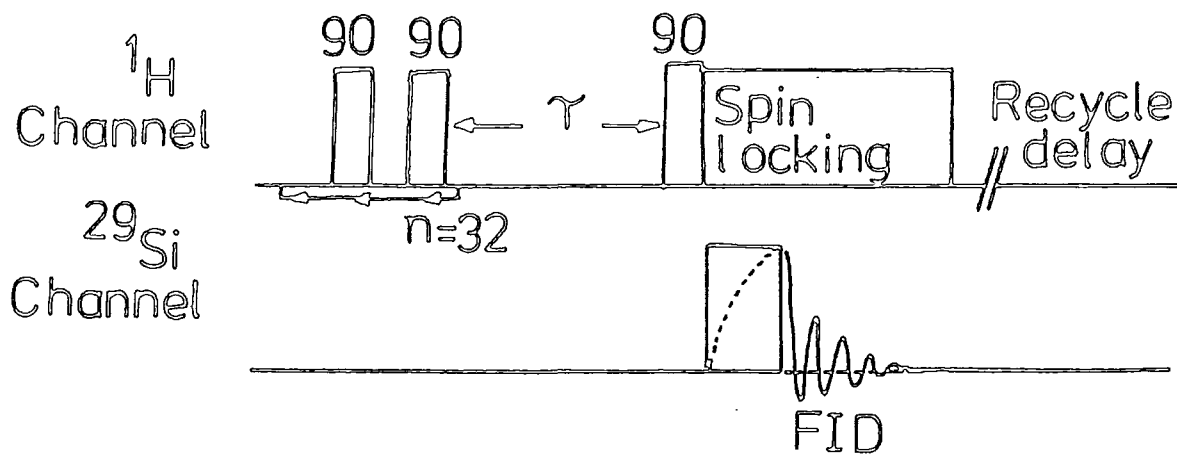
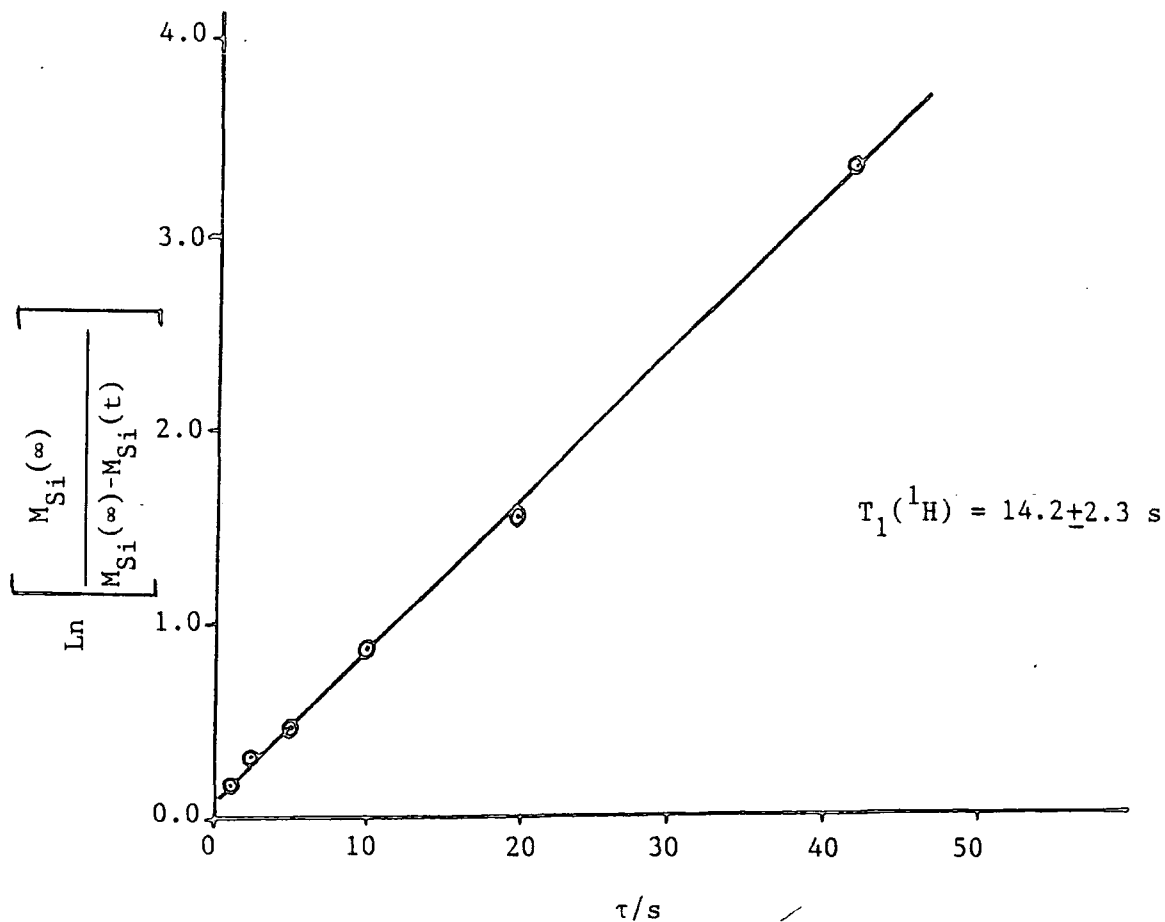


FIGURE 4.12 A PLOT OF THE EXPERIMENTAL DATA OBTAINED USING THE PULSE SHOWN IN FIGURE 4.11 ON  $\text{Na}_2\text{SiO}_4 \cdot 5\text{H}_2\text{O}$



in Figure 4.11. The proton magnetisation is initially saturated by means of  $32,90^0+x$  pulses separated by a delay of 2 ms. The proton magnetisation is then allowed to recover towards its equilibrium value for a time  $\tau$ , following which, the silicon signal is acquired via the usual  $^{29}\text{Si}$  CP technique. Since the silicon magnetisation is derived from the proton spin reservoir, the observed increase in the intensity of the silicon signal magnetisation with  $\tau$ , is governed via equation 4.13.

$$(4.13) \quad M_{\text{Si}}(\tau) = M_{\text{Si}}(0) [1 - \text{EXP}(-\tau/T_1(^1\text{H}))]$$

The value of  $T_1(^1\text{H})$  was calculated as  $14.2 \pm 2.3$  s via this technique. The experimental plot of the data is shown in Figure 4.12. Using this  $T_1(^1\text{H})$  value the ratio  $(T_1(^1\text{H})/T_1(^1\text{H})\text{Q}_8^3\text{M}_8)$  becomes 3.50. The origin of the two component  $T_1(^1\text{H})$  value observed for this compound is unknown.

This technique for assessing the sensitivity of silicon containing compounds to the Hartmann-Hahn matching condition, however, should be used with caution, since measurements of the proton  $T_1^{\text{S}}$  would only be of use provided that the rate of relaxation is determined by homonuclear dipolar interactions, and the correlation time for the molecular motion of the protons is such that:

$$\omega_{\text{I}}^2 \tau_{\text{c}}^2 \gg 1. \quad (13)$$

Considering the differing rates of cross-relaxation ( $T_{1\text{S}}^{-1}$ ) for the three silicon compounds (Table 4.3), it may be seen that  $T_{1\text{S}}^{-1}$  decreases in the sequence  $\text{Na}_2\text{SiO}_3 \cdot 5\text{H}_2\text{O} > \text{TMS SALT} > \text{Q}_8^3\text{M}_8$ . This order reflects the increasing separation between  $^{29}\text{Si}$  and  $^1\text{H}$  spins.

Measurements of the proton  $T_{1\rho}^{\text{S}}$  from variable contact time experiments are subject to a number of experimental problems, since long contact times can cause heating of the probe circuit elements, thereby

resulting in the loss of the Hartmann-Hahn matching condition as the quality factor of the probe circuit changes. Further errors in the measurement may also occur as a consequence of phase instability of the proton spin-locking field.<sup>(14)</sup> However, examination of the results outlined in Tables 4.1 and 4.2 reveal that while the values calculated from variable contact time experiments are not the same as those measured directly, the trend in the  $T_{1\rho}$  values as one goes from  $\text{Q}_8^3\text{M}_8$  to  $\text{Na}_2\text{SiO}_3 \cdot 5\text{H}_2\text{O}$  is the same.

In the preceding discussion, we have seen that  $\text{Q}_8^3\text{M}_8$  and the TMS salt exhibit very similar proton relaxation characteristics and sensitivity to the Hartmann-Hahn matching condition. Figures 4.9 and 4.10 suggest that in order to avoid modulation of  $T_{1S}^{-1}$  when setting the match, the spinning frequencies in both cases should not exceed 1.5 kHz. It should be noted that in Figures 4.9 and 4.10 the peaks observed are separated by twice the rotor frequency, although samples were rotated at the magic angle. This observation is a consequence of the poor resolution in the "Hartmann-Hahn spectrum" at the particular contact times employed.

#### 4.4 DETERMINING S SPIN $T_1$ VALUES VIA CP

One of the many useful experiments which may be performed employing the CP technique is the determination of the S spin ( $^{29}\text{Si}$ )  $T_1$  values via CP from the abundant spins. The pulse sequence written for this purpose is illustrated in Figure 4.13. This so-called  $T_1$ CP experiment, originally devised by Torcha et al,<sup>(15)</sup> consists of two similar but not identical pulse sequences. The first sequence starts with the application of a resonant  $B_{1H}$  field to the proton spins,

FIGURE 4.13

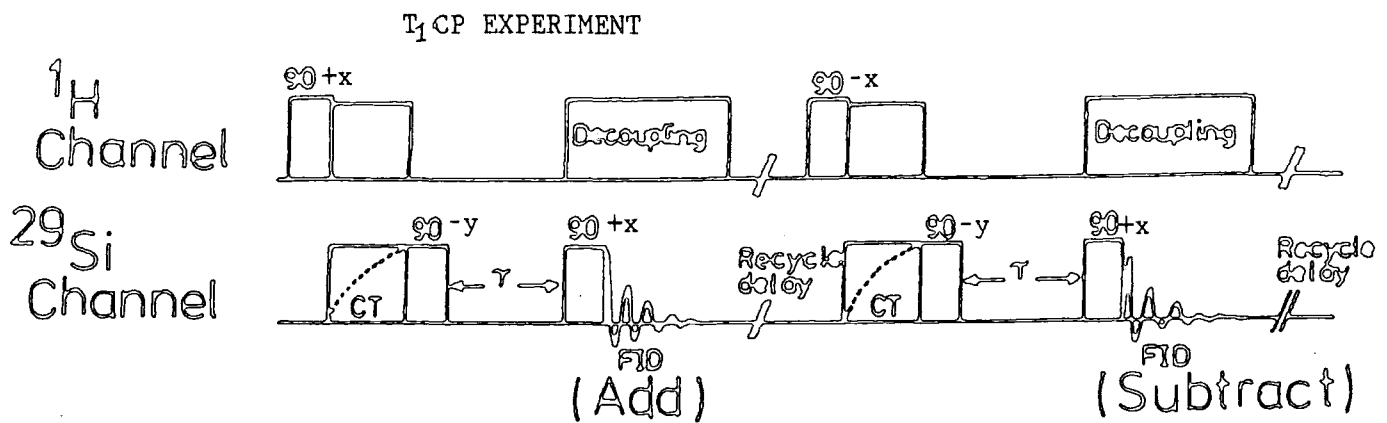
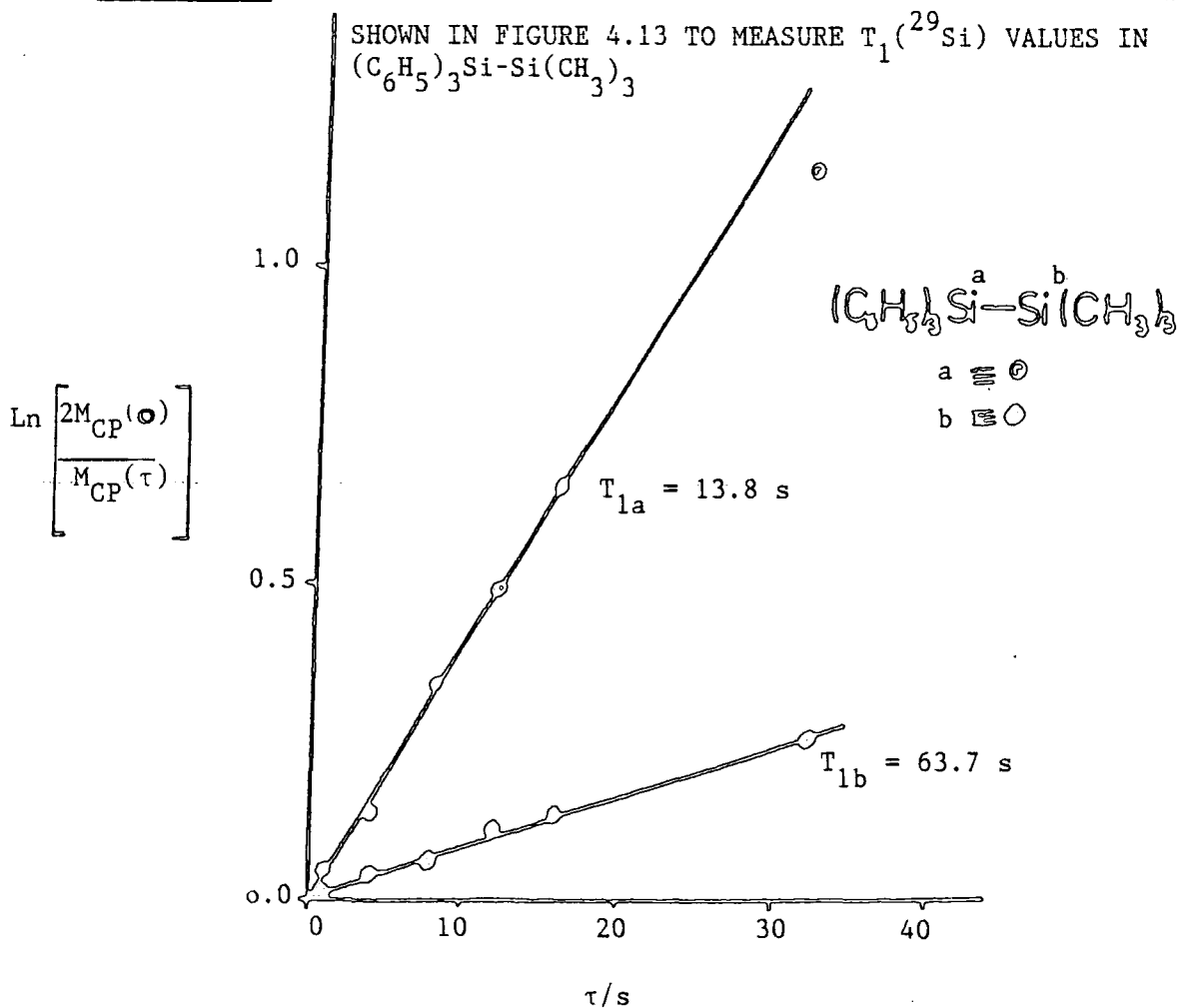


FIGURE 4.14

A PLOT OF THE EXPERIMENTAL DATA OBTAINED USING THE PULSE SHOWN IN FIGURE 4.13 TO MEASURE  $T_1(^{29}\text{Si})$  VALUES IN  $(\text{C}_6\text{H}_5)_3\text{Si}-\text{Si}(\text{CH}_3)_3$



rotating the proton magnetisation until it is directed along the +Y direction in the rotating frame of reference, where it is spin-locked. The  $^{29}\text{Si}$  magnetisation is then derived by the application of a  $B_{1S}$  field such that  $\alpha=1.0$ . After the  $^{29}\text{Si}$  magnetisation is established along  $B_{1S}$  (assumed to be along the X axis), the proton spin-locking field is switched off, and the silicon magnetisation is rotated by the  $B_{1Si}$  field (which has been phase shifted to lie along the -Y direction) from the X axis to the Z axis. In the absence of the  $B_1$  field, the proton enhanced silicon magnetisation decays exponentially from its initial value  $M_{CP}(0)$ , to the equilibrium value  $M(0)$  with time  $\tau$ . Following this delay time  $\tau$ , the remaining silicon magnetisation may be measured from the signal intensity observed in the resultant FID acquired. The second part of this pulse sequence is identical to that of the first, except that the initial  $B_{1H}$  field is phase shifted by  $180^\circ$ , this causes spin temperature inversion, so the sign of the proton-enhanced silicon signal is opposite to that obtained in the first pulse sequence. The silicon magnetisation is then rotated along the -Z direction and recovers from the value  $-M_{CP}(0)$  to the equilibrium value  $M(0)$  with time  $\tau$ . If one FID is then subtracted from the other the change in the silicon signal intensity with delay time  $\tau$  may be described by equation 4.14.

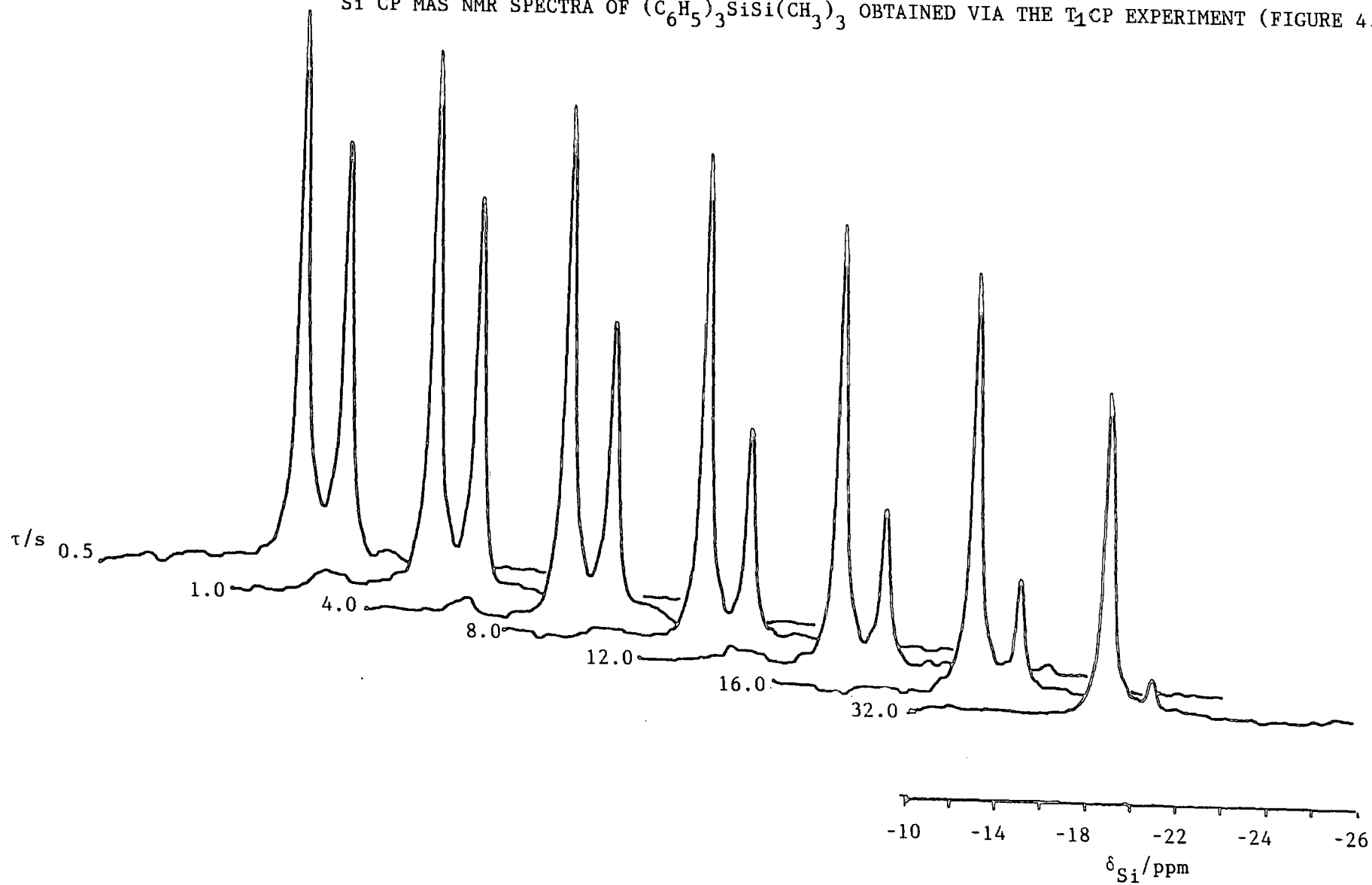
$$(4.14) \quad M(\tau) = 2M_{CP}(0) \cdot \text{EXP}(-\tau/T_1(^{29}\text{Si}))$$

This technique offers a number of advantages over other methods of determining  $^{29}\text{Si}$   $T_1$  values. <sup>(15)</sup>

- (i) The  $^{29}\text{Si}$  signal is enhanced by CP
- (ii) Spectral artifacts are suppressed
- (iii) It is no longer necessary to wait  $5 \times T_1(^{29}\text{Si})$  between experiments, but only  $5 \times T_1(^1\text{H})$ .

FIGURE 4.15

$^{29}\text{Si}$  CP MAS NMR SPECTRA OF  $(\text{C}_6\text{H}_5)_3\text{SiSi}(\text{CH}_3)_3$  OBTAINED VIA THE  $T_1$ CP EXPERIMENT (FIGURE 4.13)



The application of this experiment is illustrated using the compound 1,1,1-triphenyltrimethyldisilane  $((\text{C}_6\text{H}_5)_3\text{SiSi}(\text{CH}_3)_3)$ . This compound exhibits two resonances in the  $^{29}\text{Si}$  CP MAS NMR spectrum, at -18.4 and -21.0 ppm respectively. The spectra obtained at different delay times ( $\tau$ ), are shown in Figure 4.15. The experimental plot used to determine the silicon  $T_1$  values of these peaks is illustrated by Figure 4.14. The peaks at -18.4 ppm and -21.0 ppm have been assigned to silicon atoms present in the  $\text{Si}(\text{CH}_3)_3$  and  $\text{Si}(\text{C}_6\text{H}_5)_3$  moieties respectively. The  $^{29}\text{Si}$   $T_1$  values are determined as 13.8 and 63.7 seconds respectively.

This experiment has also been used to measure the  $^{29}\text{Si}$   $T_1$  values for the silicon-containing compounds  $\text{Q}_8^3\text{M}_8$ , TMS salt and  $\text{Na}_2\text{SiO}_3 \cdot 5\text{H}_2\text{O}$ . These data are summarised in Table 4.4.

TABLE 4.4

COMPOUND	$T_1(^{29}\text{Si})/\text{s}$
$\text{Q}_8^3\text{M}_8$	27.8 $\tau$
TMS SALT	63.1
$\text{Na}_2\text{SiO}_3 \cdot 5\text{H}_2\text{O}$	566.0

$\tau$   $T_1(^{29}\text{Si})$  value for the peak at 11.9 ppm

#### 4.5 CONCLUSIONS

The studies outlined in this chapter indicate that of the three potential CP standards studied  $\text{Q}_8^3\text{M}_8$  is the best, since it exhibits the best sensitivity to the Hartmann-Hahn matching condition. However, since the CP characteristics of the two compounds  $\text{Q}_8^3\text{M}_8$  and the TMS salt are very similar, it would appear that the sodium salt of

trimethylsilyl-1-propanesulphonic acid may be employed as a secondary replacement standard, as an alternative to  $Q_8^3M_8$ . The use of this compound offers the advantage that it is considerably cheaper and more readily available.

The optimum conditions for acquiring  $^{29}Si$  CP MAS NMR spectra of these compounds and for setting the Hartmann-Hahn matching condition are summarised in Table 4.5.

The technique whereby  $^{29}Si$   $T_1$  values may be determined by a time saving technique which relies upon the CP process, has been demonstrated. This technique has been used in the study of silica xerogels in Chapter Six.

TABLE 4.5

COMPOUND	$\omega_r^{\text{opt}}/\text{kHz}$	$CT^{\text{opt}}/\text{ms}$	$\Delta\nu_{\frac{1}{2}}^{\text{min}}/\text{Hz}$	AQ+RD/s <sup>†</sup> (without flip back)	AQ+RD/s <sup>†</sup> (with flipback)	RELATIVE SENSITIVITY
$\text{Q}_8^3\text{M}_8$	0.4-0.7	12.9	$\approx 5.0$	5.12	0.48	1.00
TMS SALT	0.4-0.7	2.8	3.5	7.18	0.45	0.70
$\text{Na}_2\text{SiO}_3 \cdot 5\text{H}_2\text{O}$	2.0-2.5	1.9	5.8	15.62	1.30	0.27

†+ These values represent the values of AQ + RD which yield the best conditions for obtaining spectra with the highest (S/n) ratio per unit time

\* The relative sensitivity is defined by the ratio  $(ab_{kl}^{\text{Q}_8^3\text{M}_8}/ab_{kl})$

## 5.0 CHAPTER FIVE

### $^{29}\text{Si}$ NMR STUDIES OF CRYSTALLINE INORGANIC AND ORGANIC

#### SILICON-CONTAINING MATERIALS

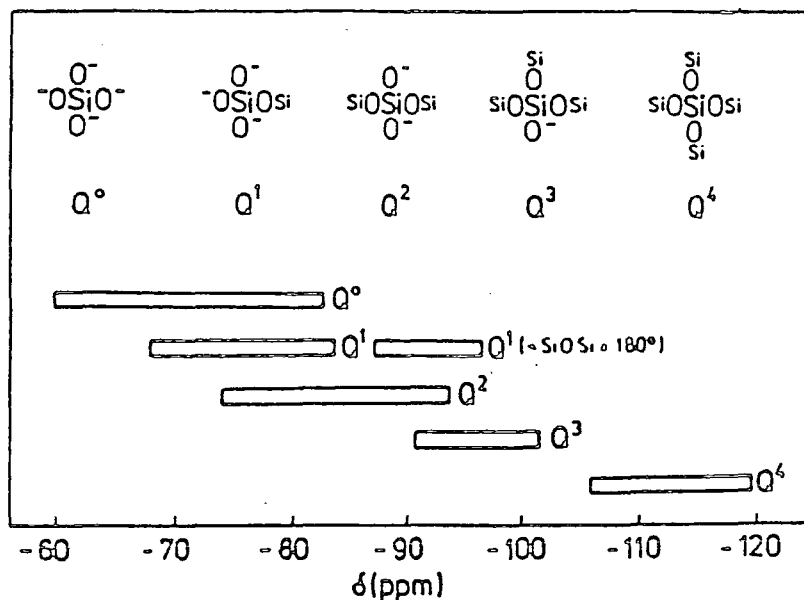
##### 5.1 INTRODUCTION

In recent years, the literature has furnished a wealth of information concerning chemical structures from  $^{29}\text{Si}$  solid-state MAS NMR studies of crystalline<sup>(1-4)</sup> and non-crystalline silicates,<sup>(5-7)</sup> aluminosilicates,<sup>(4)</sup> zeolites,<sup>(4)</sup> polysiloxanes,<sup>(8)</sup> polysilanes<sup>(9)</sup> and other organosiloxane compounds.<sup>(10)</sup> Much of the work on inorganic silicates, has been concerned with the measurements of the isotropic chemical shifts and the correlation of these with various structural parameters.<sup>(11)</sup>

The first major  $^{29}\text{Si}$  NMR study of inorganic materials was by Lippmaa et al.<sup>(1)</sup> It was reported that solid-state  $^{29}\text{Si}$  isotropic chemical shifts of silicates are determined primarily by the degree of condensation of the silicon-oxygen tetrahedra. Increasing the degree of condensation from  $Q^0$  to  $Q^4$  causes increased shielding of the  $^{29}\text{Si}$  nucleus, as a result, isotropic chemical shifts become more negative with respect to TMS. More extensive studies of a large number of silicates,<sup>(2)</sup> revealed that other structural factors, such as bond angles, inter-atomic distances, electrostatic bond strengths of the cations and (in the case of aluminosilicates and zeolites), the distribution and content of aluminium also cause significant changes in these shifts, resulting in the overlapping of the chemical shift ranges caused by different  $Q^n$  units (Figure 5.1)<sup>(4)</sup>

FIGURE 5.1

THE RANGES OF ISOTROPIC CHEMICAL SHIFTS FOR SILICON SITES WITH DIFFERENT DEGREES OF CONDENSATION OF  $\text{SiO}_4$  TETRAHEDRA<sup>(4)</sup>

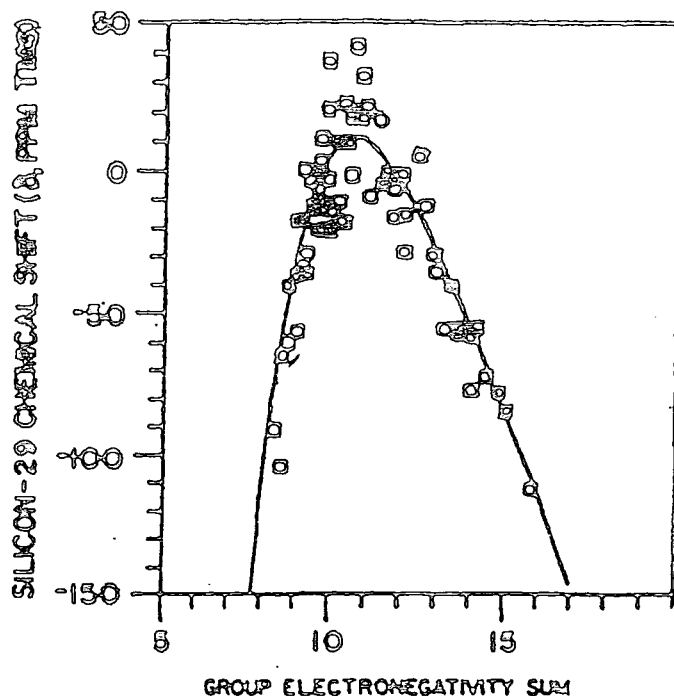


In order to aid the interpretation of observed isotropic chemical shifts in these materials various correlations have been proposed. In inorganic silicates empirical correlations between  $^{29}\text{Si}$  isotropic chemical shifts and Si-O bond lengths, bond energies<sup>(12)</sup>  $\text{Si}-\overset{\text{O}}{\text{Si}}$  bond angles,<sup>(13)</sup> mean T-O-T distances (where T = Si or Al),<sup>(14)</sup>  $\sigma$  orbital hybridisation,<sup>(15)</sup> electrostatic bond strengths of the cations<sup>(12)</sup> and ligand electronegativities<sup>(11)</sup> have been proposed for tetrahedrally coordinated silicon, and with mean Si-O bond lengths for minerals in which the silicon atom is octahedrally coordinated.<sup>(16)</sup>

One of the first publications to discuss  $^{29}\text{Si}$  shifts was published by Lauterbur.<sup>(20)</sup> It was demonstrated that in comparing  $^{13}\text{C}$  and  $^{29}\text{Si}$  chemical shifts for a series of compounds  $(\text{CH}_3)_n\text{M}(\text{OR})_{4-n}$ , where n is varied from 0-4 (M=Si or C), significant differences in substituent effects were observed for the two nuclei. A sagging pattern is exhibited in the case of the  $^{29}\text{Si}$  chemical shifts. This phenomenon was attributed to (p-d) $\pi$  bonding effects. From more

extensive studies of silicon containing materials,<sup>(11,21)</sup> it was observed that a "U" shaped relationship exists between <sup>29</sup>Si isotropic chemical shifts and the sum of the electronegativities of ligands bonded to the silicon (Figure 5.2).

FIGURE 5.2<sup>(11)</sup>



## 5.2 THEORETICAL INTERPRETATION OF <sup>29</sup>Si ISOTROPIC CHEMICAL SHIFTS

In spite of the fact that the theory of nuclear shielding is well established, the relationship between <sup>29</sup>Si isotropic chemical shifts and theoretical concepts is not straightforward.

According to Pople<sup>(17)</sup> the shielding constant  $\sigma$  of a nucleus A, which determines its chemical shift may be expressed as the sum of three terms

$$(5.1) \quad \sigma^A = \sigma_{\text{dia}}^A + \sigma_{\text{para}}^A + \sum_{B \neq A} \sigma^{AB}$$

where  $\sigma_{\text{dia}}$  is the diamagnetic term which depends upon the electron density at the nucleus given by Lambs formula:<sup>(18)</sup>

$$(5.2) \quad \sigma_{\text{dia}} = \frac{\mu_0 e^2}{12\pi} \sum_i \langle r_i^{-1} \rangle$$

where  $\mu_0$  is the permeability constant,  $e$  is the electronic charge,  $m$  is the electronic mass, and  $r_i$  is the distance of the  $i^{\text{th}}$  electron from the nucleus. From Gutowsky et al, the paramagnetic term  $\sigma_{\text{para}}$  is given as<sup>(19)</sup>

$$(5.3) \quad \sigma_{\text{para}} = -(\mu_0 e^2 \hbar^2 / 8\pi m^2 \Delta E) [\langle r^{-3} \rangle_p P_u + \langle r^{-3} \rangle_d D_u]$$

where  $\Delta E$  is the mean excitation energy,  $\langle r^{-3} \rangle_p$  and  $\langle r^{-3} \rangle_d$  are the mean inverse cubes of the distances of the valence p and d electron from the nucleus, and  $P_u$  and  $D_u$  represent the imbalance of the p and d populations.  $\sum_{B \neq A} \sigma^{AB}$  is the contribution from other atoms. It is generally accepted that change in the  $\sigma_{\text{para}}$  term is the most dominant factor determining isotropic chemical shifts in silicon-containing compounds<sup>(4)</sup>.

Problems in theoretical calculations of  $^{29}\text{Si}$  isotropic chemical shifts arise because of uncertainties in the magnitude of substituent effects on the values of the  $\Delta E$ ,  $\langle R^{-3} \rangle$ ,  $P_u$  and  $D_u$  terms in equation 5.3. There is also uncertainty as to whether (p-d) $\pi$  bonding occurs. One semi-empirical theory put forward to explain the nature of Figure 5.2 was proposed by Engelhardt et al.<sup>(4)</sup> In this theory, the tetrahedrally coordinated silicon atom is considered to form - by  $sp^3$  hybrid orbitals - localised  $\sigma$ -bonds to the four ligands. The average excitation energy  $\Delta E$  is taken as constant, any contribution of the silicon d-orbitals is excluded, and the paramagnetic shielding constant ( $\sigma_{\text{para}}^*$ ) is calculated relative to  $\sigma_{\text{para}}^0$ , which reflects the shielding of the hypothetical non-polar " $\text{SiSi}_4$ " molecule. Following these assumptions the final expression of the relative screening constant  $\sigma^*$  was given as equation 5.4

$$(5.4) \quad \sigma_{\text{para}}^* = \frac{\sigma_{\text{para}}}{\sigma_{\text{para}}^0} = \left[ \left( \frac{1+0.35f}{Z_0} \right) \left( 4 - \sum_i h_i \right) \right]^3 \left[ \frac{1 \sum_i h_i}{2i} - \frac{1 \sum_i \sum_j h_i h_j}{6i > j} \right]$$

where  $Z_0$  is the effective nuclear charge of silicon,  $f$  is an empirical

factor and values of  $h_i$  may be calculated from equation 5.5 from a knowledge of the electronegativities of the four ligands ( $\epsilon N_i$ ) and silicon ( $\epsilon N_{Si}$ ).

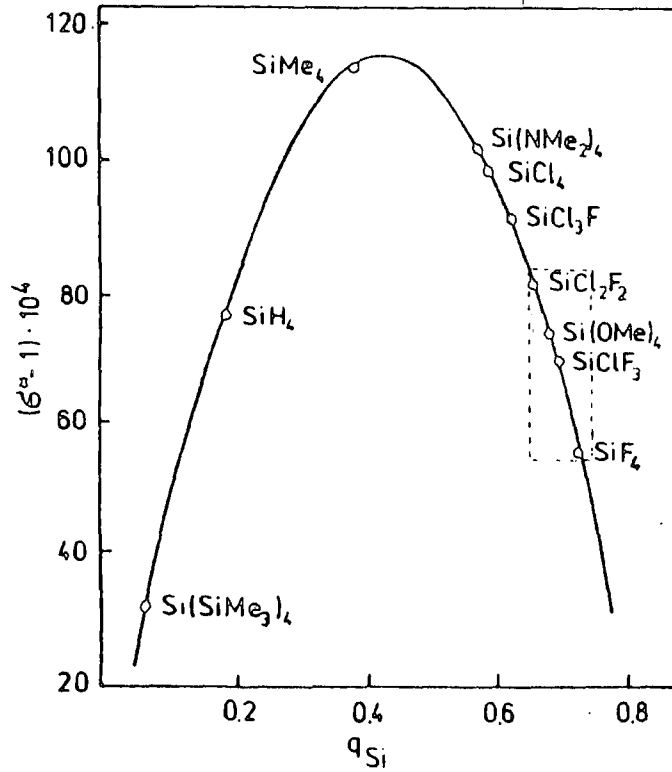
$$(5.5) \quad h_i = 1 - 0.16(\epsilon N_i - \epsilon N_{Si}) + 0.035(\epsilon N_i - \epsilon N_{Si})^2$$

The net charge of the central silicon atom ( $q_{Si}$ ) is given by equation 5.6

$$(5.6) \quad q_{Si} = 4 - \sum_{i=1}^4 h_i$$

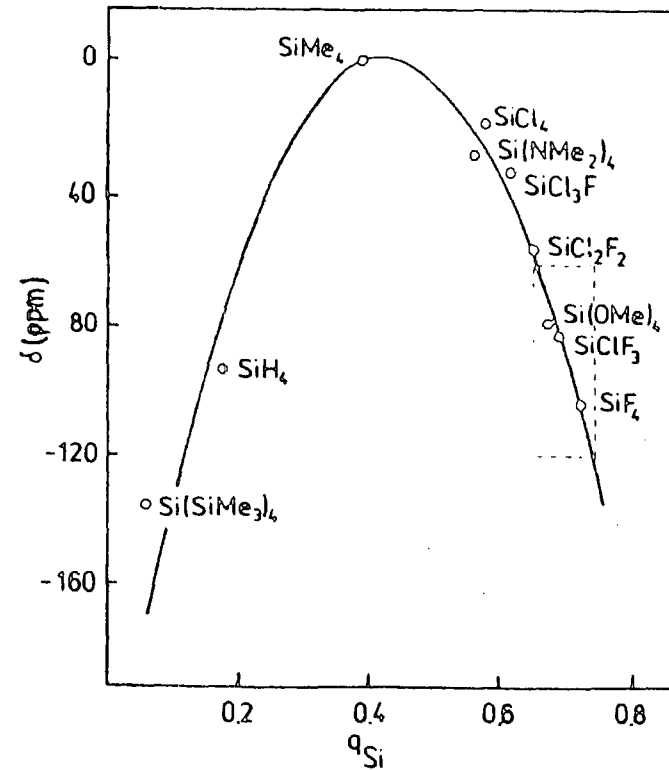
This approach achieved qualitative success in accounting for the u-shaped relationship between silicon shieldings and ligand electronegativities. Interesting information concerning the relationship between  $\sigma^*$  and  $q_{Si}$  was also obtained. These two parameters are related by a parabola-like curve (Figures 5.3 and 5.4),  $\sigma^*$  reaching a maximum when  $q_{Si} = 0.4$ . When  $q_{Si} < 0.4$ , an increase in  $q_{Si}$  results in high frequency shifts, however, when  $q_{Si} > 0.4$ , low frequency shifts occur as  $q_{Si}$  increases. The net charge of the silicon atom is determined by the electronegativity of the ligands  $\sigma$ -bonded to the tetrahedrally coordinated silicon atom (or the fractional s-character of the silicon-ligand hybrid orbitals). When  $q_{Si} > 0.6$ , the experimental shifts may be linearly correlated with  $\sigma^*$ , and also when  $q_{Si} < 0.2$ . This fact, is reflected in the empirical correlations between  $^{29}Si$  isotropic chemical shifts and the sum of the group electronegativities of the four ligands bonded to the central silicon atom, proposed by Janes and Oldfield.<sup>(11)</sup> In the case of inorganic silicates (where  $q_{Si} > 0.6$ ) the correlation between  $q_{Si}$  and chemical shifts, can also provide a direct explanation of the low frequency shifts observed as the degree of condensation of  $SiO_4$  tetrahedra increases, since the effective electronegativity of bridging oxygens is greater than non-bridging oxygens. Englehardt et al.<sup>(40)</sup> were able to rationalise correlations between  $^{29}Si$  isotropic

FIGURE 5.3



Calculated paramagnetic screening constants  $\sigma^*$  plotted against the net atomic charge of the central silicon atom  $q_{Si}$ .

FIGURE 5.4



experimental  $^{29}Si$  chemical shifts  $\delta$  of  $SiX_4$  compounds plotted against the net atomic charge of the central silicon atom  $q_{Si}$ .

The relevant range of  $SiO_4$  sites in silicates/aluminosilicates is marked by dashed lines

chemical shifts and Si-O-T bond angles, Si-O bond lengths and cation-oxygen bond strengths in terms of changes in the s-character of the oxygen hybrid orbitals

### 5.3 $^{29}\text{Si}$ SHIELDING TENSORS

In the study of silicate minerals where the structure is unknown, and  $^{29}\text{Si}$  isotropic chemical shifts are measured, it is not possible to employ the above correlations to obtain definitive information concerning the structural ( $Q^n$ ) units present. In rapid magic-angle spinning experiments only the isotropic part of the second rank chemical shielding tensor ( $\sigma$ ) is obtained. Information concerning the principal components is lost. The determination of the principal components of the tensor  $\sigma$  is important for several reasons. Firstly, it may help to provide a better explanation for, and physical descriptions of, the trends observed in  $^{29}\text{Si}$  chemical shifts, and in the case of silicate minerals, it may provide conformation as to the suggested nature of the silicon-oxygen tetrahedra present in minerals of unknown structure. Secondly, the tensor components provide data which may be used to test theoretical equations. Finally, shielding tensor information may yield evidence of molecular motion.

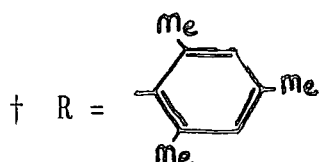
The importance of such measurements have, thus, prompted several workers to examine the principal components of the shielding tensor for silicon atoms in a variety of silicate minerals and organosilicon compounds.

The first  $^{29}\text{Si}$  NMR study of solid-state silicon compounds was published in 1972.<sup>(10)</sup> The principal components of the  $^{29}\text{Si}$  shielding tensor in a variety of organosilicon compounds were reported (Table 5.1). In general the  $^{29}\text{Si}$  shielding anisotropies were observed to be relatively small. In certain cases, it also appears that distortion of the molecular structure upon crystal formation was responsible for deviations of the shielding tensor from axial symmetry. Following

this publication, however, only three other reports have been published that give values for the principal components observed for organosilicon compounds<sup>(22,23,24)</sup> (Table 5.1). Interest has been predominantly directed towards the determination of these parameters in silicate minerals.

TABLE 5.1

COMPOUND	$\sigma_{\text{iso}}$ /ppm	$\sigma_{\text{xx}}$ /ppm	$\sigma_{\text{yy}}$ /ppm	$\sigma_{\text{zz}}$ /ppm	$\Delta\sigma$ /PPM	$\eta$	REFERENCE
$(\text{CH}_3)_4\text{Si}$	0	0	0	0	0	1.00	10
$(\text{CH}_3)_3\text{SiOCH}_3$	-18.7	-33	-31	8	40	0.08	10
$(\text{CH}_3)_2\text{Si}(\text{OCH}_3)_2$	3.7	-12	-12	35	47	0.00	10
$\text{CH}_3\text{Si}(\text{OCH}_3)_3$	42.0	23	35	68	39	0.46	10
$\text{Si}(\text{OCH}_3)_4$	80.0	80	80	80	0	1.00	10
$[(\text{CH}_3)_3\text{Si}]_3\text{CH}$	4.7	-8	4	18	20	0.90	10
$(\text{CH}_3)_3\text{SiC}_6\text{H}_5$	10.3	-2	4	29	17	0.32	10
$[(\text{CH}_3)_3\text{Si}]_2\text{O}$	-3.3	-16	-8	14	26	0.46	10
$[(\text{CH}_3)_2\text{SiO}]_3$	18.0	-8	0	62	66	0.18	10
$[(\text{CH}_3)_2\text{SiO}]_4$	20.0	4	4	53	49	0.00	10
$\text{R}_2\text{Si}=\text{SiR}_2^\dagger$	64.0	-15	27	180	174	0.36	23
$\text{R}_2\text{Si}-\text{SiHR}_2^\dagger$	-55.0	-72	-56	-37	27	0.89	23



In 1981 Grimmer et al<sup>(25)</sup> published the  $^{29}\text{Si}$  NMR spectra of polycrystalline tricalcium silicate hydrate ( $\text{Ca}_6[\text{Si}_2\text{O}_7(\text{OH})_6]$ ) and

tetra-methylammonium silicate hydrate ( $[\text{N}(\text{CH}_3)_4]_8\text{Si}_8\text{O}_{20}\cdot 69\text{H}_2\text{O}$ ). Values for the principal components of the shielding tensors for the silicon nuclei in each compound, (which are located in  $\text{Q}^1$  and  $\text{Q}^3$  environments respectively), are reported. The results were interpreted on the basis of the known structures of these two compounds, using arguments analogous to those used to explain  $^{31}\text{P}$  shielding anisotropies observed in phosphates and phosphonyl compounds.<sup>(26)</sup> Such arguments were used to gain a qualitative understanding of the relationship between bonding geometry and chemical shielding anisotropy. Each silicate  $\text{Q}^n$  unit was considered to form via the perturbation of the structure of the idealised  $(\text{SiO}_4)^{4-}$  anion. The idealised  $(\text{SiO}_4)^{4-}$  tetrahedron has four equal Si-O bonds (where the oxygens are terminal in the case of  $\text{Q}^0$  units and bridging in the case of  $\text{Q}^4$  units) hence  $\Delta\sigma = 0$ . End silicate tetrahedra (i.e.  $\text{Q}^1$  units) were considered to form when  $\pi$ -bond character is transferred from the Si- $\text{O}_b$  bridging bond to the three equal Si- $\text{O}_t$  terminal bonds. For these units the Si- $\text{O}_b$  bond lies along a local axis of  $\text{C}_{3v}$  symmetry. Conversely, branching silicate tetrahedra were considered to form when  $\pi$ -bond character is transferred from the three equal Si- $\text{O}_b$  bridging bonds to the Si- $\text{O}_t$  bond. In this case the Si- $\text{O}_t$  bond lies along a local axis of  $\text{C}_{3v}$  symmetry. In situations where a silicon nucleus lies upon an axis of  $\text{C}_{3v}$  symmetry, one of the three principal components is directed along the axis of symmetry and is designated  $\sigma_{||}$ . The other two principal components are equal and lie in a plane perpendicular to the this axis and are designated as  $\sigma_{\perp}$ . The shielding tensors exhibit axial symmetry. Grimmer et al, stated that the most (least) shielded principal component of the tensor, corresponds to the direction of the Si-O bond containing the highest (lowest) multiple bond character.<sup>(25)</sup> Thus for  $\text{Q}^1$  units, the transfer of  $\pi$ -bond character from the symmetry axis to

the other bonds causes deshielding parallel to the axis and increased shielding perpendicular to the axis, (i.e.  $\sigma_{\perp} > \sigma_{\parallel}$ ) and a negative shielding anisotropy is observed. Conversely, for  $Q^3$  units the transfer of  $\pi$ -bond character results in increased shielding parallel to the symmetry axis and decreased shielding perpendicular to it, (i.e.  $\sigma_{\parallel} > \sigma_{\perp}$ ) and a positive shielding anisotropy is observed. In the case of  $Q^2$  silicate units the interpretation is more difficult, there is no axial symmetry ( $\eta \neq 0.0$ ). However, provided local  $C_{2v}$  symmetry prevails, the most shielded principal component lies in the  $T^0$ -Si- $O_T$  plane bisecting the angle. Measurements of the principal components may be used to investigate minerals of unknown structure<sup>(27)</sup> and to confirm assignments made on the basis of isotropic chemical shift measurements. Grimmer has also shown that in order to explain shielding anisotropies in silicate minerals it is not necessary to invoke (p-d)  $\pi$ -bonding. The results may also be explained in terms of the fractional s-character of the silicon and oxygen hybrid orbitals involved in the Si-O bond.<sup>(28)</sup> In a study of the axially symmetric shielding tensors observed for silicon nuclei in six silicate minerals of known structure, Grimmer observed a linear relationship between the shielding tensor component  $\sigma_{\parallel}$  /ppm and the length of the Si-O bond it is directed along,  $d_{\parallel}$  (Si-O)/nm, Grimmer<sup>(28)</sup> derived equation 5.7a

$$(5.7a) \quad \sigma_{\parallel}(\text{Si-O}) = 2070 - 1.222 \times 10^{-4} d_{\parallel}(\text{Si-O})$$

A similar correlation was also observed for the shielding tensor  $\sigma_{\perp}$  and the Si-O bond lengths  $d_{\perp}$ (Si-O)/nm (see Figure 5.4a and Table 5.2). This is given by equation 5.7b

$$(5.7b) \quad \sigma_{\perp}(\text{Si-O}) = 2.250 - 1.334 \times 10^4 d_{\perp}(\text{Si-O})$$

Changes in the  $O-\text{Si}-O$  bond angles ( $\theta$ ), change the fractional

s-character of the silicon orbital in the Si-O bond ( $p^{\text{Si}}$ ) and cause the changes in the Si-O bond lengths.<sup>(29)</sup> Grimmer,<sup>(28)</sup> also reported a linear correlation between Si-O bond lengths and  $\text{O}-\overset{\text{Si}}{\text{O}}$  bond angles ( $\theta$ )

$$(5.8) \quad d(\text{Si-O}) = 0.25589 - 8.6 \times 10^{-4} \theta$$

The fractional s-character of the silicon orbital in the Si-O bond is given by equation 5.9

$$(5.9) \quad p^{\text{Si}} = \left[ \frac{\cos \theta}{1 - \cos \theta} \right]$$

TABLE 5.2

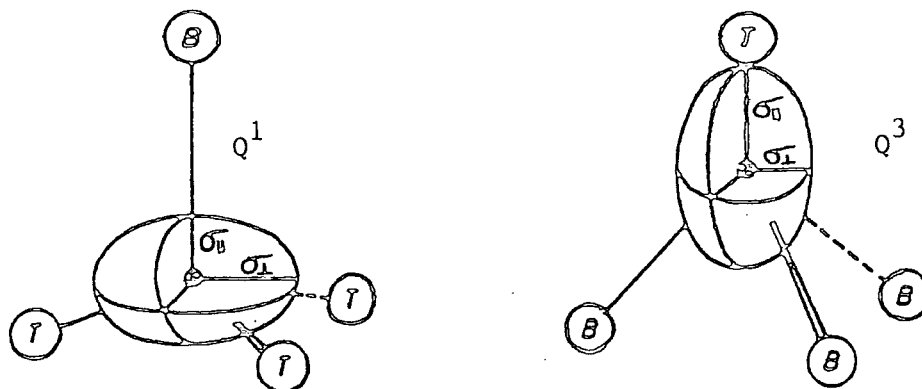
Si BOND LENGTHS AND  $^{29}\text{Si}$  CHEMICAL SHIFT TENSOR DATA OF SILICATES

SAMPLE	$q^n$	$d_{  }(\text{Si-O})$ /nm	$\sigma_{  }$ /ppm	$d_{\perp}(\text{Si-O})$ /nm	$\sigma_{\perp}$ /ppm
$\text{Ca}_3\text{SiO}_5$	$q^0$	0.1635	73.0	0.1635	73.0
$\text{Ca}_3\text{Si}_2\text{O}_7$	$q^1$	0.1667	30.3	0.1605	97.8
$\text{BaSi}_2\text{O}_5$	$q^3$	0.1561	158.9	0.1631	63.6
$[\text{N}(\text{Me})_4]_8\text{Si}_8\text{O}_{20} \cdot 69\text{H}_2\text{O}$	$q^3$	0.1569	152.0	0.1608	73.0
$((\text{CH}_3)_3\text{Si})_8\text{Si}_8\text{O}_{20}$	$q^3$	0.1588	131.3	0.1600	98.5
$\text{SiO}_2(1\text{-quartz})$	$q^4$	0.1609	107.4	0.1609	107.4

From these equations it may be seen a short Si-O bonds results from the silicon orbital possessing a high degree of s-character and the shorter the bond, the greater the shielding along that bond axis.

FIGURE 5.5

A PICTORIAL REPRESENTATION OF THE ORIENTATION OF THE  $^{29}\text{Si}$  SHIELDING TENSOR IN IDEALISED  $Q^1$  AND  $Q^3$  UNITS



In a similar way, shielding along a given Si-O bond may also be correlated with the fractional s-character for the bridging oxygen hybrid orbitals ( $P^0$ ). In a study of the structural data for more than 32  $Q^4$  units in 11 tectosilicates Gibbs et al, <sup>(29)</sup> have established a correlation between Si-O bond lengths ( $d(\text{Si-O})$ ) and  $P^0$ , given in equation 5.10

$$(5.10) \quad d(\text{Si-O}) = 0.169 - 0.16P^0$$

where  $P^0$  is given by equation 5.11

$$(5.11) \quad P^0 = \frac{\cos\phi}{-(1-\cos\phi)}$$

where  $\phi$  is the Si-O-Si bond angle.

In summary, it may be seen that the shielding along a given Si-O bond is dependent upon the bond length, which in turn is determined by the fractional s-character of the silicon and oxygen orbitals involved. Linear correlations between Si-O bond lengths and bond direction related shielding tensor components have been proposed. <sup>(28)</sup> In using these correlations to obtain structural information, however, caution is required. Firstly, the very good correlations reported by Grimmer <sup>(28)</sup> (equations 5.7a and 5.7b) are perhaps surprising, since it

is known that in polyatomic molecules, the paramagnetic term of the tensor component along a given bond is dependent upon all the other ligands attached to the nucleus. One possible explanation for Grimmers observation is that the electronic distribution resulting from the effect of the other three ligands determines both the Si-O bond length and the paramagnetic term for the shielding component along Si-O.<sup>(30)</sup> Secondly, a study made by Smith et al<sup>(12)</sup> reported that in the case of certain minerals containing  $Q^1$  units, axial symmetry was not observed (Table 5.3).

TABLE 5.3

NMR PARAMETERS OF SOME SILICATE MINERALS CONTAINING  $Q^1$  STRUCTURAL UNITS

MINERAL	$\frac{\sigma_{ISO}}{\text{ppm}}$	$\frac{\sigma_{XX}}{\text{ppm}}$	$\frac{\sigma_{YY}}{\text{ppm}}$	$\frac{\sigma_{ZZ}}{\text{ppm}}$	$\frac{\Delta\sigma}{\text{ppm}}$	$\eta$
Aker-manite	73	134	84	1	-108	0.69
Lawsonite	81	123	92	28	-80	0.58
Tricalcium Silicate Hydrate	84	109	109	35	-64	0.00
Gehlenite	72	122	74	20	-78	0.92

In this chapter, the  $^{29}\text{Si}$  isotropic chemical shifts, and the principal components of the shielding tensors are reported for a number of inorganic silicates, and organosilicon compounds.

The purpose of this work was to demonstrate the advantages and limitations of measuring  $^{29}\text{Si}$  shielding tensors when investigating the structure of these materials, and to examine factors which may determine shielding anisotropies in these systems.

## 5.4 EXPERIMENTAL

### THE DETERMINATION OF THE PRINCIPAL COMPONENTS OF $^{29}\text{Si}$ SHIELDING TENSORS

In principle, there are a number of methods which may be employed to determine the principal components of the  $^{29}\text{Si}$  shielding tensor. One method is to use a least-squares fit of the general expression for the powder pattern, to that observed for the sample. This method is subject to a number of errors since

- (1) Difficulties will be introduced if the sample under investigation contains multiple silicon sites
- (2) Errors may also occur in the calculation of the isotropic shift, since it is calculated from the average of the principal components.

An alternative method exists. Upon magic-angle-spinning (provided  $\omega_r < |\hbar \chi_{\text{CSA}}|$ ), the chemical shift powder pattern is decomposed into a collection of sharp peaks separated by integral multiples of the spinning frequency. Analysis of the distribution of the spinning sideband intensities then permits the calculation of the principal components. (31,32,33) This method offers the advantages that the isotropic chemical shifts are measured directly, the presence of multiple silicon species may be detected, and because the static powder pattern is broken up into a series of sharp lines, the number of transients required to obtain spectra with a signal to noise ratio, adequate for analysis is less than those required for the static spectra.

There exist a number of techniques whereby the principal components of the shielding tensor can be calculated from the intensity distribution of the spinning sidebands, the moments analysis method proposed by Maricq and Waugh, (31) the graphical method proposed

by Herzfeld and Berger,<sup>(32)</sup> and computer simulation of the spectra.<sup>(33)</sup> In this thesis, only the moments analysis and computer simulation methods will be considered.

#### 5.4.1 THE MOMENTS ANALYSIS METHOD

This was the first method for the determination of the principal components of shielding tensors. It is based on the fact that once the isotropic chemical shift has been determined, the only information required is the values for the shielding anisotropy and asymmetry parameter. These may be obtained by the calculation of the moments of the spectrum.

The  $i^{\text{th}}$  moment of a spectrum is defined by equation 5.13

$$(5.13) \quad M^i = \omega_r^i \frac{\sum_{N=-N}^{N=+N} N^i A_N}{\sum A_N}$$

where  $A_N$  is the intensity of the  $N^{\text{th}}$  sideband,  $\omega_r$  is the rotor spinning frequency and  $N$  is the number of sidebands. Sidebands are numbered outwards from the centreband, which is numbered zero, positive towards lower frequency, and negative towards higher frequency (e.g. -3, -2, -1, 0, +1, +2, +3, +4,). The lower order moments are given below

$$(5.14) \quad M_0 = 1$$

$$(5.15) \quad M_1 = 0$$

$$(5.16) \quad M_2 = \left[ \frac{\delta^2}{15} \right] (3 + \eta^2)$$

$$(5.17) \quad M_3 = \left[ \frac{2\delta^3}{35} \right] (1 - \eta^2)$$

$$(5.18) \quad M_4 = \left[ \frac{15}{7} \right] M_2 + 2\omega_r^2 M_2$$

In these equations the symbol  $\delta$  is used to denote shielding anisotropy, to distinguish it from the symbol  $\delta$  which is usually used for isotropic chemical shifts, however, in this chapter the reported anisotropies are defined differently, and are given the symbol  $\Delta\sigma$ , in

order to avoid any confusion. The relationship between  $\Delta\sigma$  and  $\delta$  is given by equations 5.19 and 5.20

$$(5.19) \quad \Delta\sigma = \sigma_{zz} - \frac{1}{2}(\sigma_{xx} + \sigma_{yy})$$

$$(5.20) \quad \Delta\sigma = \frac{3\delta}{2}$$

The intensities of the spinning sidebands are measured experimentally and the second and third moments are calculated. Given equations 5.16 and 5.17 a cubic solution for  $\delta$  may be found. The value of the asymmetry parameter  $\eta$  (defined by equation 5.21) is determined by inserting the values of  $\delta$  back into one of the two moments equations.

$$(5.21) \quad \eta = \frac{(\sigma_{yy} - \sigma_{xx})}{(\sigma_{zz} - \sigma_{ISO})}$$

The values of the three principal components may then be calculated given equations 5.22a, 5.22b and 5.22c.

$$(5.22a) \quad \sigma_{xx} = \sigma_{ISO} - \frac{\delta}{2}(1+\eta)$$

$$(5.22b) \quad \sigma_{yy} = \sigma_{ISO} - \frac{\delta}{2}(1-\eta)$$

$$(5.22c) \quad \sigma_{zz} = \sigma_{ISO} + \delta \quad \text{where } \sigma_{ISO} = -\delta$$

The use of this method does, however, have a number of disadvantages. Firstly, the calculation of the moments critically depends upon the intensity of the outer spinning sidebands (see equation 5.13). The intensity of these peaks are very difficult to measure accurately because of their weakness, in order to measure them accurately excellent signal to noise is required. In the case of insensitive nuclei, such as silicon-29 this is uneconomical in terms of spectrometer time. Secondly, work by Clayden et al<sup>(34)</sup> has shown that this method yields inconsistent results for nearly axially symmetric shielding tensors. (This disadvantage also occurs for the graphical method proposed by Hertzfeld et al).<sup>(32,34)</sup>

## 5.5 COMPUTER SIMULATION OF THE SPECTRA

In order to simulate and fit a spinning-sideband spectrum to the experimental spectrum, a mathematical description of the spectrum is required. The complete derivation of the expressions describing these spectra has been published by several workers<sup>(31,32)</sup> and will not be repeated here. A computer program has been written by L.H. Merwin at Durham University to perform the necessary calculations.<sup>(33)</sup> It was employed in these studies. Hence, the following discussion will be restricted to acquiring a physical picture of the processes giving rise to the spinning sidebands, and the principles upon which these calculations were carried out. The reader is referred to the above reference for further details of the computer program used.<sup>(33)</sup>

Consider, initially, a single type of chemically distinct nucleus in a molecule which is rotating at the magic angle. In order to explain the nature of the shielding interactions observed it is first necessary to translate these interactions from the laboratory frame, to a rotor fixed axis system, and then to the principal axis system (PAS). Maricq and Waugh<sup>(31)</sup> have shown that when this is done, the Hamiltonian describing the shielding interaction is of the form

$$(5.23) \quad \mathcal{H}_{CS} = \gamma B_0 I_Z [\sigma_i + \delta \xi(t)]$$

$\sigma_i$  is the isotropic trace of the shielding tensor,  $\delta$  is the shielding anisotropy,  $\gamma, B_0$  and  $I_Z$  have their usual meanings. The term  $\xi(t)$  contains all the time dependent terms induced by sample spinning,  $\xi(t)$  has the form

$$(5.24) \quad \xi(t) = C_1 \cos(\omega_r t) + S_1(\omega_r t) + C_2 \cos(\omega_r t) + S_2 \sin(2\omega_r t)$$

where

$$(5.24a) \quad C_1 = \frac{1}{2} \sin 2\theta \sin \beta [\cos \beta (\eta \cos 2\gamma - 3) \cos \alpha - \eta \sin 2\gamma \sin \alpha]$$

$$(5.24b) \quad S_1 = \frac{1}{2} \sin 2\theta \sin \beta [\cos \beta (3 - \eta \cos 2\gamma) \sin \alpha - \eta \sin 2\gamma \cos \alpha]$$

$$(5.24c) \quad C_2 = \frac{1}{2} \sin^2 \theta \left\{ \left[ \frac{3}{2} \sin^2 \beta + (\eta) \cos 2\gamma (1 + \cos^2 \beta) \right] \cos 2\alpha \right. \\ \left. - \eta \cos \beta \sin 2\gamma \sin 2\alpha \right.$$

$$(5.24d) \quad S_2 = \frac{1}{2} \sin^2 \theta \left\{ - \left[ \frac{3}{2} \sin^2 \beta + (\eta) \cos 2\gamma (1 + \cos^2 \beta) \right] \sin 2\alpha \right. \\ \left. - \eta \cos \beta \sin 2\gamma \sin 2\alpha \right.$$

where  $\eta$  is the asymmetry parameter.

The three angles  $\alpha, \beta, \gamma$  are the three Euler angles which define the orientation of the rotor fixed axis system relative to the principal axis system. The orientation of the rotor with respect to  $B_0$  is described by the two angles,  $\theta$  which is the angle between  $B_0$  and the rotor axis, and  $\omega_r t$  (see Figure 5.4b). In these experiments  $\theta$  is the magic angle and  $\omega_r$  is the angular spinning speed.

In a static powder, the resonance frequency of a nucleus in a molecule is dependent upon the orientation of the PAS with respect to  $B_0$ , as a consequence of the anisotropic nature of the shielding interaction. The static powder spectrum results from the superposition of contributions from all the randomly orientated molecules in the powder. When the sample is rotated at the magic angle, the instantaneous resonance frequency of the nuclei in question changes as the molecule changes its orientation with respect to  $B_0$ , during the course of one rotation. The angular frequency of the  $j^{\text{th}}$  nucleus, as a function of time is given as

$$(5.25) \quad \omega_j(t) = \omega_0 \sigma_{\text{ISO}} + \omega_0 \delta \xi_j(t)$$

$\omega_0$  is the Larmor precession frequency. In a specific time period, the principal shielding axis in the molecule changes orientation and develops a phase angle  $\phi$

$$(5.26) \quad \phi_j(t) = \int_0^t \omega_j(t) dt = \omega_0 \sigma_{\text{ISO}} t + \omega_0 \delta \int_0^t \xi_j(t) dt$$

Given that the free induction decay is represented by equation 5.27,

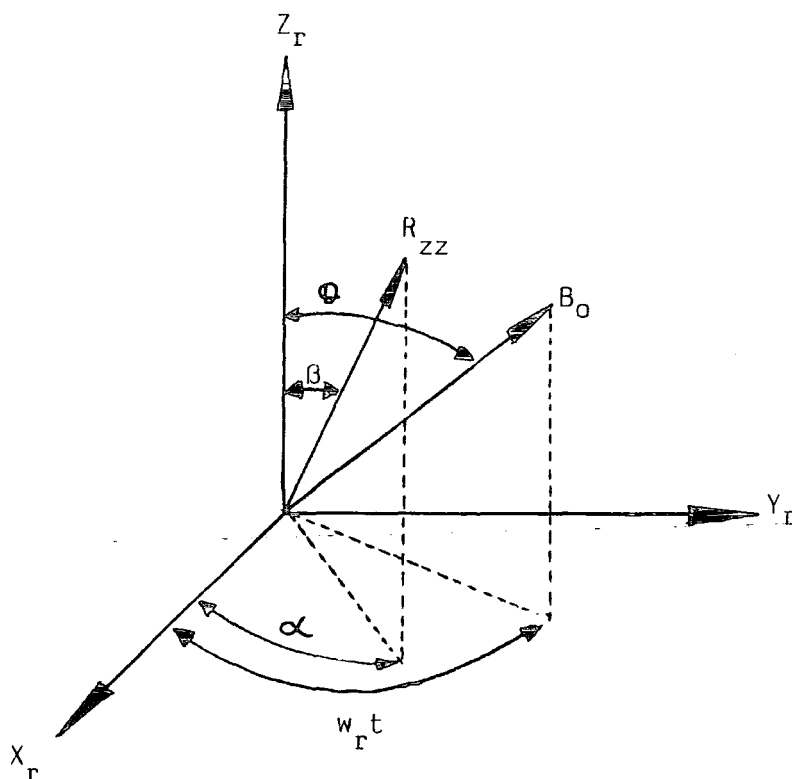
$$(5.27) \quad g(t) = \exp[i\phi_j(t)]$$

Summation for all orientations (i.e. over all possible values of  $\alpha$ ,  $\beta$  and  $\gamma$ ) produces an equation describing the spinning-sideband spectrum

$$(5.28) \quad g(t) = \exp(i\omega_0 \sigma_{IS0} t) \cdot \sum_{\alpha} \sum_{\beta} \sum_{\gamma} \exp[i\omega_0 \delta f_0^t \xi(t) dt]$$

The summation for all nuclei is required because if one considers equation 5.25, each nucleus will have its own spinning-sideband pattern, centred about the isotropic chemical shift. The orientation of the principal axis system in the rotor is defined by the angles  $\alpha$  and  $\beta$ . The angle  $\beta$  is the angle between the rotor axis ( $Z_r$ ) and the unique tensor axis  $R_{ZZ}$ . The angle  $\alpha$  is the projection of  $R_{ZZ}$  on the rotor x,y plane. The sum  $(\alpha + \omega_r t)$  thus indicates the position of  $R_{ZZ}$  with respect to  $B_0$  as a function of time (see Figure 5.4b)

FIGURE 5.4b



At the start of the experiment xy magnetisation is derived either by cross-polarisation or by a  $90^\circ$  pulse. As the sample rotates, the magnetisation will dephase, as all the different nuclei experience different resonance frequencies as the phase angle (the orientation of the PAS with respect to  $B_0$ ) continuously changes. At the end of the rotor period however, all the nuclei are back in their original

orientations with respect to  $B_0$  the total phase angle developed by any nucleus zero, and the magnetisation is restored. The complete FID is thus characterised by a series of rotational echoes. The intensity of successive echoes is also governed by the usual  $T_1$  and  $T_2$  processes, so the FID will normally decay exponentially.

Consider a single nucleus. As the sample is rotated, the PAS will pass through angles from  $(\theta-\beta)$  to  $(\theta+\beta)$  with respect to  $B_0$ , and the nucleus will develop instantaneous resonance frequencies which contribute to only a portion of the full static linewidth. Thus it is possible that a given nucleus may not contribute to all the intensities of the spinning sidebands. In addition, for a nucleus with a specific angle  $\beta$ , the phase of the sidebands produced will depend upon the angle  $\alpha$ , and both absorptive and dispersive components are produced, depending upon the initial orientation of  $\alpha$ . Thus in order to reproduce the spinning sideband spectrum, summation over all possible orientations is required, and since all the tensor information is contained within one rotational echo, in order to model the intensity of the spinning sideband, the limits for the time integral in equation 5.28 need only be 0 to  $2\pi/\omega_r$ . The calculation of the rotational echoes may be achieved by evaluating the integral of equation 5.28 in  $N2\pi/\omega_r$  steps. The time integral of equation 5.28 has the following form.

$$(5.29) \quad \int_0^t \xi(\alpha, \beta, \gamma, t) dt = \frac{1}{\omega_r} [S_1 + \frac{1}{2} S_2 + C_1 \sin(\omega_r t) - S_1 \cos(\omega_r t) + \frac{1}{2} (C_2 \sin(2\omega_r t) - S_2 \cos(2\omega_r t))]$$

This integral must then be determined for all possible values of  $\alpha$ ,  $\beta$  and  $\gamma$  over a time period of 0 to  $(2\pi/\omega_r)$ . Thus the FID is given by equation

$$(5.30) \quad g(t) = \sum_{\alpha} \sum_{\beta} \sum_{\gamma} \exp\left\{ \int_0^t \exp[i(\omega_0 \delta \xi(\alpha, \beta, \gamma))] dt \right\}$$

Note that the term  $\exp(i\omega_0\sigma_{\text{ISO}}t)$  is dropped in equation 5.30, since this term serves only to give an overall offset to each spinning sideband. This is equivalent to placing the centreband at the isotropic chemical shift frequency. Fourier transform then yields the frequency domain spectrum. In an effort to keep the time required for computation to a minimum while still retaining accuracy of the final computed spectrum, Merwin<sup>(33)</sup> suggests that, in order to sum the time integral of equation 5.28 through all orientations, each of the angles  $\alpha$ ,  $\beta$  and  $\gamma$  are stepped in  $9^\circ$  increments. In Merwin's program, the intensity of the experimental spinning sidebands are compared with those calculated, and values for the anisotropy ( $\delta$ ) and asymmetry ( $\eta$ ) parameters are changed by means of a Simplex routine until the sum of the squares of the difference between the intensities of the corresponding sidebands is a minimum. In order to run this program, input parameters of the Larmor frequency, rotor speed, numbers of the spinning sidebands and their intensities, the isotropic chemical shift, and estimated anisotropy and asymmetry parameters are required. The anisotropy and asymmetry parameters are estimated by moments analysis.

## 5.6 RESULTS AND DISCUSSION

### 5.6.1 THE DIHYDROGEN SILICATE HYDRATES

The ability of slow-spinning  $^{29}\text{Si}$  CP MAS NMR experiments, and subsequent computation of the tensor properties, to yield information that is not available from rapid MAS experiments is illustrated by the study of the two sodium dihydrogensilicate hydrates  $\text{Na}_2\text{H}_2\text{SiO}_4(\text{H}_2\text{O})_4$  and  $\text{Na}_2\text{H}_2\text{SiO}_4(\text{H}_2\text{O})_8$ .

The  $^{29}\text{Si}$  CP MAS NMR spectra of both these compounds have the same isotropic chemical shift at -68.6 ppm (Figures 5.7 and 5.10). This was confirmed by obtaining the  $^{29}\text{Si}$  CP MAS NMR spectrum of a physical

mixture of the two compounds. It is impossible to distinguish between these two compounds by rapid  $^{29}\text{Si}$  MAS NMR experiments. Slow-spinning  $^{29}\text{Si}$  CP MAS NMR experiments, however, reveal subtle differences in the environment of the silicon nuclei in each compound (Figures 5.5, 5.6 and 5.8, 5.9). These differences are reflected in the anisotropy calculated from computer fitting of the spinning sidebands. The results are summarised in Table 5.4.

TABLE 5.4

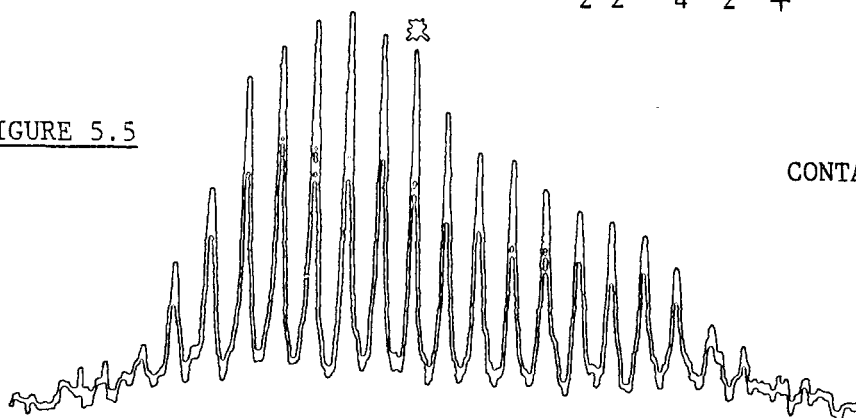
COMPOUND	$\eta$	$\Delta\sigma$ /ppm	$\sigma_{\text{iso}}$ /ppm	$\sigma_{\text{xx}}$ /ppm	$\sigma_{\text{yy}}$ /ppm	$\sigma_{\text{zz}}$ /ppm
$\text{Na}_2\text{H}_2\text{SiO}_4(\text{H}_2\text{O})_4$	0.51	74.0	68.6	31.4	56.5	117.9
$\text{Na}_2\text{H}_2\text{SiO}_4(\text{H}_2\text{O})_8$	0.64	89.3	68.6	19.8	57.9	128.1

† errors in  $\sigma_{\text{ii}}$  are typically ca  $\pm 2$

The crystal structures of both  $\text{Na}_2\text{H}_2\text{SiO}_4(\text{H}_2\text{O})_4$  and  $\text{Na}_2\text{H}_2\text{SiO}_4(\text{H}_2\text{O})_8$  have been published (space groups P1 and Ibca respectively), in each case the compounds are known to contain one isolated  $\text{H}_2\text{SiO}_4^{2-}$  anion in the asymmetric unit and exhibit a high degree of ionic character. (35,36) The X-ray diffraction results

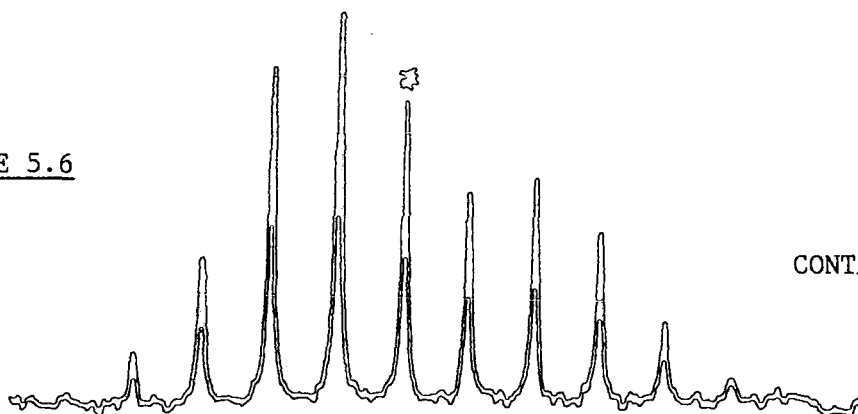
$^{29}\text{Si}$  CP MAS NMR SPECTRA OF DISODIUM DIHYDROGEN SILICATE PENTAHYDRATE  
 $\text{Na}_2\text{H}_2\text{SiO}_4(\text{H}_2\text{O})_4$

FIGURE 5.5



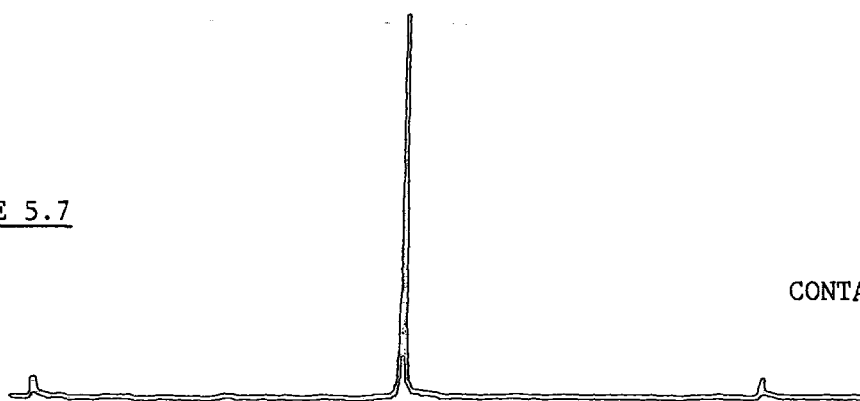
$\omega_r = 205$  Hz  
CONTACT TIME = 6 ms  
NS = 1240  
RD = 20 s

FIGURE 5.6

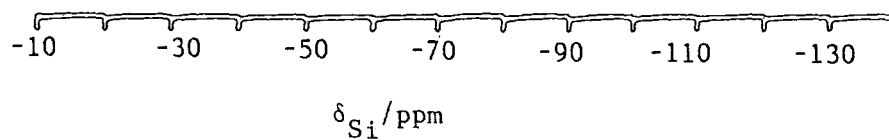


$\omega_r = 407$  Hz  
CONTACT TIME = 6 ms  
NS = 700  
RD = 20 s

FIGURE 5.7



$\omega_r = 2.2$  kHz  
CONTACT TIME = 32  
NS = 24  
RD = 20 s



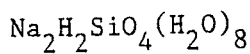
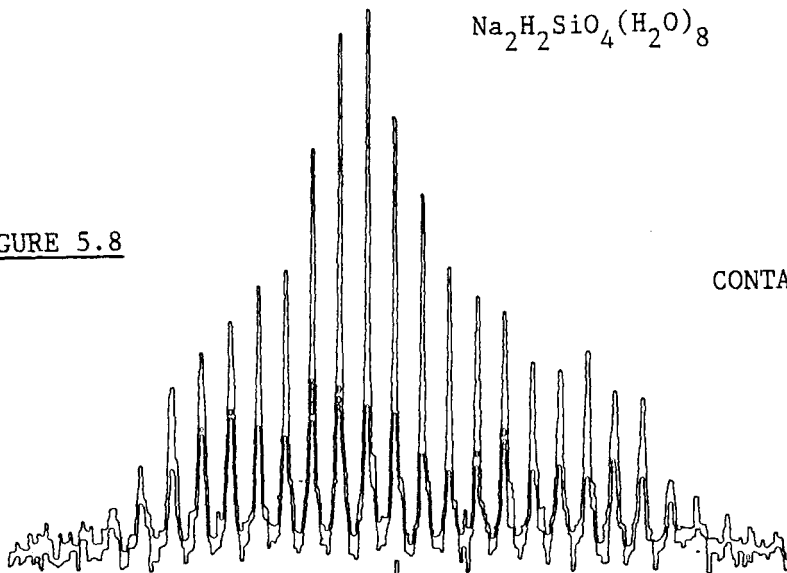
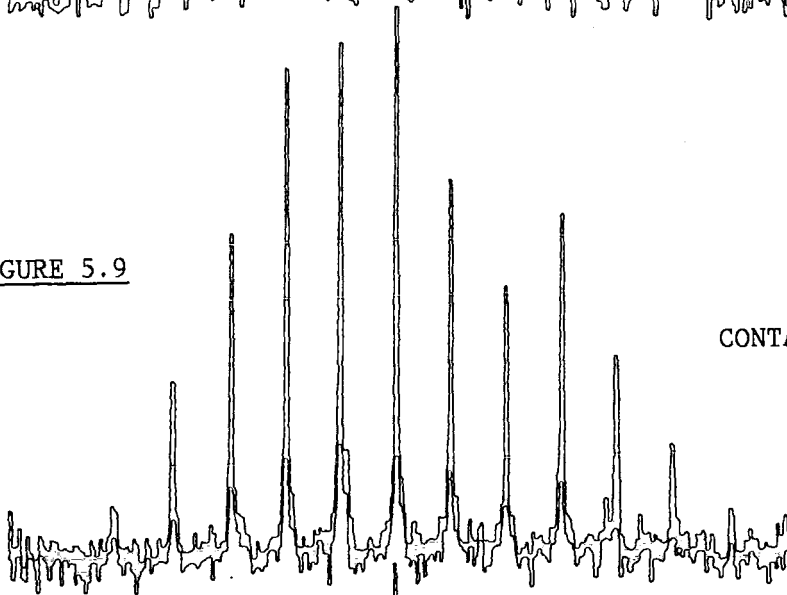


FIGURE 5.8



$\omega_r = 201 \text{ Hz}$   
CONTACT TIME = 6 ms  
NS = 9640  
RD = 4 s

FIGURE 5.9

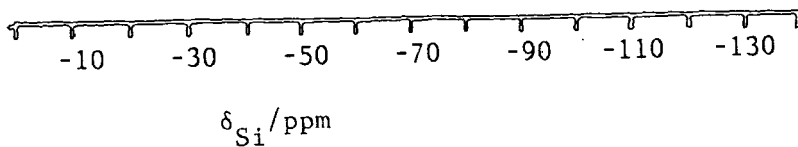


$\omega_r = 402 \text{ Hz}$   
CONTACT TIME = 1.5 ms  
NS = 1000  
RD = 4 s

FIGURE 5.10



$\omega_r = 3.00 \text{ kHz}$   
CONTACT TIME = 6 ms  
NS = 32  
RD = 10 s



clearly reveal differences in the geometry of the silicon-oxygen tetrahedra in the two compounds. In the case of the compound  $\text{Na}_2\text{H}_2\text{SiO}_4(\text{H}_2\text{O})_4$  there are two hydroxyl groups associated with each silicon atom,<sup>(35)</sup> but these are distributed randomly over the four possible sites. For the compound  $\text{Na}_2\text{H}_2\text{SiO}_4(\text{H}_2\text{O})_8$ ,<sup>(36)</sup> however, the exact position of these hydroxyl groups in relation to the geometry of the silicon-oxygen tetrahedron may be determined. (Figures 5.11 and 5.12).

In the compound  $\text{Na}_2\text{H}_2\text{SiO}_4(\text{H}_2\text{O})_8$ , the high degree of ionic character of the  $\text{H}_2\text{SiO}_4^{2-}$  anion suggests that in the shielding of the silicon nucleus, electric field gradients may be important (the effects of paramagnetic impurities were considered negligible). In order to test this hypothesis it was suggested<sup>(37)</sup> that by the use of electric field gradient calculations (as usually applied to quadrupolar nuclei), it may be possible to calculate the asymmetry parameter. These calculations were performed in the following way.

The electric field gradient tensor in the principal axis system has three components  $V_{xx}$ ,  $V_{yy}$  and  $V_{zz}$  where

$$(5.31a) \quad V_{xx} = \frac{\partial^2 V}{\partial X^2} \quad (b) \quad V_{yy} = \frac{\partial^2 V}{\partial Y^2} \quad \text{and} \quad V_{zz} = \frac{\partial^2 V}{\partial Z^2}$$

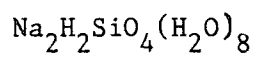
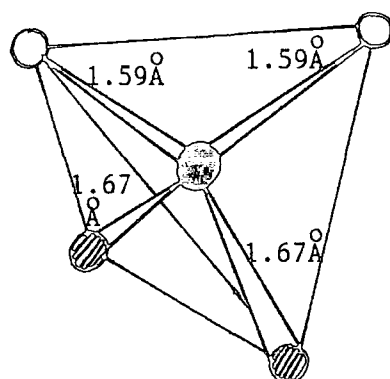
where  $V$  is the electric potential.

The trace of this tensor<sup>(V)</sup> is zero and the asymmetry parameter  $\eta^{\text{EFG}}$  is a measure of the electrical asymmetry about the silicon atom.

$$(5.32) \quad \eta^{\text{EFG}} = (V_{xx} - V_{yy}) / V_{zz}$$

The EFG is assumed to be set up by point charges of  $Z$ , and the contribution of one point charge to each component of the EFG tensor is given by the expression in Table 5.5.

FIGURE 5.11

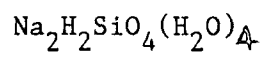
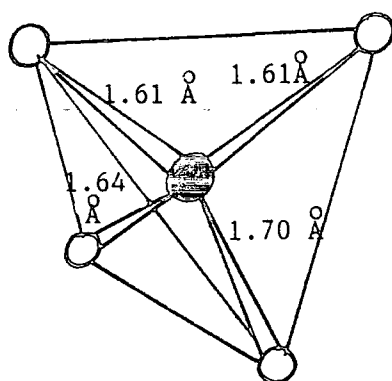
SPACE GROUP  $Ibca$ 

○ Si

○ O

● OH

FIGURE 5.12

SPACE GROUP  $P\bar{1}$ 

● Si

○ O

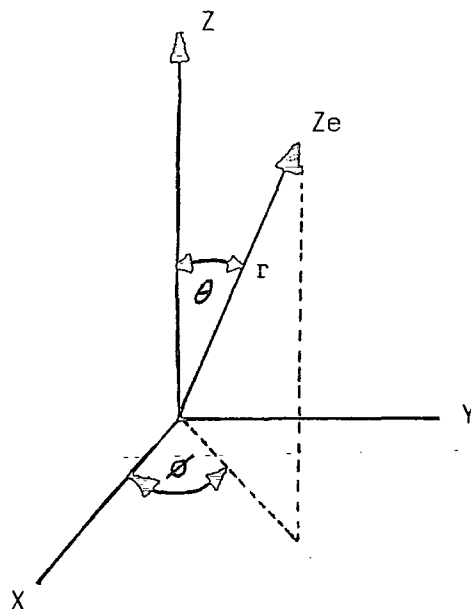
TABLE 5.5

COMPONENTS OF THE ELECTRIC FIELD GRADIENT TENSOR FOR A CHARGE OF  $Ze$   
ELECTRONIC UNITS

$$\begin{aligned}
 V_{XX} &= Ze r^{-3} (3 \sin^2 \theta \cos^2 \phi - 1) & V_{XY} &= V_{YX} = Ze r^{-3} (3 \sin^2 \theta \sin \phi \cos \phi) \\
 V_{YY} &= Ze r^{-3} (3 \sin^2 \theta \sin^2 \phi - 1) & V_{XZ} &= V_{ZX} = Ze r^{-3} (3 \sin \theta \cos \theta \cos \phi) \\
 V_{ZZ} &= Ze r^{-3} (3 \cos^2 \theta - 1) & V_{YZ} &= V_{ZY} = Ze r^{-3} (3 \sin \theta \cos \theta \sin \phi)
 \end{aligned}$$

The angles  $\theta$  and  $\phi$  define the position of point charges ( $Ze$ ) relative to the principal axis system (Figure 5.14)

Figure 5.14

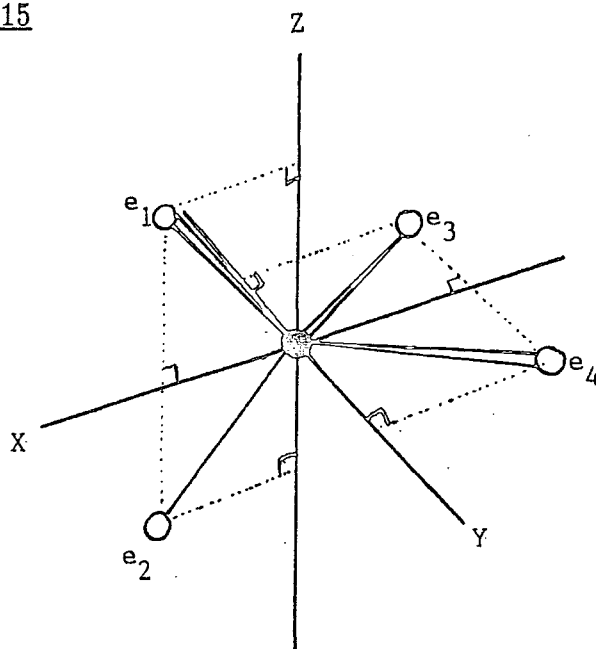


The resultant tensor becomes diagonalised when the coordinate axes are correctly chosen.

For the geometry of the  $\text{H}_2\text{SiO}_4^{2-}$  anion in the compound  $\text{Na}_2\text{H}_2\text{SiO}_4(\text{H}_2\text{O})_8$  (Figure 5.11), the coordinate axes are chosen as illustrated in Figure 5.15, since X-ray diffraction studies of this compound indicate there is almost local  $C_{2v}$  symmetry about the silicon.



FIGURE 5.15



The corresponding angles of  $\theta$  and  $\phi$  for the point charges  $e_1$ ,  $e_2$ ,  $e_3$  and  $e_4$  are given in Table 5.6.

TABLE 5.6

$e_n$	$\theta$	$\phi$
$e_1$	31.55	0
$e_2$	121.55	0
$e_3$	90.00	232.95
$e_4$	90.00	127.05

This choice of the coordinate axes appear to be close to the correct one since  $V_{XY} \approx V_{YX} \approx V_{ZX} \approx V_{XZ} \approx V_{YZ} \approx V_{ZY} \approx 0$ . On the assumption that these point charges are absent on the oxygen atoms of the Si-OH groups, the asymmetry parameter is  $\eta^{\text{EFG}} = 0.70$ . This value is in reasonable agreement with that observed from slow-spinning  $^{29}\text{Si}$  CP MAS NMR experiments.

### 5.6.2 DATOLITE

The mineral Datolite has the formula  $\text{CaBSiO}_4(\text{OH})$  and like  $\text{Na}_2\text{H}_2\text{SiO}_4(\text{H}_2\text{O})_4$  and  $\text{Na}_2\text{H}_2\text{SiO}_4(\text{H}_2\text{O})_8$ , also contains isolated  $\text{Q}^0$  units. The  $^{29}\text{Si}$  CP MAS NMR spectrum of this compound exhibits a single isotropic chemical shift at -82.8 ppm (Figure 5.18). This value is in close agreement with that observed by Smith et al (-83 ppm).<sup>(12)</sup> The magnitude of the asymmetry ( $\eta$ ) parameter, however, differs significantly from those reported in the literature,<sup>(12)</sup> but is in close agreement with that observed by Grimmer<sup>(39)</sup> (Table 5.7) (see also Figures 5.16 and 5.17). No explanation for these differences can be offered.

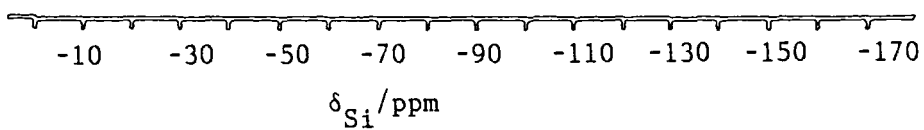
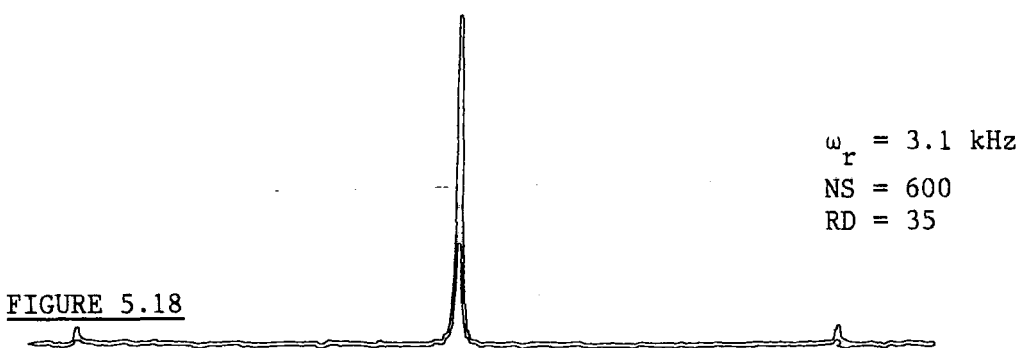
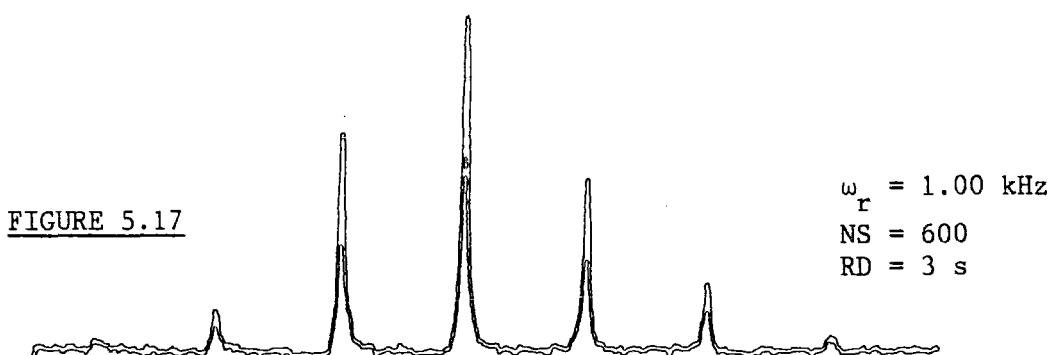
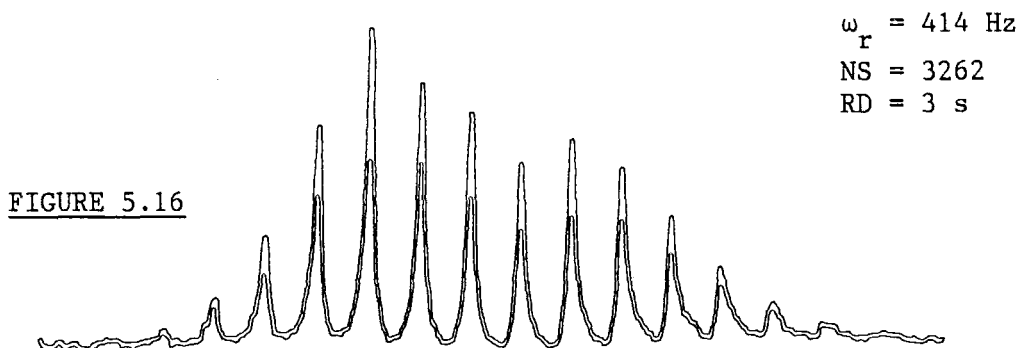
TABLE 5.7

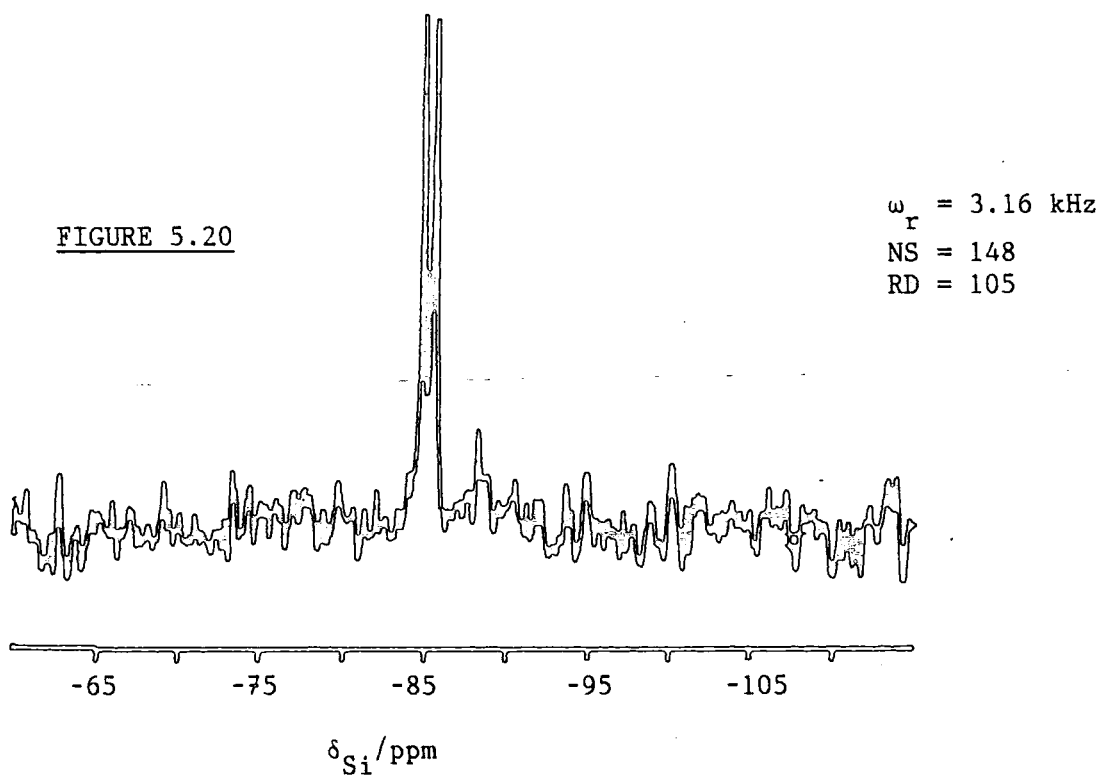
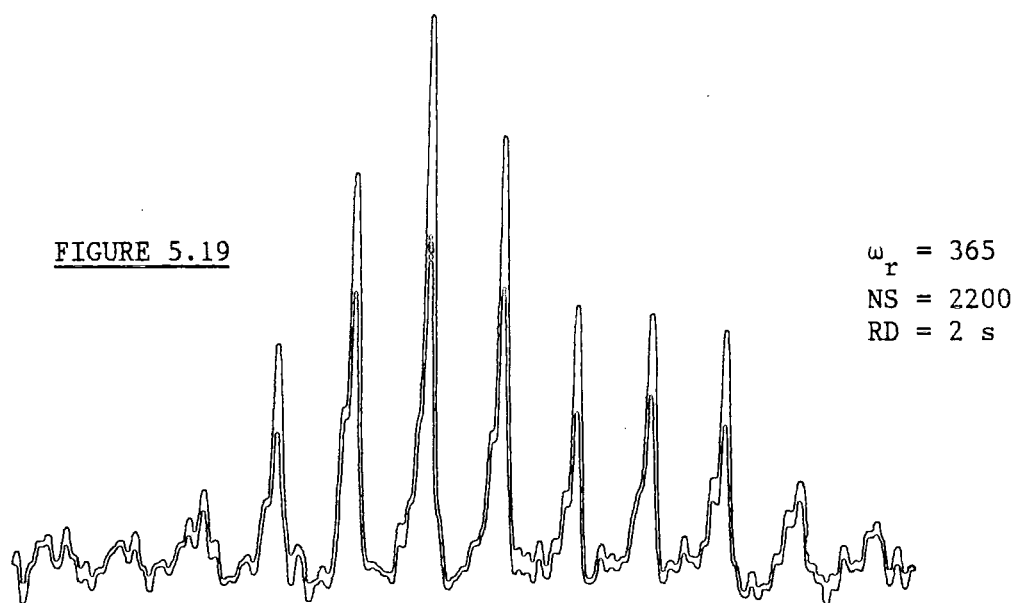
NMR PARAMETERS FOR THE MINERAL DATOLITE  $\text{CaBSiO}_4(\text{OH})$

REFERENCE	$\Delta\sigma$ /ppm	$\eta$	$\sigma_{ZZ}$ /ppm	$\sigma_{YY}$ /ppm	$\sigma_{ZZ}$ /ppm	$\sigma_{\text{ISO}}$ /ppm
THIS WORK	97.1	0.66	29.1	71.8	147.5	82.8
SMITH et al <sup>(12)</sup>	96	0.25	43	59	147	83

### 5.6.3 TILLEYITE AND THORTVEITITE

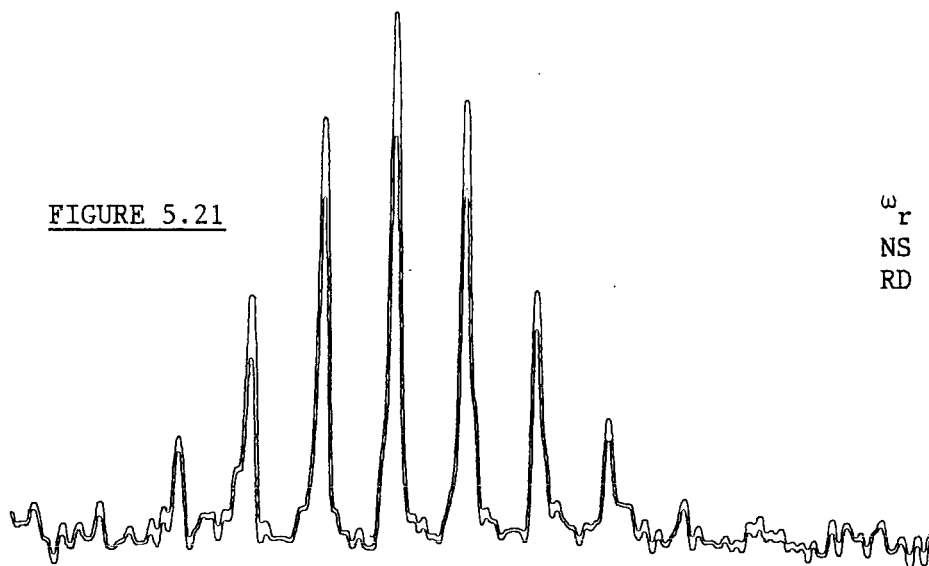
The  $^{29}\text{Si}$  MAS NMR spectra of the minerals tilleyite and thortveitite have been obtained (Figures 5.19, 5.20 and 5.21, 5.22 respectively). The  $^{29}\text{Si}$  MAS NMR spectrum of thortveitite exhibits a single isotropic chemical shift at -95.2 ppm. The crystal structure of this mineral has been published<sup>(40)</sup> and reveals two  $\text{Si}_2\text{O}_7^{6-}$  anions in each unit cell (space group  $\text{C2/m}$ ). The Si-O-Si bond angle is  $180^\circ$  and the asymmetric unit consists of the  $\text{O}_{1/2}\text{SiO}_3^{3-}$  moiety. Thus the  $^{29}\text{Si}$  NMR results confirm the X-ray diffraction studies. Slow-spinning  $^{29}\text{Si}$  MAS NMR experiments have been performed upon this mineral, the results

$^{29}\text{Si}$  MAS NMR SPECTRA OF DATOLITE

$^{29}\text{Si}$  MAS NMR SPECTRA OF TILLEYITE

$^{29}\text{Si}$  MAS NMR SPECTRA OF THORTVEITITE

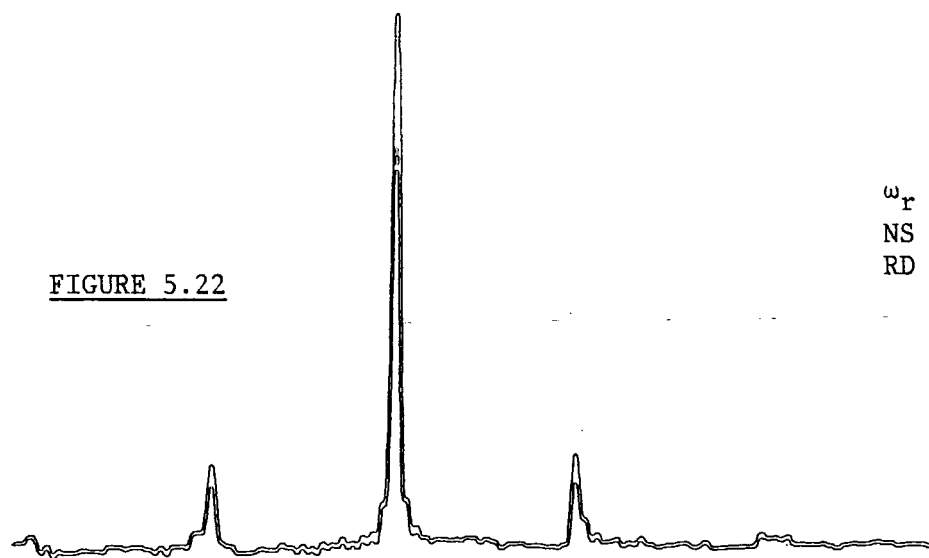
FIGURE 5.21

 $\omega_r = 546$ 

NS = 818

RD = 3 s

FIGURE 5.22

 $\omega_r = 1.41$  kHz

NS = 720

RD = 3 s

-20 -40 -60 -80 -100 -120 -140 -160 -180

 $\delta_{\text{Si}}/\text{ppm}$

are summarised in Table 5.8.

The results of these slow-spinning experiments are unexpected, since from Grimmer's work<sup>(25)</sup> one would expect an axially symmetric shielding tensor to be observed for silicon nuclei in the mineral thortveitite. In reality however, significant deviation of the shielding tensor from axial symmetry is observed ( $\eta \approx 1.0$ ). This could be the result of the presence of paramagnetic impurities, however, analysis of this sample using Inductive Plasma Spectrophotometry failed to yield consistent results owing to difficulties in sample preparation, and electron spin resonance (e.s.r.) proved unable to detect the presence of any unpaired electrons in this sample.

The  $^{29}\text{Si}$  MAS NMR spectrum of Tilleyite or pentacalcium disilicate biscarbonate ( $\text{Ca}_5\text{Si}_2\text{O}_7(\text{CO}_3)_2$ ) exhibits two isotropic chemical shifts at -79.6 ppm and -81.1 ppm, with an intensity ratio of 1:1 (Figure 5.20). This result suggests the presence of two silicon sites in the asymmetric unit. The crystal structure of this mineral has been published<sup>(41)</sup> (space group  $\text{P}2_1/\text{a}$ ). The asymmetric unit consists of two silicon atoms in the disilicate anion  $\text{Si}_2\text{O}_7^{6-}$ . The bond angle  $\text{Si}-\text{O}-\text{Si}$  is  $165^\circ$ . The two silicon atoms are crystallographically inequivalent. Slow-spinning  $^{29}\text{Si}$  MAS NMR experiments reveal that, as with thortveitite, significant deviation of the shielding tensor from axial symmetry is observed (Figure 5.19 and Table 5.8). ESR studies of this mineral failed to detect the presence of unpaired electrons.

TABLE 5.8

MINERAL	$\frac{\sigma_{\text{ISO}}}{\text{ppm}}$	$\frac{\sigma_{\text{xx}}}{\text{ppm}}$	$\frac{\sigma_{\text{yy}}}{\text{ppm}}$	$\frac{\sigma_{\text{zz}}}{\text{ppm}}$	$\frac{\Delta\sigma}{\text{ppm}}$	$\eta$
Thortveitite	95.2	62.7	94.9	128.0	49.2	0.98
Tilleyite	79.6 } 81.1 }	115.0	81.8	43.3	-55.6	0.92

Closer inspection of the crystal structures of these minerals reveals that for tilleyite all the terminal Si-O bonds are not the same length, hence one would not expect any local axis of  $C_{3V}$  symmetry at either silicon site (Figure 5.24). In this case the lack of axial symmetry for the  $^{29}\text{Si}$  shielding tensor is not surprising. However, for thortveitite all the terminal Si-O bonds are very similar in length (Figure 5.23), given the experimental errors of the original measurements, and although the silicon atoms do not appear to lie upon an axis of  $C_{3V}$  symmetry, one might expect near axial symmetry to be observed. For thortveitite, the magnitude of the asymmetry parameter is surprising. These results are consistent with those of Smith et al.,<sup>(12)</sup> that the observation of axial symmetry for  $Q^1$  units is not a general rule, and at least part of the reason why axial symmetry is not observed for all  $Q^1$  units arises from distortion of the Si-O terminal bond lengths, such that they are unequal (as in tilleyite), however, it would appear that for thortveitite additional unidentified factors must be operating, to cause such large values of  $\eta$ .

FIGURE 5.23

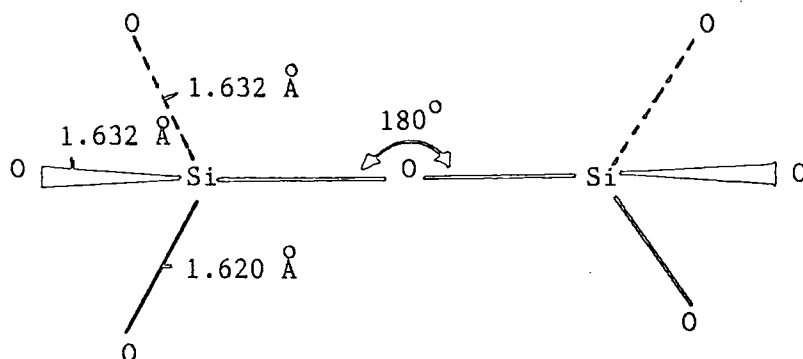
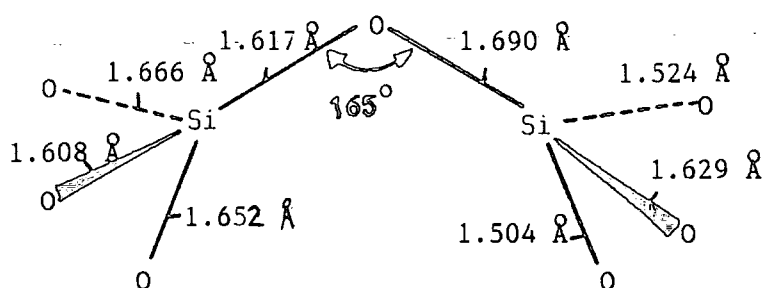
THORTVIETITE

FIGURE 5.24

TILLEYITE5.6.4 MINERALS CONTAINING Q<sup>3</sup> UNITS

In this section, five minerals known to contain Q<sup>3</sup> units have been studied using slow-spinning <sup>29</sup>Si CP MAS NMR techniques. The

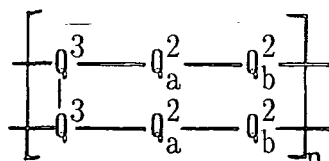
crystal structures of four of these minerals are known (xonotlite, apophyllite, and  $[\text{N}(\text{Me})_3]_8\text{Si}_8\text{O}_{20}\cdot 69\text{H}_2\text{O}$ ), but the structures of the other two minerals (octasilicate and kanemite) are not. Each of these minerals will be discussed in turn.

#### 5.6.4.1 XONOTLITE. $(\text{Ca}_6\text{Si}_6\text{O}_{17}(\text{OH})_2)$

The  $^{29}\text{Si}$  CP MAS NMR spectrum of the mineral xonotlite (hexacalcium dihydrogenhexasilicate), exhibits three isotropic chemical shifts at -86.6, -87.2 and -97.8 ppm (Figure 5.26). These are assigned to silicon nuclei in  $Q^2$ ,  $Q^2$  and  $Q^3$  environments respectively. This spectrum, however, differs from that published previously, in which only two isotropic chemical shifts at -86.8 and -97.8 ppm are observed.<sup>(1)</sup> The crystal structure of this mineral has been published<sup>(42)</sup> (space group P12/a1) the results show there are three silicon atoms in the asymmetric unit. In contrast to previous reports, this result indicates that in this double chain silicate (Figure 5.26a), the  $Q^2$  units, a and b are not equivalent. This result is consistent with the published crystal structure.

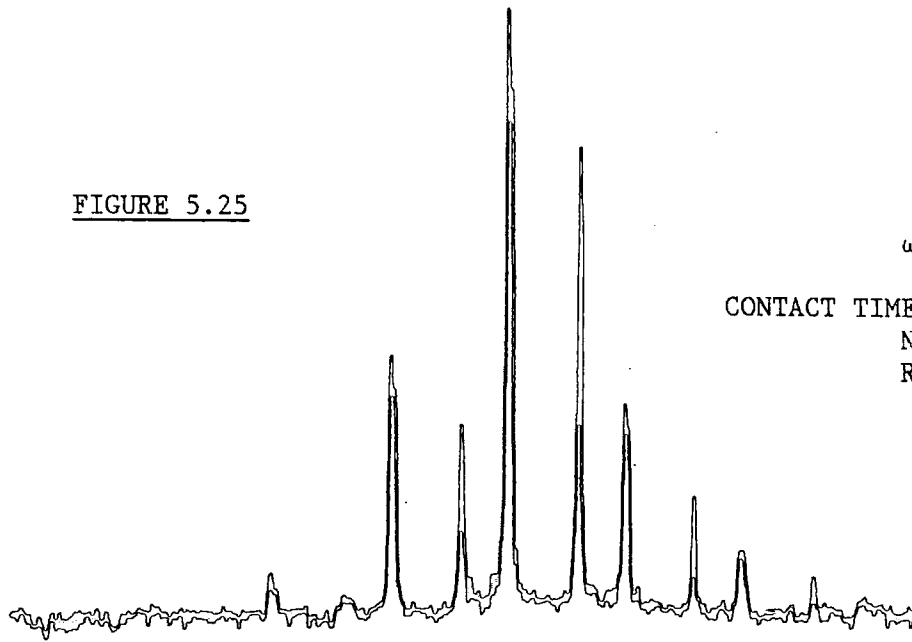
FIGURE 5.26a<sup>(1)</sup>

#### XONOTLITE



Slow-spinning  $^{29}\text{Si}$  CP MAS NMR experiments reveal that the shielding tensor for silicon atoms in  $Q^2$  environments exhibits significant deviations from axial symmetry. The silicon atoms in  $Q^3$  environments exhibit an axially symmetric shielding tensor. The results obtained from analysis of the intensity distribution of the spinning-sidebands (Figure 5.25) are summarised in Table 5.9.

FIGURE 5.25



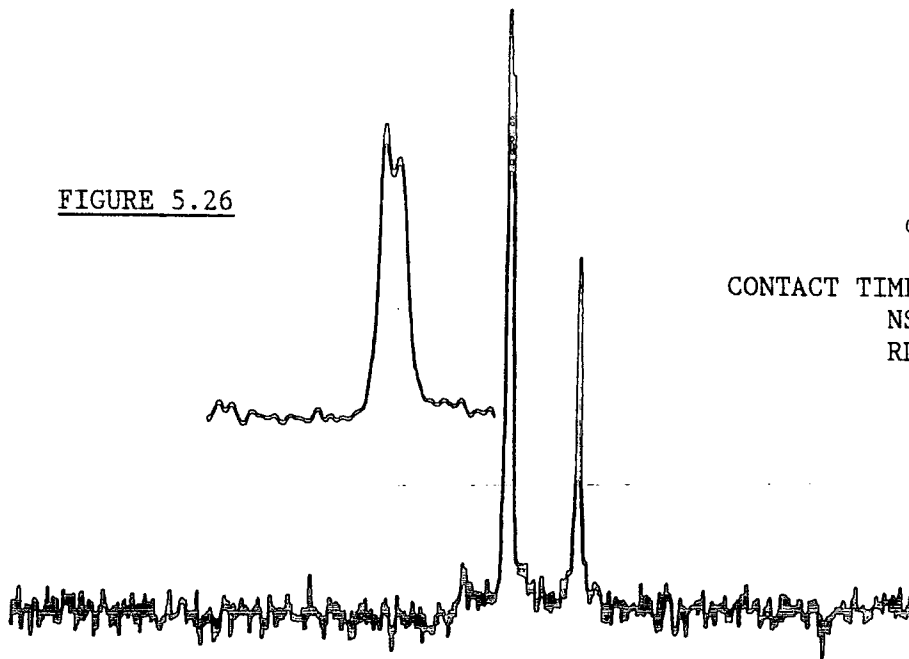
$\omega_r = 725 \text{ Hz}$

CONTACT TIME = 4 ms

NS = 3402

RD = 2 s

FIGURE 5.26

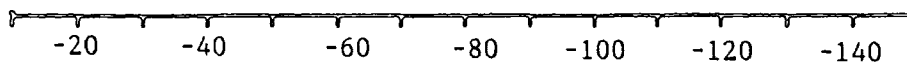


$\omega_r = 3.1 \text{ kHz}$

CONTACT TIME = 2 ms

NS = 475

RD = 2 s



$\delta_{\text{Si}}/\text{ppm}$

TABLE 5.9

MINERAL	Q <sup>n</sup>	$\sigma_{\text{ISO}}/\text{ppm}$	$\sigma_{\text{XX}}/\text{ppm}$	$\sigma_{\text{YY}}/\text{ppm}$	$\sigma_{\text{ZZ}}/\text{ppm}$	$\Delta\sigma/\text{ppm}$	$\eta$
XONOTLITE	Q <sup>2</sup>	86.6	52.4	81.8	126.5	59.4	0.7
	Q <sup>2</sup>	87.2					
	Q <sup>3</sup>	97.8	79.6	79.6	134.2	54.6	0.00
APOPHYLLITE	Q <sup>3</sup>	93.2	70.5	70.5	138.6	68.0	0.00
[N(Me <sub>4</sub> )] <sub>8</sub> Si <sub>8</sub> O <sub>20</sub> ·69H <sub>2</sub> O	Q <sup>3</sup>	99.4	77.4	77.4	144.2	66.8	0.00
	Q <sup>3</sup>	99.9					
KANEMITE	Q <sup>3</sup>	95.7	79.8	79.8	127.5	47.7	0.00
	Q <sup>3</sup>	97.3	82.2	82.2	127.6	45.5	0.00
OCTOSILICATE	Q <sup>3</sup>	100.2	76.3	76.3	148.0	71.7	0.00
	Q <sup>3</sup>	111.4	104.6	111.4	118.2	10.2	1.00

† errors in  $\sigma_{ii}$  values are typically ca  $\pm 2$  ppm

#### 5.6.4.2 APOPHYLLITE ((Na<sub>0.16</sub>K<sub>0.84</sub>)Ca<sub>4</sub>(Si<sub>8</sub>O<sub>20</sub>)F·8H<sub>2</sub>O).

The <sup>29</sup>Si CP MAS NMR spectrum of apophyllite (sodium potassium calcium fluorsilicate hydrate), exhibits a single isotropic chemical shift at -93.2 ppm (Figure 5.28). The value is in good agreement with that observed by Nesbitt.<sup>(43)</sup> The crystal structure of this compound has been published. (space group P4/mnc)<sup>(44)</sup> Apophyllite is a sheet silicate containing one silicon atom in the asymmetric unit, in a Q<sup>3</sup> environment. Slow-spinning <sup>29</sup>Si CP MAS NMR experiments (see Figure 5.27 and Table 5.9) show the silicon nuclei exhibit an axially symmetric shielding tensor.

#### 5.6.4.3 [N(Me)<sub>4</sub>]<sub>8</sub>Si<sub>8</sub>O<sub>20</sub>·69H<sub>2</sub>O

The <sup>29</sup>Si CP MAS NMR spectrum of this compound exhibits two isotropic chemical shifts at -99.4 and -99.9 ppm (Figure 5.30). This

$^{29}\text{Si}$  CP MAS NMR SPECTRA OF APOPHYLLITE

FIGURE 5.27

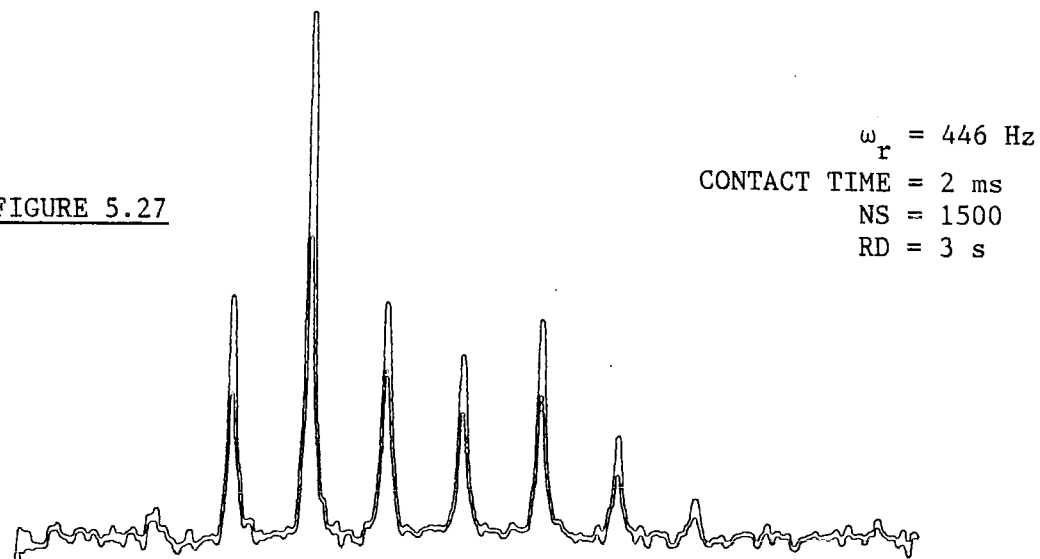
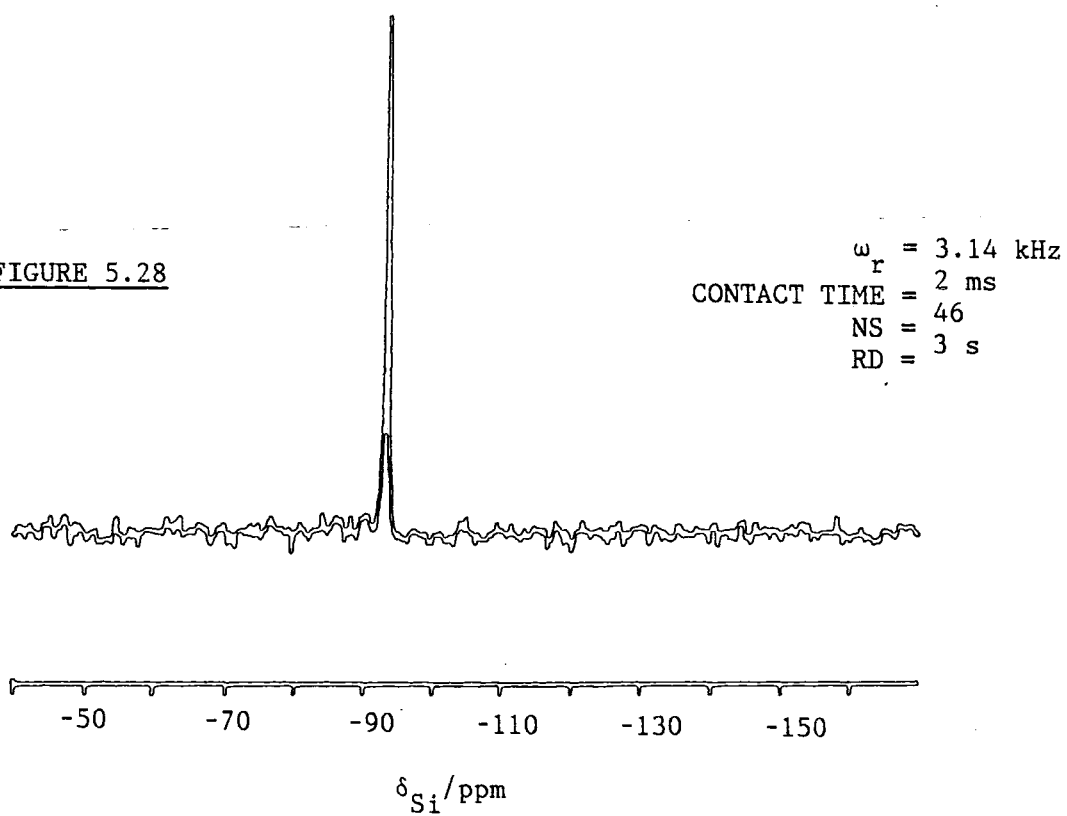
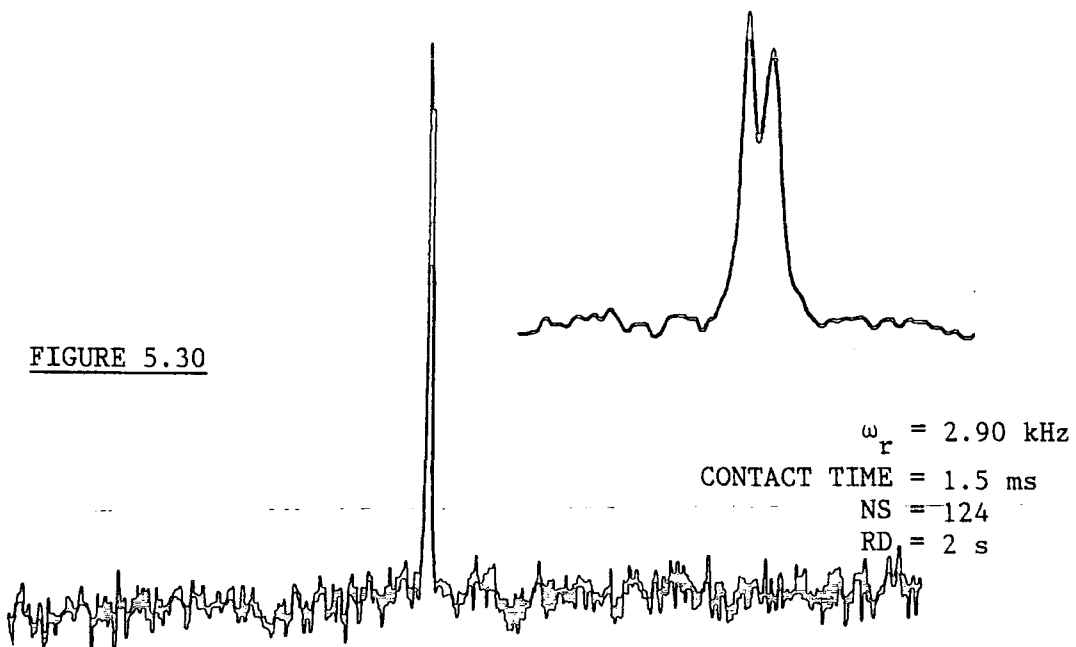
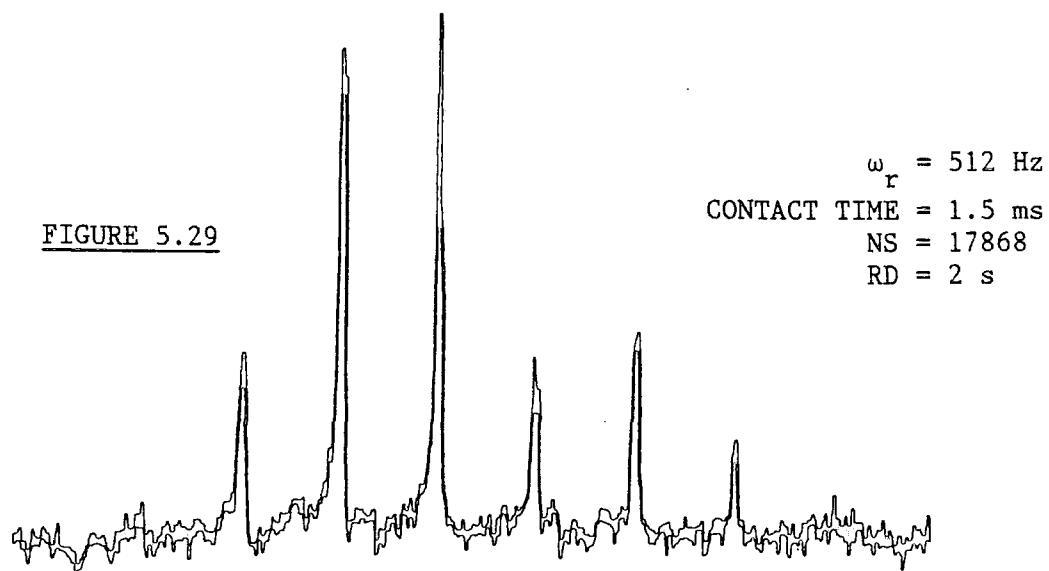


FIGURE 5.28



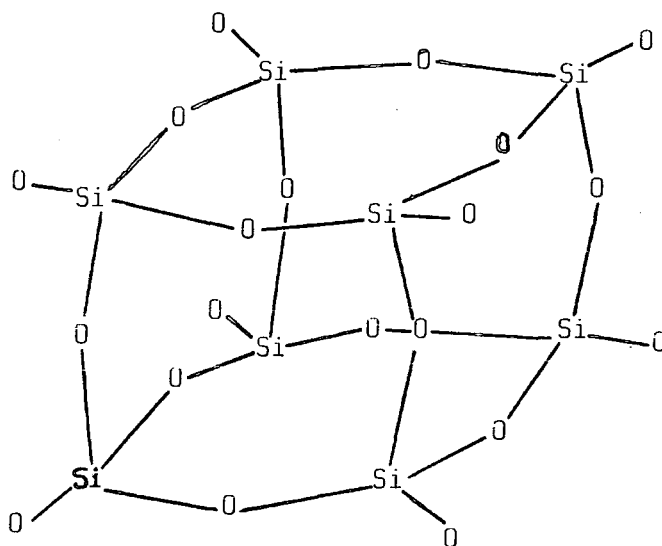
$^{29}\text{Si}$  CP MAS NMR SPECTRA OF  $[\text{N}(\text{Me})_4]_8\text{Si}_8\text{O}_{20}\cdot 69\text{H}_2\text{O}$ 

-40      -60      -80      -100      -120      -140      -160

$\delta_{\text{Si}}/\text{ppm}$

compound has been studied by a number of workers, who have reported only a single isotropic chemical shift, variously as  $-99.3$ ,<sup>(1)</sup>  $-97.7$ ,<sup>(22)</sup>  $-95$ <sup>(45)</sup> and  $-99 \pm 2$ <sup>(25)</sup> ppm. These resonances are assigned to  $Q^3$  units present in the cubic anion (Figure 5.31).

FIGURE 5.31



The reason why two resonances were observed in this study is unknown, since it is reported that the published crystal structure<sup>(46)</sup> indicates that in the cube-shaped anion, all eight silicon atoms are identical. Nevertheless, axial symmetry is observed for the shielding tensor, confirming the silicon nuclei to be in  $Q^3$  units. (Figure 5.29) The measured principal components and anisotropy are in reasonable agreement with published values (see Tables 5.9 and 5.10)

TABLE 5.10

$\sigma_{\text{ISO}}$ /ppm	$\sigma_{\parallel}$ /ppm	$\sigma_{\perp}$ /ppm	$\Delta\sigma$ /ppm	REFERENCE
$99 \pm 2$	$152 \pm 2$	$73 \pm 2$	$78.5 \pm 1$	25
97.7	142.4	75.4	65.0	22
95.0	148.0	68.0	80.0	45

#### 5.6.4.4 OCTOSILICATE AND KANEMITE

The  $^{29}\text{Si}$  CP MAS NMR spectrum of kanemite exhibits two isotropic chemical shifts at -95.7 ppm and -97.3 ppm (Figure 5.33). These peaks are both assigned to silicon atoms present in  $\text{Q}^3$  environments and the observed shifts are in good agreement with those published (-95.9 ppm and -97.8 ppm respectively).<sup>(43)</sup>

The silicon atoms in both environments exhibit axially symmetric shielding tensors (Figure 5.32 and Table 5.9). Examination of the principal components for the shielding tensors would appear to indicate that the observation of two isotropic chemical shifts, arises as a consequence of differences in bridging Si-O bond lengths, since values of  $\sigma_{11}$  for the two peaks are very similar (Table 5.9).

In a previous  $^{29}\text{Si}$  MAS NMR study of this mineral,<sup>(43)</sup> the structure of the mineral has been proposed as a sheet silicate. The results obtained in this work suggest that two  $\text{Q}^3$  environments exist, as a result of puckering of the silicate chain.

The  $^{29}\text{Si}$  CP MAS NMR spectrum of octosilicate exhibits two isotropic chemical shifts at -100.2 ppm and -111.4 ppm, assigned to silicon atoms in  $\text{Q}^3$  and  $\text{Q}^4$  environments respectively (Figure 5.35). The shifts observed in this work are in good agreement with those published,<sup>(43)</sup> and assignments are supported by  $^{29}\text{Si}$  slow-spinning CP MAS NMR experiments (Figure 5.34 and Table 5.9).

The crystal structure of this mineral is unknown, However, from fast-spinning  $^{29}\text{Si}$  MAS NMR experiments, Nesbitt<sup>(43)</sup> has proposed that the structure of this mineral is that of two silicate sheets linked by four-membered rings (Figure 5.36). The results outlined here are consistent with this hypothesis.

$^{29}\text{Si}$  CP MAS NMR SPECTRA OF KANEMITE

FIGURE 5.32

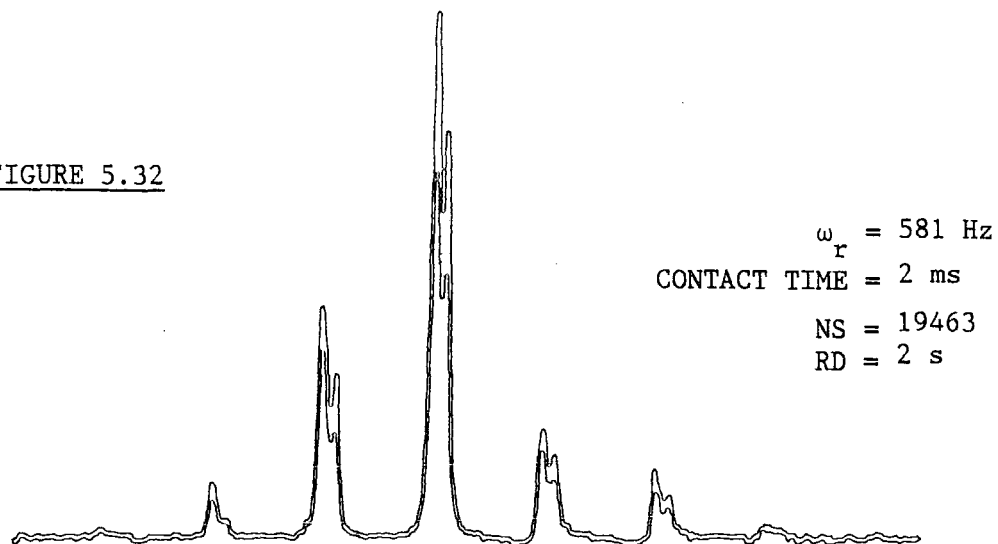
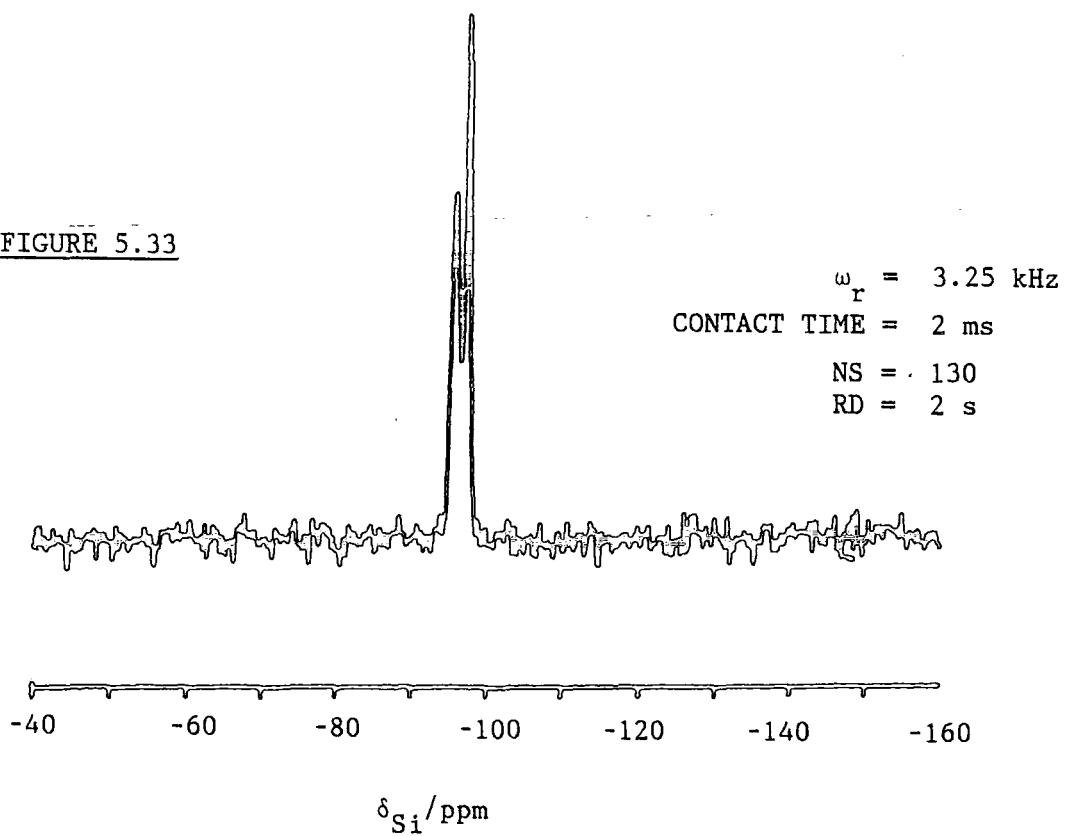
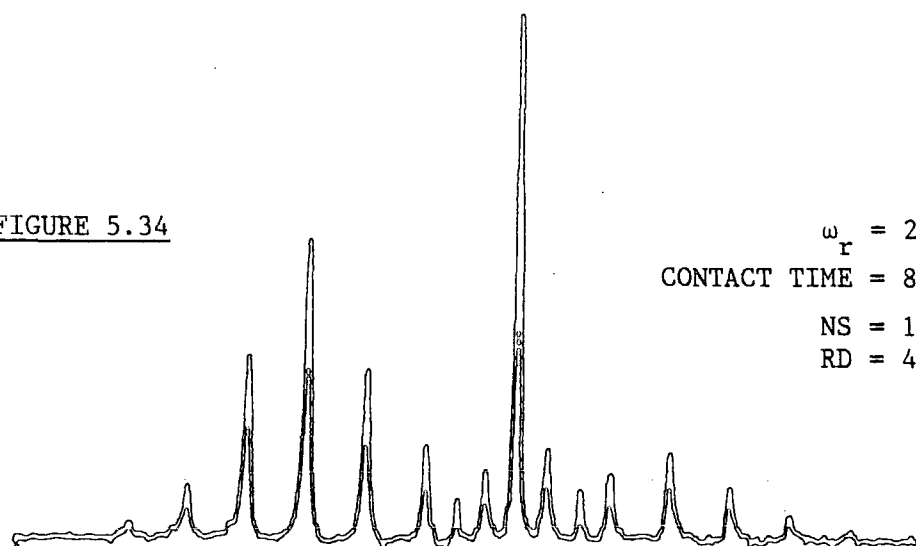


FIGURE 5.33



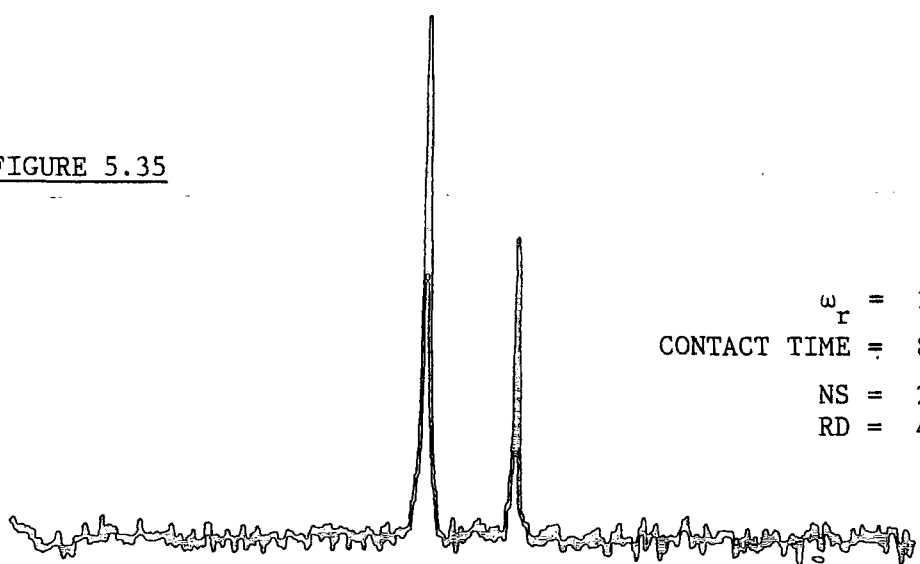
$^{29}\text{Si}$  CP MAS NMR SPECTRA OF OCTOSILICATE

FIGURE 5.34



$\omega_r = 290 \text{ Hz}$   
CONTACT TIME = 8 ms  
NS = 1876  
RD = 4 s

FIGURE 5.35



$\omega_r = 2.86\text{kHz}$   
CONTACT TIME = 8 ms  
NS = 26  
RD = 4 s

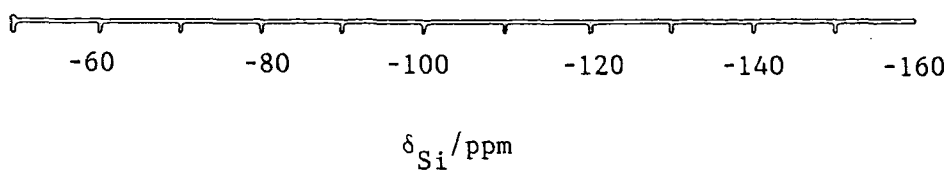
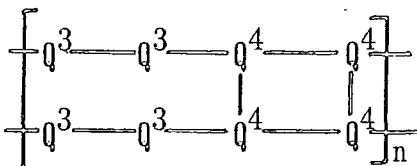


FIGURE 5.36

OCTOSILICATE<sup>(43)</sup>

These results suggest that silicon nuclei in  $Q^3$  environments generally exhibit axial symmetry.

### 5.6.5 ORGANOSILICON COMPOUNDS

THE  $^{29}\text{Si}$  CP MAS NMR spectra of a number of organosilicon compounds have been acquired, and slow-spinning  $^{29}\text{Si}$  CP MAS NMR experiments have allowed the calculation of the principal components of the shielding tensors. The results from these calculations are summarised in Table 5.11. In order to facilitate the acquisition of these spectra the proton longitudinal relaxation times of some of these compounds have been measured. Typical values of  $T_1(^1\text{H})$  range between 6 and 40 seconds. Measurements are summarised in Table 5.12.

TABLE 5.12

PROTON  $T_1(^1\text{H})$  VALUES FOR SELECTED ORGANOSILICON COMPOUNDS

COMPOUND	$T_1(^1\text{H})/\text{s}$
$(\text{C}_6\text{H}_5)_3\text{SiSi}(\text{CH}_3)_3$	8.74±0.06
$(\text{C}_6\text{H}_5)_3\text{SiOSi}(\text{C}_6\text{H}_5)_3$	14.22±0.31
$(\text{C}_6\text{H}_5)_8\text{Si}_4$	38.14±0.58
TMS SALT	5.70

The results outlined in Table 5.11 indicate that the isotropic chemical shifts of the molecules do not change appreciably from the solution to the solid-state. Therefore, effects caused by intermolecular

interactions may be considered as negligible, there are no major structural changes with phase.

#### 5.6.5.1 1,1,1-TRIMETHYLTRIPHENYLDISILANE ((C<sub>6</sub>H<sub>5</sub>)<sub>3</sub>SiSi(CH<sub>3</sub>)<sub>3</sub>)

The first high-resolution <sup>29</sup>Si CP MAS NMR spectrum of the compound 1,1,1-trimethyltriphenyldisilane was published by Gerstein in 1983.<sup>(24)</sup> Two resonances were observed at -18.4 ppm and -20.5 ppm, these were assigned to silicon atoms present within the Si(CH<sub>3</sub>)<sub>3</sub> and Si(C<sub>6</sub>H<sub>5</sub>)<sub>3</sub> moieties respectively. From the non-spinning powder pattern, the shielding anisotropies of the two silicon atoms were determined to be 18 ppm and -31 ppm respectively. Both shielding tensors were observed to be axially symmetric.

The <sup>29</sup>Si CP MAS NMR spectrum of the ~~compound~~ obtained in this work (Figure 5.38) exhibits two resonances at -18.9 ppm and -21.0 ppm, in close agreement with those published.<sup>(24)</sup> The crystal structure of this compound has been published,<sup>(52)</sup> (space group P $\bar{3}$ ) the asymmetric unit has been shown to consist of one third of the molecule. Each of the silicon atoms lie on an axis of C<sub>3v</sub> symmetry. Thus one would expect slow-spinning <sup>29</sup>Si CP MAS NMR experiments to reveal axially symmetric shielding tensors, and this is indeed the case (Figure 5.37). The results obtained (Table 5.11) are consistent with those published,<sup>(24)</sup> a positive anisotropy being observed for the Si(CH<sub>3</sub>)<sub>3</sub> group while a negative anisotropy is seen for the silicon atom of the Si(C<sub>6</sub>H<sub>5</sub>)<sub>3</sub> group.

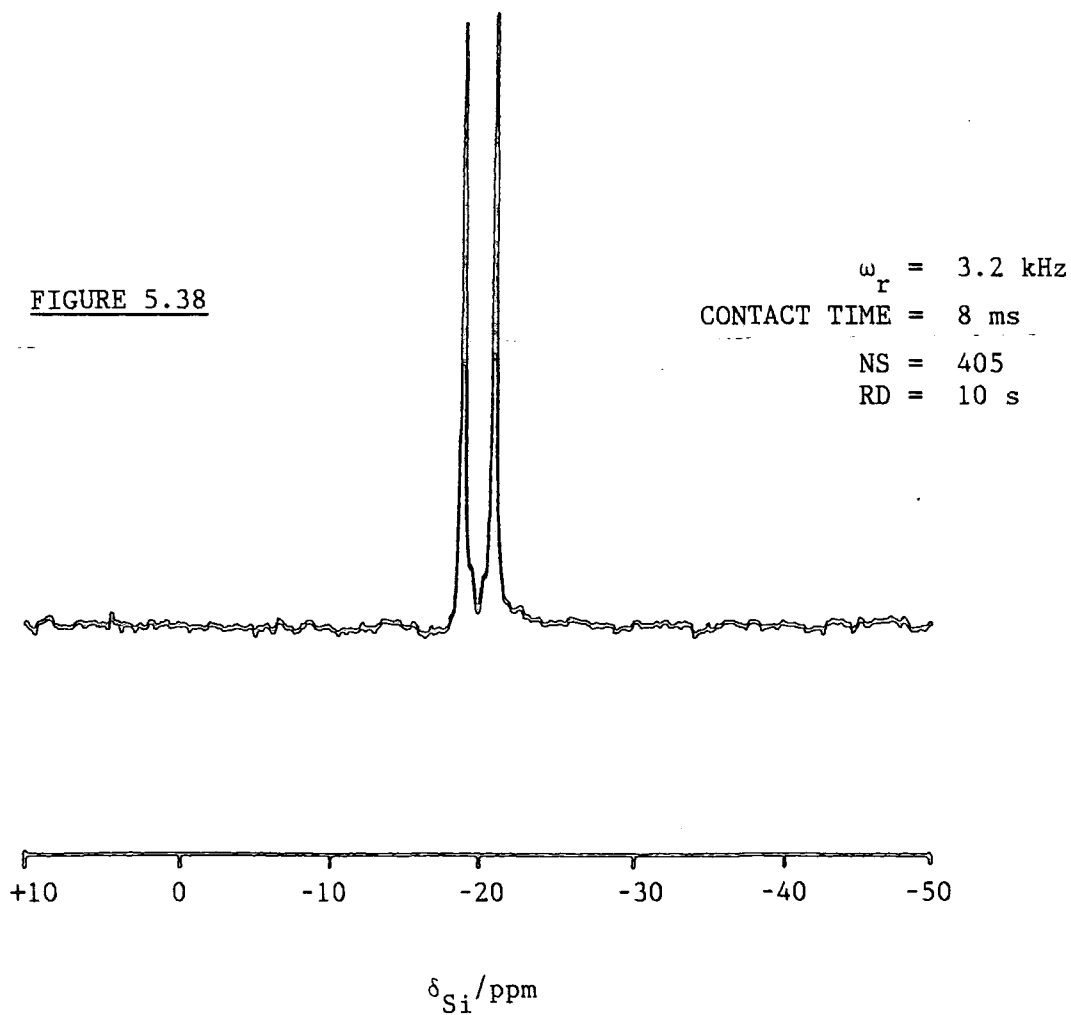
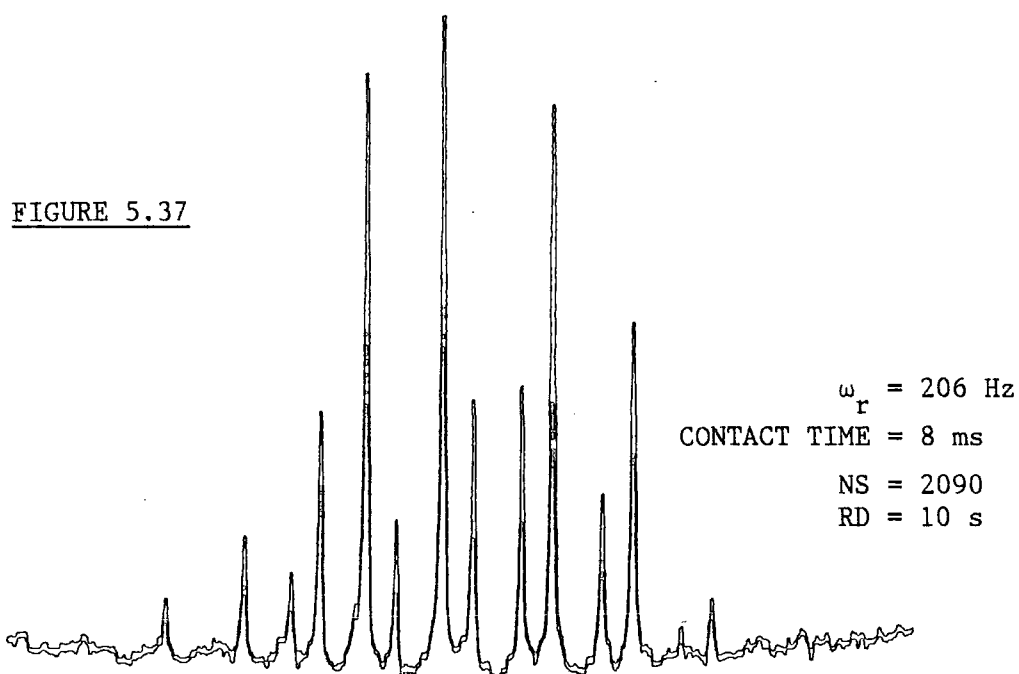
$^{29}\text{Si}$  CP MAS NMR SPECTRA OF 1,1,1-TRIMETHYL TRIPHENYLSIDILANE

TABLE 5.11

NMR PARAMETERS OF A NUMBER OF ORGANOSILICON COMPOUNDS

COMPOUND	$\delta_{\text{Si}}/\text{ppm}$		$\frac{\Delta\sigma}{\text{ppm}}$	$\frac{\sigma_{\text{xx}}}{\text{ppm}}$	$\frac{\sigma_{\text{yy}}}{\text{ppm}}$	$\frac{\sigma_{\text{zz}}}{\text{ppm}}$	$\eta$
	SOLUTION	SOLID					
<sup>*</sup> (C <sub>6</sub> H <sub>5</sub> ) <sub>3</sub> SiSi(CH <sub>3</sub> ) <sub>3</sub>	-18.4 (47)	-18.9	21.9	11.6	11.6	33.5	0.00
<sup>*</sup> (C <sub>6</sub> H <sub>5</sub> ) <sub>3</sub> SiSi(CH <sub>3</sub> ) <sub>3</sub>	-20.4 (47)	-21.0	-33.6	32.2	32.2	-1.4	0.00
(C <sub>6</sub> H <sub>5</sub> ) <sub>3</sub> SiSi(C <sub>6</sub> H <sub>5</sub> ) <sub>3</sub>	-26.6 (48)	-25.4	-25.4	37.2	37.2	1.8	0.00
(C <sub>6</sub> H <sub>5</sub> ) <sub>3</sub> SiOSi(C <sub>6</sub> H <sub>5</sub> ) <sub>3</sub>	-28.5 <sup>b</sup>	-17.0	27.9	1.5	13.9	35.6	0.67
(C <sub>6</sub> H <sub>5</sub> ) <sub>3</sub> SiH	-21.1 (49)	-21.4	45.0	-0.4	13.2	51.4	0.45
(C <sub>6</sub> H <sub>5</sub> ) <sub>8</sub> Si <sub>4</sub>	-20.9 (50)	-24.2 <sup>c</sup>	-44.8	51.7	26.6	-5.7	0.84
(C <sub>6</sub> H <sub>5</sub> CH <sub>2</sub> ) <sub>3</sub> SiH <sup>d</sup>	-3.8 (51)	-4.5	11.6	-2.8	4.1	12.2	0.90
TMS SALT	-	+1.18	8.7	-6.0	-2.1	4.5	0.69

a. The errors in  $\sigma_{ii}$  values are typically ca  $\pm 2$  ppm

b. CH<sub>2</sub>Cl<sub>2</sub> solution

chemical shift.

c. The average isotropic  $\lambda$ . A typical error in  $\eta$  is  $\pm 0.1$ , but the error range of (C<sub>6</sub>H<sub>5</sub>CH<sub>2</sub>)<sub>3</sub>SiH is such that  $0.62 < \eta < 1.0$ . Exact axially is difficult to establish by spinning sideband analysis for this compound

In the case of both isotropic and axially symmetric tensors, the local symmetry at silicon can be used to assign a definite shielding value to a particular silicon-ligand bond. For example, in the case of an axially symmetric tensor, the observed shielding value  $\sigma_{ZZ}$  corresponds to the unique silicon-ligand bond. If one considers that such a tensor component depends upon the fractional s-character of the hybrid orbitals involved, relative to those of the remaining bonds, then using arguments analogous to those used by Grimmer<sup>(28)</sup> (for silicates), it follows that, in the case of the silicon atom present

in the  $\text{Si}(\text{C}_6\text{H}_5)_3$  moiety, the observation of a negative shielding anisotropy suggests that the Si-C bond possesses a greater degree of s-character than the Si-Si bond. On the other hand, for the silicon atom present in  $\text{Si}(\text{CH}_3)_3$ , the observation of a positive anisotropy suggests that the Si-Si bond has more s-character than the Si-C bond. Thus, there is a greater degree of s-character in Si-C bonds in the moiety  $\text{Si}(\text{C}_6\text{H}_5)_3$  than in the  $\text{Si}(\text{CH}_3)_3$  group. This conclusion appears to be supported from measurements of silicon-carbon coupling constants for the compound  $\text{C}_6\text{H}_5\text{Si}(\text{CH}_3)_3$ . Summerhays and Deprez<sup>(53)</sup> have derived a linear correlation between the Si-C coupling constants ( $^1\text{J}(\text{Si-C})$ ) and the s-character of the Si-C bond ( $P_{\text{Si-C}}^{\text{s}}$ )

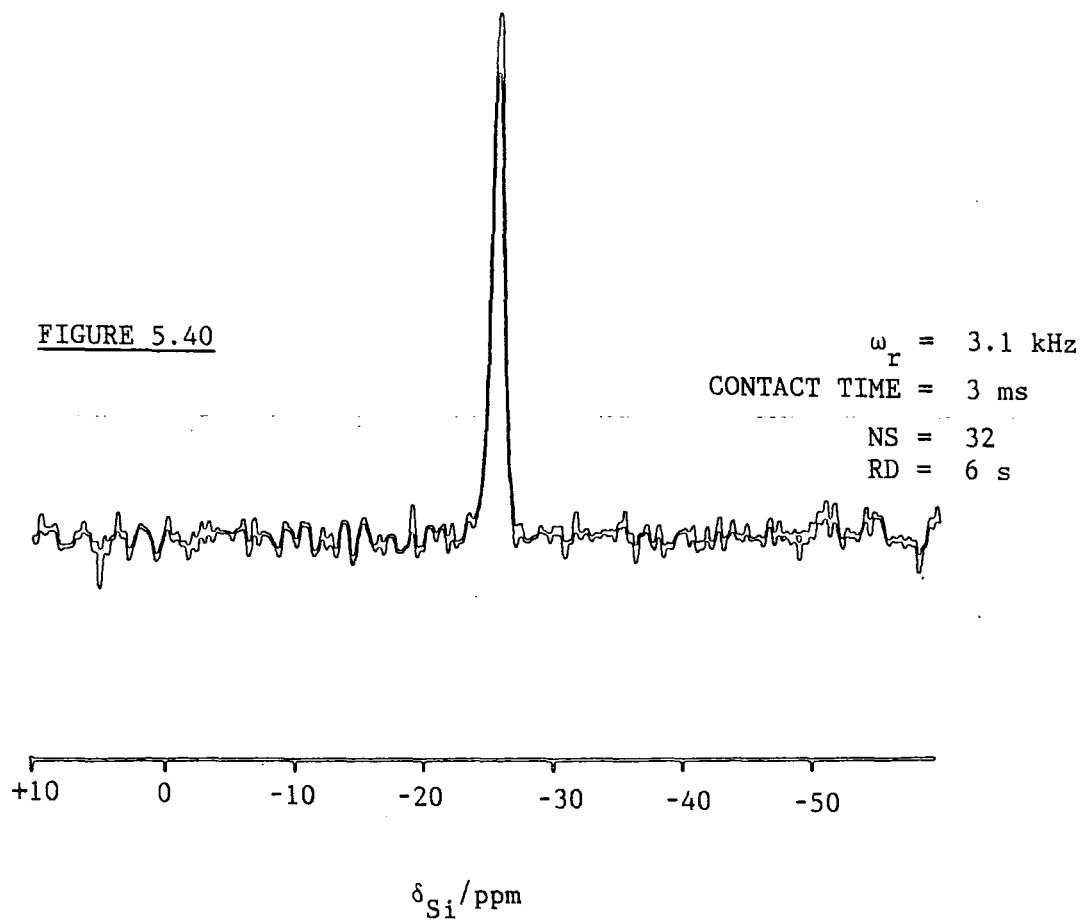
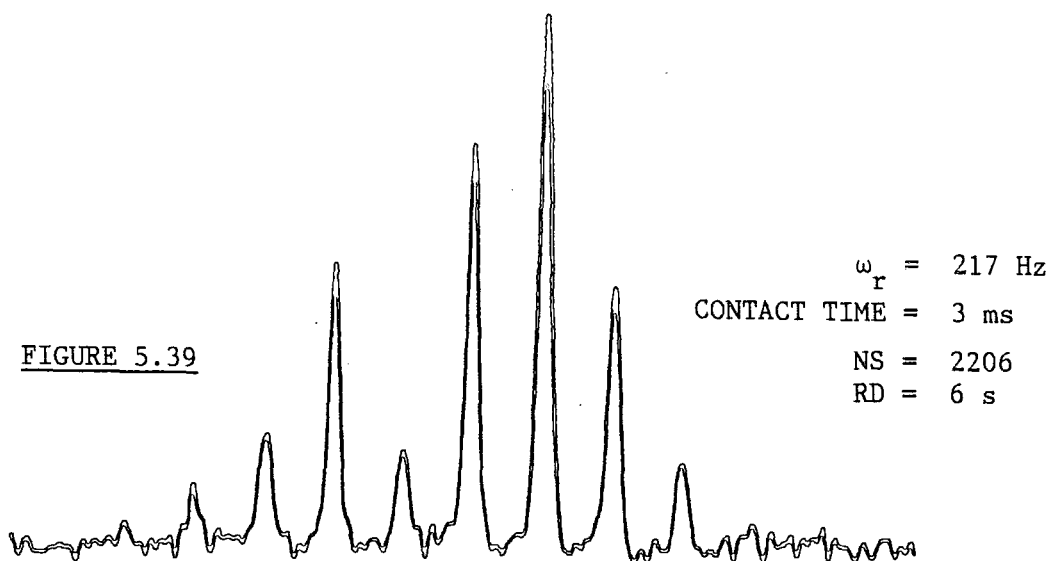
$$(5.33) \quad ^1\text{J}(\text{Si-C}) = -1055.4 P_{\text{Si-C}}^{\text{s}} + 15.9 \text{ Hz}$$

and analysis of the values of  $^1\text{J}(\text{Si-C})$  for the methyl and aromatic carbon atoms (-52.2 Hz<sup>(54)</sup> and -66.5 Hz<sup>(55)</sup> respectively) indicates the s-character for these bonds are 25.4% and 27.9% respectively.

It was not possible to measure the  $^1\text{J}(\text{Si-C})$  and  $^1\text{J}(\text{Si-Si})$  coupling constants in  $(\text{C}_6\text{H}_5)_3\text{Si-Si}(\text{CH}_3)_3$ , owing to the complexity of the solution state spectra.

#### 5.6.5.2. HEXAPHENYLDISILANE $(\text{C}_6\text{H}_5)_3\text{SiSi}(\text{C}_6\text{H}_5)_3$ (HPDS)

The  $^{29}\text{Si}$  CP MAS NMR spectrum of HPDS exhibits a single isotropic

$^{29}\text{Si}$  CP MAS NMR SPECTRA OF HEXAPHENYLDISILANE

chemical shift at -25.4 ppm (Figure 5.40). This value is in agreement with the solid-state result reported in the literature.<sup>(9)</sup> The asymmetric unit would appear to consist of the  $(C_6H_5)_3Si$  moiety, although the crystal structure of the pure compound has not yet been published.

Slow-spinning  $^{29}Si$  CP MAS NMR experiments (Figure 5.39 and Table 5.11) reveal an axially symmetric shielding tensor and a negative anisotropy, once again indicating a greater degree of s-character for the Si-C bonds than for the Si-Si bonds, as expected from the results for  $(C_6H_5)_3SiSi(CH_3)_3$ .

#### 5.6.5.3 OCTAPHENYLCYCLOTETRASILANE $((C_6H_5)_8Si_4)$

The  $^{29}Si$  CP MAS NMR spectrum of octaphenylcyclotetrasilane (OPCT) exhibits two partly-resolved resonances at -23.84 ppm and -24.36 ppm. This level of resolution was not achieved in an earlier study of this compound.<sup>(9)</sup> The crystal structure of this compound has been published,<sup>(56)</sup> the space group is C2/c and there are four molecules per unit cell. However, the asymmetric unit consists of half a molecule, and there is no local symmetry at the silicon site. The spectrum (Figure 5.42) indicates that  $^{29}Si$  NMR can resolve the differences between the two silicon atoms in the asymmetric unit. Slow spinning  $^{29}Si$  CP MAS NMR experiments (Figure 5.41 and Table 5.11) reveal significant deviations of the shielding tensor from axial symmetry, as might be expected given the cyclic structure of this compound.

#### 5.6.5.4 HEXAPHENYLDISILOXANE $((C_6H_5)_3SiOSi(C_6H_5)_3)$

The solid-state  $^{29}Si$  CP MAS NMR spectrum of hexaphenyldisiloxane exhibits a single isotropic chemical shift at -17.0 ppm (Figure 5.44), indicating the asymmetric unit consists of half the molecule. The crystal structure of this compound has been published,<sup>(57)</sup> (space group is  $P\bar{1}$ ) and there is one molecule per unit cell. The molecules

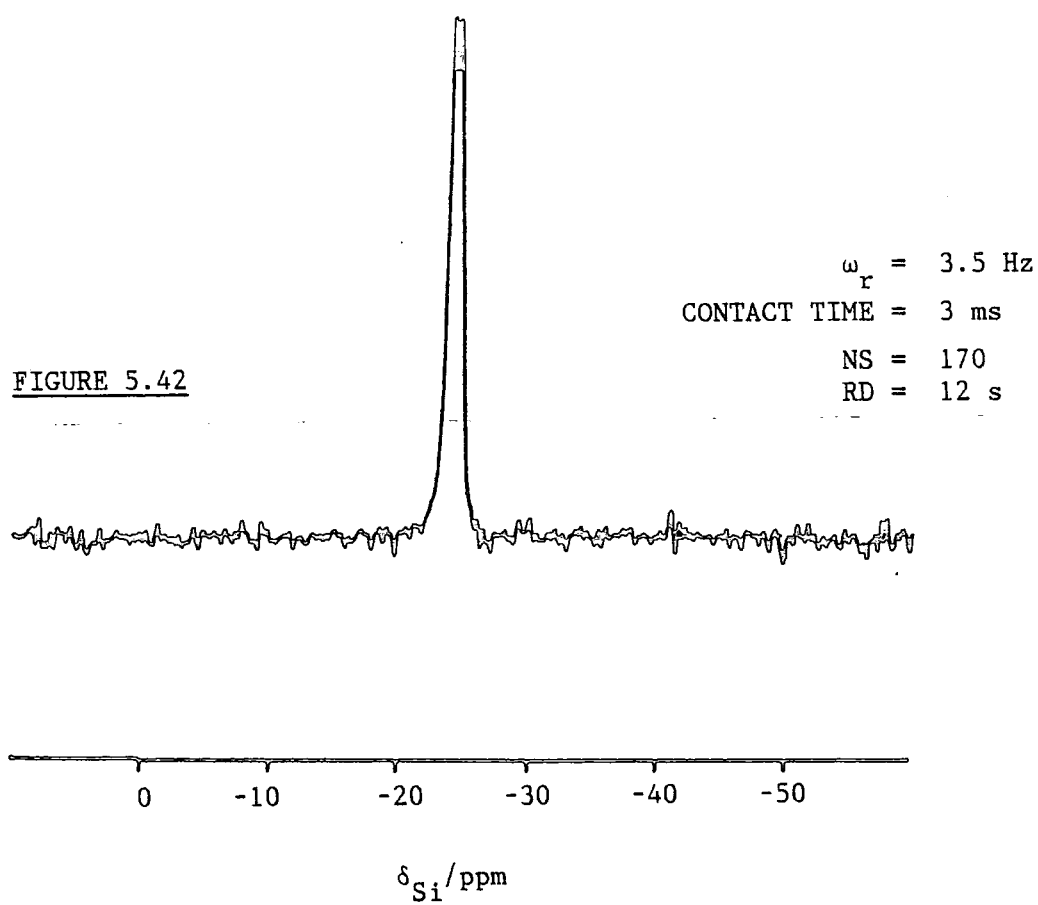
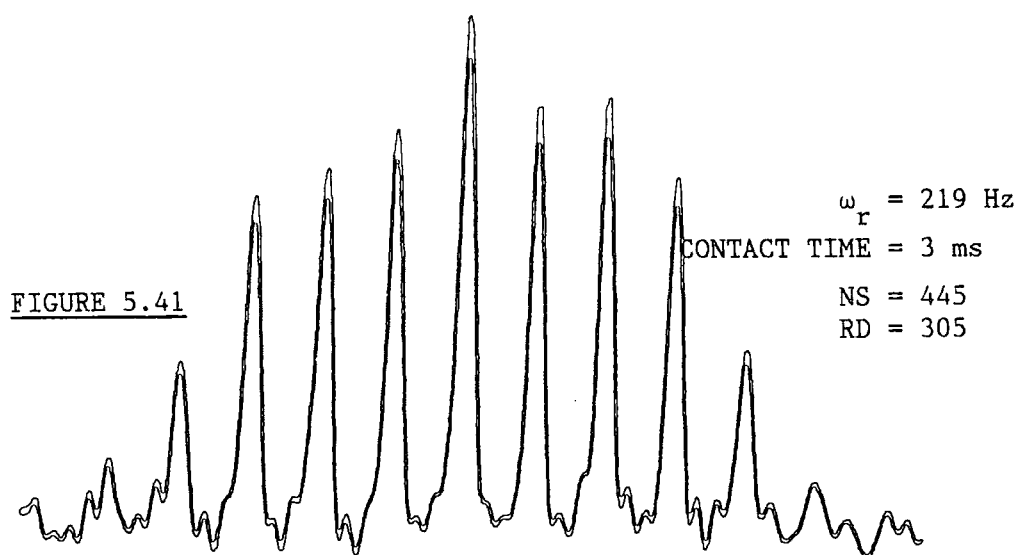
are centrosymmetric, so that the Si-O-Si fragment is linear and the asymmetric unit consists of the  $(C_6H_5)_3Si-O_{1/2}$  fragment, as shown by the NMR work. The molecular formula of this compound suggests there might be an axially symmetric shielding tensor. Slow-spinning experiments, however, reveal significant deviations from axial symmetry (Figure 5.43 and Table 5.11). Examination of the crystal structure<sup>(57)</sup> shows that two of the Si-C bond lengths differ significantly from the third, and there is no local symmetry at silicon. Distortions of the molecular structure upon crystal packing result in deviations from axial symmetry.

#### 5.6.5.5 TRIPHENYLSILANE $(C_6H_5)_3SiH$ AND TRIBENZYLSILANE

##### $((C_6H_5CH_2)_3SiH)$

The  $^{29}Si$  CP MAS NMR spectra of triphenylsilane and tribenzylsilane exhibit single isotropic chemical shifts at -21.4 ppm and -4.5 ppm respectively (see Figures 5.46 and 5.48 respectively), thereby suggesting one molecule in the asymmetric unit in each case. The crystal structure of triphenylsilane has been published<sup>(58)</sup> (space group  $P2_1/c$ ) and confirms this result. Once again, slow-spinning  $^{29}Si$  CP MAS NMR spectra exhibit significant deviations from axial symmetry for both compounds (Figures 5.45 and 5.47 and Table 5.11). The crystal structure of triphenylsilane shows that all three Si-C bond lengths are different (i.e. there is no three-fold symmetry axis). The deviation from axial symmetry is, of course, caused by distortions of the molecular structure upon crystal packing. Tribenzylsilane has a markedly lower anisotropy than the other compounds studied here, indicating a more even distribution of electron density at silicon arising from the similar effects of hydrogen and  $SP^3$ -carbon substituents. The accuracy of measurements of  $\Delta\sigma$  and  $\eta$  are lower in consequence.

The shielding anisotropy of hexaphenyldisiloxane, triphenylsilane

$^{29}\text{Si}$  CP MAS NMR SPECTRA OF OCTAPHENYLCYCLOTETRASILOXANE

$^{29}\text{Si}$  CP MAS NMR SPECTRA OF HEXAPHENYLDISILOXANE

FIGURE 5.43

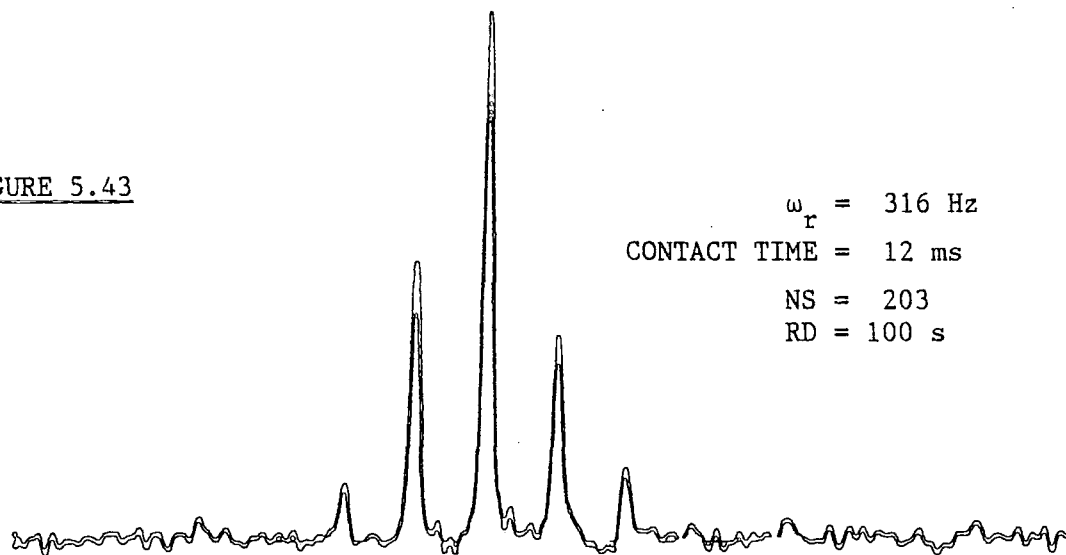
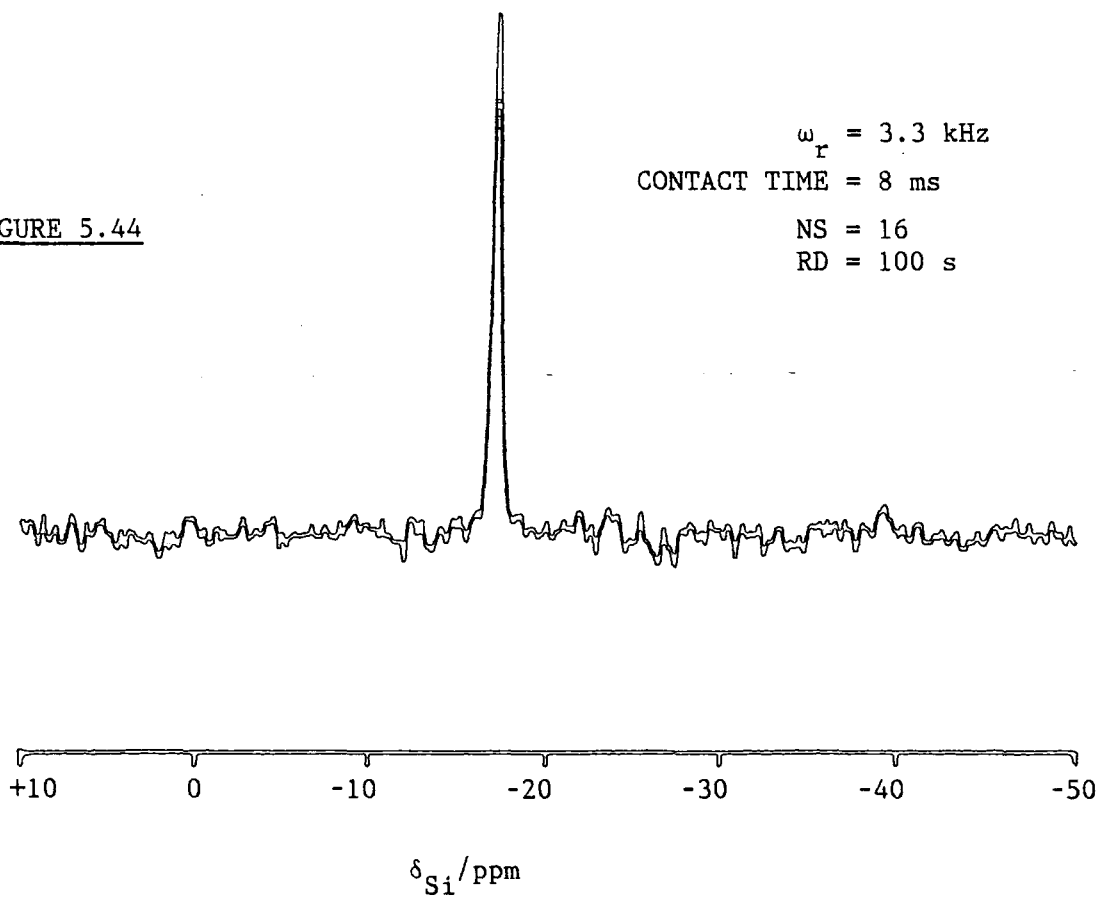


FIGURE 5.44



$^{29}\text{Si}$  CP MAS NMR SPECTRA OF TRIPEHENYLSILANE

FIGURE 5.45

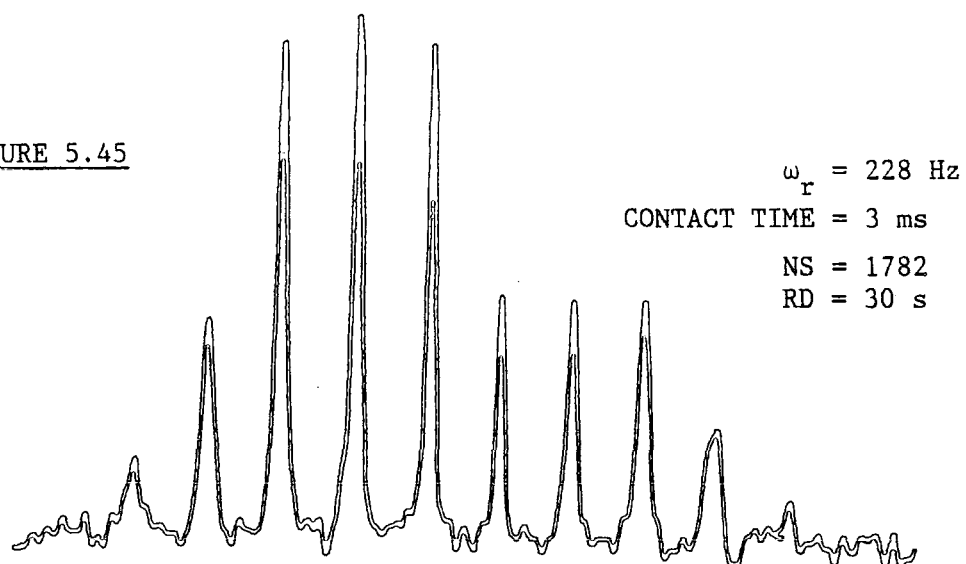
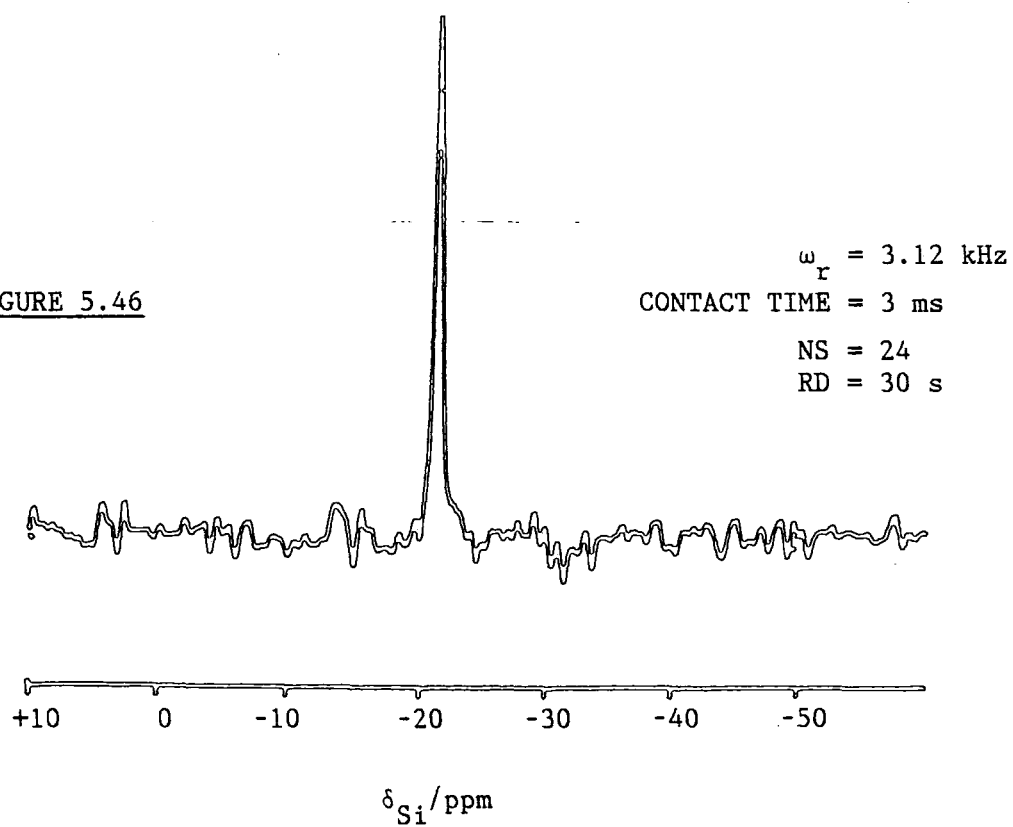


FIGURE 5.46



and tribenzylsilane will presumably be influenced by the fact that there is a greater degree of s-character in the Si-O and two Si-H bonds respectively, than in the Si-C bonds. For example, for triphenylsilane the Si-H and Si-C coupling constants have been measured ( $^1J(\text{Si-H}) = 205.10 \text{ Hz}^{(59)}$  and  $^1J(\text{Si-C}) = -70.0 \text{ Hz}^{(60)}$ ). Rastelli and Pazzoli<sup>(62)</sup> have proposed a simple relationship between  $^1J(\text{Si-H})$  and the s-character of the silicon orbital directed towards hydrogen ( $\alpha_{\text{H}}$ ).

$$(5.34) \quad ^1J(\text{Si-H}) = 810\alpha_{\text{H}}^2$$

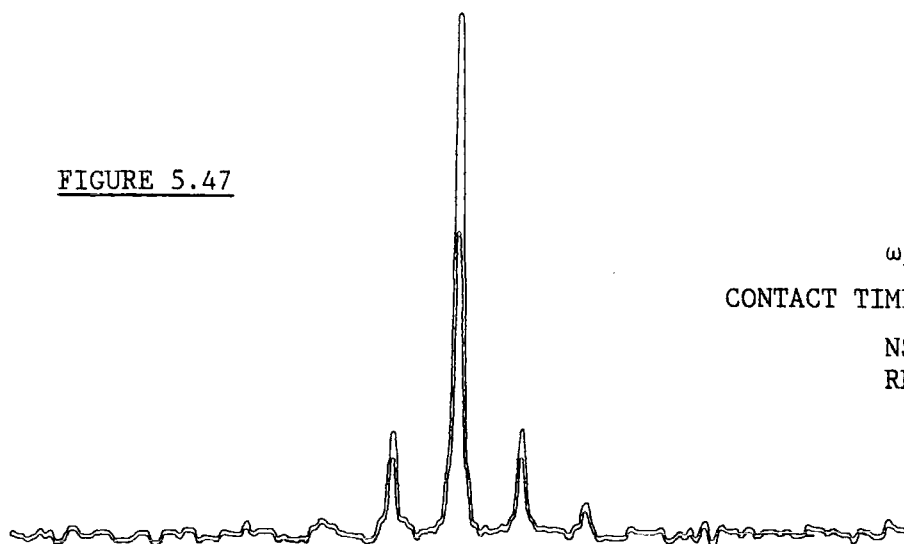
The percentage s-character of the Si-H and Si-C bonds for triphenylsilane may be calculated as 50.3% and 28.5% respectively. However, the lack of symmetry at the silicon in the solid-state, implies that the relationship between s-character and shielding anisotropies are difficult to evaluate. In particular, for these three compounds, values of  $\eta$  are substantial and relatively small changes in  $\sigma_{\text{YY}}$  would result in  $\Delta\sigma$  changing sign. The directions of the principal axes are, of course, not fully defined.

#### 5.6.5.6 TRIMETHYLSILYL-1-PROPANESULPHONIC ACID (i.e. TMS SALT)

The  $^{29}\text{Si}$  CP MAS NMR spectrum of the sodium salt of trimethylsilyl-1-propanesulphonic acid (TMS Salt), exhibits a single isotropic chemical shift at +1.18 ppm (Figure 5.51), suggesting the presence of one molecule in the asymmetric unit. Slow spinning  $^{29}\text{Si}$  CP MAS NMR experiments (Figure 5.50 and Table 5.11) reveal a much smaller shielding anisotropy for the silicon in this compound compared with the other compounds studied in this work (with the exception of tribenzylsilane). This is expected given that the silicon atom is bonded to four aliphatic carbon atoms, and the fractional s-character of the Si-C hybrid orbitals are probably very similar. The results also reveal significant deviations from axial symmetry, suggesting

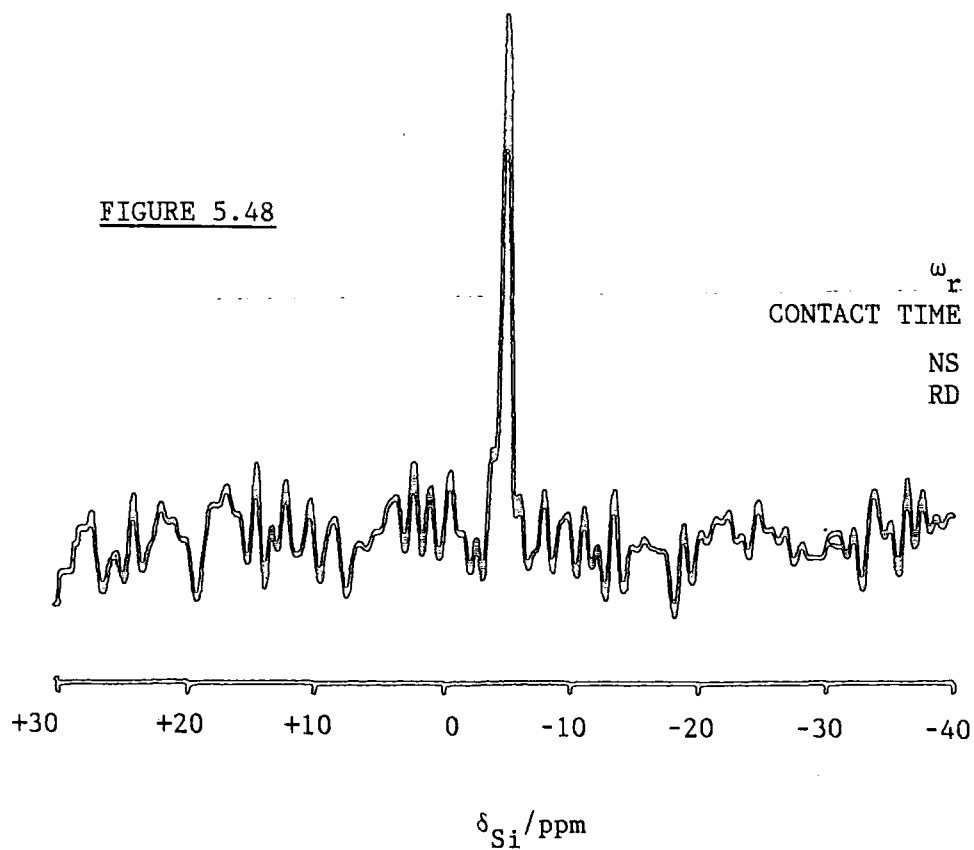
$^{29}\text{Si}$  CP MAS NMR SPECTRA OF TRIBENZYLSILANE.

FIGURE 5.47



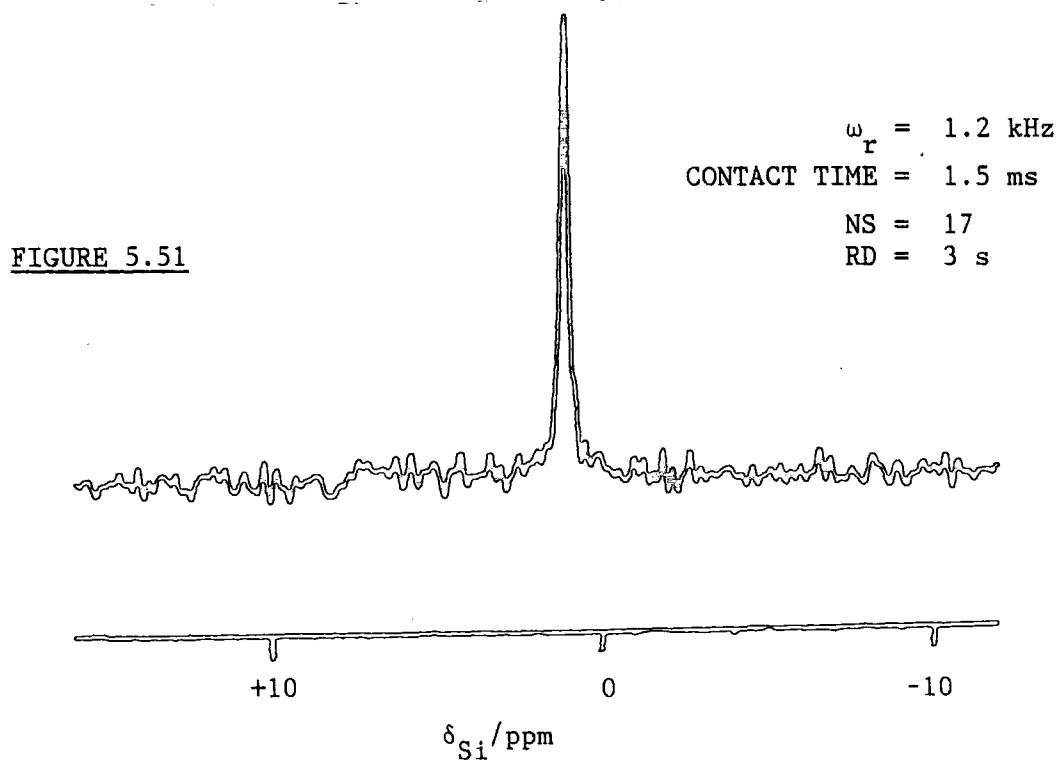
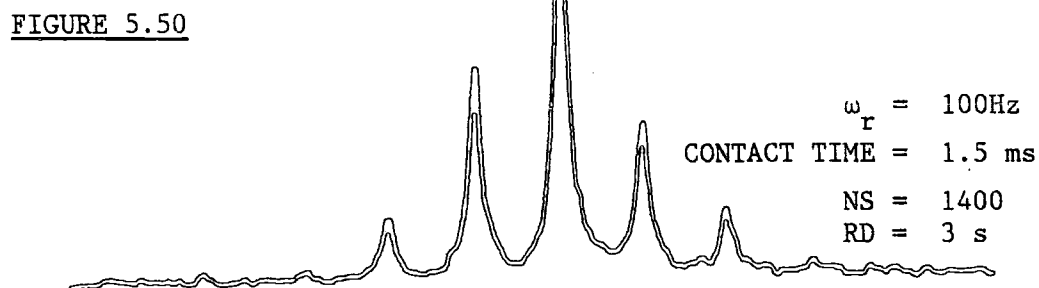
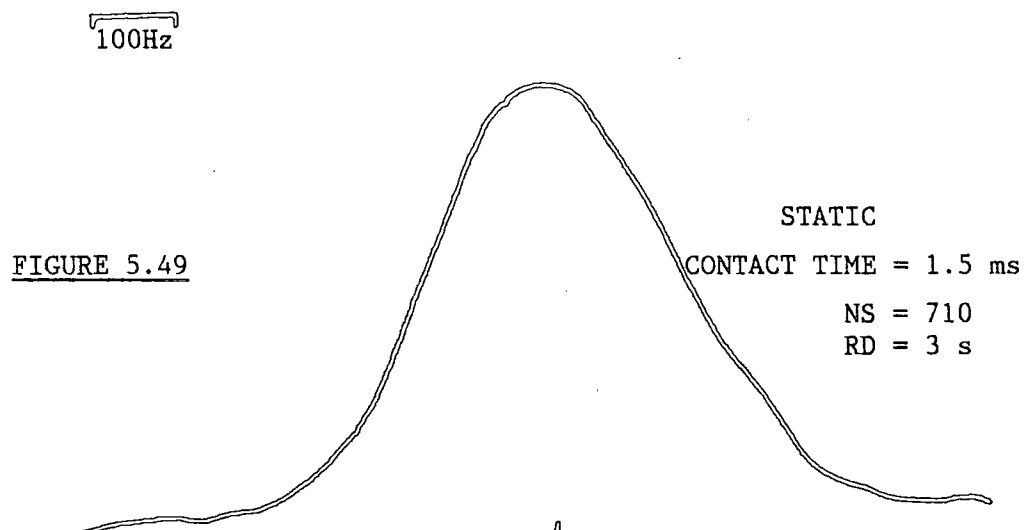
$\omega_r = 196 \text{ Hz}$   
CONTACT TIME = 3 ms  
NS = 1480  
RD = 30 ms

FIGURE 5.48



$\omega_r = 3.30 \text{ kHz}$   
CONTACT TIME = 3 ms  
NS = 170  
RD = 30 s

$^{29}\text{Si}$  CP MAS NMR SPECTRA OF THE SODIUM SALT OF TRIMETHYLSILYL-1-PROPANE  
SULPHONIC ACID.



that the three Si-CH<sub>3</sub> bond lengths are not all the same. Once again, relatively small changes in  $\sigma_{yy}$  would result in  $\Delta\sigma$  changing sign, and given the experimental errors, it is not possible to be certain about the sign of  $\Delta\sigma$ . The crystal structure of this compound has not been published.

### 5.7 CONCLUSIONS

In this chapter, it has been argued that <sup>29</sup>Si isotropic chemical shifts, for a variety of crystalline silicon-containing compounds, may be rationalised in terms of the fractional s-character of the silicon-ligand hybrid orbitals. The existence of (d-ρ)π bonding interactions have not been invoked. Moreover, experiments on a number of organosilicon compounds suggest that, as with silicate minerals, the shielding along a given silicon-ligand bond is determined by the fractional s-character of the hybrid orbital. In these arguments, it is assumed that increasing the ligand electronegativity results in increased shielding along the bond axis. Englehardt et al, suggests this argument would only be true if the net charge on the silicon atom  $q_{Si} > 0.4$ .

More specifically, the isotropic chemical shifts and principal components of the <sup>29</sup>Si shielding tensor, for a variety of silicon-containing compounds have been determined. In cases where the crystal structures of the compounds are known, (with the possible exception of thortveitite) NMR yields consistent results. In situations where the crystal structures are unknown, these techniques outlined in this chapter enable the investigation of local Si site symmetry in these compounds, however, it may be seen that caution is required when using these techniques to investigate the structures of silicate minerals, for while it appears to be a general rule that silicon nuclei in Q<sup>3</sup> environments exhibit axial symmetry, this is not necessarily the case for silicon nuclei in Q<sup>1</sup> environments.

## 6.0 CHAPTER SIX

### SOLID-STATE NMR STUDIES OF SILICA XEROGELS

#### 6.1 INTRODUCTION

Porous silicate gels are of immense and growing industrial importance. The long established uses may be grouped according to the following functions<sup>(1,2)</sup>

- (1) Reinforcing, stiffening and hardening of organic solids
- (2) Reducing adhesion between solid surfaces
- (3) Increasing the viscosity of liquids
- (4) Increasing adhesion of adhesives
- (5) Creating various optical effects
- (6) Surfactant effects
- (8) Adsorbants
- (9) Catalyst supports
- (10) Sources of reactive silica
- (11) Cloud seeding
- (12) Chromatographic column packing

No attempt is made here to review the literature, or patents concerned with the industrial applications for silica. For further information the reader is referred to two articles published by Vail and Iler.<sup>(1,3)</sup> There are many different types of silicas of industrial interest.<sup>(1)</sup>

In this work, however, attention is focused upon one type, silica xerogels. Xerogels are silicas formed in a liquid medium (usually water), from which the liquid has been subsequently removed. This causes the structure of the resultant xerogel to become compressed, and the porosity reduced to some degree by surface tension forces.<sup>(1)</sup>

Early workers believed the structure of silica xerogels to be "a solid silica punctuated by a multitude of different size capillary pores", or "a mat or felt of filaments, needles etc. forming a three

dimensional network".<sup>(4)</sup> Plank<sup>(5)</sup> proposed, however, that silica xerogels are composed of discrete particles, having a diameter which may be estimated from surface area measurements, as of the order of 5 nm. Elkin et al<sup>(6)</sup> estimated the average size of the silica particles (assumed to be spherical), in a freshly prepared silica xerogel, to be around 3-6 nm in diameter, by small angle x-ray scattering measurements. Electron-microscope studies of silica xerogels also suggest the existence of particles of this size, which make up the silica xerogel.<sup>(7)</sup> Thus a corpuscular model for the structure of silica xerogels has been developed, and employed to explain many of the properties of silica xerogels.

## 6.2 THE FORMATION OF SILICA XEROGELS

The silica xerogels studied in this work have been prepared via the rapid addition of an aqueous alkaline sodium silicate solution to sulphuric acid. Species present within the silicate solution (under conditions of low pH) rapidly polymerise via condensation reactions to form large macromolecular species, or what have become known as primary silica particles, around 1-2 nm in diameter.<sup>(7)</sup> A silica hydrosol is thus formed, which rapidly forms a clear glassy material, known as a silica hydrogel, as the primary particles become linked together to form chain-like structures. The hydrogel is a mixture of porous silica, water and sodium sulphate.

For industrial applications, typically, highly concentrated reagents are employed, so the reagents must be mixed thoroughly, in a time period which is short in comparison with the time taken for the hydrosol to form the hydrogel (the gel time).

The hydrogel, once it is formed, then contracts as water is lost from the hydrogel (at room temperature) and surface tension forces cause the primary particles to become more closely packed together. This process, known as syneresis, is accompanied by an increase in the

mechanical strength of the xerogel and fracturing. Once the hydrogel has reached an appropriate mechanical strength, it is milled and washed free of electrolyte. Following adjustment of the pH of the hydrogel, it may be treated in one of two ways.<sup>(2)</sup>

- (1) The hydrogel may be milled and dried to form a xerogel. Xerogels produced in this way, typically exhibit large surface areas ( $800 \text{ m}^2 \text{ g}^{-1}$ ), and low pore volumes ( $\sim 0.4 \text{ cm}^3 \text{ g}^{-1}$ ). These xerogels are typically employed as desiccants since they have a capacity for water adsorption of up to 28% (w/w).<sup>(2)</sup>

Alternatively

- (2) The hydrogel may be steeped in boiling water for a specified period of time. This process is known as hydrothermal aging. Upon drying, a xerogel of reduced surface area and modified pore structure is produced. By careful control of these processes, the structure of the resultant xerogel may be tailored to suit a variety of industrial applications.<sup>(2)</sup>

Since 1970, there has been much research activity stimulated by the growing need for specially structured wide pore silicas, prepared in this way.

### 6.3 THE SURFACE STRUCTURE OF SILICA XEROGELS

The surface of a silica xerogel is usually understood to mean the boundary that is impervious to nitrogen, since surface areas are most often determined by nitrogen adsorption.

Xerogels prepared via the acidification of sodium silicate solutions are amorphous and heterogeneous, due to the irregular packing of the primary silica particles and incompleteness of the condensation reactions between species present in the silicate solutions.<sup>(8)</sup> As a consequence, silanol groups may be located in a number of possible environments.<sup>(1)</sup>

- (1) Surface silanol groups

- (2) Silanol groups buried beneath the surface of the siloxane network
- (3) Silanol groups located in crevices at the point of contact between particles
- (4) Silanol groups located in pores so small that nitrogen molecules cannot penetrate them, but water molecules can (i.e. micropores)

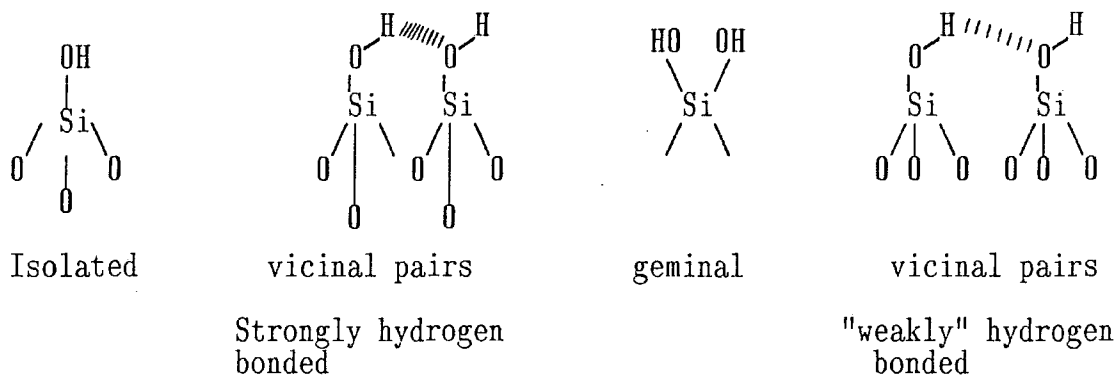
Silanol groups located on the surface of the silica govern molecular adsorption,<sup>(8)</sup> however, the availability of these silanol groups to adsorbing molecules depends upon the structure of the xerogel surface. The nature of xerogel surfaces have been investigated over many years using a suite of techniques.

The properties of the silanol groups upon the surface of silicas have been studied using infra red (IR) spectroscopy.<sup>(9,10)</sup> The observed adsorption bands can be used to distinguish between different types of silanol groups, and adsorbed water molecules. There have also been many studies undertaken concerned with the dehydration/rehydration of silicas, and the determination of the surface concentration of silanol groups. Such determinations have involved the reaction of silanol groups with various reagents (e.g.  $D_2O$ <sup>(11)</sup>,  $SOCl_2$ <sup>(12)</sup>,  $BCl_3$ <sup>(12)</sup>,  $AlCl_3$ <sup>(13)</sup>,  $CH_3Li$ <sup>(14)</sup>,  $B_2H_6$ <sup>(15)</sup>,  $Ca^{2+}$ <sup>(16)</sup> and  $LiAlH_4$ <sup>(16)</sup>), however, certain difficulties make the accuracy of the results open to question about the accessibility of the silanol groups, and the stability of the reaction products. In order to overcome these problems, various techniques involving IR,<sup>(17)</sup>  $^{29}Si$  CP/NMR,<sup>(18)</sup> and  $^1H$  relaxation time measurements<sup>(19)</sup> have been proposed to measure the surface concentration of silanol groups.

As a general rule, starting with a fully hydroxylated silica xerogel, the surface concentration of silanol groups is about  $5.0 \text{ OH nm}^{-2}$ . (1) Infra red and  $^{29}Si$  NMR techniques reveal the existence of a

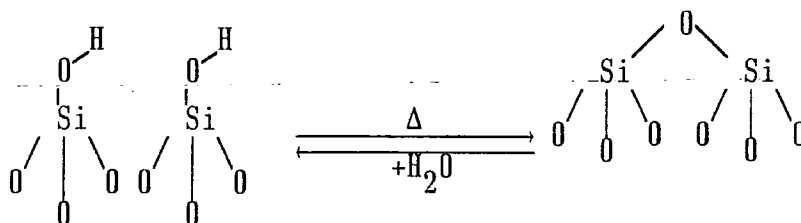
number of different types of silanol groups upon the surface of a xerogel, isolated (i.e. single), geminal, vicinal (i.e. adjacent pairs of SiOH groups weakly hydrogen bonded) and more strongly hydrogen bonded vicinal pairs (Figure 6.1).

FIGURE 6.1



When a silica is heated, the silanol groups most readily lost are those vicinal groups which are undergoing "Weak" hydrogen bonding. They are lost via condensation reactions, forming strained siloxane bridges. (Figure 6.2).

FIGURE 6.2



The majority of the silanol groups upon the surface of a xerogel are thought to exist in pairs,<sup>(9)</sup> most of which are lost upon heating to 800°C.<sup>(19)</sup> Heating xerogel to 400°C removes ca. half of the silanol groups, however, many of the remaining silanol groups are still paired (i.e. vicinal), and the siloxane bridging bonds are strained. Hence rehydration can occur readily, and the reaction shown in Figure 6.2 may be reversible. However, above 400°C, more vicinal

silanol groups are lost via condensation reactions, and rearrangement of the surface structure of the silica may occur, causing the siloxane bonds to become less strained. Complete removal of the silanol groups, however, may only be achieved by heating to temperatures in excess of 1000°C. The removal of the silanol groups becomes more difficult as the temperature is increased. (See Table 6.1)

TABLE 6.1<sup>(20)</sup>

TEMPERATURE° C	$N_{OH}/nm^2$
700	1.20
800	0.90
900	0.65
1000	0.40

### 6.3.1 SURFACE MODELS

Studies of silicas using x-ray diffraction, have suggested that the surface structure of silica surfaces resembles that of  $\beta$ -cristobalite or other crystalline phases. Many dehydration/rehydration studies of silicas have invoked these models in order to interpret the results.

De Boer et al<sup>(23)</sup> suggest that a silica surface resembles that of the (111) face of  $\beta$ -cristobalite (Figure 6.3). The silanol groups on this surface are arranged in a hexagonal array, separated by 5 Å. The theoretical surface concentration of silanol groups is 4.55 OH nm<sup>-2</sup>. This value is in close agreement to that observed for silicas that have been repeatedly dehydrated and rehydrated.<sup>(1)</sup> For silicas where the surface concentration of silanol groups exceed 4.55 OH nm<sup>-2</sup>, the presence of lattice defects, giving rise to geminal and buried uncondensed silanol groups is invoked (Figure 6.4). These are lost as the xerogel is heated (Figure 6.5). This model, however, cannot account for hydrogen bonding between silanol groups or silica

surfaces, where the surface concentration of silanol groups is less than  $4.55 \text{ OH nm}^{-2}$ . Peri and Hensley,<sup>(13)</sup> proposed that the surface of silica resembles that of the (100) face of  $\beta$ -cristobalite (Figure 6.6). In this model each surface silicon site is a geminal silanol site, the silanol groups are undergoing mutual hydrogen bonding. The surface concentration of silanol groups is  $7.90 \text{ OH nm}^{-2}$ . Upon dehydration, random condensation of the silanol groups (Figure 6.7) ultimately results in the formation of a silica surface that resembles the (111) face of  $\beta$ -cristobalite (Figure 6.3).

In these models, however, only isolated silanol groups would exist upon the surface of the xerogel following dehydration, however,  $^{29}\text{Si}$  CP MAS NMR<sup>(21)</sup> has shown that there is still a substantial proportion of geminal silanol groups upon silica surfaces heated to  $800^\circ \text{ C}$ . In order to account for this result, it was proposed that the silica surface contained segments resembling both the (100), and (111) faces of  $\beta$ -cristobalite (Figure 6.8). The surface concentration of silanol groups per  $\text{nm}^2$  is  $N_{\text{OH}}/\text{nm}^2 = 7.90 + 4.55(1-fg)$ , where  $fg$  is the fraction of geminal silanol groups.

### 6.3.2 THE ADSORPTION OF WATER

If one considers a silica surface with a very low concentration of surface silanol groups, although it is possible that water molecules can be bonded to siloxane areas ( $\equiv\text{Si-O-Si}\equiv$ )<sup>(22)</sup> it is considered unlikely that this interaction will be strong enough to break hydrogen bonds between water molecules. Hence siloxane areas of the surface remain essentially hydrophobic. The silanol groups are the preferred sites for water adsorption. The adsorbed water molecules are orientated "oxygen down" on the silanol groups.<sup>(1)</sup> Hydrogen bonded clusters of water molecules then form, even before all the silanol groups have adsorbed water to form  $\equiv\text{SiOH:OH}_2$  species. The reason for this, is that water molecules are more strongly adsorbed

FIGURE 6.3

A DIAGRAM SHOWING THE (111) FACE OF  
 $\beta$ -CRISTOBALITE

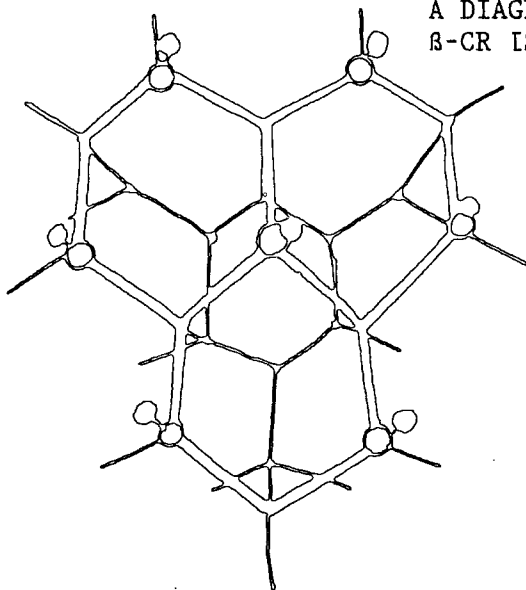
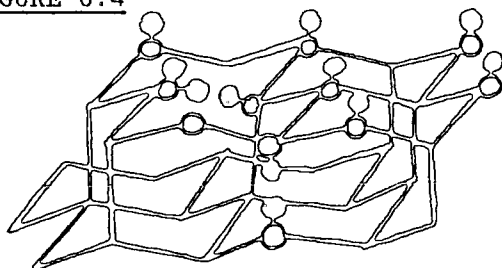


FIGURE 6.4

THE (111) FACE OF  $\beta$ -CRISTOBALITE  
 DEFECTS IN THE STRUCTURE SHOWN



$-\text{H}_2\text{O}$

FIGURE 6.5

A DIAGRAM SHOWING THE SURFACE  
 STRUCTURE OF THE (111) FACE OF  
 $\beta$ -CRISTOBALITE

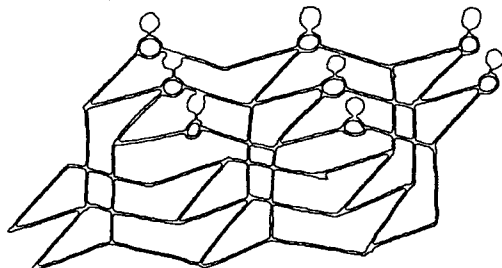
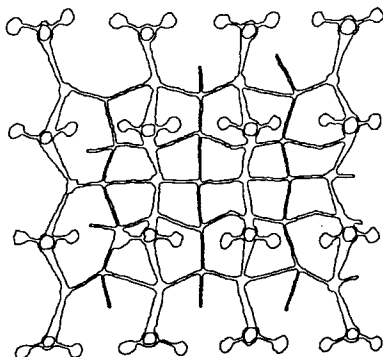
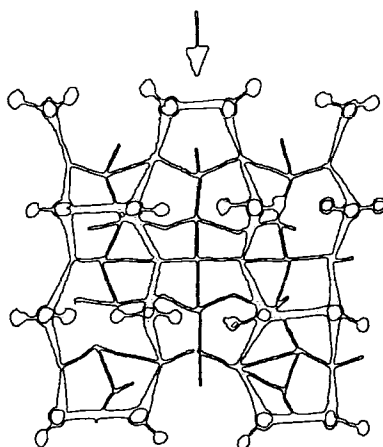


FIGURE 6.6



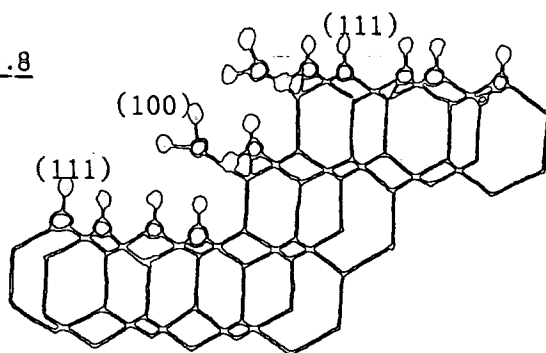
A DIAGRAM SHOWING THE (100)  
FACE OF  $\beta$ -CRISTOBALITE  
EACH OF THE SURFACE SILICON  
SITES HOLDS TWO HYDROXYL  
GROUPS

FIGURE 6.7



A DIAGRAM OF A PARTIALLY  
DEHYDRATED  $\beta$ -CRISTOBALITE  
(100) FACE

FIGURE 6.8



A DIAGRAM SHOWING THE SILICA  
SURFACE AS PROPOSED BY MACIEL  
AND SINDORF<sup>(21)</sup>



surface area and increase in pore diameter. The extent to which these changes occur increases with temperature, and duration of treatment. These observations have been interpreted in terms of the corpuscular model for silica xerogels.

In the theory of the corpuscular structure of xerogels, the silica is presented as an assembly of spherical particles packed together. The diameter of these particles ( $d/\text{nm}$ ) may be estimated from surface area measurements using equation 6.1. (27)

$$(6.1) \quad d = \frac{6}{\rho A}$$

Where  $\rho$  = the density of silica ( $2.2 \text{ g cm}^{-3}$ ) and  $A$  is the surface area as measured via nitrogen adsorption ( $\text{m}^2 \text{ g}^{-1}$ ). The reduction of surface area and increase in pore diameter, is associated with the formation of secondary particles around 10-20 nm in diameter and tertiary structures around 100-200 nm in diameter. There are a number of mechanisms that govern how these form.

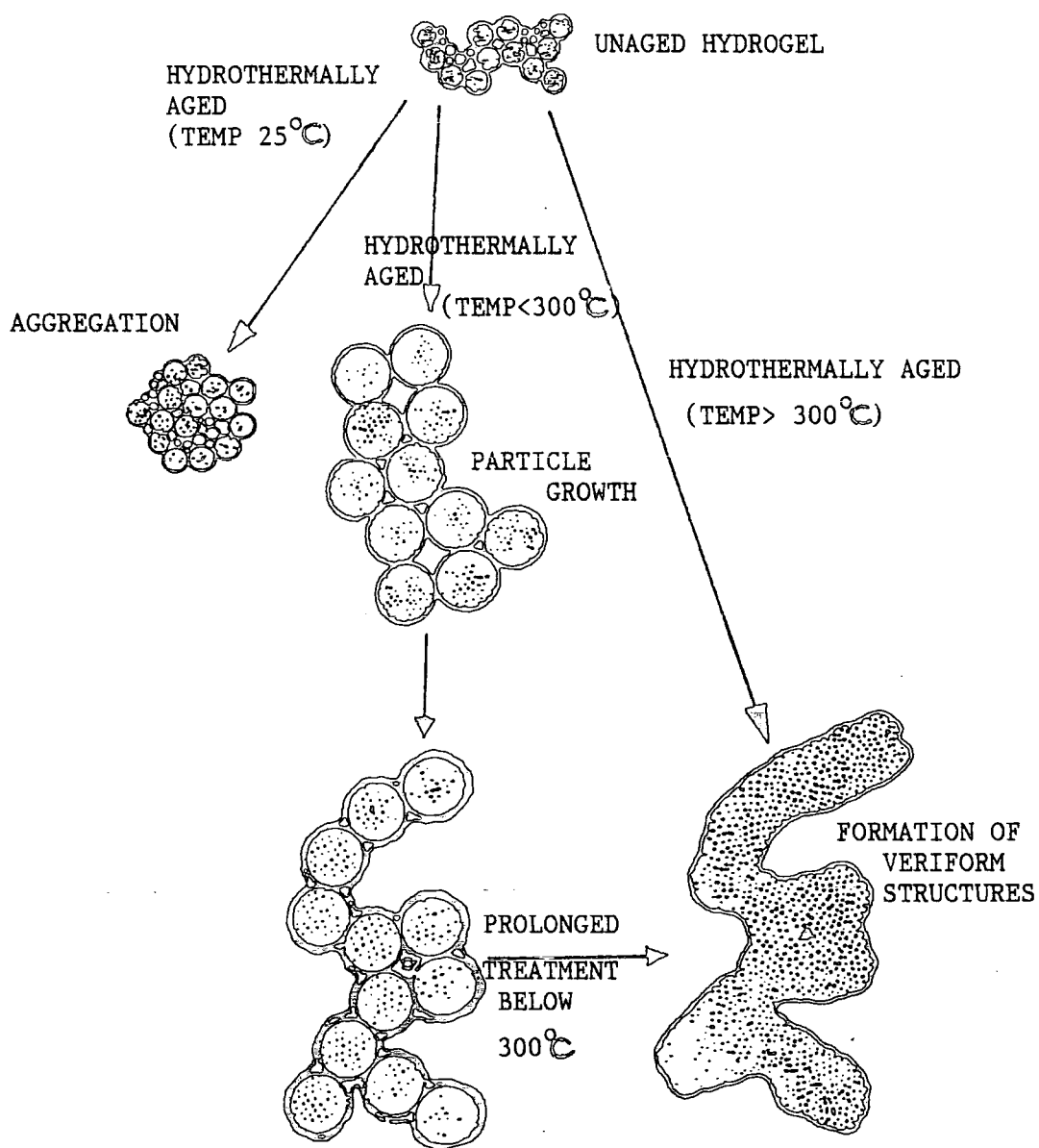
(1) The aggregation mechanism

In the first stage of this process the primary particles become more closely packed together to form secondary particles, but they retain their individuality. This is later followed by condensation reactions between the silanol groups upon the surface of the primary particles. This process predominates at low temperature (i.e.  $25^\circ\text{C}$ ) (25,26) (Figure 6.9)

(2) The growth mechanism

During the process of hydrothermal aging dissolution of silica takes place from the surfaces of small particles. Silica is then deposited from solution upon larger particles, such that larger particles grow in size at the expense of smaller particles, via a growth mechanism (Ostwald ripening). Or silica may become deposited at the points of contact between particles.

FIGURE 6.9



This results in the intergrowth of the particles to form veriform or worm-like structures (Figure 6.9).

The mechanism that predominates is determined by the conditions of hydrothermal aging. Electron-microscopy has shown that at temperatures in excess of  $300^{\circ}\text{C}$ , the reduction of surface area with hydrothermal aging is caused predominantly by the intergrowth of particles to form veriform structures, ultimately transforming the xerogel structure from a globular to a more "sponge" like form (Figure 6.9). When hydrothermal aging is performed at temperatures below  $300^{\circ}\text{C}$  the loss of surface area is caused predominantly by the growth mechanism. The silica particles grow, become more uniform in size and spherical in shape. As a consequence particle packing becomes more uniform. This process is also accompanied by a decrease in the particle packing density. Following more prolonged treatment at low temperature (i.e.  $< 300^{\circ}\text{C}$ ) intergrowth of the particles occurs.

All these changes are reflected in the structural properties of the resultant xerogels. Upon aging at temperatures below  $300^{\circ}\text{C}$ , there is a decrease in the surface area, an increase in the pore volume and diameter, and the porosity becomes more uniform. Thermogravimetric work has shown that the aging process also causes an apparent increase in the degree of hydration per unit area. (26,28) There are two explanations that have been put forward in order to account for this observation.

- (1) There may occur an increase in the surface concentration of silanol groups, as a consequence of splitting of siloxane bonds (Figure 6.10a) or by dissolved hydrated silica being deposited upon the surface of silica particles (Figure 6.10b)

FIGURE 6.10a

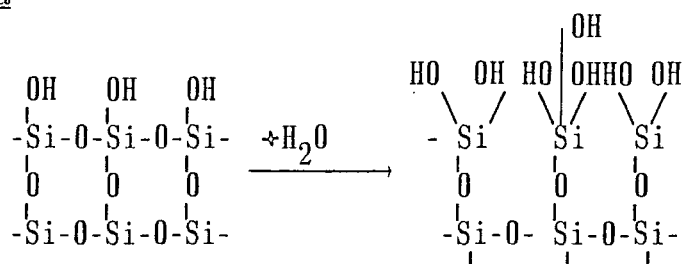
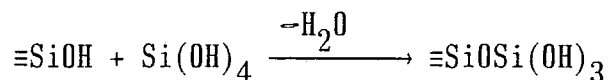


FIGURE 6.10b



As a result each of the surface silicon atoms would be attached not to one, but two or three hydroxyls. In this way the degree of hydration per unit surface area could be increased, during the course of hydrothermal aging.

Alternatively

- (2) The observed increase in the degree of hydration per unit area may be attributed to an increase in microporosity with aging. Water molecules, and uncondensed silanol groups can then be trapped within the micropores. These may only be removed by heating the xerogels to temperatures much higher than those usually required to remove adsorbed water.

The process of hydrothermal aging is known to cause an increase in microporosity.<sup>(8,30,31)</sup> As silica is deposited from solution at the point of contact between particles, the orifices of the pores become greatly narrowed forming eventually, micropores. With aging, the ability of larger-sized molecules to enter these pores diminishes. This process gives rise to a molecular-sieve effect. Under prolonged or very intense treatment these pores become completely sealed and microporosity decreases.

At low temperatures (i.e. <300°C), the rate of hydrothermal aging is independent of the amount of silica in the water. The rate of

aging is determined by the rate of cleavage of the siloxane linkages. The cleavage is thought to occur as a consequence of a nucleophilic bimolecular substitution reaction. Hence, the presence of salt anions should have the principal influence upon the kinetics of hydrothermal aging. Studies concerned with hydrothermal, aging kinetics,<sup>(29)</sup> indicate that of the anions studied, the following order of their catalytic activity exists  $F^- > SO_4^{2-} > Cl^-$ . The rate of hydrothermal aging also increases as the pH of the hydrogel is increased.

### 6.5 NMR STUDIES OF SILICA XEROGELS

The first  $^1H$  NMR studies of silica xerogels were concerned with relaxation measurements on protons, in water molecules adsorbed upon the surface.<sup>(33)</sup> Measurement of the  $T_1$  and  $T_2$  relaxation times indicated a two phase system. This two phase behaviour was then explained in terms of a stochastic theory of exchange.<sup>(34)</sup> This technique enabled measurements of the average lifetimes of protons in adsorbed phases and the surface concentration of silanol groups to be made.<sup>(19)</sup> More recently, however,  $^1H$  CRAMPS has been shown to be an extremely useful tool for the investigation of proton environments within xerogels.<sup>(35,36)</sup> The use of this technique will be discussed later.

In addition  $^{29}Si$  MAS NMR and  $^{29}Si$  CP MAS NMR techniques have been employed to study the surface and bulk structures of silica xerogels. The first  $^{29}Si$  CP MAS NMR spectrum of a silica xerogel was published by Maciel et al in 1981.<sup>(37)</sup> Using this technique it was shown that quantitatively reliable data concerning the fraction of isolated and geminal silanol groups can be obtained. This technique has been used extensively in studying the process of dehydration and rehydration of silicas,<sup>(18,38)</sup> the reactions of various molecules upon the surfaces of silicas,<sup>(38,39,40,41,42)</sup> the reactivities of surface silanol groups,<sup>(43)</sup> and the surface concentration of silanol groups.<sup>(43)</sup>

This technique, has the advantage that because the  $^{29}\text{Si}$  NMR method is based upon the properties of the silicon, rather than the hydroxyl environment, calculations of the surface concentration of silanol groups are much less sensitive to potential sources of error than other techniques. Single pulse  $^{29}\text{Si}$  MAS NMR techniques have been shown to yield quantitative information concerning the bulk structure of silica xerogels. (44,45)

In this chapter a variety of  $^1\text{H}$  and  $^{29}\text{Si}$  NMR techniques have been employed to the study of silica xerogels, in order to gain a better understanding of their structural properties and the nature of the changes that take place when silica xerogels are prepared or treated in different ways.

## 6.6. EXPERIMENTAL

This section contains a brief description of how some of the silica xerogels studied in this chapter were prepared. Other samples of silica xerogels studied, whose preparation is not described, were obtained courtesy of Unilever Research. For reasons of industrial confidentiality no description of their preparation is given. Each xerogel is identified by a serial number given in this section. Methods whereby these xerogels were characterised are discussed in Chapter Three.

### 6.6.1 SILICA XEROGEL PREPARATION

#### 6.6.1a SILICA XEROGELS A1, A2, A3, AND A4

These silica xerogels were prepared by the rapid addition of an aqueous alkaline sodium silicate solution of composition 22.78%  $\text{SiO}_2$  (w/w) and 6.90%  $\text{Na}_2\text{O}$  (w/w) (density  $\rho = 1.29 \text{ g cm}^{-3}$ ) to a 40.00% (w/w) solution of sulphuric acid (density,  $\rho = 1.30 \text{ g cm}^{-3}$ ). The weight ratio of silicate to acid is 2.36:1. The resultant 16%  $\text{SiO}_2$  (w/w) hydrosol contained  $1.0 \pm 0.1\text{N}$  excess acid (as determined by titration with an 1M NaOH solution). A rigid clear hydrogel formed in around

15 minutes. In the case of xerogel A4, the sodium silicate and acid were mixed together rapidly in a small sample chamber 8 mm in diameter, using the "Jet mixer" located at the Unilever Research Laboratories in Port Sunlight. The xerogel samples A2, and A3 were prepared by pumping both solutions simultaneously into the mixing head of a "high sheer" "Silver Stone" mixer.

The hydrogel once formed, was then left for an hour, before it was broken up into fragments around 5-10 mm in diameter, before washing it between 5 and 8 times with deionized water at room temperature, to remove sodium sulphate. Xerogel A4 was washed 5 times. Xerogels A2 and A3 were obtained from the same hydrogel batch, and washed 8 times.

A 12% (w/w) slurry of each of the xerogels in deionized water was then prepared. For xerogels A3 and A4, the pH of the solution was adjusted to pH7 by the addition of sodium hydroxide solution. For xerogel A2, the pH of the xerogel was adjusted to pH7 by the addition of ammonium hydroxide solution. A sample of each of the unaged silica hydrogels was then obtained, then freeze dried (using liquid nitrogen) for several days. These samples are given the serial numbers A2.0.0, A3.0.0 and A4.0.0.

The remaining samples of each hydrogel were heated in a 12%(w/w) slurry in deionized water at 100°C under reflux conditions, in order to hydrothermally age the gels. Samples of each of the hydrogels were removed after various times (up to a total of 22 hours), and freeze dried using liquid nitrogen, as before.

Silica xerogel A1 was prepared via the same method by C. Black at Unilever Research. The pH of the hydrogel was adjusted to pH7 using ammonium hydroxide solution, then hydrothermally aged for differing periods of time and dried as above.

### 6.6.1b SILICA XEROGEL S3

This silica xerogel was prepared via the rapid addition of a sodium silicate solution of composition 25% SiO<sub>2</sub> (w/w) and 7.7% Na<sub>2</sub>O (w/w) to a 35% (w/w) solution of sulphuric acid. The volume ratio of silicate to acid being 2.516:1. The heat of neutralisation caused the resultant hydrosol to have a temperature of 42°C. A rigid clear hydrogel formed in 8 minutes.

### 6.6.1c SILICA XEROGEL G1

This silica xerogel was prepared by the rapid addition of a sodium silicate solution of composition 25% SiO<sub>2</sub> (w/w) and 7.7% Na<sub>2</sub>O (w/w) to a 40% (w/w) solution of sulphuric acid. The volume ratio of silicate to acid being 2.56:1. The heat of neutralisation causes the resultant hydrosol to have a temperature of 48°C. A clear rigid hydrogel formed in 3 to 4 minutes.

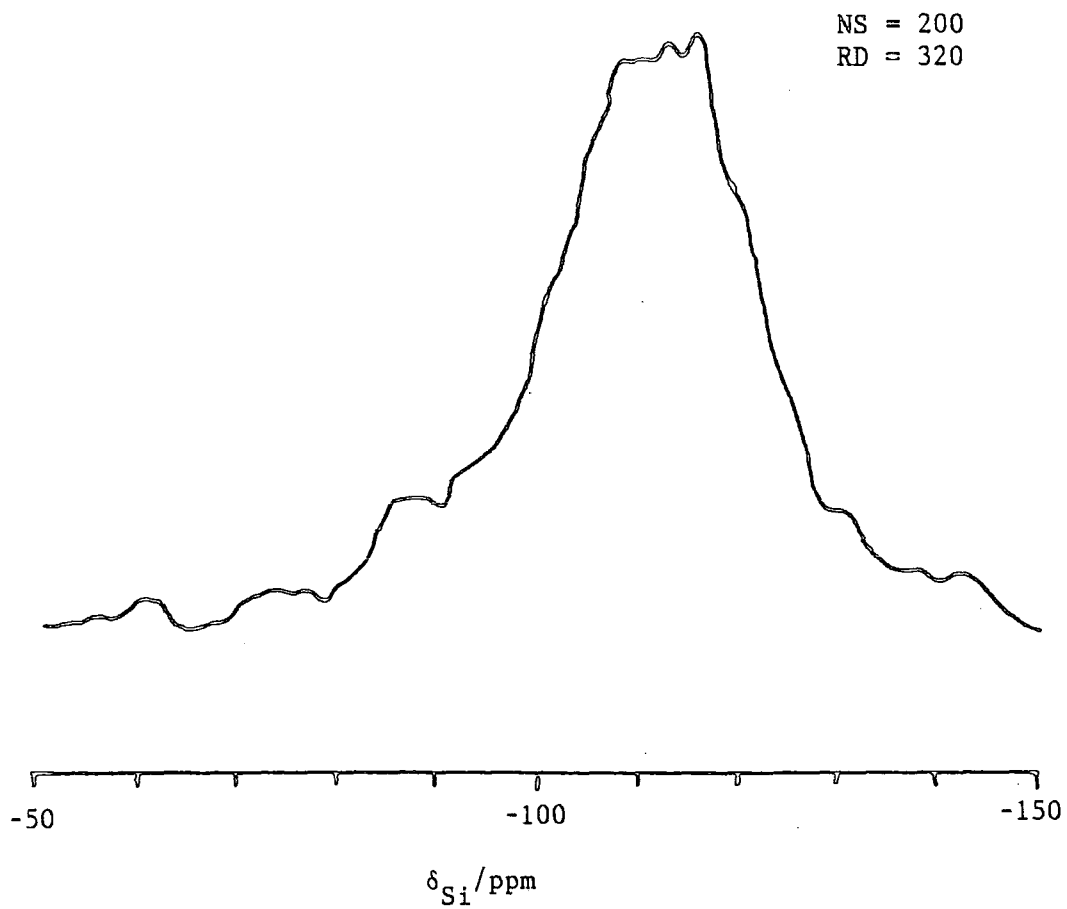
Samples of the silica hydrogels S3 and G1 were washed with deionized water to pH3 or pH7, then dried either in a fan oven at 110°C for at least 12 hours, or freeze dried using liquid nitrogen for several days. Both hydrogels were prepared in 500 ml beakers, using a specially adapted "Silver Stone" mixer and mixing head.

## 6.7 RESULTS AND DISCUSSION

A typical static <sup>29</sup>Si single pulse NMR spectrum of a silica xerogel (Figure 6.11) exhibits a broad signal, with a linewidth in excess of 950 Hz, caused as a consequence of heteronuclear (<sup>29</sup>Si-<sup>1</sup>H) dipolar interactions, shielding anisotropy and the dispersion of chemical shifts. Considering the distance between the silicon and proton spins to be similar to that observed for the sodium silicate hydrates (ca 2.8Å)<sup>(46)</sup>, the linewidth one would expect for Si-OH groups as a consequence of heteronuclear dipolar interactions may be estimated using equation 6.2<sup>(47)</sup> as ≈ 3.8 KHz (i.e. 96 ppm).

Furthermore, for silicon nuclei in these systems, shielding anisotropy

STATIC  $^{29}\text{Si}$  SINGLE PULSE NMR SPECTRUM OF SILICA XEROGEL S-TYPE(1)



is unlikely to exceed 60 ppm. These interactions may be removed from the spectrum by spinning at rates around  $\omega_r \approx 4$  KHz, or by spinning at  $\omega_r \geq 3$  KHz and employing high-power proton decoupling.

$$(6.2) \quad \Delta\nu\frac{1}{2} = \left[ \frac{\mu_0}{4\pi} \right] \frac{\gamma_H \gamma_{Si} \hbar}{4\pi^2 r_{Si-H}^3} (1-3\cos^2\theta) \text{ where } \theta = 90^\circ$$

The  $^{29}\text{Si}$  single-pulse MAS NMR spectrum of a typical xerogel (Figure 6.12) exhibits three broad resonances at ca -92 ppm, -100 ppm and -110 ppm. These resonances are assigned to silicon nuclei in  $Q^2$ ,  $Q^3$  and  $Q^4$  environments respectively.<sup>(37)</sup> No silicon nuclei in  $Q^1$  environments are observed. The static CPMG spectrum of this xerogel (obtained in the presence of high-power proton decoupling), exhibits a linewidth of only 10 Hz (Figure 6.13). Inspection of Figure 6.12 reveals that the linewidth of the resonances observed increases from  $Q^2$  to  $Q^4$ . Since the linewidths are inhomogeneous (ie the linewidths result from the superposition of many resonances of differing chemical shift), this increasing linewidth upon going from  $Q^2$  to  $Q^4$  reflects the increasing number of possible silicon environments within these structural units.

In order to make quantitative measurements of the fraction of silicon atoms in each of the  $Q^n$  environments, it is important that one should be certain that all the silicon signal is observed in the  $^{29}\text{Si}$  single-pulse MAS NMR spectra. In order to determine the best conditions required to obtain quantitative data, two experiments were performed upon xerogel S-Type(1).

#### 6.7.1.1 $T_1(^{29}\text{Si})$ MEASUREMENTS

The  $^{29}\text{Si}$  longitudinal relaxation times ( $T_1(^{29}\text{Si})$ ) of silicon nuclei in the xerogel were determined using the progressive saturation method.<sup>(48)</sup> Calculations indicate the  $T_1(^{29}\text{Si})$  values for silicon atoms in  $Q^3$  and  $Q^4$  environments to be around  $41 \pm 5$  s and  $51 \pm 6$  s respectively (Figures 6.14 and 6.15). Unfortunately owing to the poor



signal to noise of the spectra obtained, and the small intensity of the  $Q^2$  resonance, it was not possible to calculate the  $T_1(^{29}\text{Si})$  value for silicon nuclei in  $Q^2$  environments. The results obtained are consistent with those published by Fyfe et al,<sup>(44)</sup> and suggest that quantitatively reliable data may be obtained from  $^{29}\text{Si}$  single-pulse MAS NMR spectra, provided recycle times of the order of 5 minutes are employed.

#### 6.7.1.2 INTENSITY MEASUREMENTS

A known mass of the sodium salt of 3-(trimethylsilyl)- 1- propane sulphonic acid (TMS salt) (0.1239 g) was weighed into a rotor containing 0.1845 g of the xerogel. Correcting for the amount of "water" present within the xerogel, (10.5%(w/w) as determined by heating the sample in a stream of nitrogen to 1000°C) the ratio of the number of silicon atoms present within the xerogel to the number within the TMS salt may be calculated as 4.84:1. The  $^{29}\text{Si}$  single-pulse MAS NMR spectrum of this physical mixture was then acquired (Figure 6.17). The resonance at 1.18 ppm is assigned to silicon atoms within the TMS salt, known to have a  $T_1(^{29}\text{Si})$  value of 63.1 s. The ratio of intensities was then measured by direct integration. The results indicate that provided recycle times of the order of 280-320 s are employed, > 98% of the silicon signal may be observed. Integration of spectra acquired under these conditions, therefore, allows the fraction of silicon atoms in each of the  $Q^n$  environments ( $P(Q^n)$ ) to be determined.

In order to simplify the proceeding discussion, data obtained from the  $^{29}\text{Si}$  single-pulse MAS NMR spectra of silica xerogels obtained under conditions where  $\omega_r = 3.3$  KHz, recycle times of typically 300 s and a proton decoupling field of 62.5 KHz are summarised in Table 6.2. Selected spectra of some of these xerogels are shown later in this

FIGURE 6.14

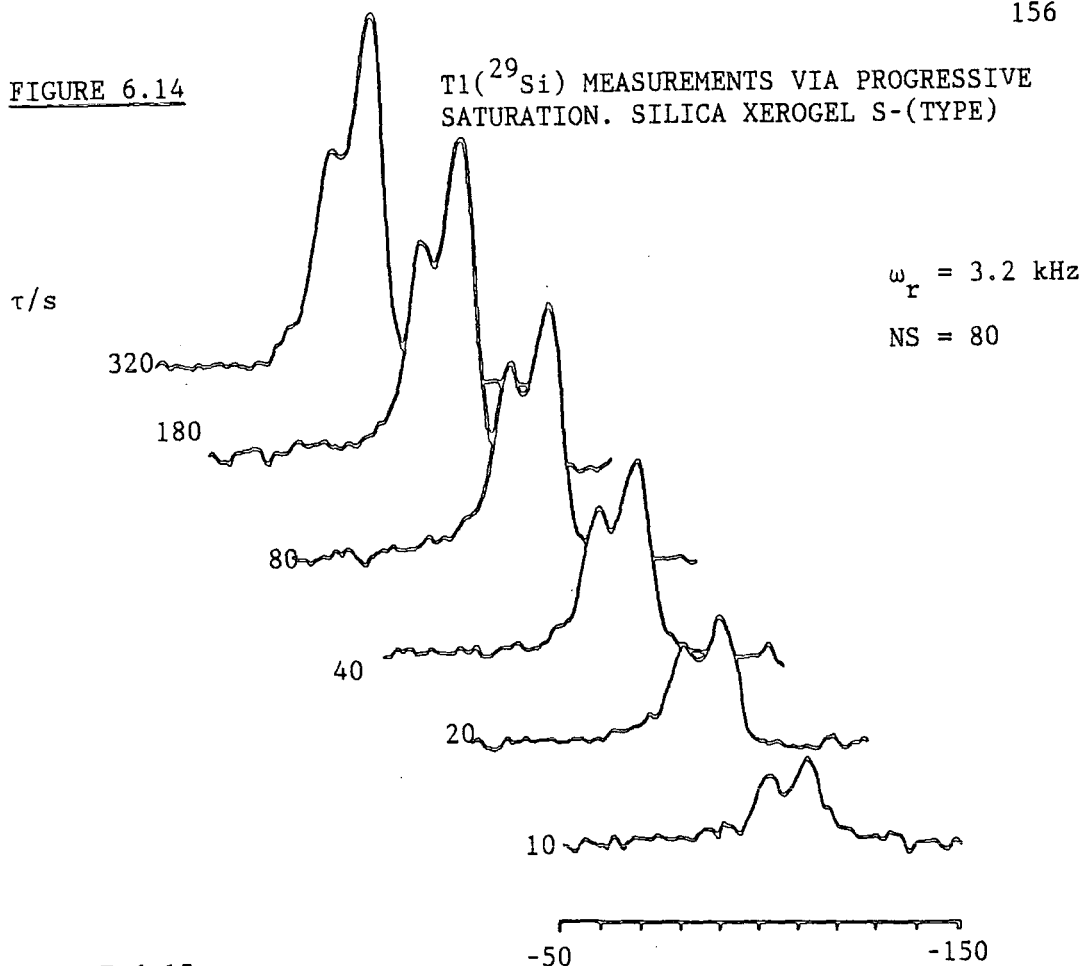
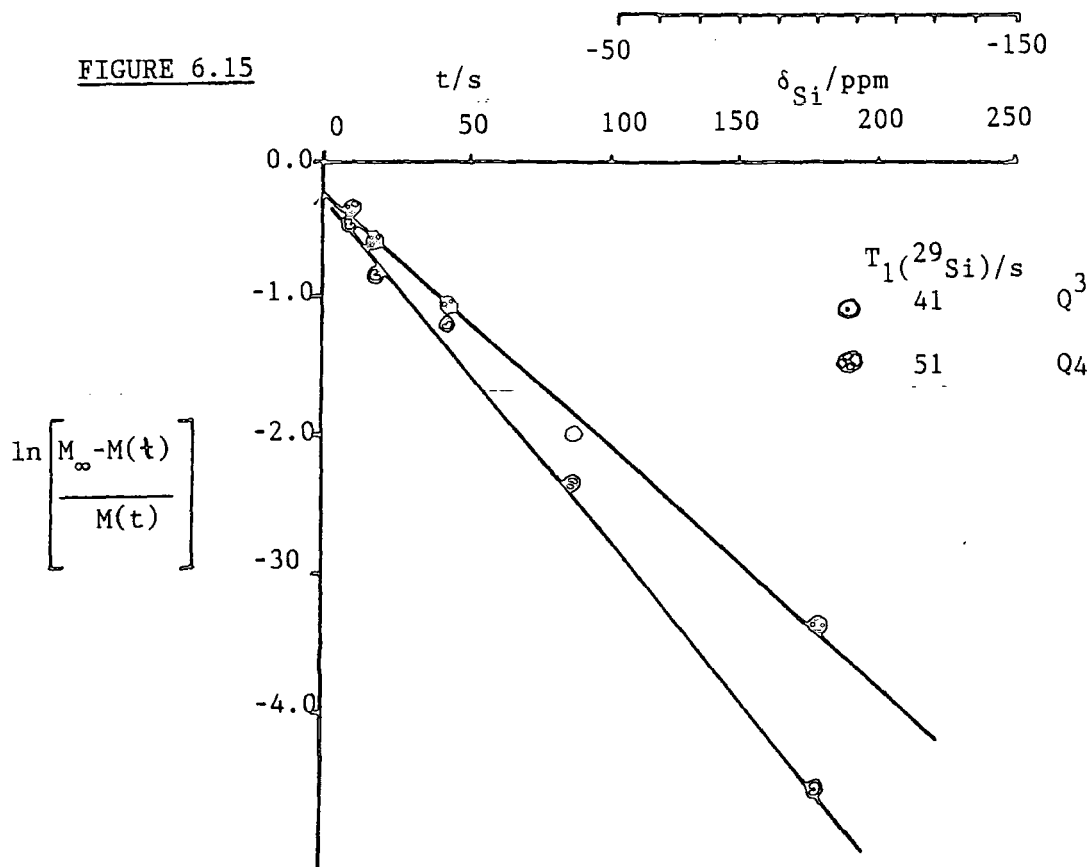
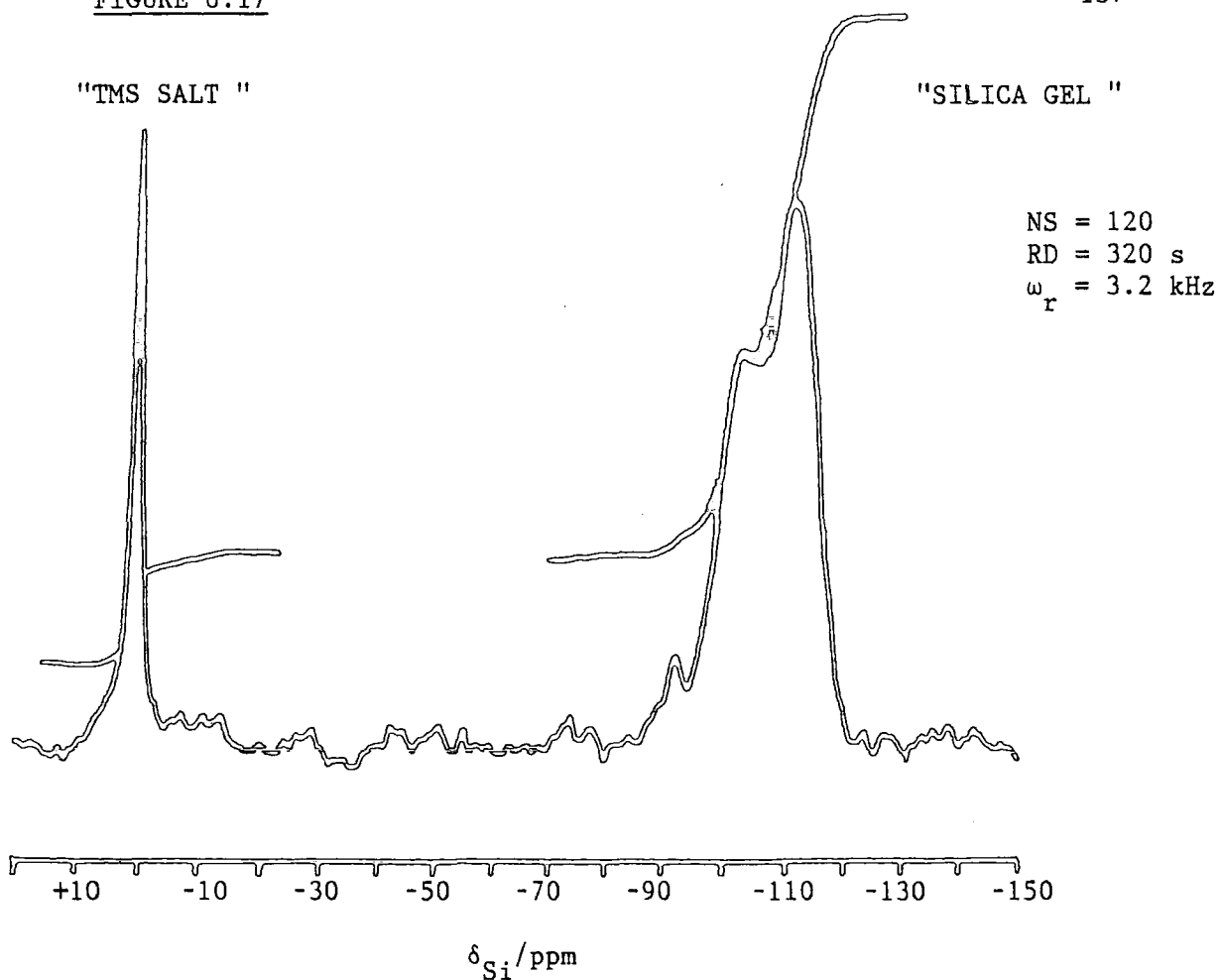


FIGURE 6.15





THE  $^{29}\text{Si}$  SINGLE PULSE MAS (PROTON DECOUPLED) SPECTRUM OF A PHYSICAL MIXTURE OF THE SODIUM SALT TRIMETHYLSILY-1-PROPANE SULPHONIC ACID AND SILICA XEROGEL S-TYPE(1)

chapter. Errors in measurements of the fraction of silicon atoms in each of the  $Q^n$  environments are estimated to be ca  $\pm 10\%$ .

### 6.7.2 STRUCTURAL MODELS OF SILICA XEROGELS

The data obtained from the single-pulse  $^{29}\text{Si}$  MAS NMR spectra of silica xerogels provides information concerning the bulk structure. Given that the average molecular formula of a pure silica may be expressed by

$$(6.3) \quad \text{H}_{(4-\bar{Q})_n} \text{Si}_n \text{O}_{(4-\bar{Q})_n \frac{2}{2}}$$

where  $\bar{Q}$  is the average degree of connectivity, defined by equation 6.4

$$(6.4) \quad \bar{Q} = \sum_{n=2}^4 nP(Q^n)$$

the average molecular weight and the bulk density of silanol groups may then be calculated using equations 6.5 and 6.6 respectively

$$(6.5) \quad \bar{M}_w = 96.114 - 9.0075\bar{Q}$$

$$(6.6) \quad N_{\text{OH}}/\text{g} = \frac{(4-\bar{Q})}{\bar{M}_w}$$

In an effort to glean some information concerning the environment of the silanol groups within silica xerogels, the data obtained from the  $^{29}\text{Si}$  MAS NMR single-pulse spectra of a number of silica xerogels, concerning the fraction of silicon atoms in each of the  $Q^n$  environments, was analysed in terms of a number of structural models.

TABLE 6.2

XEROGEL	$\frac{A}{m^2 g^{-1}}$	$P(Q^2)^+$	$P(Q^3)^+$	$P(Q^4)^+$	COMMENTS
S-TYPE (1)	800	0.040	0.340	0.620	FROM CROSFIELD CHEMICALS
S-TYPE (2)	381	0.000	0.240	0.760	"
MICROSIL GP	210	0.000	0.110	0.890	"
SP 51	-	0.000	0.200	0.800	"
FISHER S-157	750	0.065	0.370	0.565	LITERATURE VALUE (ref 44)
A1.0	806.7	0.068	0.362	0.570	HYDROTHERMALLY AGED SAMPLE
A1.2	598.8	0.054	0.224	0.722	"
A1.3	557.2	0.043	0.224	0.733	"
A1.4	528.0	0.034	0.238	0.728	"
A1.5	511.1	0.022	0.184	0.794	"
A2.0	682.3	0.057	0.398	0.545	"
A2.0.3	719.9	0.040	0.330	0.630	"
A2.0.7	582.2	0.030	0.312	0.658	"
A2.6.8	395.8	0.025	0.176	0.799	"
A3.0	655.3	0.057	0.381	0.562	"
A3.0.3	688.0	0.042	0.333	0.625	"
A3.1.2	489.3	0.030	0.270	0.700	"
A3.4.5	372.5	0.019	0.206	0.775	"
A4.0	803	0.050	0.350	0.600	"
A4.2	397	0.020	0.210	0.770	"

+ errors in intensity measurements are assumed to be ca 10%  
a errors in surface area measurements are  $\pm 10\%$  from the absolute surface area.

as determined from the complete BET adsorption isotherm (see Chapter 2)

TABLE 6.2 cont'd

XEROGEL	$\frac{A^a}{m^2 g^{-1}}$	$P(Q^2)^+$	$P(Q^3)^+$	$P(Q^4)^+$	COMMENTS
A4.3	367	0.000	0.230	0.770	HYDROTHERMALLY AGED SAMPLE
A4.6	313	0.000	0.210	0.790	"
S3.1	-	0.070	0.387	0.543	SEE SECTION 6.7.5.1
S3.2	-	0.050	0.370	0.580	"
S3.3	-	0.040	0.380	0.580	"
S3.4	-	0.030	0.320	0.650	"
G1.1	-	0.060	0.440	0.500	"
G1.2	-	0.040	0.420	0.540	"
G1.3	-	0.070	0.280	0.650	"
G1.4	-	0.050	0.270	0.680	"
PORASIL A BEADS	-	0.065	0.370	0.565	LITERATURE VALUE (ref 44)

+ errors in intensity measurements are assumed to be ca 10%  
a errors in surface area measurements are  $\pm 10\%$  from the absolute surface area as determined from the complete BET adsorption isotherm (see Chapter 2)

### 6.7.2.1 THE RANDOM DISTRIBUTION MODEL

In this model, the silanol groups are assumed to be randomly distributed throughout the xerogel. The distribution of the silicon atoms in different  $Q^n$  environments is then determined by a binomial distribution

$$(6.7) \quad P(Q^2) = (1-x)^2$$

$$(6.8) \quad P(Q^3) = 2x(1-x)$$

$$(6.9) \quad P(Q^4) = x^2$$

where  $x$  is defined as  $\sqrt{P(Q^4)}$ .

If this model correctly describes the structure of the silica xerogels, then a plot of  $P(Q^2)/P(Q^3)$  against  $(1-\sqrt{P(Q^4)})/2\sqrt{P(Q^4)}$  should produce a straight lined graph, which passes through the origin, having a slope equal to unity, This plot is shown in figure 6.18.

### 6.7.2.2 THE SINGLE DISCRETE PARTICLE THEORY

In this model, the silica xerogel is assumed to be composed of discrete spherical particles of fully condensed silica (density,  $\rho = 2.2 \text{ g cm}^{-3}$ ), the diameter of these particles is estimated from surface area measurements using equation 6.2. Given that the average separation between silicon atoms of adjacent silicon-oxygen tetrahedra is the distance  $C/\text{nm}$ , then the average number of silicon atoms across the diameter of the particle ( $n_d$ ), the total number of silicon atoms in each particle ( $n_t$ ) and the number of surface silicon sites ( $n_s$ ) may be calculated using equations 6.10, 6.11 and 6.12 respectively

$$(6.10) \quad n_d = (d/c)$$

$$(6.11) \quad n_t = \frac{\pi n_d^3}{6}$$

$$(6.12) \quad n_s = \frac{\pi}{6} [n_d^3 - (n_d - 2)^3]$$

The ratio ( $n_s/n_t$ ) may then be expressed in terms of the surface area

(A/m<sup>2</sup> g<sup>-1</sup>) by equation 6.13a

$$(6.13a) \quad \left[ \frac{n_s}{n_t} \right]_{\text{calc}} = (\rho AC) - \frac{(\rho AC)^2}{3} + \frac{(\rho AC)^3}{27}$$

This ratio ( $n_s/n_t$ ) may also be calculated from data obtained from <sup>29</sup>Si single-pulse MAS NMR spectra via equation 6.13b

$$(6.13b) \quad \left[ \frac{n_s}{n_t} \right]_{\text{nmr}} = P(Q^2) + P(Q^3)$$

The average separation between silicon atoms of adjacent silicon-oxygen tetrahedra has been estimated from small angle x-ray diffraction experiments as  $C = 0.31 \text{ nm}$ .<sup>(44)</sup> If this model correctly describes the structure of silica xerogels, then a plot of  $(n_s/n_t)_{\text{nmr}}$  against  $(n_s/n_t)_{\text{calc}}$  should produce a straight lined graph, which passes through the origin, having a slope equal to unity. This plot is shown in Figure 6.19.

Considering Figure 6.18 and 6.19, it may be seen that there is a slightly better correlation of the data obtained in the <sup>29</sup>Si single-pulse MAS NMR experiments with the single-discrete particle model rather than the random-distribution model, although given the quality of the data, it is difficult to draw any firm conclusions from this. However, a plot of  $(n_s/n_t)_{\text{nmr}}$  values against surface area (A/m<sup>2</sup> g<sup>-1</sup>) does suggest that the average separation between silicon atoms of adjacent silicon-oxygen tetrahedra is around 0.3nm (Figure 6.20).

These results suggest that the <sup>29</sup>Si NMR data is not inconsistent with a corpuscular model for the xerogels, in which all the silanol groups are located at the surface of the silica particles. The surface concentration of silanol groups ( $N_{\text{OH}}/\text{nm}^2$ ), and the fraction of those silanol groups that are isolated ( $f_i$ ) or geminal ( $f_g$ ) can be calculated using equations 6.14, 6.15a and 6.16a respectively. The fraction of surface silicon Q<sup>3</sup> ( $F(Q^3)$ ) and Q<sup>2</sup> sites ( $F(Q^2)$ ) may be

calculated by equations 6.15b and 6.16b respectively

$$(6.14) \quad N_{\text{OH}}/\text{nm}^2 = \frac{(4-Q) \times 6.023 \times 10^{23}}{M_w \cdot A}$$

$$(6.15a) \quad f_i = \frac{P(Q^3)}{2P(Q^2) + P(Q^3)} \quad (6.15b) \quad F(Q^3) = \frac{P(Q^3)}{P(Q^2) + P(Q^3)}$$

$$(6.16a) \quad f_g = \frac{2P(Q^2)}{2P(Q^2) + P(Q^3)} \quad (6.16b) \quad F(Q^2) = \frac{P(Q^2)}{P(Q^2) + P(Q^3)}$$

The single discrete particle model, however, may not correctly represent the true structural characteristics of the silica xerogels, since silica particles in xerogels may not be exactly spherical, and the model does not take into account any coordination between silica particles. However, given the errors in the experimental measurements more sophisticated structural models have not been used in this work. In calculating the fraction of isolated or geminal silanol groups, or  $Q^2$  and  $Q^3$  surface silicon sites, from single-pulse  $^{29}\text{Si}$  MAS NMR spectra, difficulties are encountered owing to the small intensity of the  $Q^2$  resonances, and the length of time required to obtain good spectra. These difficulties can be circumvented using  $^{29}\text{Si}$  CP MAS NMR techniques. (37,38)

### 6.7.3 $^{29}\text{Si}$ CP MAS NMR TECHNIQUES

In the  $^{29}\text{Si}$  CP MAS NMR experiment, since the silicon magnetisation is derived from the proton-spin reservoir, this technique discriminates in favour of those silicon nuclei near to protons (i.e. at the surface)<sup>(42)</sup> thereby giving enhancement of the  $Q^2$  and  $Q^3$  resonances predominantly. The technique also offers the advantage that owing to the short proton longitudinal relaxation times ( $T_1(^1\text{H}) < 1$  s), spectra with good signal to noise can be acquired in only a few hours.

The method initially proposed by Maciel and Sidorf<sup>(37,38)</sup> for determining the fraction of isolated ( $f_i$ ) and geminal ( $f_g$ ) silanol

FIGURE 6.18

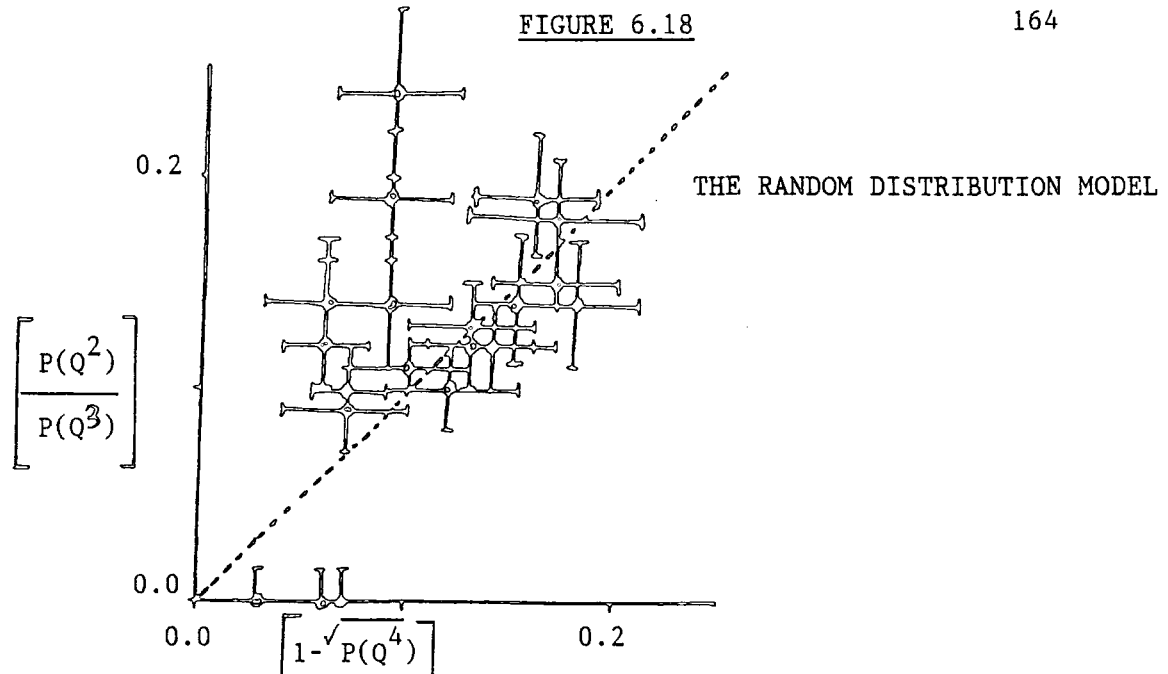


FIGURE 6.19

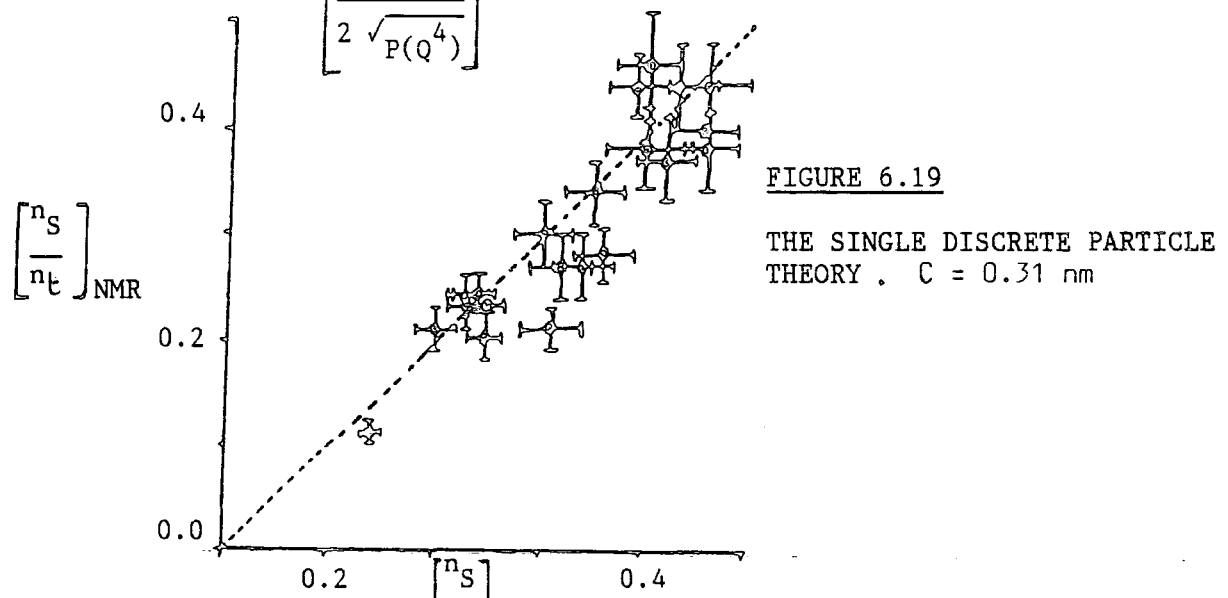
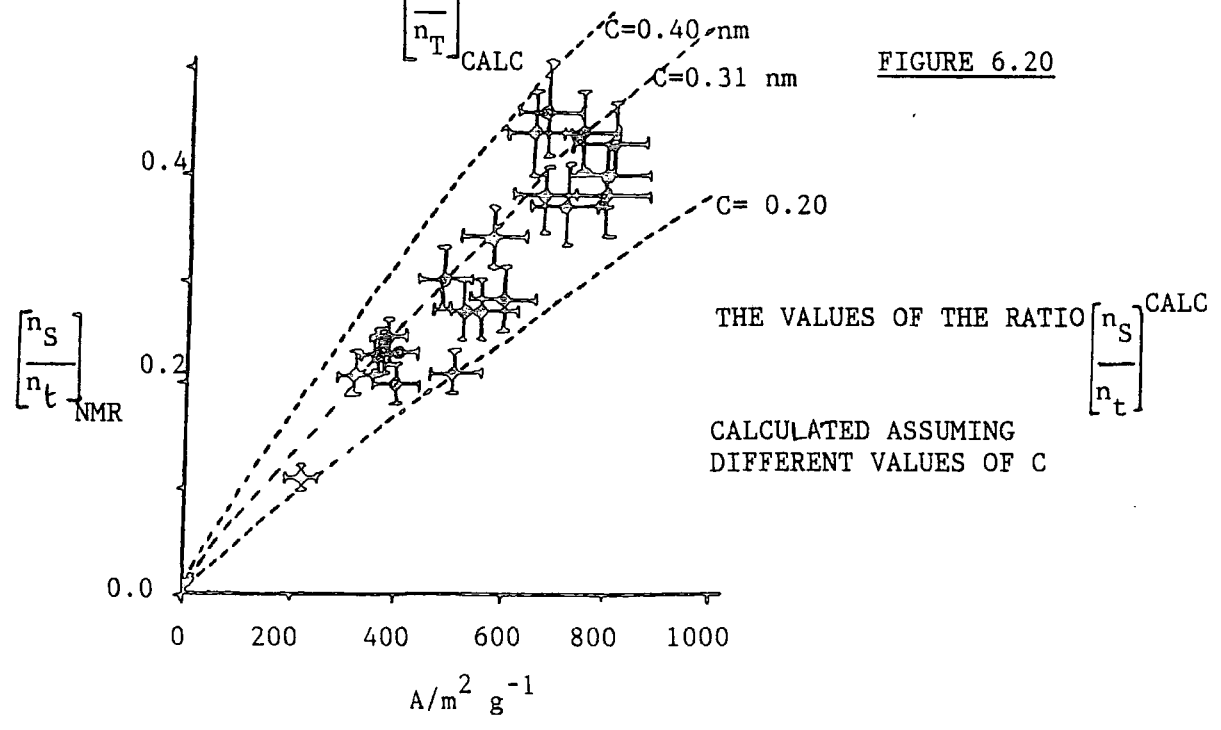


FIGURE 6.20



groups, relies upon the two types of surface silicon site exhibiting specific cross-polarisation dynamics. In order to see if this technique could be used for the xerogels studied in this work, it was necessary to examine the  $^{29}\text{Si}$  CP MAS NMR dynamics of a number of xerogels via variable contact-time experiments. The experimental variation of the signal intensity of the  $Q^2$ ,  $Q^3$  and  $Q^4$  peaks with contact time was measured. Using equation 4.1, values for the rate of cross-relaxation ( $T_{IS}^{-1}$ ) (when  $\alpha = 1.0$  and  $\omega_r = 3.3$  KHz), and proton relaxation in the rotating frame of reference, (in a spin locking field of 62.5 KHz) ( $T_{1\rho}^{-1}$ ) were determined. Proton longitudinal relaxation times (measured directly) for these systems never exceeded 0.4 s, therefore recycle times of 2 s were used for these experiments. Figure 6.21 shows a typical series of spectra for xerogel A4.0.0, obtained in a  $^{29}\text{Si}$  CP MAS NMR variable contact-time experiment. Figures 6.22, 6.23 and 6.24 show plots of the natural log of the signal intensity for each of the  $Q^n$  peaks, as a function of contact time, for a number of xerogels. The solid lines are the theoretical curves generated by equation 4.1, from which values of  $T_{IS}$  and  $T_{1\rho}$  were obtained. The results of these experiments are summarised in Table 6.3.

**TABLE 6.3**

XEROGEL	%H <sub>2</sub> O ( $\omega/\omega$ )	Q <sup>2</sup>		Q <sup>3</sup>		Q <sup>4</sup>	
		T <sub>IS</sub> /ms	T <sub>1ρ</sub> /ms	T <sub>IS</sub> /ms	T <sub>1ρ</sub> /ms	T <sub>IS</sub> /ms	T <sub>1ρ</sub> /ms
A4.0.0	8.3	1.5	13.9	2.5	15.6	8.0	29.0
S-TYPE(1) UNWASHED	28.0	2.9	>100	3.2	>100	10.5	>100
S-TYPE(1) DRIED	10.8	1.0	76.0	1.4	76.0	6.0	80.0

For all the xerogels studied, it was observed that  $Q^2$  units undergo cross-polarisation more readily than  $Q^3$  units, and  $Q^3$  units more readily than  $Q^4$  units. The results obtained are consistent with those published.<sup>(39)</sup> This trend reflects the proximity of the silicon atoms in the different  $Q^n$  environments to the proton spins. The results (summarized in Table 6.3) indicate that the values of  $T_{1\rho}$  for those protons that cross-polarize to the  $Q^2$  and  $Q^3$  units in a given xerogel, are the same within experimental <sup>error</sup>, and that  $T_{IS} \gg T_{1\rho}$ . Therefore, provided  $^{29}\text{Si}$  CP MAS NMR spectra are acquired under conditions where the contact time  $\gg T_{IS}$  ( $\approx 10$  ms), quantitative information concerning the fraction of isolated or geminal silanol groups, or surface silicon  $Q^2$  sites, can be obtained from direct intensity measurements of the  $Q^2$  and  $Q^3$  resonances. The values of  $f_g$  and  $f_i$  calculated, from  $^{29}\text{Si}$  CP MAS NMR spectra acquired under these conditions, are in good agreement with those measured from single-pulse  $^{29}\text{Si}$  MAS NMR spectra, in favourable cases. In unfavourable cases (i.e. where the intensity of the  $Q^2$  resonance in single-pulse spectra was difficult to measure), this technique was employed, in order to improve the accuracy of these measurements.

In considering Figures 6.21 and 6.22, it is seen for xerogel A4.0.0 that measurements of the proton  $T_{1\rho}$  values appear to suggest two proton environments, since the  $T_{1\rho}$  values measured for those proton that undergo cross-polarization to  $Q^4$  and,  $Q^2$  and  $Q^3$  environments are significantly different. However, by performing a delayed contact-time experiment as shown in Figure 6.25, the proton  $T_{1\rho}$  values for each of the  $Q^n$  environments may be calculated by measuring how the signal intensity of a given  $Q^n$  peak in the  $^{29}\text{Si}$  CP MAS NMR spectrum decays as the delay period ( $\tau$ ) is increased. The results indicate that the  $T_{1\rho}$  of the protons that undergo cross-polarization to the  $Q^2$ ,  $Q^3$  and  $Q^4$  environments are the same

$^{29}\text{Si}$  CP DATA SHOWING VARIATION OF SIGNAL INTENSITIES FOR EACH OF THE  $Q^n$  ENVIRONMENTS WITH CONTACT TIME  
XEROGEL A4.0.0

FIGURE 6.21

 $\omega_r = 3.2 \text{ kHz}$ 

NS = 2400

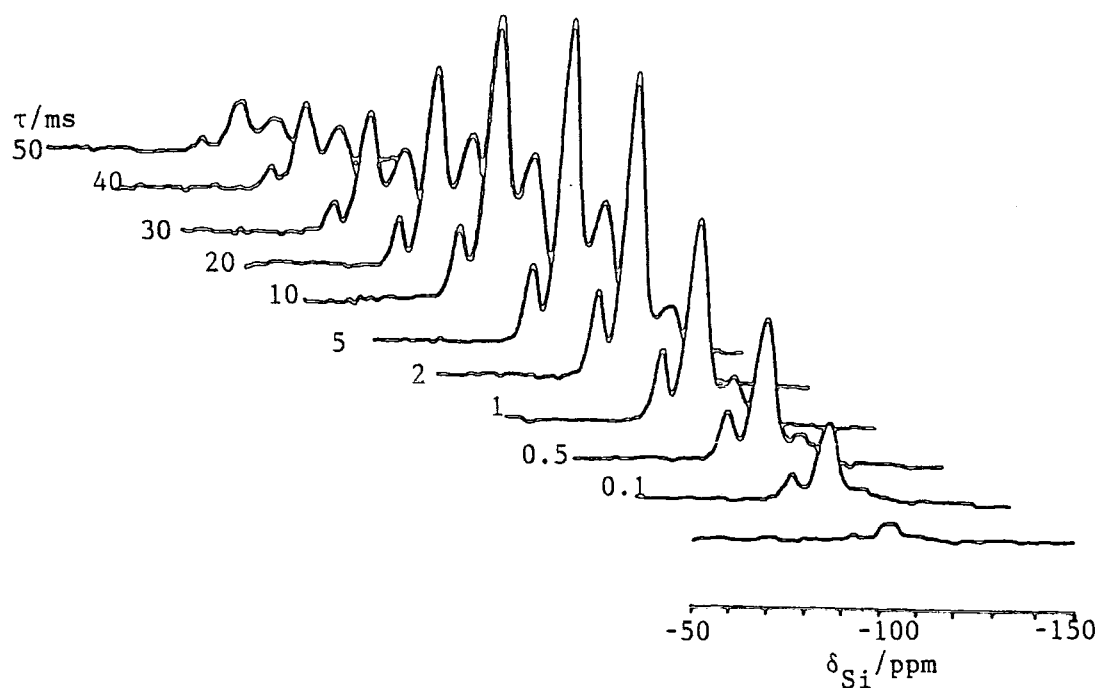


FIGURE 6.22

GRAPHICAL REPRESENTATION OF CP DATA FOR XEROGELS A 4.0.0  
(SOLID LINES CALCULATED FROM THEORETICAL EQUATIONS)

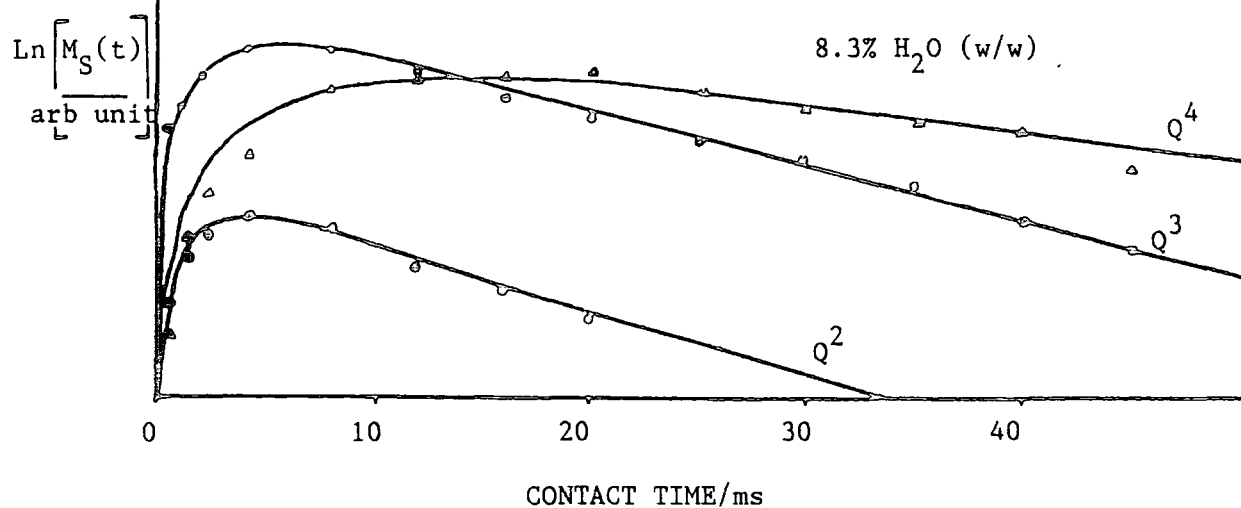


FIGURE 6.23

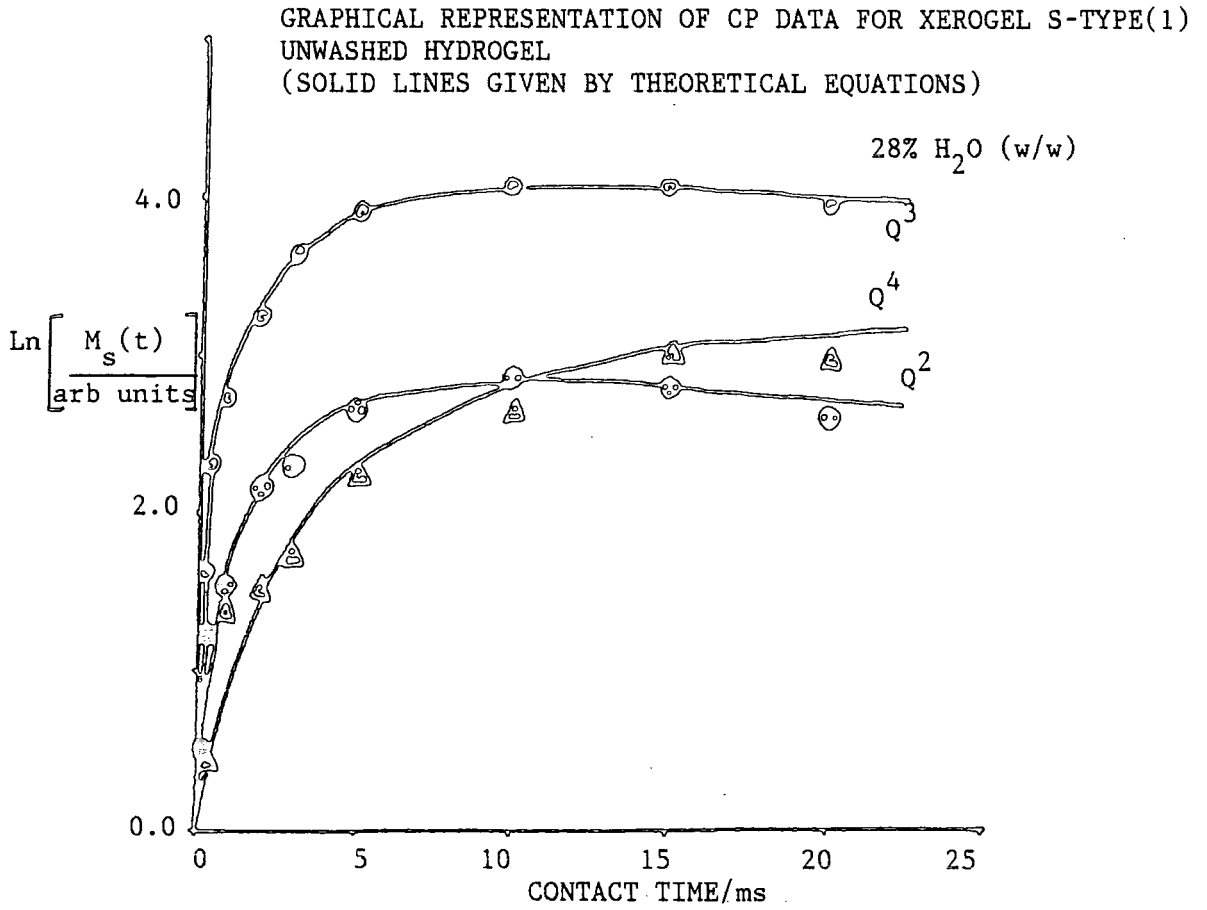


FIGURE 6.24

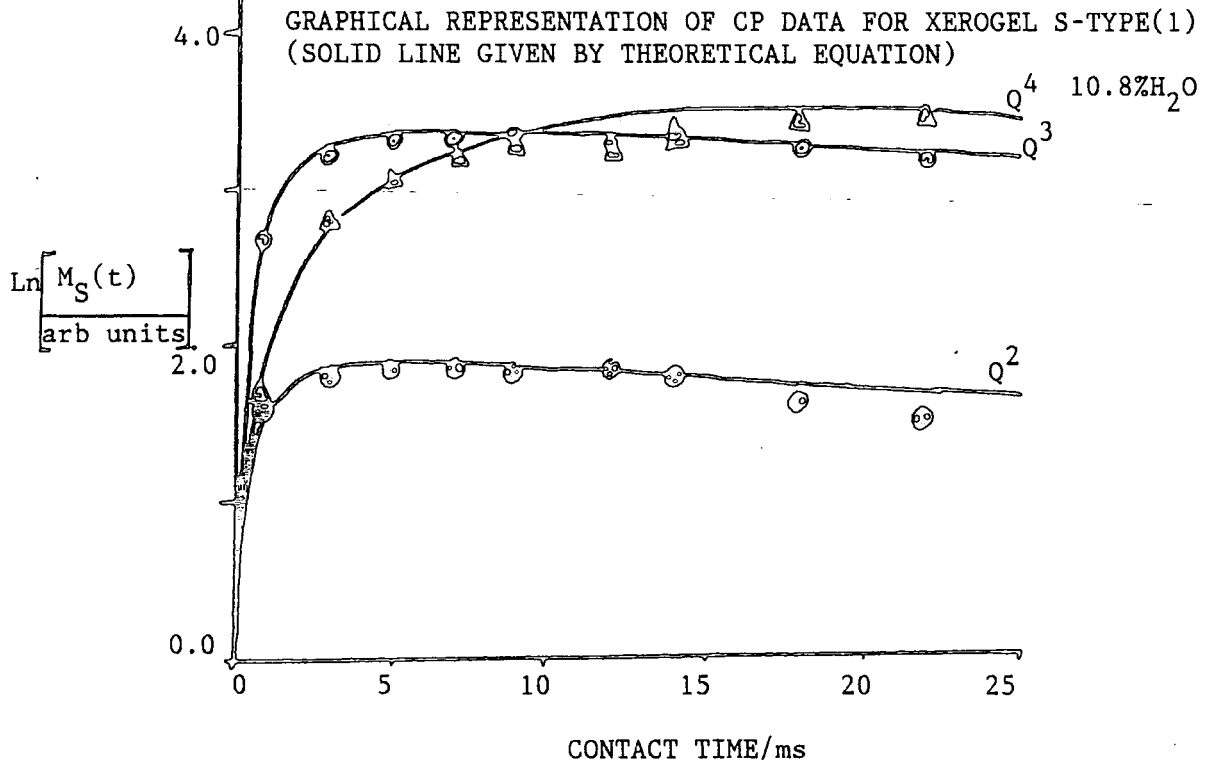


FIGURE 6.25

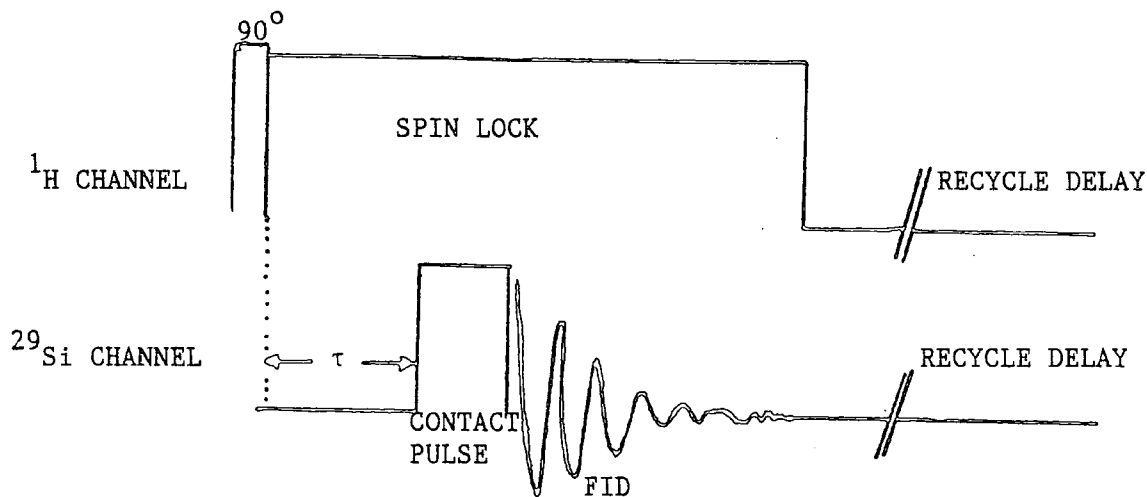
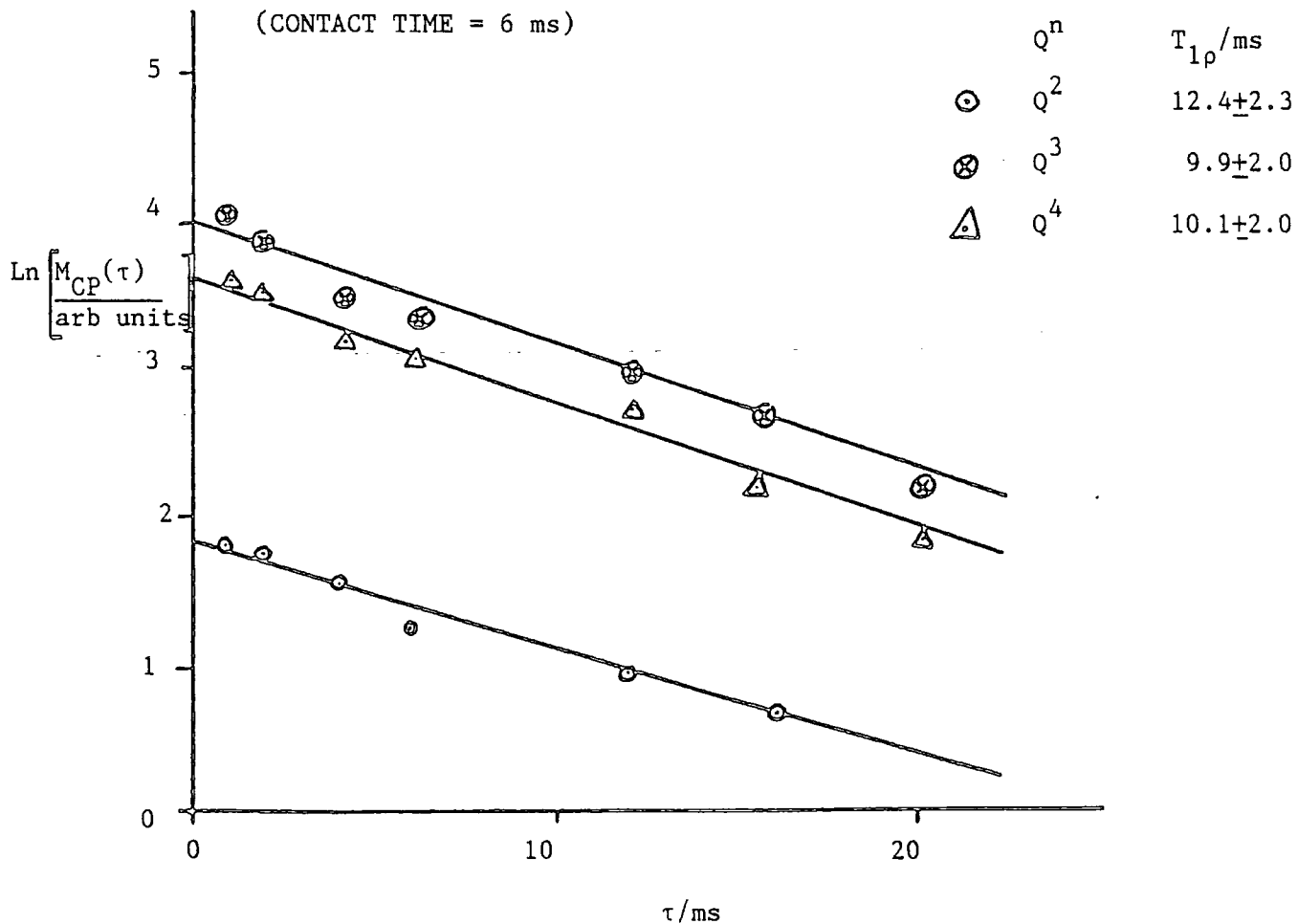


FIGURE 6.26

GRAPHICAL REPRESENTATION OF DATA OBTAINED FOR XEROGEL A4.0.0 USING THE DELAYED CONTACT TIME EXPERIMENT

(CONTACT TIME = 6 ms)



within experimental error (Figure 6.26). Therefore, it seems likely that the longer value of  $T_{1\rho}$  observed for the  $Q^4$  resonance in Figure 6.22 reflects a distribution of  $Q^4$  environments that undergo cross-polarization at slightly different rates.

It should be noted that while  $^{29}\text{Si}$  CP MAS NMR techniques may be employed to obtain quantitative information concerning the fraction of isolated and geminal silanol groups, quantitative information concerning the fraction of silicon atoms in  $Q^4$  environments cannot be obtained. The intensity of the  $Q^4$  resonance is very sensitive to the Hartmann-Hahn matching condition, and there is the possibility of the existence of  $Q^4$  sites which do not readily undergo cross-polarization. Examination of the data summarized in Table 6.3 suggests that the cross-polarization characteristics of a given xerogel are sensitive to the degree of hydration. This result is reasonable in view of the nature of the samples, however any comparison between  $T_{IS}$  values observed for a given peak for different xerogels is not really valid, since in these systems, the rate of cross-relaxation ( $T_{IS}^{-1}$ ) is extremely sensitive to the Hartmann-Hahn matching condition (see Chapter Four) and probe tuning characteristics, which will change for different samples.

In addition to  $^{29}\text{Si}$  CP MAS NMR spectra producing information concerning the surface structure of silica xerogels,  $^{29}\text{Si}$  CP MAS NMR measurements using the T1CP experiment (see Chapter Four) can also provide information concerning the  $^{29}\text{Si}$  longitudinal relaxation times of those silicon nuclei that undergo cross-polarization. This experiment offers the advantage that because the intensity of the  $Q^2$  and  $Q^3$  resonances are enhanced by CP, more accurate measurements of  $T_1(^{29}\text{Si})$  values for these resonances may be made, than in the more conventional progressive-saturation experiments. Figure 6.27 shows a typical series of spectra obtained for a xerogel using the T1CP

experiment. Figure 6.28 shows the experimental plot of the data obtained from this experiment from which  $T_1(^{29}\text{Si})$  values may be determined. The T1CP experiment has been performed upon a number of silica gels, together with direct measurements of the proton longitudinal relaxation times. The data obtained from these experiments are summarized in Table 6.4.

TABLE 6.4

XEROGEL	$\frac{[\text{Na}^+]}{\text{ppm}}$	CONTACT TIME/ms	$T_1(^{29}\text{Si})$			$T_1(^1\text{H})/\text{ms}$
			q <sup>2</sup>	q <sup>3</sup>	q <sup>4</sup>	
UNAGED						
A1.0.0	50	3.0	26.3±3.0	27.5±2.2	44.7±3.0	76.2
A1.0.0	50	20.0	-	29.4±6.0	46.7±3.0	76.2
AGED 2hrs						
A1.2.0	50	3.0	6.2±1.2	14.2±2.0	24.5±1.7	39.0
AGED 5hrs						
A1.5.0	50	3.0	6.0±1.1	10.7±1.7	9.8±1.4	36.6
A1.5.0	50	20.0	-	9.8±2.0	6.9±2.5	36.6
UNAGED						
A3.0.0	1560	8.0	17.3±2.7	27.5±2.7	59.2±4.0	61.8
AGED 0.3hrs						
A3.0.3	1560	3.0	11.5±1.3	15.3±1.5	26.9±3.2	53.1
AGED 2hrs						
A3.2.0	1560	3.0	11.5±2.5	14.2±1.5	25.2±3.0	43.3

+ Estimated error = 5%

In silica, it is known that ( $T_1(^{29}\text{Si})$ ) values are very sensitive to the water content or silanol group concentration.<sup>(44,50)</sup> It is interesting to note that there is a roughly linear correlation between  $T_1(^{29}\text{Si})^{-1}$  values and  $T_1(^1\text{H})^{-1}$  values for the xerogels studied (Figure 6.29). The rate of longitudinal relaxation for silicon sites that undergo cross-polarization is very sensitive to changes in the rate of

FIGURE 6.27

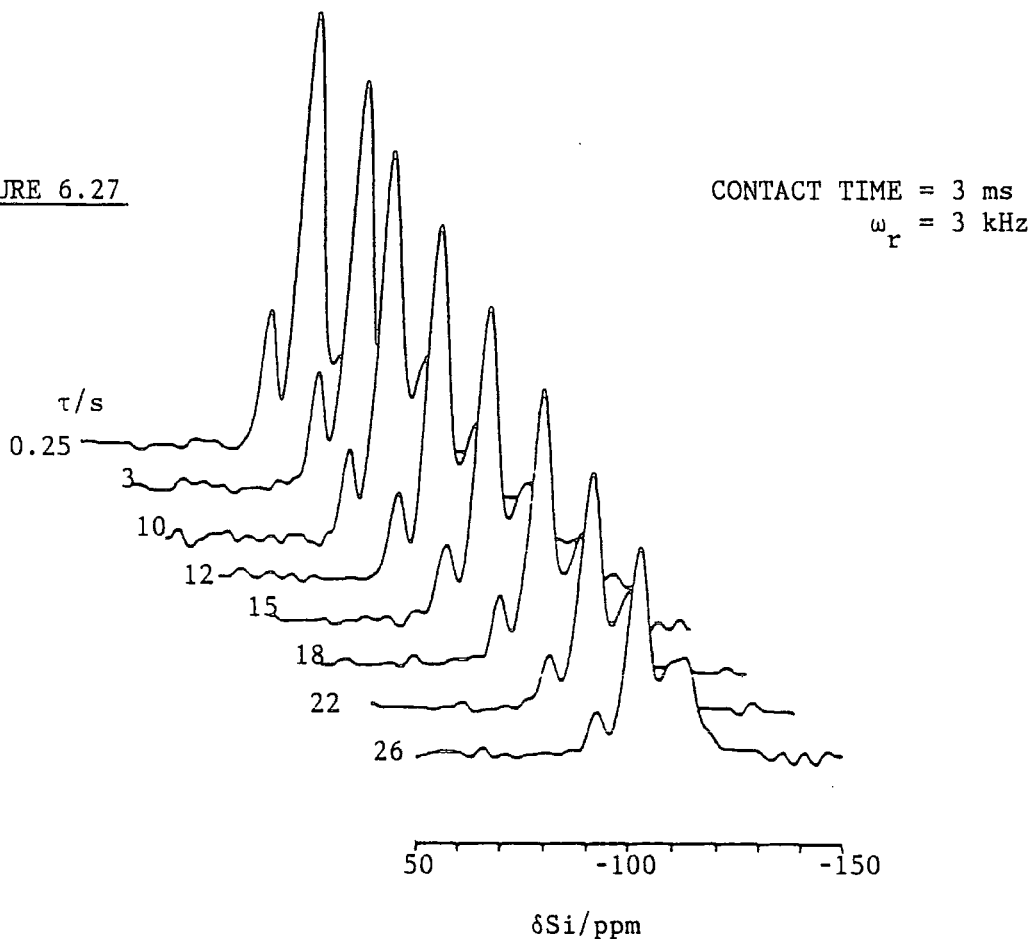


FIGURE 6.28

GRAPHICAL REPRESENTATION OF DATA OBTAINED  
T1CP EXPERIMENT

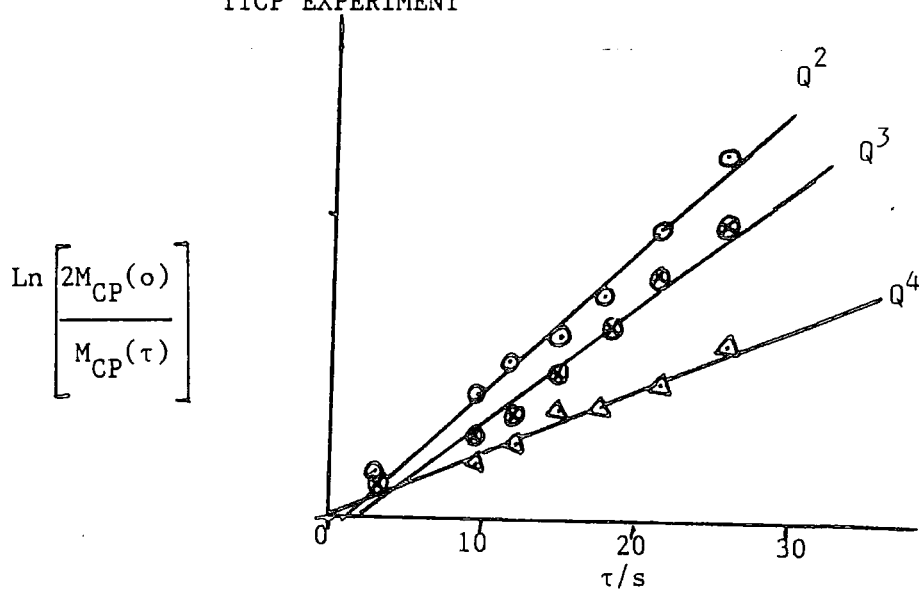
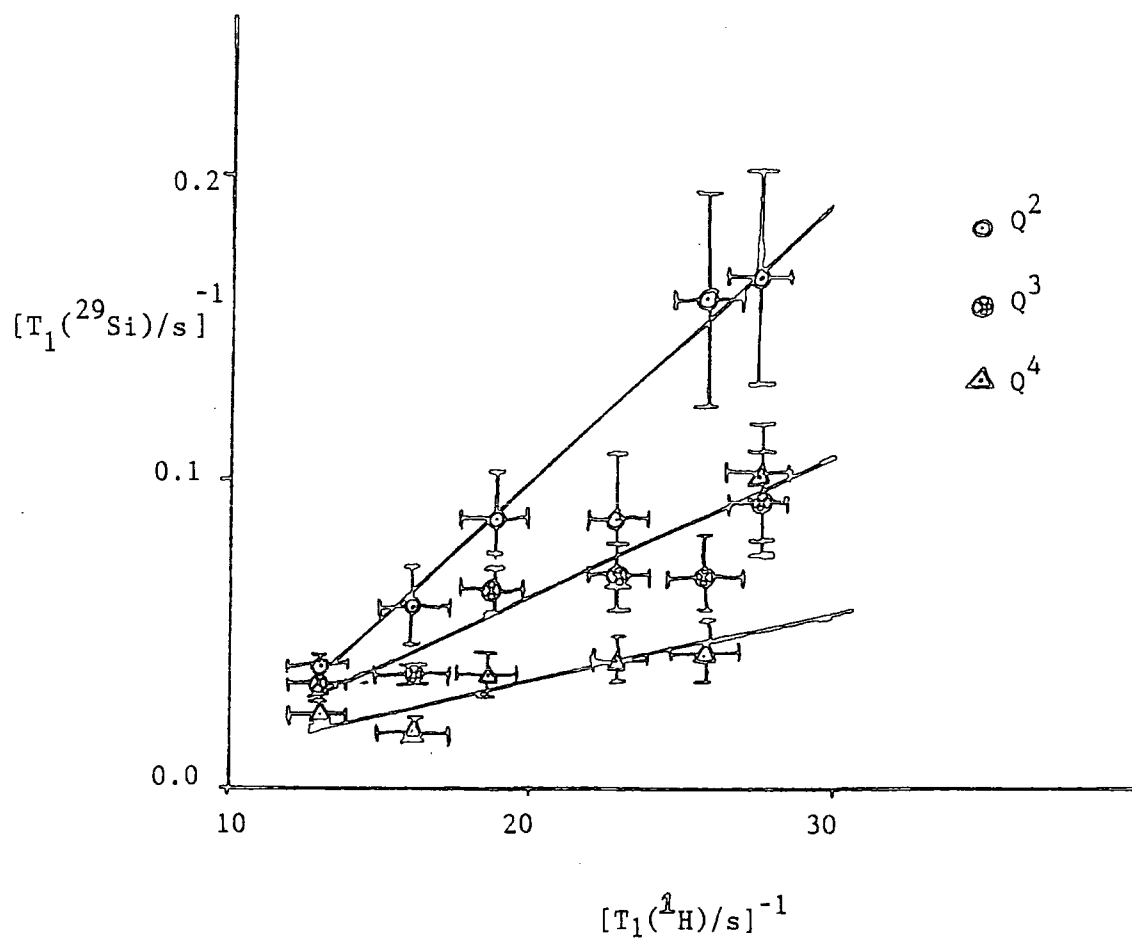


FIGURE 6.29

A PLOT SHOWING A ROUGHLY LINEAR CORRELATION BETWEEN  $T_1(^{29}\text{Si})^{-1}$  VALUES FOR SILICON ATOMS IN EACH OF THE THREE  $Q^n$  ENVIRONMENTS AND  $T_1(^1\text{H})^{-1}$  VALUES



proton longitudinal relaxation. However, the sensitivity of the  $T_1(^{29}\text{Si})$  values to changes in  $T_1(^1\text{H})$ , decreases upon going from  $Q^2$  to  $Q^4$ . These results indicate that the principal mechanism of  $^{29}\text{Si}$  longitudinal relaxation in silica xerogels is the  $^{29}\text{Si}$ - $^1\text{H}$  dipolar interaction. The decreasing sensitivity on going from  $Q^2$  to  $Q^4$  reflects the proximity of the silicon nuclei in these environments to protons. There is no significant change in the rate of  $^{29}\text{Si}$  longitudinal relaxation, for a given xerogel, as the contact time is increased. This observation suggests that the  $^{29}\text{Si}$  nuclei detected at different contact times experience the same heteronuclear ( $^{29}\text{Si}$ - $^1\text{H}$ ) dipolar interaction. This observation is surprising in view of Figure 6.22. However, given the errors in measuring  $T_1(^{29}\text{Si})$  values, the variable contact time/delayed contact time experiments are probably more sensitive tests as to whether there are silicon environments, assigned to a given  $Q^4$  unit, that undergo CP at different rates.

#### 6.7.4 $^1\text{H}$ CRAMPS STUDIES OF SILICA XEROGELS

In addition to using  $^{29}\text{Si}$  NMR techniques and proton relaxation measurements, in order to obtain information concerning the structure of silica surfaces,  $^1\text{H}$  CRAMPS has been shown to yield information concerning these systems. During the course of the authors own experiments on silica xerogels using this technique, two publications by Maciel et al have appeared in the literature.<sup>(35,36)</sup> The results outlined in this section are generally consistent with those published. However, there are subtle differences. This is not entirely unexpected, given that the exact form of any  $^1\text{H}$  CRAMPS spectrum of a xerogel is very sensitive to the degree of hydration and sample history.

##### 6.7.4.1 $^1\text{H}$ CRAMPS STUDIES OF SILICA XEROGEL S-TYPE(1)

Silica xerogel S-TYPE(1) is a commercial silica, produced by Crosfield Chemicals, with a surface area of  $800 \text{ m}^2 \text{ g}^{-1}$ . It is

typically used as a desiccant.

The static  $^1\text{H}$  single-pulse NMR spectrum of a hydrated sample of the xerogel (10.8%  $\text{H}_2\text{O}$ (w/w)) exhibits a single resonance with a linewidth of only 500 Hz (Figure 6.30). The observation of such a narrow linewidth indicates that within the sample, there is already substantial averaging of the  $^1\text{H}$ - $^1\text{H}$  homonuclear dipolar interaction as a consequence of molecular motion. The residual dipolar interaction is, however, still sufficiently large as to obscure valuable chemical information concerning the environments of the protons within the xerogel. Magic angle spinning (MAS) may be observed to yield spectra of improved resolution (Figure 6.31). The resolution, however, is still relatively poor, even when spinning at a rate of 4.2 KHz. Random molecular motion causes the dipolar interaction between proton spins to change independently of the time dependence imposed by MAS, thereby leading to broadening. The best resolution appears to be achieved using  $^1\text{H}$  CRAMPS (Figure 6.32). The improved resolution, is thought to arise as a consequence of the fact that, the time dependence imposed upon the homonuclear dipolar interaction by the multiple pulse sequence is more rapid than that imposed by MAS. As a result, the extent to which the dipolar interactions between spins may change independently of the imposed time dependence is less than in the case of MAS. For these systems, therefore, multiple pulse techniques are more efficient than MAS in averaging these interactions, provided  $t_c \ll \omega_r^{-1}$  ( $t_c$  = the cycle time = 24  $\mu\text{s}$ ).

The  $^1\text{H}$  CRAMPS spectrum of the xerogel sample after it has been heated in a fan oven at 220°C for several weeks (Figure 6.33), exhibits two resonances at 1.8 ppm and 2.2-2.6 ppm. The narrow peak at 1.8 ppm is assigned to non-acidic isolated surface groups.<sup>(35)</sup> The broader resonance at 2.2-2.6 ppm may arise from those silanol groups that undergo mutual hydrogen bonding, located either upon the surface,

$^1\text{H}$  CRAMPS SPECTRA OF SILICA XEROGEL S-TYPE(1)

(NS typically equals 64, RD = 5 s)

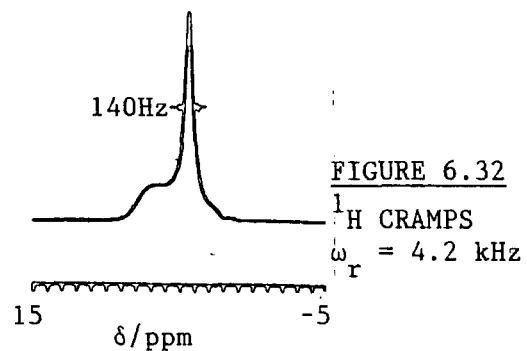
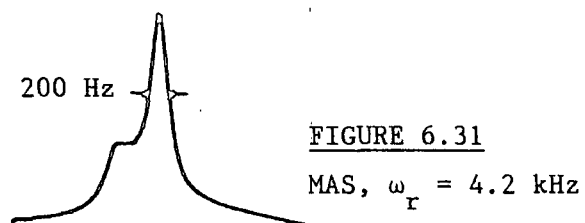
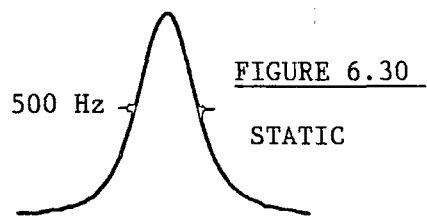


FIGURE 6.33  
DEHYDRATED IN OVEN AT 280°C  
FOR SEVERAL WEEKS



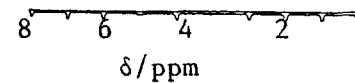
FIGURE 6.41  
EXPOSED TO WATER VAPOUR FOR  
<1 Hr



FIGURE 6.42  
EXPOSED TO WATER VAPOUR  
FOR 2 Hrs



FIGURE 6.43  
EXPOSED TO WATER VAPOUR FOR  
> 3 Hrs

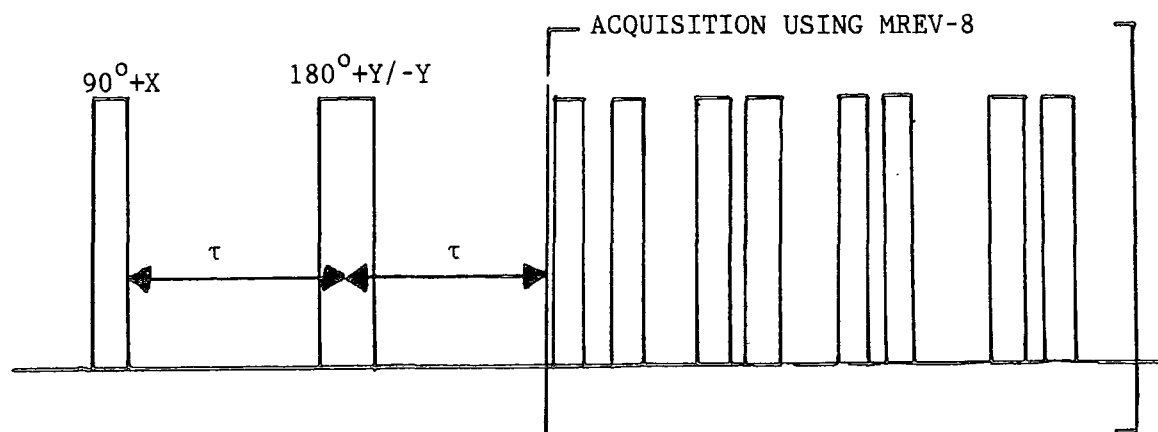


within micropores, or trapped beneath the surface of the siloxane network. However, given the fact that this xerogel is pretreated in the manufacturing operation by heating to  $500^{\circ}\text{C}$ ,<sup>(7)</sup> it seems unlikely that this sample will exhibit any marked degree of microporosity.<sup>(1)</sup> The origin of this broad signal was investigated by performing three experiments.

### (1) DIPOLAR DEPHASING EXPERIMENTS

In the dipolar dephasing experiment (used by Maciel et al<sup>(36)</sup>), shown in Figure 6.34, the proton magnetisation is initially rotated by a  $90^{\circ}$  pulse into the x,y plane, following which the spin isochromats dephase under the influence of the homonuclear dipolar and chemical shift interactions for a time period  $\tau$ . After this delay a  $180^{\circ}$  pulse causes the chemical shifts to be refocused after another  $\tau$  period. However, the dipolar interactions are not refocused. The proton signal is then detected using the CRAMPS technique. The intensity of any peak, detected in the resultant spectrum, will depend upon the extent to which those protons interact with other proton spins, causing dipolar dephasing during the time period  $2\tau$ .

FIGURE 6.34



The  $^1\text{H}$  CRAMPS spectra of the dehydrated xerogel using this pulse sequence, obtained at different values of  $\tau$ , are shown in Figure 6.35.

When  $\tau = 100 \mu\text{s}$ . the broad signal at 2.2-2.6 ppm was removed from the spectrum. This observation is consistent with that made by Maciel,<sup>(36)</sup> and suggests that the protons that give rise to this resonance experience strong homonuclear dipolar interactions, such as one might expect for silanol groups that undergo mutual hydrogen bonding.

### (2) DEUTERIUM EXCHANGE EXPERIMENTS

The  $^1\text{H}$  CRAMPS spectrum of the dehydrated silica xerogel after it was exposed to  $\text{D}_2\text{O}$  vapour for a week in a closed vessel, is shown in Figure 6.36. The spectrum exhibits a single weak signal at 4.6 ppm caused by HOD, formed as a consequence of chemical exchange. This spectrum indicates that all silanol groups are located in positions where exchange may occur. Therefore, there are no silanol groups trapped beneath the surface of the siloxane network in this sample.

### (3) DEHYDRATION STUDIES

The  $^1\text{H}$  CRAMPS spectra of the original sample of silica xerogel after it has been dehydrated under vacuum ( $10^{-3}$  Torr) at a number of different temperatures for 12 hours, are shown in Figure 6.37. It may be seen that as the temperature of dehydration is increased, so the intensity and width of the broad resonance at 2.2-3.0 ppm decreases relative to that caused by the isolated silanol groups. This observation is consistent with the broad resonance at 2.2-3.0 ppm being caused by those hydrogen bonded vicinal silanol groups, which are preferentially removed from the silica surface upon dehydration. Clearly, it is difficult to distinguish between the removal of hydrogen bonded water molecules and dehydroxylation of the silica surface. However, the  $^1\text{H}$  CRAMPS spectra do indicate that, dehydration at  $400^\circ\text{C}$  under vacuum is sufficient to remove both hydrogen bonded water and vicinal silanol groups, since no broad peak, at 2.2-3.0 ppm, can be detected at in the  $^1\text{H}$  CRAMPS spectrum of the sample treated in

FIGURE 6.35

## DIPOLAR DEPHASING EXPERIMENT

SAMPLE DEHYDRATED IN OVEN AT 220°C FOR  
SEVERAL WEEKS

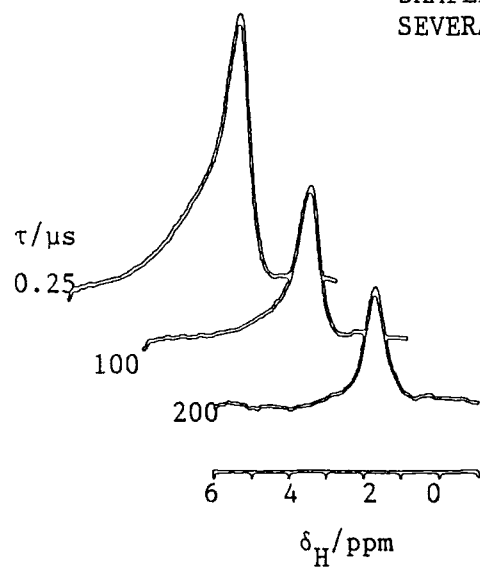
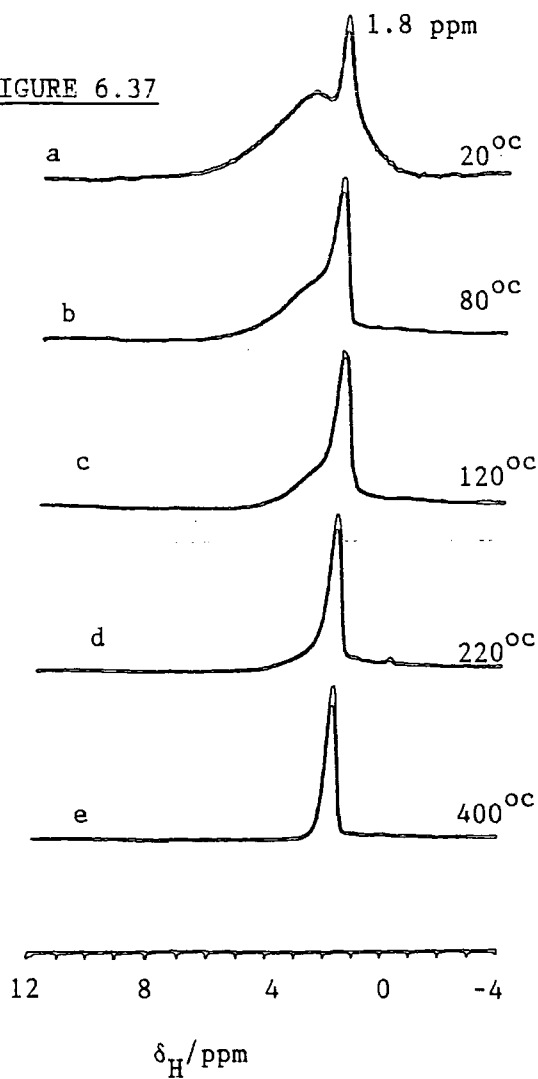


FIGURE 6.37

## DEHYDRATION EXPERIMENT

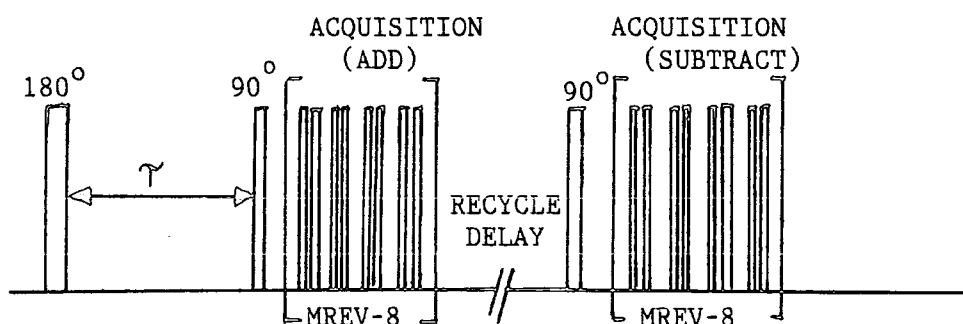
SAMPLES HEATED UNDER VACUUM  
( $10^{-3}$  TORR) FOR 12 Hrs



this way.

The proton longitudinal <sup>relaxation</sup> characteristics of the oven dehydrated sample of xerogel may be investigated <sup>by</sup> the pulse sequence shown in Figure 6.38. This pulse sequence involves the Freeman-Hill modification of the conventional inversion recovery experiment, <sup>(51)</sup> and <sup>1</sup>H CRAMPS to detect the resultant signal.

FIGURE 6.38



The experimental results (see Figures 6.39 and 6.40) indicate that, for this xerogel, the  $T_1(^1\text{H})$  values observed for the isolated and mutually hydrogen bonded silanol groups are different, being  $0.31 \pm 0.04\text{s}$  and  $0.13 \pm 0.04\text{s}$  respectively. This result indicates that any exchange between protons of these two environments is slow on the timescale of the measured  $T_1(^1\text{H})$  values.

This observation is not consistent with those of Maciel<sup>(36)</sup>, who observed that for Fisher S-679 silica, the peaks at 1.8 ppm and 2.2 ppm for a dehydrated sample exhibited the same  $T_1(^1\text{H})$  value. Therefore, caution is required when using direct measurements of  $T_1(^1\text{H})$  to determine the surface concentration of silanol groups, as with the technique initially proposed by Bermudez,<sup>(19)</sup> since this method relies upon all the silanol groups exhibiting common proton relaxation characteristics.

### REHYDRATION STUDIES

The process of rehydration of a sample of silica xerogel S-Type(1), after it had been dehydrated in a fan oven at  $220^\circ\text{C}$  for

FIGURE 6.39

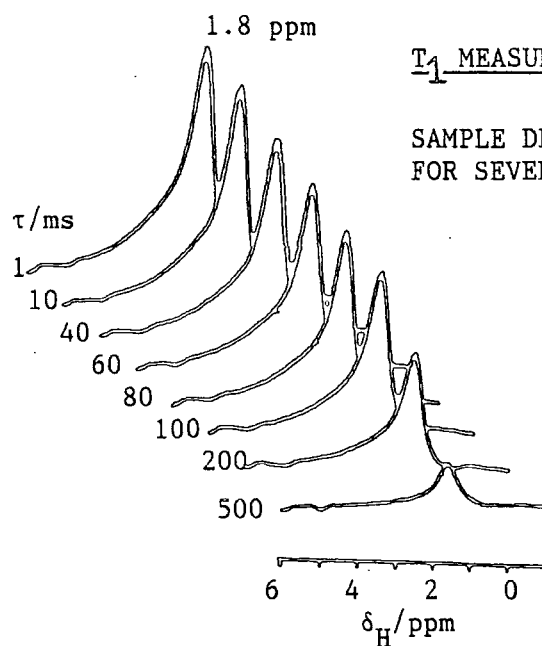
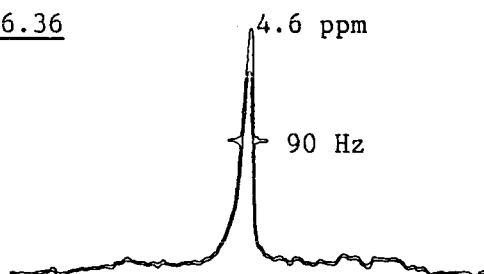
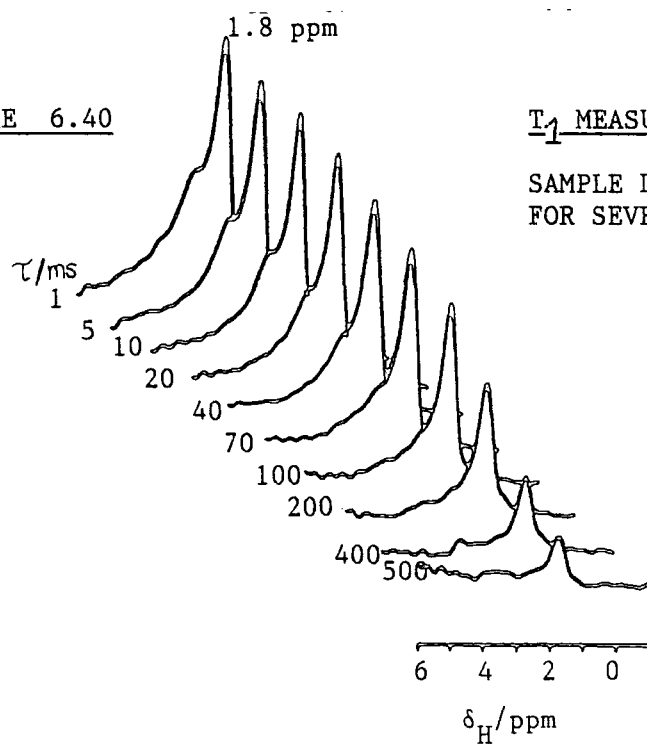


FIGURE 6.36

D<sub>2</sub>O EXCHANGE EXPERIMENT

SAMPLE EXPOSED TO D<sub>2</sub>O VAPOUR  
FOR ca 1 WEEK

FIGURE 6.40



several weeks, was monitored, by obtaining  $^1\text{H}$  CRAMPS spectra of the xerogel, as it was exposed to water vapour in a closed vessel at room temperature, for various periods of time.

Starting with the dehydrated xerogel, (Figure 6.33), as water molecules become adsorbed upon the surface of the silica, a new peak at 2.8-3.1 ppm emerges (Figure 6.41). With further exposure to water vapour, it increases in intensity relative to the resonance at 1.8ppm, and appears to move to higher frequency until it approaches the resonance frequency of protons in molecular water (Figures 6.42 and 6.43). In addition, there appears to be an increase in intensity and width of the broad underlying resonance(Figure 6.42).

Measurements of the proton longitudinal relaxation times of the xerogel during the initial stages of hydration (Figure 6.44, 6.45, 6.46, 6.47 and 6.48) indicate that, for the xerogel exposed to water vapour for less than 1 hour, the  $T_1(^1\text{H})$  value for the peak at 2.8-3.1 ppm is different from that of the isolated silanol group. The  $T_1(^1\text{H})$  values for the isolated silanol groups in these samples remain the same, within experimental error, to that observed in the original dehydrated sample. In Figure 6.47, as the delay time in the  $T_1(^1\text{H})$  experiment is increased, and the intensity of the resonances at 1.8 ppm and 3.1 ppm diminish, a third resonance emerges at 3.9 ppm (Figure 6.47a, 6.47b and 6.47c). These spectra suggest the existence of a second environment for adsorbed water molecules. Unfortunately, in spite of extensive efforts, it was not possible to reproduce this particular spectrum (Figure 6.47c) in subsequent experiments. The fact that this peak at 3.9 ppm emerges as  $\tau$  is increased, suggests that the protons in this environment have a  $T_1(^1\text{H})$  greater than that of the protons that give rise to the peak at 3.1 ppm, and that the rate of exchange between these proton environments is slow on the time scale of the  $^1\text{H}$  CRAMPS experiment.

FIGURE 6.44

 $T_1$  MEASUREMENT

SAMPLE WAS EXPOSED TO WATER VAPOUR FOR ca 15 minutes

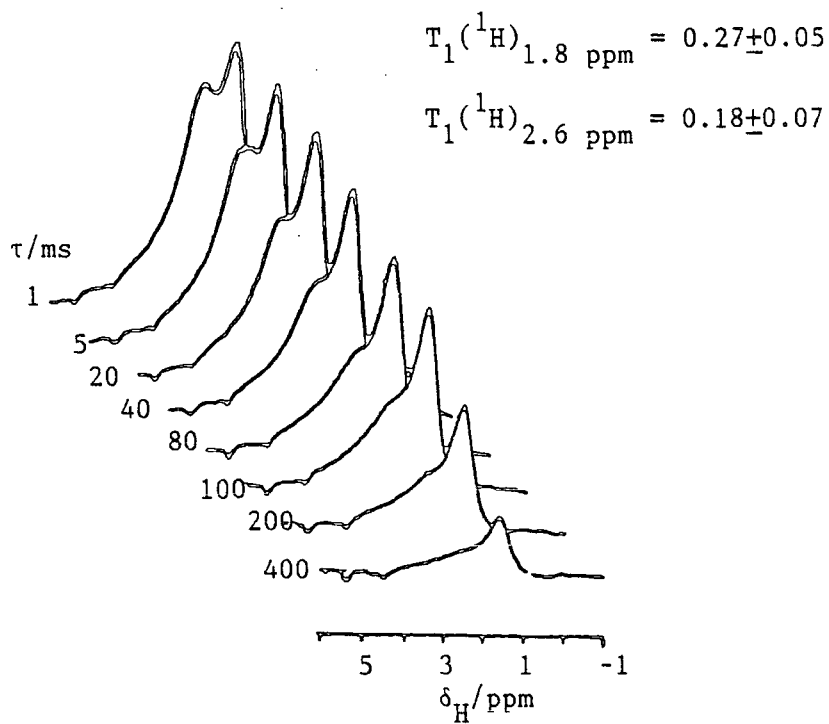
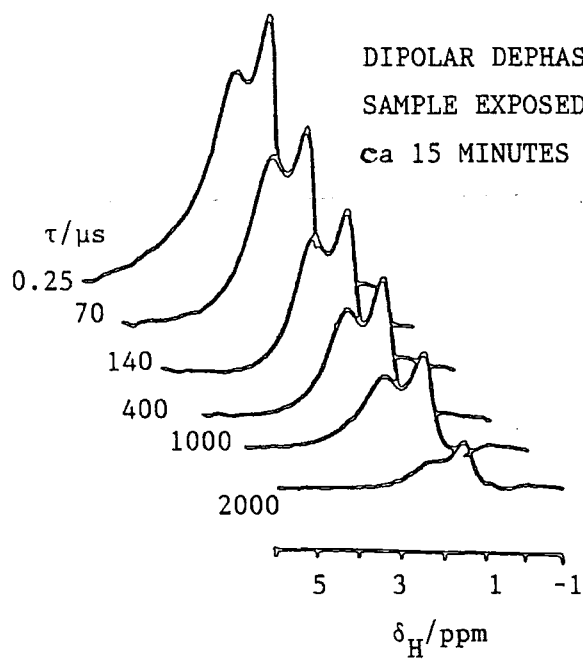


FIGURE 6.45

## DIPOLAR DEPHASING EXPERIMENT

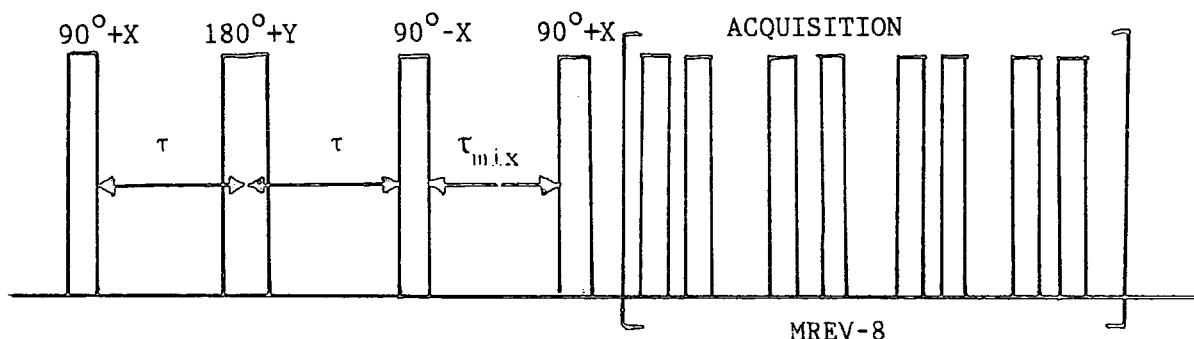
SAMPLE EXPOSED TO WATER VAPOUR FOR ca 15 MINUTES



Dipolar dephasing experiments performed upon the xerogel, after it has been exposed to water vapour for around 1<sup>1</sup>/<sub>2</sub> hours (Figure 6.49), confirm that the protons that give rise to the broad resonance, underlying the narrow peak at 3.1 ppm, experience strong dipolar interactions while the protons that give rise to the peaks at 1.8 ppm and 3.2 ppm undergo relatively weak dipolar interactions.

In the publication by Maciel et al<sup>(36)</sup>, a third type of <sup>1</sup>H CRAMPS relaxation experiment is suggested. This experiment is designed to show spin exchange directly. The pulse sequence is shown in Figure 6.50.

FIGURE 6.50



In this experiment, the proton magnetisation is rotated into the x,y plane by an initial  $90^\circ$  pulse. The spin isochromats then dephase under the influence of the dipolar interaction for a time period  $2\tau$ , in order to create differences between the intensity of those peaks caused by protons that experience different (<sup>1</sup>H-<sup>1</sup>H) dipolar interactions. The proton magnetisation is then "flipped back" parallel to  $B_0$ , where spin exchange occurs between the different proton environments during the mixing period ( $\tau_m$ ) prior to detection of the signal using <sup>1</sup>H CRAMPS.

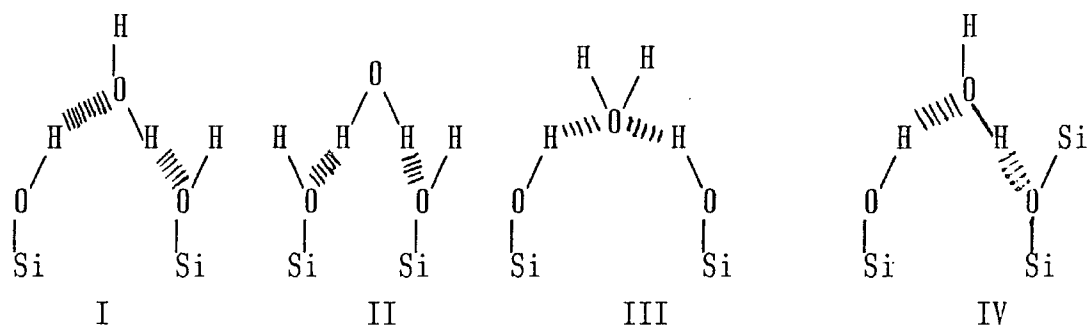
In the experiment shown in Figure 6.51, a dipolar dephasing delay of  $\tau = 2$  ms is employed in order to attenuate the intensities of the peak at 3.2 ppm and the underlying broader resonance. <sup>1</sup>H CRAMPS

spectra were then acquired at a number of different  $\tau_m$  times. Qualitatively, it may be seen from Figure 6.51, that there occurs little change in the relative intensity of the resonances at 1.8 ppm and 3.2 ppm, or growth in the intensity of the underlying broader resonance as the mixing time is increased to 10 ms, confirming that for this xerogel, at relatively low levels of hydration, the rate of spin exchange between the different proton environments is slow.

The peak at 2.8-3.1 ppm is assigned to physically adsorbed water molecules. During the initial stages of rehydration,  $T_1(^1\text{H})$  measurements (Figures 6.39, 6.40, 6.44, 6.46, and 6.47) indicate that  $T_1(^1\text{H})$  values for the isolated silanol groups (1.8 ppm) remain relatively constant. The apparent  $T_1(^1\text{H})$  value for physically adsorbed water (2.8-3.1 ppm) is very close to that observed for the broad peak assigned to mutually hydrogen bonded silanol groups or hydrogen bonded water (Figures 6.46, 6.47, 6.40 and 6.44).

These observations are not inconsistent with conclusions published by IR workers.<sup>(10)</sup> Water molecules are adsorbed preferentially at vicinal silanol sites, and form two hydrogen bonds to the surface,<sup>(22)</sup> giving rise to a number of possible surface structures (Figure 6.52). Further adsorption of water occurs at these sites, even before a complete monolayer forms. This process, therefore, leads to the formation of clusters of physically adsorbed water molecules. In the initial stages of rehydration the isolated or geminal silanol groups hardly participate in water adsorption. This may explain why  $T_1(^1\text{H})$  for the isolated groups, remains relatively constant during the initial stages of rehydration.

FIGURE 6.52



As the degree of hydration increases, however, it seems likely that water molecules will also become adsorbed upon isolated silanol groups to form the species shown in Figure 6.53. The peak at 3.9 ppm in Figure 6.47c is tentatively assigned to water molecules in this type of environment.

FIGURE 6.53



V

Clearly, one would expect the mobility of the protons in species like I to IV, to be significantly less than those in species like V, or isolated silanol groups. Therefore, water molecules of surface species like I to IV have protons that exhibit much shorter  $T_1(^1\text{H})$  values than protons in surface species like V or isolated silanol groups. If this assignment of the origin of the peak at 3.9 ppm is correct, then the observation of this type of water is going to be very sensitive to the degree of hydration, the surface concentration of silanol groups and sample history. This might explain the difficulties experienced in trying to reproduce Figure 6.47c.

The increase in intensity and width of the broad peak underlying the resonance at 3.2 ppm (Figures 6.41 and 6.42) with hydration is thought to be caused by the reaction of water molecules with strained siloxane bonds to regenerate vicinal silanol groups, and the formation of more hydrogen bonded water molecules.

As the level of hydration is increased further, the peak at 3.2 ppm, corresponding to physically adsorbed water, increases in intensity as more water molecules are adsorbed onto the surface, and moves to higher frequency (Figure 6.48). As it does so, so the mobility of the adsorbed water molecules increases and the  $T_1(^1\text{H})$  increases (Figure 6.54, 6.57 and 6.58).

Considering the  $^1\text{H}$  CRAMPS spectrum of the xerogel which has been exposed to water vapour for ca 2 hours, the spectrum is essentially dominated by the intense resonance at ca 3.1 ppm and the broad underlying peak (Figure 6.42). Once again, dipolar dephasing experiments (Figure 6.55), indicate that the protons that give rise to the broad underlying peak undergo mutual hydrogen bonding. It is also observed that at higher levels of hydration spin exchange occurs more readily. The spectra shown in Figure 6.56, obtained using the pulse sequence shown in Figure 6.50 employing a dipolar dephasing period of  $\tau_m = 5$  ms, reveal changes in the relative intensities of the resonances at 1.8 and 3.0 ppm. These interactions are caused by spin diffusion, rather than chemical exchange, since if chemical exchange caused this effect over a 5 ms time period one would not expect to resolve the two peaks in the  $^1\text{H}$  CRAMPS spectrum. However, it is surprising that in this experiment no growth in intensity of the broad underlying resonance can be detected (Figure 6.56). One explanation for this may be that water molecules are adsorbed preferentially upon other adsorbed water molecules, therefore, water clusters will form

FIGURE 6.46

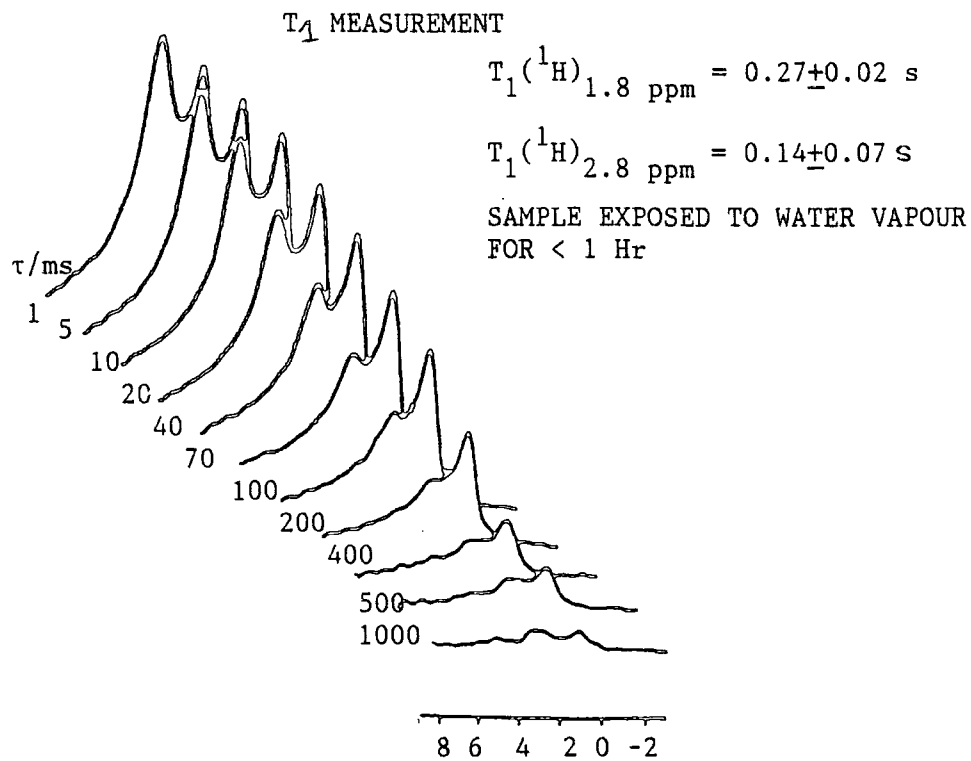


FIGURE 6.47a

$T_1$  MEASUREMENT  
SAMPLE EXPOSED TO WATER  
VAPOUR FOR < 1 Hr

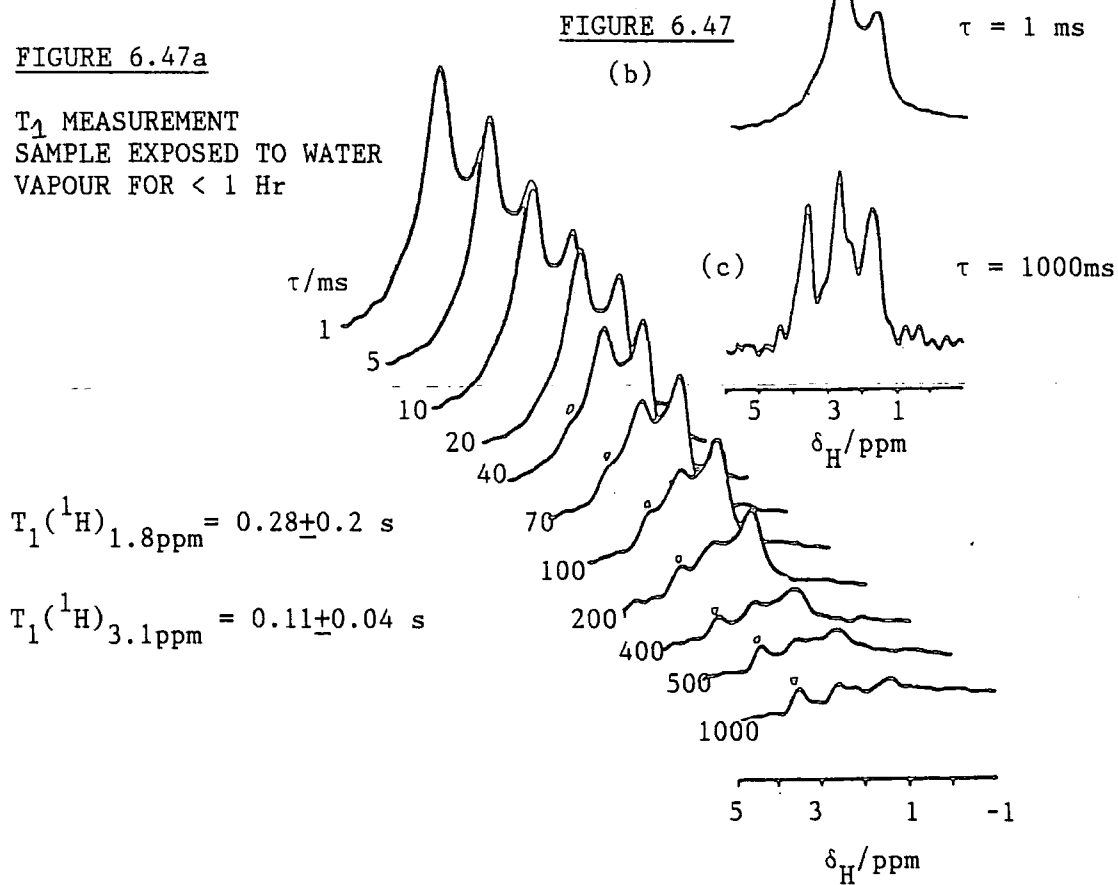


FIGURE 6.48  $T_1$  MEASUREMENT

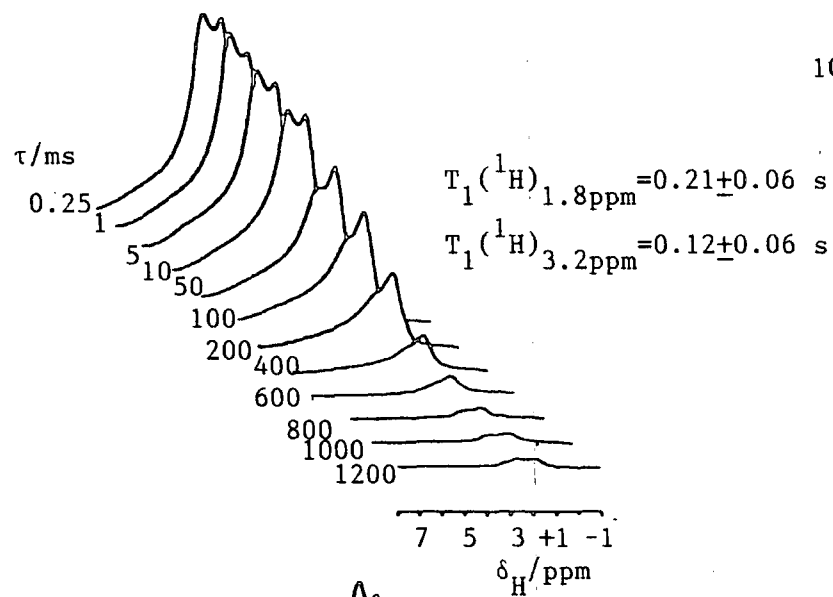
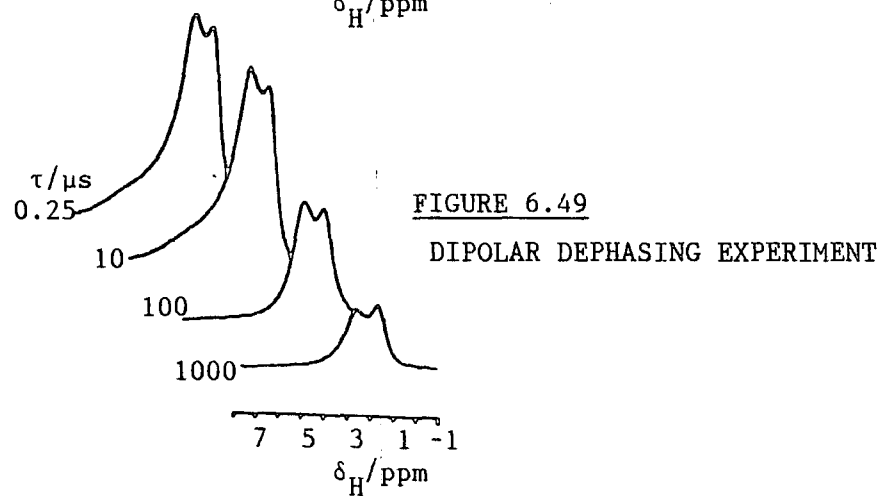
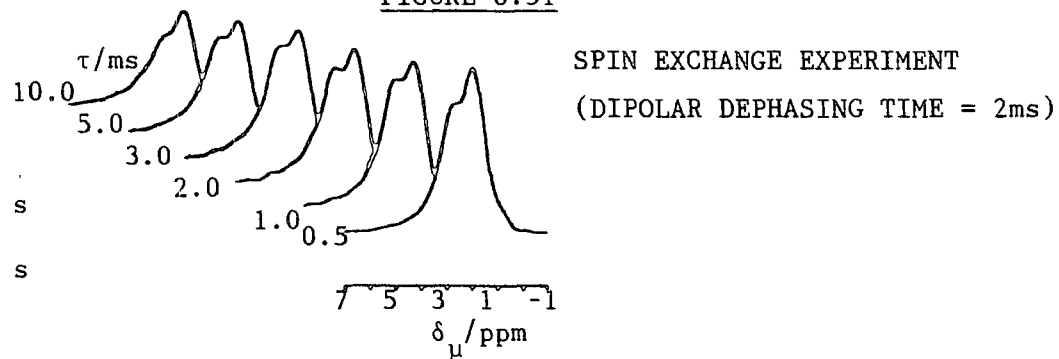


FIGURE 6.51



IN FIGURES 6.48, 6.49 and 6.51 THE SAMPLE WAS EXPOSED TO WATER VAPOUR FOR ca  $1\frac{1}{2}$  Hrs

FIGURE 6.54  $T_1$  MEASUREMENT

$$T_1(^1\text{H})_{3.1\text{ppm}} = 0.10 \pm 0.04 \text{ s}$$

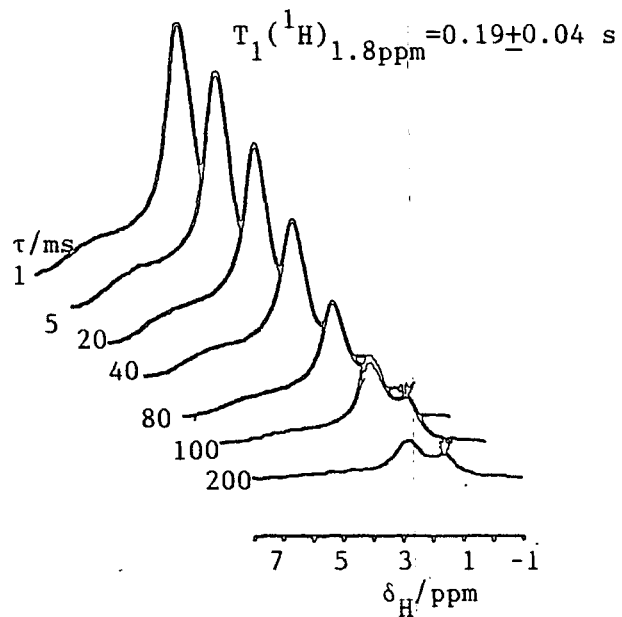


FIGURE 6.55

DIPOLAR DEPHASING EXPERIMENT

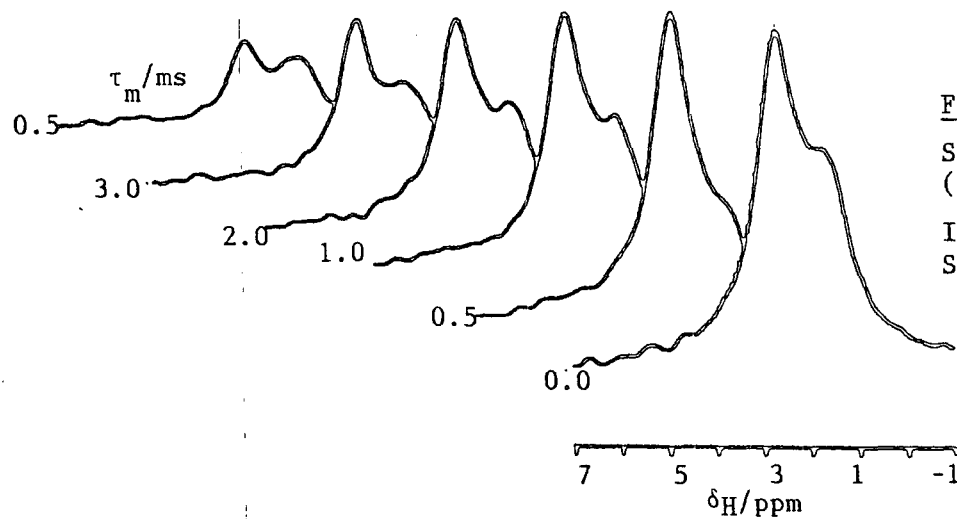
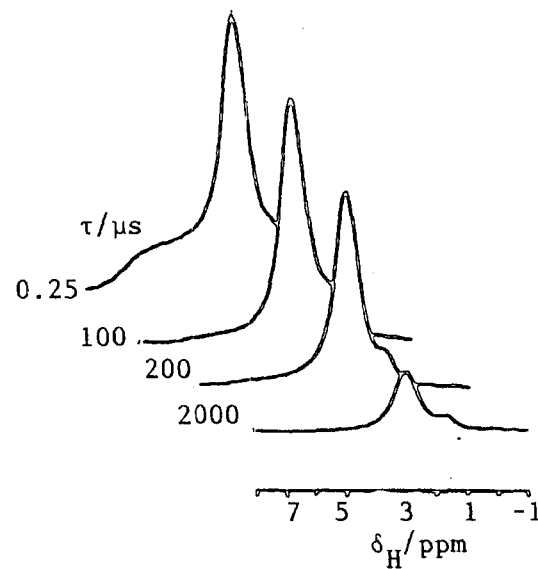


FIGURE 6.56

SPIN EXCHANGE EXPERIMENT  
(DIPOILAR DEPHASING TIME = 2 MS)

IN FIGURES 6.54, 6.55 and 6.56 THE  
SAMPLE WAS EXPOSED TO WATER FOR ca 2 Hrs

(and increase in size with hydration) at certain regions on the silica surface, while at other regions vicinal silanol groups and hydrogen bonded water molecules may occur, but no clusters of water molecules.

#### SUMMARY

$^1\text{H}$  CRAMPS may be employed to distinguish between various types of proton environments upon the surface of silica xerogels, and to investigate their relaxation characteristics. Measurements of the proton longitudinal relaxation characteristics of these systems are not inconsistent with the observations of other workers,<sup>(19,33,36)</sup> that in any non  $^1\text{H}$  CRAMPS  $T_1(^1\text{H})$  measurements, the  $T_1(^1\text{H})$  obtained will be determined by the population of each of the protons in those environments ( $T_i$ ), such that the value of  $T_1(^1\text{H})$  observed will be determined by an equation of the form

$$(6.17) \quad T_1(^1\text{H})^{-1} = \sum_i P_i T_{1i}^{-1}$$

As the level of hydration increases, and the proportion of adsorbed water increases relative to the silanol groups, the observed  $T_1(^1\text{H})$  value will decrease and there is an increase in the magnitude of the  $^{29}\text{Si}$ - $^1\text{H}$  heteronuclear dipolar interaction. This causes an increase in the rate of  $^{29}\text{Si}$  longitudinal relaxation (Figure 6.29).

### 6.7.5 TREATMENT OF SILICA XEROGELS

#### 6.7.5.1 WASHING AND DRYING

The effects of washing and drying silica xerogels, in different ways, upon the structure of the resultant xerogel has been investigated using  $^{29}\text{Si}$  MAS NMR techniques. In this study two types of silica xerogels were prepared as outlined in sections 6.61b and 6.61c. Samples of the xerogels were then washed with deionized water to pH3 or pH6, and dried, either oven dried at  $110^\circ\text{C}$  for at least 12 hours, or freeze dried using liquid nitrogen. The  $^{29}\text{Si}$  single pulse MAS NMR spectra of each sample was then obtained, under conditions such that the quantitative information concerning the fraction of

silicon atoms in each of the  $Q^n$  environments could be obtained. These data are summarised in Table 6.5 (also see Table 6.2).

TABLE 6.5

XEROGEL	$P(Q^2)$	$P(Q^3)$	$P(Q^4)$	$Q^{MEAN}$
S3.1 pH3 FREEZE DRIED	0.07	0.39	0.54	3.47
S3.2 pH3 OVEN DRIED	0.05	0.37	0.58	3.53
S3.3 pH6 FREEZE DRIED	0.04	0.38	0.58	3.54
S3.4 pH6 OVEN DRIED	0.03	0.32	0.65	3.62
G1.1 pH3 FREEZE DRIED	0.06	0.44	0.50	3.44
G1.2 pH3 OVEN DRIED	0.04	0.42	0.54	3.50
G1.3 pH6 FREEZE DRIED	0.07	0.28	0.65	3.53
G1.4 pH6 OVEN DRIED	0.05	0.27	0.68	3.63

+ errors in intensity measurements ca  $\pm 10\%$

The  $^{29}\text{Si}$  single pulse MAS NMR spectra are shown in Figure 6.59 and 6.60.

Both the S and G type silica xerogels are formed at low pH via the rapid addition of sodium silicate to sulphuric acid, and are composed of primary silica particles. As the hydrogels are washed with deionized water, in order to remove sodium sulphate and increase the pH of the hydrogel, the gel ages and the primary particles aggregate to form secondary and tertiary structures. The rate at which particles aggregate and siloxane bonds form (as a result of condensation reactions between the surface silanol groups,) increases as the pH of the hydrogel increases.<sup>(1)</sup> Therefore, the observation of a higher degree of connectivity for those xerogels washed to pH6 before drying than for xerogels washed to pH3 before drying is expected. The  $^{29}\text{Si}$  single pulse MAS NMR spectra of the various S-Type

FIGURE 6.57  $T_1$  MEASUREMENT

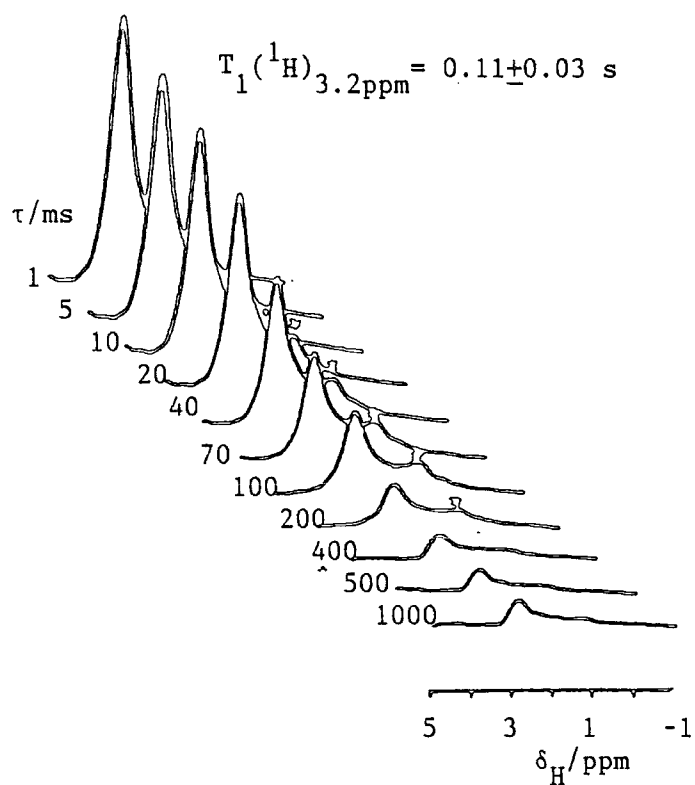
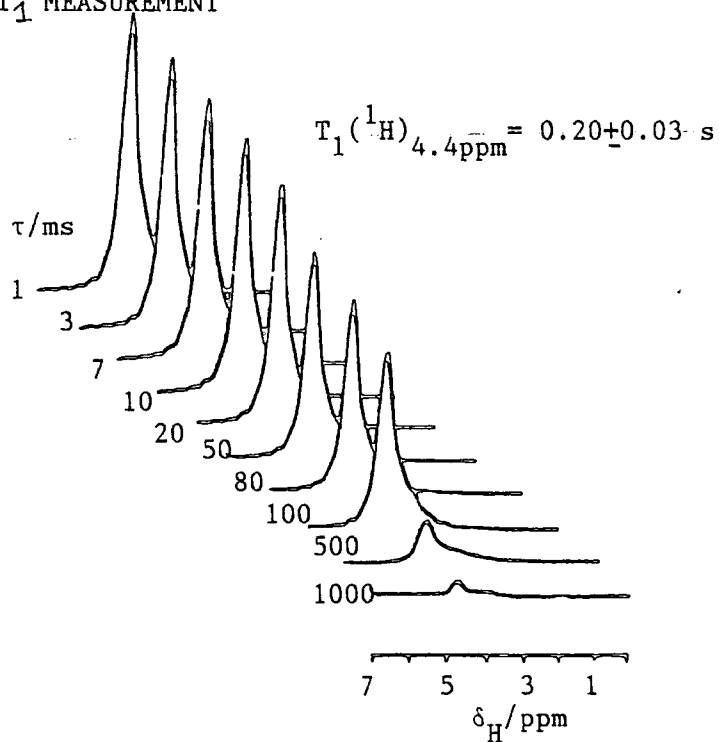


FIGURE 6.58

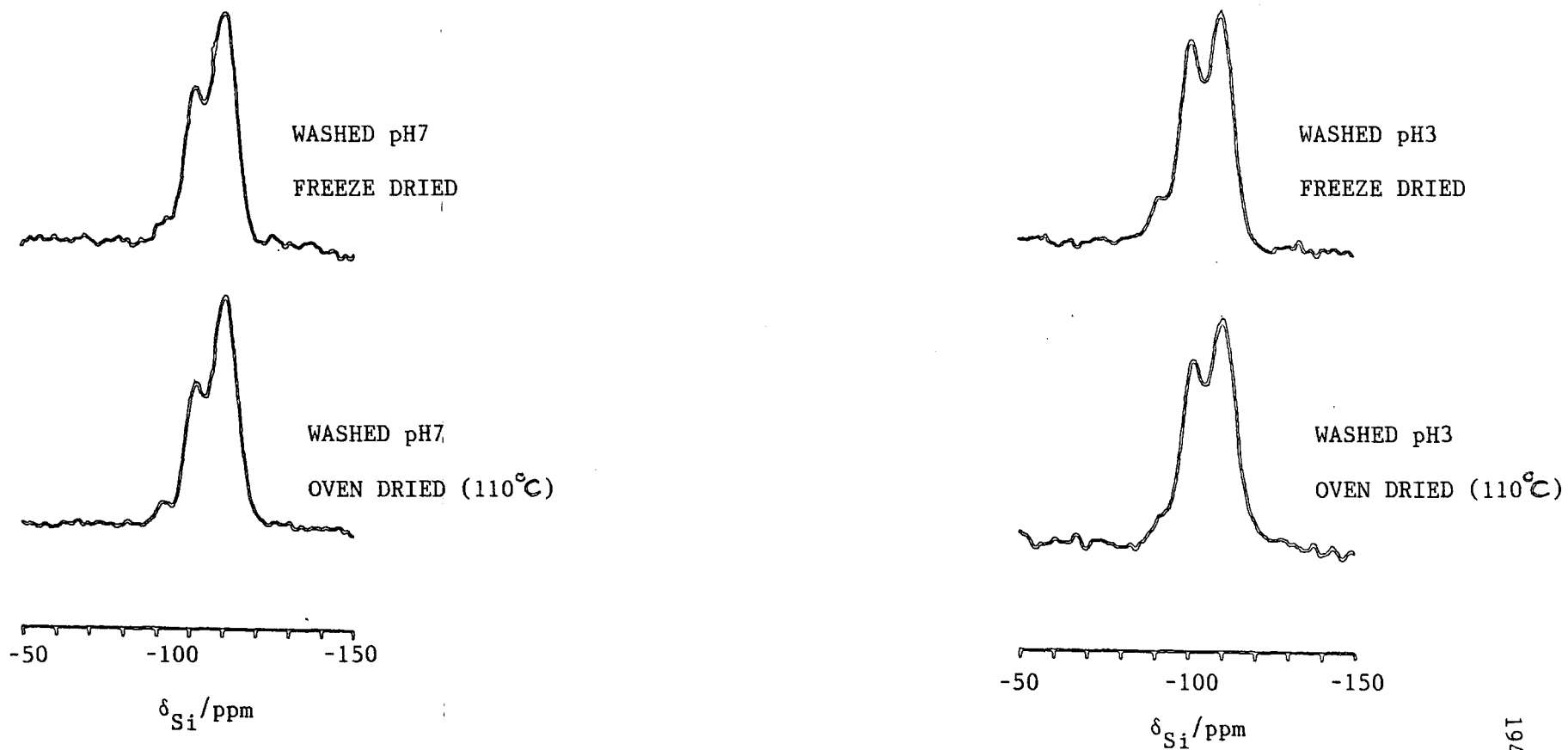
$T_1$  MEASUREMENT



IN FIGURES 6.57 and 6.58 SAMPLES WERE EXPOSED TO WATER VAPOUR FOR > 3 Hrs

FIGURE 6.59

$^{29}\text{Si}$  SINGLE PULSE MAS NMR SPECTRA OF SAMPLES OF SILICA XEROGEL S(3)



and G-Type silica xerogels (Figure 6.59 and 6.60) confirm these expectations. Furthermore, one would expect the average connectivity of the xerogel structure to increase with the severity of the drying process. Hence, one would expect a lower degree of connectivity for freeze dried xerogels rather than oven dried samples. This is in fact the case. There is no significant differences between the average degree of connectivity between S-Type and G-Type xerogels that have been treated in the same way.

#### 6.7.6 HYDROTHERMAL AGING

In the process of hydrothermal aging structural changes occur within the silica xerogel which give rise to modified surface and pore properties. These structural changes may be monitored using solid-state NMR techniques and characterisation of the physical properties of the xerogel (i.e. surface areas etc.).

In the literature, the influence of various anions upon the rate of hydrothermal aging has been described.<sup>(29)</sup> However, the role of the sodium ion in this process is at present ill defined.<sup>(29)</sup>

In this study, four silica xerogels of differing sodium content have been prepared, and hydrothermally aged at pH7 and 100°C in deionized water. Samples obtained after different stages of aging were analysed.

During the course of hydrothermal aging there occurs a simultaneous loss of surface area and increase in pore diameter. The rate at which surface area is lost with aging may be described by equation 6.18.<sup>(1,52)</sup>

$$(6.18) \quad \frac{-dA}{dt} = kA^n$$

The surface areas (measured by nitrogen adsorption) for each of the xerogels at different times of hydrothermal aging are shown in Figure 6.61, and from these data the relative rate constants for the

hydrothermal aging process, and the "order" of the reaction(s) with respect to surface area were determined for each of the xerogels. The results are summarised in Table 6.6

TABLE 6.6

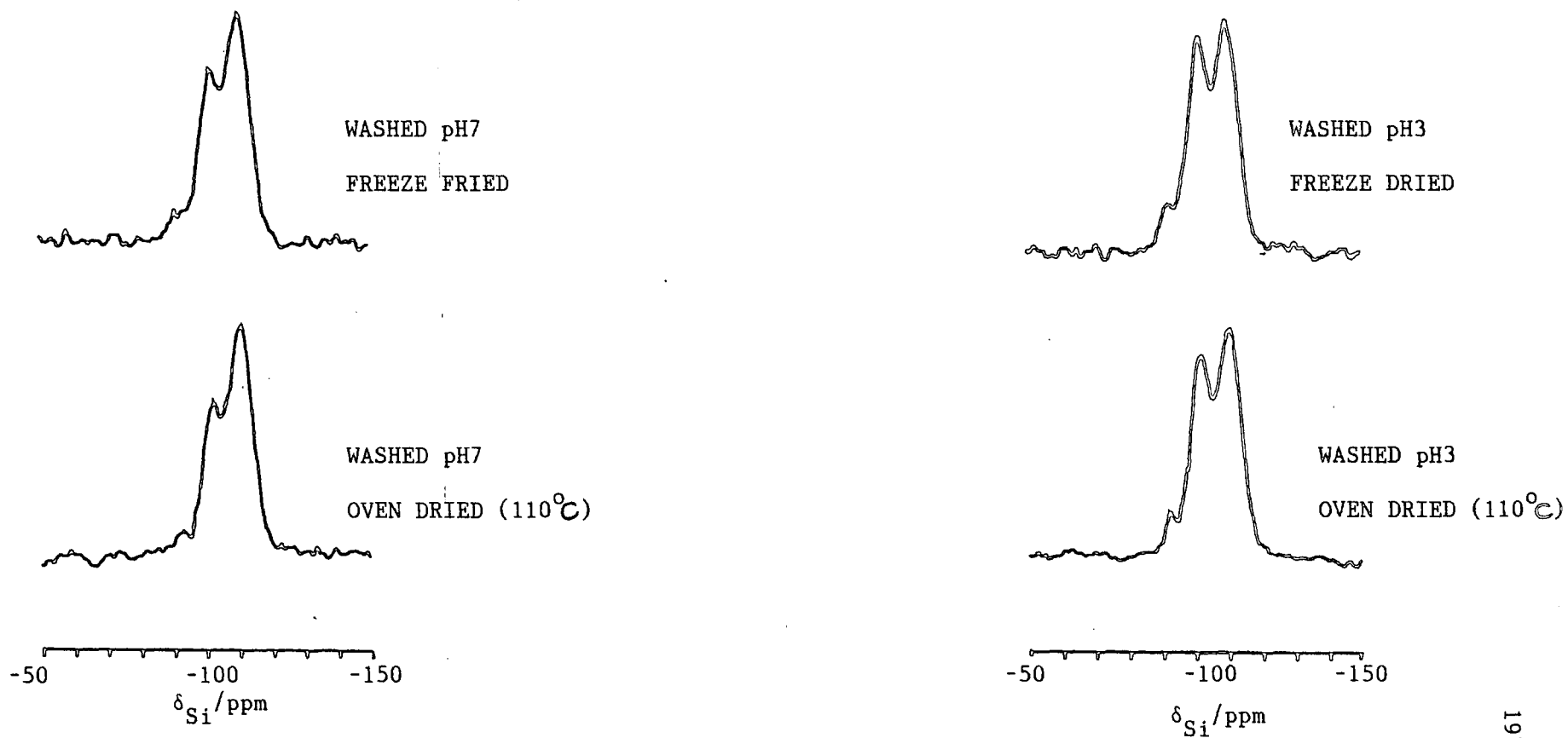
XEROGEL	[Na <sup>+</sup> ]/ppm	k <sub>rel</sub>	n
A1	50	1.0	8.0
A2	290	1.7	8.2
A3	1560	5.1	7.6
A4	5325	18.2	7.9

These results indicate that the rate of hydrothermal aging increases with sodium ion concentration. However, the order of the reaction(s) with respect to the surface area, remains relatively constant at  $7.9 \pm 0.3$ . This suggests that there is no distinguishable change in the mechanism of the reaction(s) with increasing sodium ion concentration. The "order" of the reaction(s) with respect to sodium ion concentration may be estimated as  $0.8 \pm 0.1$ . It may be argued that because of the way these xerogels were prepared, changes in the rate of surface area loss for xerogels A1 and A4 are only influenced by the presence of residual sodium sulphate in the gels. This argument, however, is not valid for xerogels A2 and A3, since the hydrogel batch prepared was split into two, to form hydrogels A2 and A3. These hydrogels will therefore contain the same amount of residual Na<sub>2</sub>SO<sub>4</sub>. Changes in the rate of hydrothermal aging may only be attributed to the presence of sodium ions.

Measurements of the average pore diameter (via mercury intrusion) indicate that, as the surface areas decrease there is an increase in the average pore diameter. A linear relationship exists between the

FIGURE 6.60

$^{29}\text{Si}$  SINGLE PULSE MAS NMR SPECTRA OF SAMPLES OF SILICA XEROGELS G(1)



average pore diameter ( $d_p$ /nm) and the average particle size, as calculated from surface area measurements using equation 6.1 (Figure 6.62). The anomalous point observed for xerogel A4 in Figure 6.62, corresponds to a measurement on the unaged xerogel A4, in which pore diameters are likely to be much smaller than the diameter of the mercury atoms. Figure 6.62 suggests that during the course of hydrothermal aging, the coordination number of the silica particles, forming the xerogel, remains essentially constant. Porosity measurements (via mercury intrusion) also support this conclusion. In the literature,<sup>(1)</sup> calculations have been made relating the coordination numbers of rigid spheres to porosity. Using the results of these calculations, it is possible to estimate the coordination numbers ( $n$ ) of the silica particles in xerogels, from the porosity measurements. This information is summarised in Table 6.7.

TABLE 6.7

TIME/HRS	POROSITY (cm <sup>3</sup> pores/cm <sup>3</sup> solid)		POROSITY (cm <sup>3</sup> pores/cm <sup>3</sup> solid)	
	XEROGEL A4		XEROGEL A1	
	[Na <sup>+</sup> ] = 5620 PPM	$n$	[Na <sup>+</sup> ] = 50 PPM	$n$
0.0	0.66	4.0	-	-
1.0	2.18	3.8	-	-
2.0	1.98	3.8	3.45	3.6
3.0	2.09	3.8	3.61	3.6
4.0	2.05	3.8	3.85	3.6
5.0	2.20	3.8	4.09	3.6

The porosity data suggests, that for the unaged sample of xerogel A4 the silica particles forming the xerogel exhibit an average coordination number of 4, and that with hydrothermal aging there is

only a slight decrease in coordination number, and that the coordination number of silica particles in xerogel A1 is slightly less than for xerogel A4 after the same aging time. In interpreting these results, however, considerable caution is required. It is possible that in the course of the measurement some damage of the original xerogel structure may occur,<sup>(1)</sup> owing to the high pressure required to force mercury atoms into the pores.

The apparent degree of hydration per unit area was determined from weight loss measurements, observed when samples of silica were heated to 1000°C. The samples were heated in a fan oven at 110°C overnight, prior to analysis. It is assumed in the calculations that the weight loss observed is caused by the condensation reactions of surface silanol groups. These measurements indicate that for xerogel A3 samples aged over 0.3 hours there is an increase in the apparent degree of hydration per unit area (Figure 6.63). Changes in the apparent degree of hydration with aging are much less defined, however, for xerogel A2. The reason why this should be the case is uncertain. However, what is clear from these results is that, firstly, after around 5 hours aging the apparent degree of hydration per nm<sup>2</sup> for xerogel A3 exceeds 7.0 OH nm<sup>2</sup>. Secondly, the degree of hydration per unit area is greatest for the xerogel with the highest sodium concentration.

In Figures 6.61 and 6.63 the observed increase in surface area and decrease in the apparent degree of hydration per unit area, for xerogels A2 and A3 upon aging from 0 to 0.3 hours, is not inconsistent with the hypothesis that upon hydrothermal aging particle growth occurs. This is because, if the silica particles that compose the xerogel are sufficiently small (i.e. ~ 1 nm in diameter), the observed surface area (A) is a fraction of the surface area of the spheres before they come together (A<sub>0</sub>).<sup>(1)</sup>

FIGURE 6.61

GRAPH SHOWING SURFACE AREA AS HYDROGEL IS HYDROTHERMALLY AGED AT pH7 and 100°C

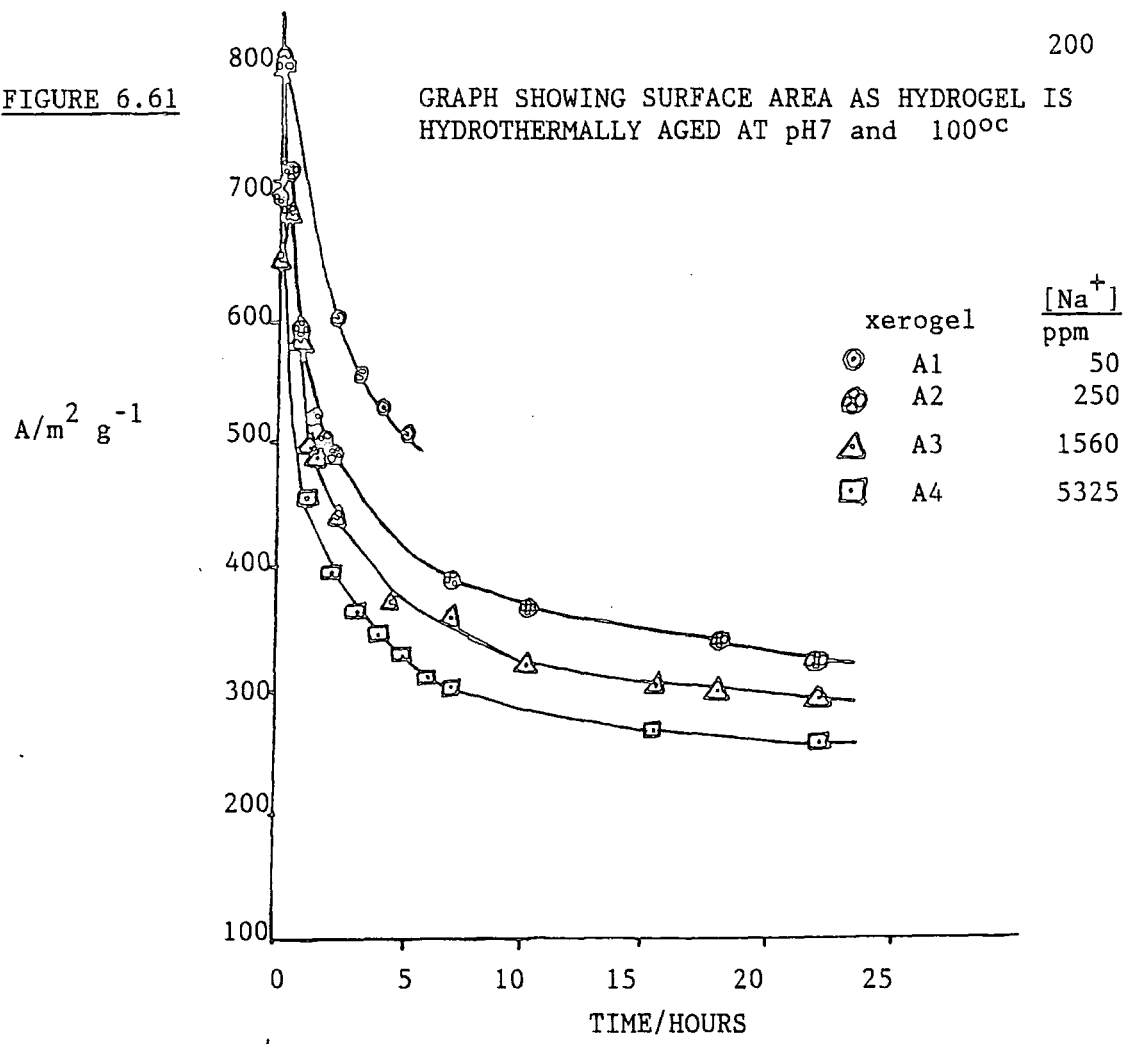
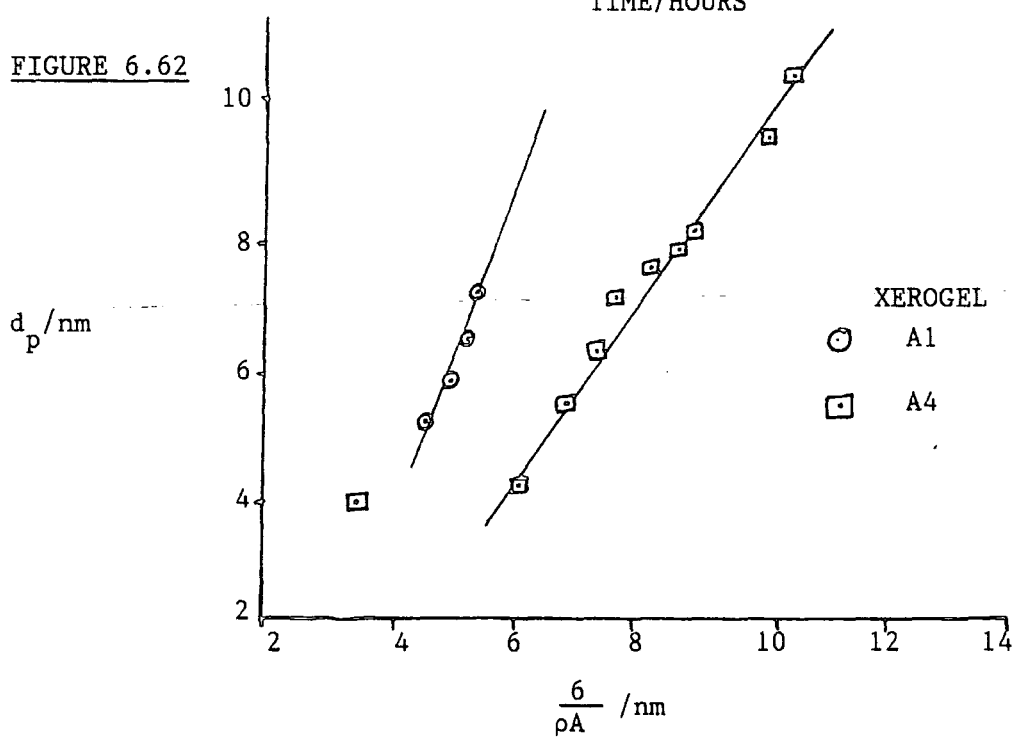


FIGURE 6.62



GRAPH DEMONSTRATING LINEAR RELATIONSHIP BETWEEN PORE DIAMETER AND PARTICLE DIAMETER

$$(6.19) \quad A = A_0 \left[ \frac{1 - an(d_0 + a)}{d_0^2} \right]$$

Where  $d_0$  is the diameter of the spheres,  $n$  is the coordination number and  $a$  is the diameter of the nitrogen molecule ( $a = 0.177$  nm).<sup>(1)</sup>

This situation occurs because surface area is lost to the nitrogen molecules at the point of contact between particles. Calculations using equation 6.19 suggest, provided the coordination number of particles in the unaged xerogel is greater than 3, particle growth causes an initial increase in the observed surface area, up to a maximum surface area after which further particle growth causes the observed surface area to fall.

In summary, measurements of the physical properties of the silica xerogels, obtained at different stages of hydrothermal aging, are consistent with the results published in the literature. In addition, the presence of sodium ions in the xerogel appears to influence the process of hydrothermal aging.

#### 6.7.6.1 SOLID-STATE NMR MEASUREMENTS

The loss of surface area with hydrothermal aging (Figure 6.61) is accompanied by an increase in the average degree of connectivity ( $Q$ ) and a decrease in the ratio  $\left[ \frac{n_s}{n_t} \right]$  as determined by <sup>29</sup>Single-pulse MAS NMR measurements. In a plot of  $\left[ \frac{n_s}{n_t} \right]_{\text{nmr}}$  against time (Figure 6.64), no significant differences between xerogels, in the rate at which this ratio decreases with time is observed. However, there appear to be significant differences in how the surface structure of the different xerogels change with aging (Figure 6.65). From Figure 6.65, it would appear that, the fraction of surface silicon  $Q^2$  sites ( $F(Q^2)$ ) is greatest for the xerogel with the lowest sodium ion concentration ( $[Na^+] = 50$  ppm) after ca. 1 hours aging.  $F(Q^2)$  then

FIGURE 6.63

GRAPH SHOWING CHANGE IN DEGREE OF HYDRATION PER UNIT AREA WITH  
HYDROTHERMAL AGING. pH7 100°C

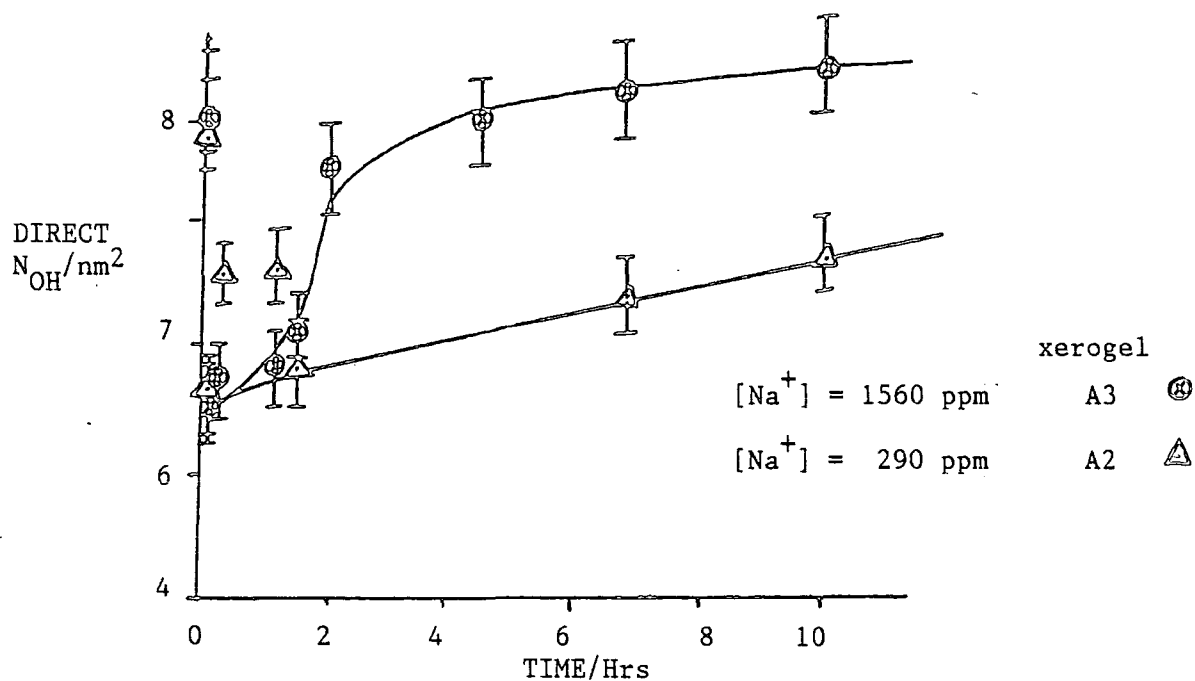
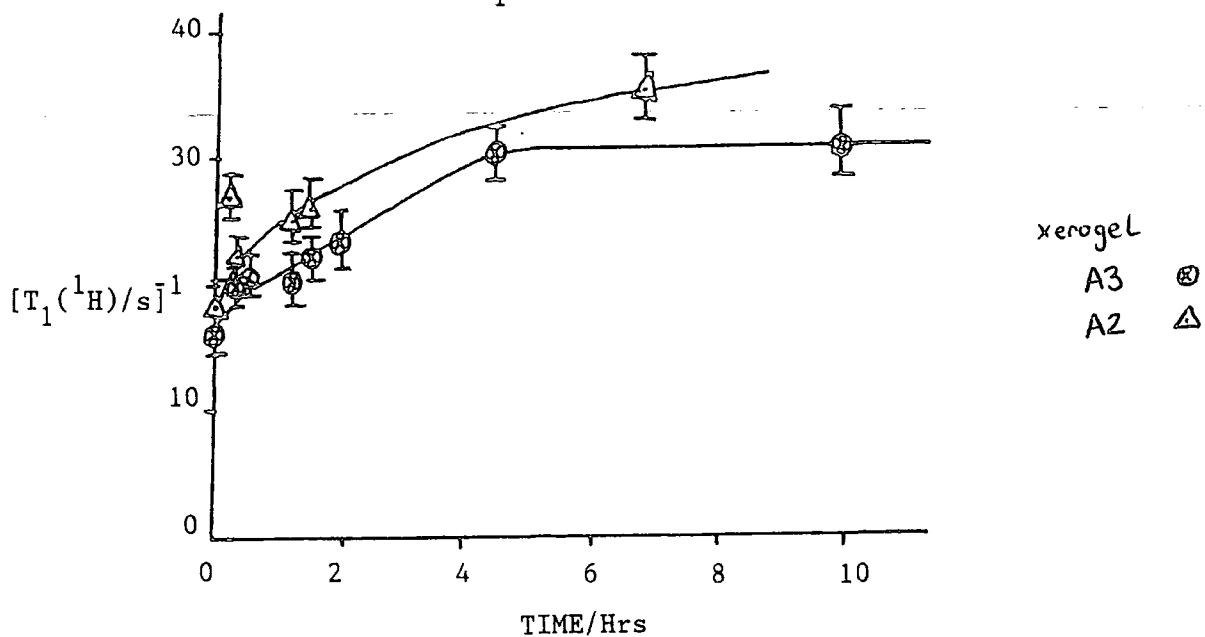


FIGURE 6.67

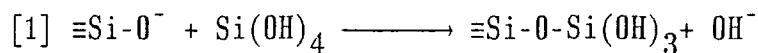
GRAPH SHOWING CHANGE IN  $T_1(^1H)^{-1}$  VALUES WITH HYDROTHERMAL AGING. pH7 100°C



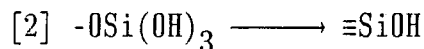
appears to decrease to ca. 0.1 after 5 hours aging. For xerogels A2 and A3 ( $[\text{Na}^+] = 290 \text{ ppm}$  and  $1560 \text{ ppm}$  respectively) there appears to be no significant change in  $F(Q^2)$  with aging up to 5 hours. However, for xerogel A4, which has the highest sodium ion content ( $[\text{Na}^+] = 5325 \text{ ppm}$ ), the fraction of surface silicon  $Q^2$  sites decreases rapidly. Indeed, after only 3 hours aging, it was no longer possible to detect any  $Q^2$  sites within samples of xerogel A4 while the existence of  $Q^2$  sites within xerogels A1, A2 and A3 was still clearly detectable, even after aging for 5 hours. Unfortunately the curves drawn in Figure 6.65 are not well defined owing to experimental error and a lack of data points. Given the way in which the xerogels are prepared, it is clear the  $^{29}\text{Si}$  NMR evidence does not conclusively prove that sodium ions influence the rate of hydrothermal aging. However, surface area measurements do indicate that the sodium ion concentration does influence the rate of hydrothermal aging. This fact has been confirmed by more accurate surface area measurements, on full BET adsorption isotherms, for selected samples of xerogels A2 and A3. (7)

During the process of hydrothermal aging at  $100^\circ\text{C}$  and  $\text{pH}7$ , the loss of surface area is thought to occur as a consequence of particle growth, as smaller silica particles dissolve producing silicic acid which is then deposited upon the surface of larger silica particles.

The kinetics of the reactions between silicic acid and colloidal silica have been investigated by Fleming. (53) It seems reasonable to assume that, the same factors which govern the rate of growth of colloidal silica particles will also influence the rate at which hydrothermal aging occurs. At high silicic acid concentration the rate of particle growth will be governed by the rate at which silicic acid molecules become chemisorbed onto the surface of silica particles, via the proposed reaction.



At lower silicic acid concentrations, surface rearrangement reactions govern the rate of particle growth, these reactions incorporate the chemisorbed silicic molecules into the surface of the silica particles.



The exact nature of the species that form when silicic acid is chemisorbed onto silica surfaces is unknown. In any case one would expect such species to readily undergo condensation reactions upon drying the hydrogels to produce xerogels,  $^{29}\text{Si}$  NMR techniques failed to detect any  $\text{Q}^1$  species in hydrothermally aged xerogels. If one assumes that upon drying a hydrothermally aged hydrogel any  $\text{Q}^1$  species present on the surface of the silica condense to form  $\text{Q}^2$  units, then it is possible to rationalise the data given in Figure 6.65 in terms of the relative rates at which these two reactions occur.

The rate at which silicic acid becomes chemisorbed to the surface of silica is proportional to the concentration of silica in solution, and the concentration of ionized surface silanol groups ( $[\text{SiO}^-]$ ). At constant pH, the concentration of salt in solution will affect the concentration of ionized surface silanol groups. Therefore, increasing the sodium ion concentration will increase the rate of this reaction. The dissolution of silica in solution (and hence the concentration of silicic acid in solution) is also promoted by the presence of sodium ions in solution. Therefore, increasing the sodium ion concentration will also increase the size of the silica particles that can be grown.

For xerogel A4, which has the highest sodium ion content ( $[\text{Na}^+] = 5325 \text{ ppm}$ ), the rate at which the silicic acid concentration decreases with aging will be more rapid than for the other xerogels, such that after only a few hours aging, the rate at which particle growth occurs

will be determined by the rate at which surface rearrangement reactions occur. As a consequence  $F(Q^2)$  decreases rapidly with aging to  $F(Q^2) \approx 0$ . For xerogels A2 and A3, the rate at which the silicic acid concentration decreases with aging is slower than for xerogel A4, hence the rate of particle growth will be determined more by the rate of reaction 1 than reaction 2. Under these conditions, it appears a "steady state" value of  $F(Q^2)$  is observed. For xerogel A1, which has the lowest sodium ion content ( $[Na^+] = 50$  ppm), the rate at which silicic acid concentration decreases with aging is the slowest for all the xerogels. As a consequence, the rate of particle growth will be governed primarily by reaction 1, producing a high value for  $F(Q^2)$ . However, as the silicic acid concentration falls, reaction 2 will become more dominant, so a slight decrease in  $F(Q^2)$  is observed with aging (Figure 6.65).

It is interesting to note, however, that while there is a variation in the fraction of surface silicon  $Q^2$  sites, the surface concentration of silanol groups, for all four xerogels, generally remains constant at  $N_{OH} = 6.0 \pm 0.6 \text{ nm}^2$  (Figure 6.66), suggesting there is no clear linear relationship between the fraction of geminal silanol groups and  $N_{OH}/\text{nm}^2$ . The values of  $N_{OH}/\text{nm}^2$  as measured by  $^{29}\text{Si}$  NMR are likely to be over-estimates of the actual surface concentration of silanol groups, since  $^{29}\text{Si}$  NMR cannot distinguish between  $\text{SiOH}$  and  $\text{SiONa}$  groups. This result does indicate, however, that any increase in the apparent degree of hydration per unit area, as measured by weight loss measurements, similar to that observed for xerogel A3 (Figure 6.63), cannot be caused by an increase in the surface concentration of silanol groups. This effect must be caused by an increase in the amount of water trapped within micropores in the xerogel structure. This conclusion is also supported by measurements of the proton longitudinal relaxation characteristics of these

xerogels (Figure 6.67). It is observed that with hydrothermal aging, there is an increase in the rate of proton longitudinal relaxation for samples of xerogels A2 and A3. This suggests that with aging, an increase in the proportion of water protons that are present within the xerogel samples occurs. It may be noted that for a given time of aging, the  $T_1(^1\text{H})^{-1}$  value for xerogel A2 is greater than for xerogel A3 (Figure 6.67). However, calculations of the degree of hydration per unit area by weight loss measurements, and measurements using  $^{29}\text{Si}$  NMR suggest that  $T_1(^1\text{H})$  values for xerogel A3 should be greater than those of xerogel A2. The reason for this observation is unknown, however, it is suggested that the presence of sodium ions upon the surface of the xerogel may influence  $T_1(^1\text{H})$  values.

FIGURE 6.64

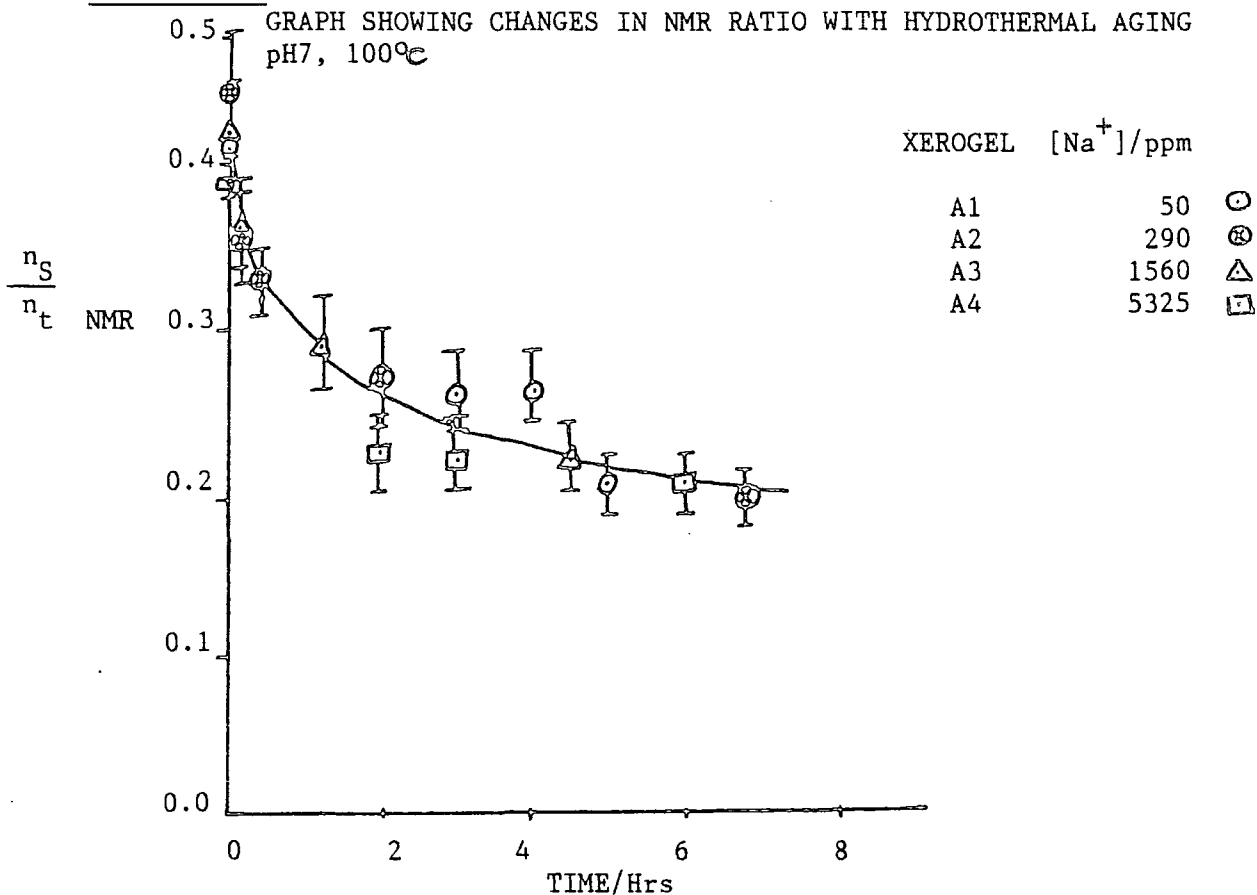
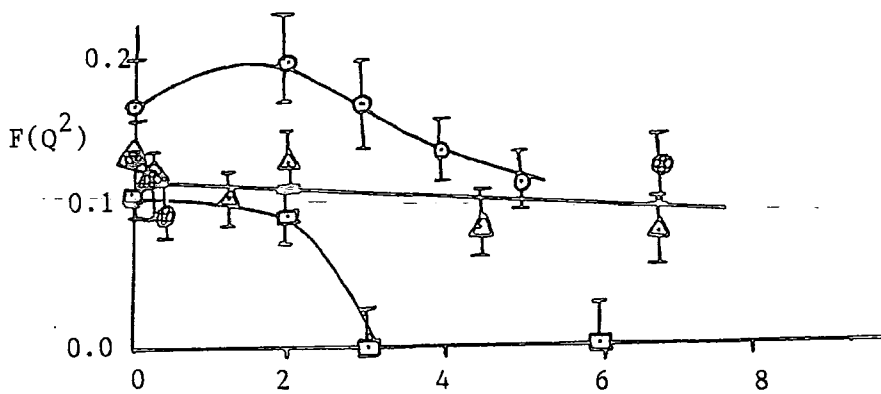


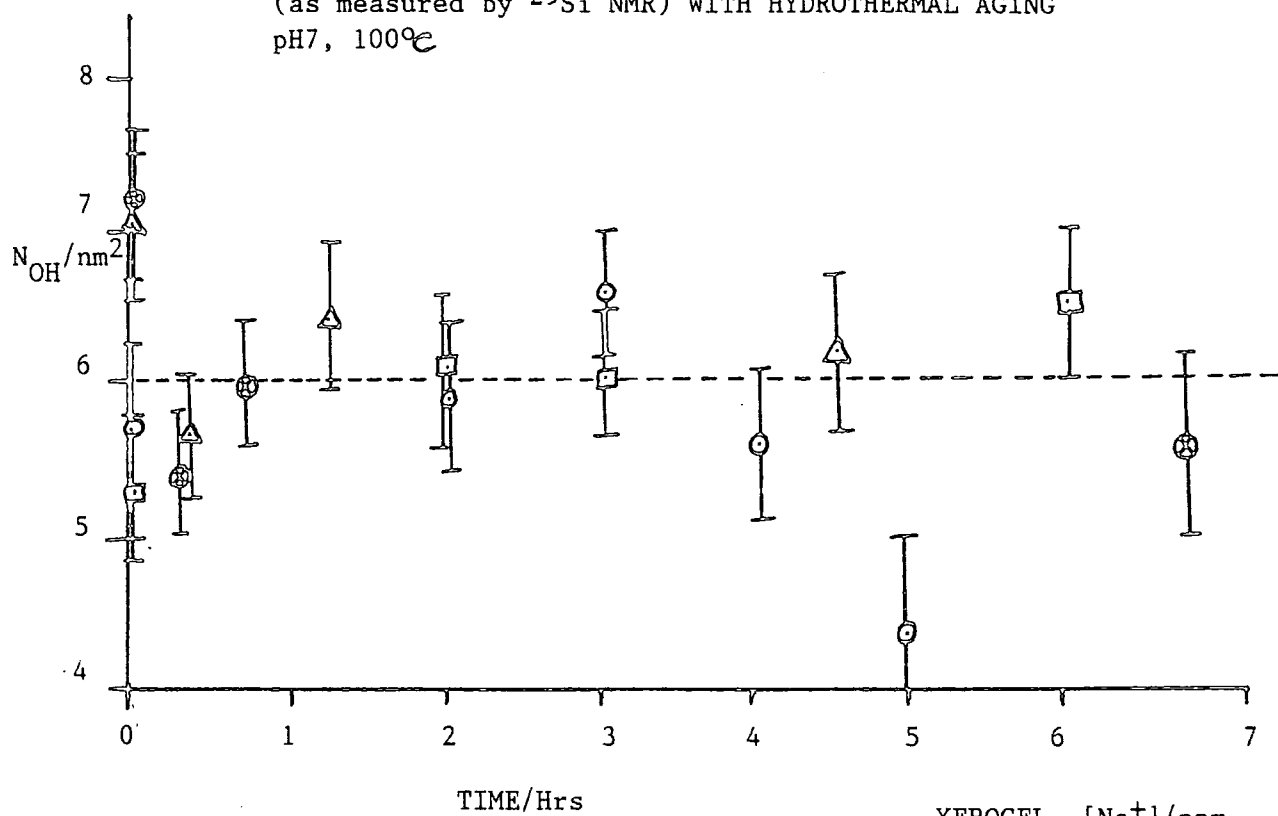
FIGURE 6.65



GRAPH SHOWING CHANGES IN  $F(Q^2)$  WITH HYDROTHERMAL AGING  
pH7, 100°C (SEE KEY TO GRAPH ABOVE)

FIGURE 6.66

FIGURE SHOWING VARIATION OF DEGREE OF HYDRATION PER UNIT AREA  
(as measured by  $^{29}\text{Si}$  NMR) WITH HYDROTHERMAL AGING  
pH7,  $100^\circ\text{C}$



## 6.8 CONCLUSIONS

In this chapter, it has been shown that solid-state single pulse and  $^{29}\text{Si}$  CP MAS NMR techniques may be employed to obtain quantitative information concerning bulk and surface structural properties of silica xerogels.  $^1\text{H}$  CRAMPS techniques and direct  $T_1(^1\text{H})$  measurements may be used to investigate the environments of protons within silica xerogels, and a roughly linear relationship between  $T_1(^1\text{H})^{-1}$  and  $T_1(^{29}\text{Si})^{-1}$  values for a given  $Q^n$  environments, reveals that the principal mechanism for silicon longitudinal relaxation in these systems is the dipolar interaction between the  $^{29}\text{Si}$ - $^1\text{H}$  spins. Both relaxation parameters are, therefore, very sensitive to the degree of hydration.

The experimental  $^{29}\text{Si}$  NMR data obtained in this study may be accounted for in terms of a corpuscular model for the xerogel structure, however, the surface structure of xerogels cannot be accurately described in terms of surface structure models based on crystalline silica phases or mixed phase surfaces, since there is no linear correlation between the fraction of geminal silanol groups (or the fraction of surface silicon  $Q^2$  sites) and the surface concentration of silanol groups.

These techniques have been demonstrated to yield information concerning the structural changes that take place as xerogels are produced in different ways.

## 7.0 CHAPTER SEVEN

### NMR STUDIES OF AQUEOUS ALKALINE SILICATE SOLUTIONS AND COLLOIDAL SILICATE SOLUTIONS

#### 7.1 INTRODUCTION

The nature of aqueous alkaline silicate solutions and the species present have been investigated over many years with a variety of techniques<sup>(1)</sup> (for example paper chromatography,<sup>(2)</sup> trimethylsilylation,<sup>(3)</sup> reactions with molybdc acid<sup>(1)</sup> and Raman spectroscopy<sup>(4)</sup>). These solutions are known to contain a variety of anionic species in dynamic equilibrium which cannot be chemically separated owing to the rapid exchange rates. The nature and distribution of these species, at a given temperature depend upon the concentration of silica in solution, the pH of the solution, the nature of the counter ion  $M^+$  and the  $M^+/Si$  ratio.<sup>(1)</sup> It is important to note, therefore, that while methods involving chemical treatment of these solutions have provided useful information concerning the nature of silicate solutions, caution is required in using these techniques because of chemical modifications that may occur in the solutions prior to analysis. However  $^{29}Si$  NMR spectroscopy can be used to study these solutions without any pretreatment, and has proved to be a powerful tool for investigating the nature of species present within silicate solutions, since, following the pioneering work of Marsmann,<sup>(5-6)</sup> Engelhardt,<sup>(7)</sup> Gould<sup>(8)</sup> and Harris<sup>(9)</sup> it was observed that characteristic signals for  $SiO_4$  groups in different structural surroundings were observed, as a consequence of exchange rates being slow on the NMR timescale, and that from the signal intensities the concentration of the various species in solution could be estimated in favorable cases.<sup>(9)</sup> There are, however, a number of factors which limit the applicability of this technique.

Since  $^{29}Si$  is a relatively insensitive nucleus, it is not

possible to examine solutions with a silica concentration much below 0.5 M on spectrometers which operate below 2.4 T, while working at higher concentrations spectral overlap is a considerable problem. Often linewidths observed are in excess of the available resolution, and a number of factors have been identified which give rise to this effect.

- [1] Linewidths increase as the number of possible environments for  $Q^n$  units increases with n
- [2] Broadening as a consequence of chemical exchange mediated by the  $H_3SiO_4^-$  anion<sup>(10)</sup>
- [3] Broadening caused by the presence of paramagnetic impurities
- [4] Broadening may also occur as higher molecular weight species form in solution, resulting in an increase in viscosity
- [5] and varying degrees of protonation of the silicate species present in solution

In addition, since  $^{29}Si$  is a dilute spin (4.7% natural abundance) each chemically distinguishable silicon site gives rise to a single resonance, as no ( $^{29}Si$ - $^{29}Si$ ) spin coupling is observed. Proton exchange is rapid on the NMR timescale, no ( $^{29}Si$ - $^1H$ ) multiplet structure is observed. The situation is further confused because the chemical shifts observed are dependent upon the solution composition.<sup>(11)</sup> Hence, there is no obvious way of assigning individual resonances to definite chemical sites. However, over a period of time various techniques have been developed which have alleviated some of these difficulties. For early workers, however, the assignment of resonances to specific silicon sites involved some degree of speculation.<sup>(9,12)</sup> Techniques that have been employed in the assignment of the resonances observed in  $^{29}Si$  NMR spectra of silicate solutions have included

- (1) observation of the changes in the spectra obtained from silicate solutions as the composition of the solution is changed and correlation with observations made using other techniques, of the changing silicate anion distribution (e.g. reference 9)
- (2)  $^{29}\text{Si}$ ,  $^{13}\text{C}$ ,  $^1\text{H}$  NMR, gas chromatographic and mass spectrometric studies of trimethylsilylated silicates<sup>(13,14)</sup>
- (3) comparison of  $^{29}\text{Si}$  chemical shifts observed in the solution-state and solid-state for silicates of known structure<sup>(15)</sup>
- (4)  $^{29}\text{Si}$  NMR studies of  $^{29}\text{Si}$  enriched silicate solutions involving homonuclear double resonance experiments<sup>(11,16,17)</sup> and 2D-J-resolved spectroscopic techniques<sup>(18)</sup>

Using these techniques the structures of nineteen different silicate anions in solution have been identified.<sup>(19)</sup>

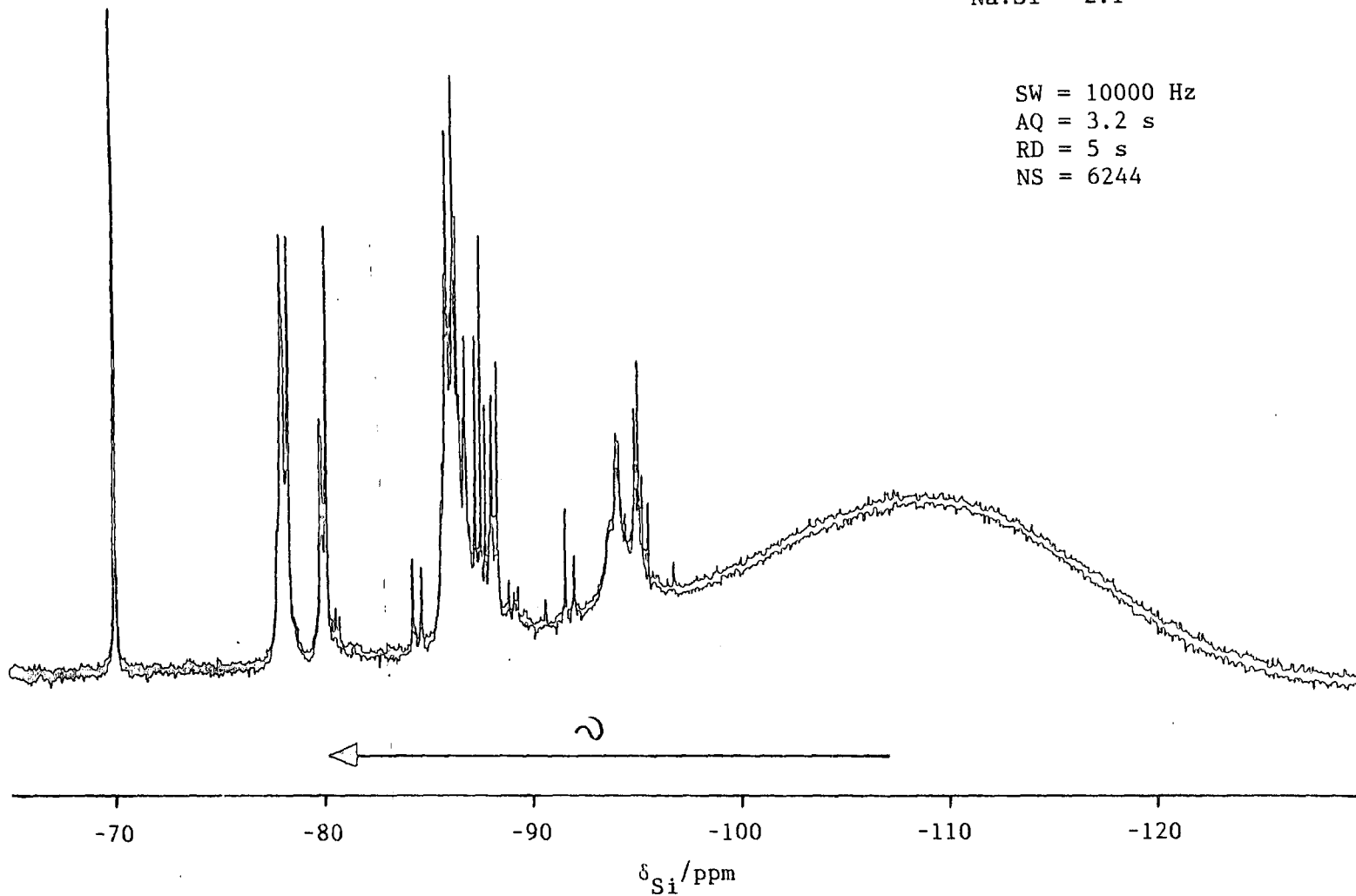
A typical  $^{29}\text{Si}$  NMR spectrum of an aqueous alkaline silicate solution (Figure 7.1), may be very complex and the full assignment of all the resonances to specific silicate species difficult. However, it is possible to more generally identify chemical shift regions, in which resonances from silicon atoms in given structural ( $\text{Q}^n$ ) environments are observed. At the highest frequency, in the shift range ca -66 to -73 ppm the resonance of the monomeric silicate anion ( $\text{Q}^0$ ) is observed. In the shift range ca -76 ppm to -83 ppm two groups of signals may be observed. The first group occurs at ca -79 ppm, and includes the peak of  $\text{Q}^1$  units in dimeric silicate anions, and (to higher frequency)  $\text{Q}^1$  units connected to  $\text{Q}^2$ ,  $\text{Q}^3$  or  $\text{Q}^4$  units. The second groups of signals occurs at ca -81 ppm, and is assigned to  $\text{Q}^2$  units in mono or disubstituted trimeric species (e.g.  $\text{Q}_2^2\text{Q}^3\text{Q}^1$ ).  $\text{Q}^2$

FIGURE 7.1

$^{29}\text{Si}$  NMR SPECTRUM OF A SODIUM SILICATE SOLUTION (OBTAINED USING INVERSE GATED DECOUPLING)

$[\text{SiO}_2] = 2.00 \text{ moles kg}^{-1}$   
 $\text{Na:Si} = 2:1$

SW = 10000 Hz  
AQ = 3.2 s  
RD = 5 s  
NS = 6244



units in four or higher membered rings or in short linear species (the occurrence of  $Q^2$  units in long chains is considered unlikely) give rise to a group of signals in the range ca -86 ppm to -91 ppm. However, signals observed at the low frequency end of this chemical shift range may have peaks originating from  $Q^3$  units of substituted trimeric species (e.g.  $Q_2^2Q^3Q^1$ ) or other  $Q^3$  units located in substituted trimeric rings (e.g.  $Q_6^3$ ). Signals arising from silicon atoms in other  $Q^3$  branching sites occur in the shift range ca -95 ppm to -101 ppm. Cross-linking  $Q^4$  silicon sites give rise to a broad signal at low frequency in the chemical shift ranges ca -103 ppm to -120 ppm. In Figure 7.1 this broad peak is caused by the quartz glass former in the probe.

In addition to these investigations, a large body of data concerned with the effects of solution composition upon the silicate anion distribution has been acquired using  $^{29}\text{Si}$  NMR techniques, (5,11,19,20) and by combining potentiometric and  $^{29}\text{Si}$  NMR techniques the qualitative and quantitative distribution, stabilities and states of protonation of silicate species in dilute sodium silicate solutions have been investigated. (21) The dynamic exchange between silicate species in solution has also been investigated, (22-25) and the condensation reactions of these species as the pH of the silicate solutions are reduced (26) or as various organosilicon compounds are hydrolysed. (26-28)

In order to obtain quantitative information concerning the distribution of silicate species in an alkaline silicate solution, it is essential to understand the dependence of the longitudinal relaxation times on sample composition. In these systems the relaxation times are often unusually short, and there have been a number of suggestions as to why this is the case.

Initially, it was suggested that such efficient  $^{29}\text{Si}$  longitudinal

relaxation arises from the rapid exchange of protons forming protonated and deprotonated silanol groups, which because this causes the  $^{29}\text{Si}$  nucleus to have different chemical shifts, fluctuating magnetic fields are generated which induce relaxation.<sup>(29)</sup> However, this idea was later rejected by Harris and Newman.<sup>(9)</sup> Instead it was concluded from their observations of aging effects in silicate solutions contained in unlined glass NMR tubes, that unidentified paramagnetic contaminants, introduced during sample preparation and/or by leaching of the NMR tubes, were probably the dominant factors in inducing  $^{29}\text{Si}$  longitudinal relaxation. More recently however, Kinrade and Swaddle<sup>(30)</sup> have suggested that the major mechanism of  $^{29}\text{Si}$  longitudinal relaxation is a dipole-dipole interaction involving the counter ion  $\text{M}^+$ , through an intramolecular process owing to the formation of a silicate anion  $-\text{M}^+$  ion pair which is long lived on the NMR timescale.

In this chapter, the  $^{29}\text{Si}$  longitudinal relaxation times of certain silicon atoms in structural units in a number of silicate solutions with different  $\text{M}^+/\text{Si}$  ratios and different alkali metal cations have been measured, in order to further investigate the effects of sample composition upon longitudinal relaxation times. In view of the large body of data already available concerning the effect of sample composition upon the distribution of species present in solution, no discussion is given on this topic. However, arguments will be put forward to demonstrate how  $^{23}\text{Na}$  NMR techniques could provide information concerning the nature of colloidal silica systems. This information could not be obtained using conventional  $^{29}\text{Si}$  NMR spectroscopic techniques.

## 7.2 EXPERIMENTAL

All aqueous alkaline silicate solutions were prepared and stored in polythene containers, using BDH precipitated silica, deionized

water and alkali metal hydroxides. The different sources of the alkali metal hydroxides are given in Table 7.1.

TABLE 7.1

<u>MOH</u>	<u>FORM</u>	<u>SOURCE</u>
LiOH.H <sub>2</sub> O	POWDER	ALDRICH CHEMICAL COMPANY INC.
NaOH	PELLETS	BDH ARISTAR GRADE
KOH	PELLETS	BDH ARISTAR GRADE
RbOH	48%(w/w) SOLUTION	ALDRICH CHEMICAL COMPANY INC.
CsOH	SOLID	ALDRICH CHEMICAL COMPANY INC.

With the exception of the lithium silicate solution, all the other solutions were heated in a water bath in order to increase the rate at which the silica dissolved. The solutions were then purged with nitrogen prior to running the experiments in this chapter.

Measurements of the rate of <sup>29</sup>Si and <sup>23</sup>Na longitudinal relaxation were measured using the inversion recovery pulse sequence. For T<sub>1</sub>(<sup>29</sup>Si) measurements, 90° and 180° pulse lengths were determined to be 16.1 μs and 33.0 μs respectively.

The <sup>23</sup>Na NMR spectrum of a sample of monodispersed colloidal silica Ludox HS-30 was also obtained. The physical and chemical properties of this colloidal silica are given in Table 7.2.<sup>(1)</sup>

TABLE 7.2

%SiO <sub>2</sub> (w/w)	%Na <sub>2</sub> O (w/w)	a R <sub>m</sub>	b A/m <sup>2</sup> g <sup>-1</sup>	c d/nm	298K <sup>d</sup> ρ/g cm <sup>-3</sup>	pH	298K <sup>e</sup> η/certi- poise
30.0	0.32	96.71	230	12.0	1.21	9.8	5.0

a  $R_m = [\text{SiO}_2]/[\text{Na}_2\text{O}]$

b specific surface area

c particle diameter

d density of solution

e viscosity

### 7.3 RESULTS AND DISCUSSION

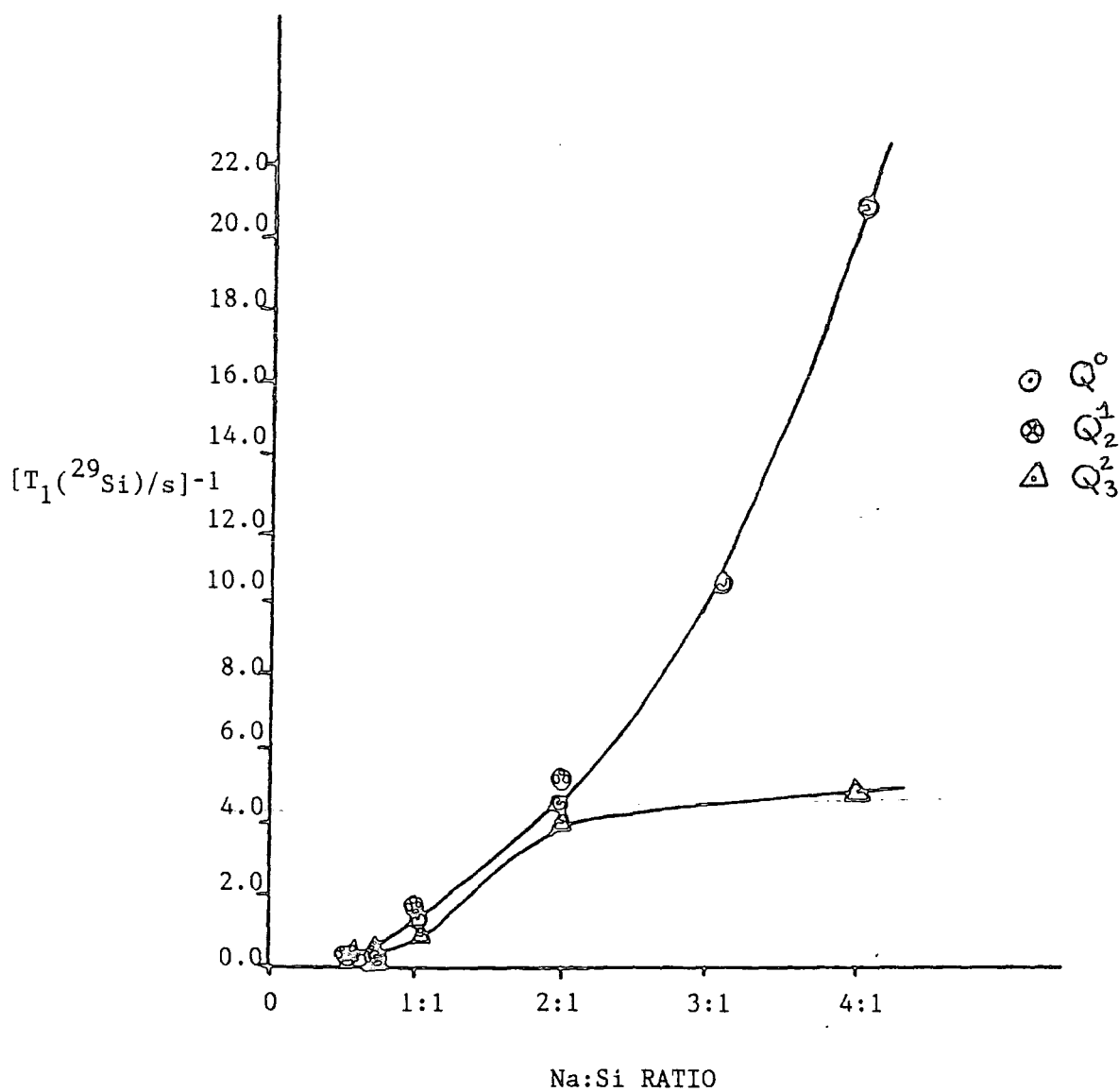
#### 7.3.1 <sup>29</sup>LONGITUDINAL RELAXATION TIME MEASUREMENTS

The effect of the Na<sup>+</sup>/Si ratio upon the rate of longitudinal relaxation times of the silicon nuclei in Q<sup>0</sup>, Q<sub>2</sub><sup>1</sup> and Q<sub>3</sub><sup>2</sup> environments has been investigated for a number of sodium silicate solutions of constant silica concentration ([SiO<sub>2</sub>] = 2.00 moles Kg<sup>-1</sup>) but differing Na<sup>+</sup>/Si ratios. These measurements are summarised in Figure 7.2. The results clearly indicate that as the Na<sup>+</sup>/Si ratio increases, there is an increase in the rate of <sup>29</sup>Si longitudinal relaxation. It is interesting to note that as the Na<sup>+</sup>/Si ratio is increased up to 2:1, the rate of longitudinal relaxation for <sup>29</sup>Si nuclei in Q<sup>0</sup> and-Q<sub>3</sub><sup>2</sup> species is very similar. However, above a ratio Na<sup>+</sup>:Si =3:1 differences between the relaxation rates increase. This observation may reflect the decreasing rate of chemical exchange which causes an apparent averaging of T<sub>1</sub>(<sup>29</sup>Si)<sup>-1</sup> values: exchange being mediated by the H<sub>3</sub>SiO<sub>4</sub><sup>-</sup> anion, and not the H<sub>2</sub>SiO<sub>4</sub><sup>2-</sup> anion, which becomes more predominant in solution as the pH (or Na<sup>+</sup>:Si ratio) is increased.<sup>(10)</sup>

The <sup>23</sup>Na NMR spectra of these sodium silicate solutions exhibit a single resonance. Measurements of the <sup>23</sup>Na longitudinal relaxation rates indicated that as the Na<sup>+</sup>/Si ratio increases above 2:1 a significant increase in the rate of longitudinal relaxation is

FIGURE 7.2

A GRAPH SHOWING CHANGES IN  $[T_1(^{29}\text{Si})/s]^{-1}$  VALUES FOR  $Q^0$ ,  $Q_2^1$  and  $Q_3^2$  SPECIES PRESENT IN A SODIUM SILICATE SOLUTION ( $[\text{SiO}_2] = 2.0 \text{ moles kg}^{-1}$ ) AS THE  $\text{Na}^+:\text{Si}$  RATIO IS INCREASED



observed (Figure 7.3). At infinite dilution, sodium hydroxide exists as hydrated ions  $[\text{Na}(\text{H}_2\text{O})_4]^+$  and  $[\text{OH}(\text{H}_2\text{O})_6]^-$ .<sup>(31)</sup> As the  $\text{Na}^+/\text{Si}$  ratio (or sodium hydroxide concentration) increases, the rate of  $^{23}\text{Na}$  longitudinal relaxation remains relatively constant,  $[\text{H}_2\text{O}]/[\text{NaOH}] \approx 10$ . This point corresponds to a  $\text{Na}^+:\text{Si}$  ratio of 2:1. Above this point, there are insufficient water molecules to fully hydrate the ions. Hence as the sodium ion concentration is increased, there is an increasing asymmetry in the electric field gradient surrounding the sodium nucleus, and an increase in the number of ion pairs formed between sodium ions and silicate anions in solution. This results in the sodium silicate solution studied here with a  $\text{Na}^+:\text{Si}$  ratio of 4:1 being unstable, since after only a few days standing at room temperature 83.4% (w/w) of the silica in solution was precipitated as fine crystals of hydrated sodium silicate. Chemical analysis indicated the average molecular formula of these crystals to be  $\text{Na}_2\text{SiO}_3 \cdot n\text{H}_2\text{O}$  where  $n \approx 7 \pm 2$ .

The  $^{29}\text{Si}$  longitudinal relaxation times of silicon nuclei in  $Q^0$ ,  $Q_2^1$  and  $Q_3^2$  environments have also been measured for a number of silicate solutions of constant silica concentration ( $[\text{SiO}_2] = 1.0 \text{ moles Kg}^{-1}$ ) but prepared with various counter ions, though the  $M^+:\text{Si}$  ratio was kept constant at 2:1. The results of these measurements are summarised in Table 7.3. The results indicate that upon going from lithium, sodium to potassium silicate solutions, there is a steady decrease in the rate of longitudinal relaxation for silicon nuclei in  $Q^0$ ,  $Q_2^1$  and  $Q_3^2$  species, there is an increase in the rate of longitudinal relaxation upon going from potassium to rubidium and caesium silicate solutions.

In silicate solutions there are a number of mechanisms that influence  $^{29}\text{Si}$  longitudinal relaxation times. In addition, chemical exchange can result in an apparent averaging of  $T_1$  values. However,

one may account for the observed  $T_1$  values in terms of the contributions  $T_{1ue}^{-1}$  from the presence of unpaired electrons,  $T_{1SC}^{-1}$  from scalar coupling,  $T_{1CSA}^{-1}$  from shielding anisotropy,  $T_{1SR}^{-1}$  from spin rotation mechanisms and  $T_{1DD}^{-1}$  from dipole-dipole interactions, (either  $^{29}\text{Si}-^1\text{H}$  or  $^{29}\text{Si}-\text{M}^+$  dipolar interactions).

$$(7.1) \quad T_1^{-1} = T_{1ue}^{-1} + T_{1SC}^{-1} + T_{1CSA}^{-1} + T_{1SR}^{-1} + T_{1DDH}^{-1} + T_{1DDM}^{-1}$$

It has been noted<sup>(9,30)</sup> that dissolved oxygen makes a trivial contribution to  $T_{1ue}^{-1}$ . In any case, these particular silicate solutions were purged with nitrogen, and since samples were prepared and stored in polythene containers, and only transferred to a quartz NMR tube in order to run the experiment, contamination by leaching of paramagnetic impurities from the NMR tube is considered negligible.

TABLE 7.3

$\text{M}^+$	$T_1(^{29}\text{Si})/\text{s}$		
	$Q^0$	$Q_2^1$	$Q_3^2$
Li	0.23±0.01	0.28±0.01	0.25±0.01
Na	0.60±0.06	0.35±0.01	1.12±0.02
K	1.05±0.01	3.48±0.07	1.41±0.01
Rb	0.57±0.01	0.43±0.03	1.08±0.03
Cs	0.54±0.02	0.29±0.05	1.08±0.01

TABLE 7.4

$\text{M}^+$	$T_{1DDH}^{-1}/\text{s}^{-1}$		
	$Q^0$	$Q_2^1$	$Q_3^2$
Li	1.6±0.2	0.89±0.09	0.32±0.04
Na	0.32±0.06	0.34±0.04	0.18±0.02
K	0.06±0.01	0.02±0.01	0.01±0.01
Rb	0.53±0.05	0.55±0.07	0.26±0.03
Cs	0.43±0.04	0.5±0.1	0.20±0.02

TABLE 7.5

M <sup>+</sup>	Q <sup>0</sup>	T <sub>1other</sub> <sup>-1</sup> /s <sup>-1</sup>	
		Q <sub>2</sub> <sup>1</sup>	Q <sub>3</sub> <sup>2</sup>
Li	2.8±0.4	2.7±0.2	3.7±0.2
Na	1.3±0.2	2.5±0.1	0.71±0.03
K	0.89±0.01	0.27±0.02	0.7±0.1
Rb	1.22±0.8	1.8±0.2	0.66±0.05
Cs	1.4±0.1	2.9±0.9	0.72±0.03

Scalar coupling ( $T_{1SC}^{-1}$ ) can be disregarded as a source of longitudinal relaxation, since there are no nuclei present which have a resonance frequency similar to that of  $^{29}\text{Si}$ . Newman suggested that in view of the small shielding anisotropy for silicon compounds,  $T_{1CSA}^{-1}$  is unlikely to make a significant contribution to the rate of  $^{29}\text{Si}$  longitudinal relaxation,<sup>(32)</sup> and this has been confirmed by variable  $B_0$  field experiments,<sup>(30)</sup> and while there is evidence to suggest that spin rotation ( $T_{1SR}^{-1}$ ) does make some contribution to the longitudinal relaxation times of small molecules, the dipole-dipole mechanisms ( $T_{1DDH}^{-1}$  and  $T_{1DDM}^{-1}$ ) appear to be the dominant causes of  $^{29}\text{Si}$  longitudinal relaxation.

Measurements of the  $\eta_{oe}$  (see Section 2.5.3) enables the calculation of the contribution to  $^{29}\text{Si}$  longitudinal relaxation from the dipolar interaction between  $^1\text{H}$  and  $^{29}\text{Si}$  spins ( $T_{1DDH}^{-1}$ ) via equations 2.45 and 2.46. The results of these calculations (Table 7.4), indicate that at room temperature, the  $^{29}\text{Si}$ - $^1\text{H}$  dipolar relaxation mechanism is significant. These results are consistent with the observations of Newman<sup>(32)</sup> and Kinrade and Swaddle<sup>(30)</sup> who noted that the contribution of this mechanism to the rate of  $^{29}\text{Si}$  longitudinal relaxation is significant at low temperatures.<sup>(30)</sup> In general  $T_{1DDH}^{-1}$  values decrease in the series  $Q^0 \geq Q^1 > Q^2$ , reflecting the

number of protons which may be associated with the silicon nuclei in these environments.  $T_{1DDH}^{-1}$  values also decrease upon going from lithium sodium to potassium silicate solutions. This effect may arise from structural changes in the water as a result of the influence of the counter ions, which are fully hydrated in these solutions, and/or changes in the viscosity or pH of these solutions. The lithium, sodium and potassium ions are surrounded tetrahedrally by four water molecules in the first co-ordination sphere. However, for rubidium and caesium ions, the coordination may well be octahedral.<sup>(33)</sup> It is thought that the change in coordination upon going from potassium to caesium may lead to changes in the way water molecules are structured around these ions, leading to changes in the  $T_{1DDH}^{-1}$  values.

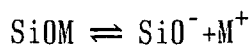
Measurements of the  $T_{1DDH}^{-1}$  values also enable the calculation of the contribution to the rate of  $^{29}\text{Si}$  longitudinal relaxation resulting from the dipolar interaction between the counter ions  $M^+$  and  $^{29}\text{Si}$  ( $T_{1DDM}^{-1}$ ) and spin rotation ( $T_{1SR}^{-1}$ ),

$$(7.2) \quad T_1^{-1} \approx T_{1DDH}^{-1} + T_{1DDM}^{-1} + T_{1SR}^{-1} = T_{1DDH}^{-1} + T_{1other}^{-1}$$

If it is assumed that  $T_{1SR}^{-1} \approx 0$  and therefore that values of  $T_{1other}^{-1}$  are determined principally by an intramolecular dipolar interaction between  $^{29}\text{Si}$  and the counter ion, one might expect  $T_{1other}^{-1}$  values to be roughly proportional to  $R$ ,<sup>(34)</sup> where

$$(7.3) \quad R = \Sigma[n\gamma_M^2 S(S+1)]$$

In this equation  $n$  is the fractional abundance of an isotope of spin  $S$  for a given  $M^+$  counter ion. Values of  $R \times 10^{-15}$  for  $\text{Li}^+$ ,  $\text{Na}^+$ ,  $\text{K}^+$ ,  $\text{Rb}^+$  and  $\text{Cs}^+$  are 37.5, 18.8, 0.6, 12.0 and 19.6 respectively. Since there is some evidence to suggest that the equilibrium constant for the process



changes very little for  $\text{Na}^+$ ,  $\text{K}^+$  and  $\text{Rb}^+$  silicate ion pairs.<sup>(30,35)</sup> one might expect  $T_{1other}^{-1}$  values to increase as  $R$  increases. Plots of

$T_{1\text{other}}^{-1}$  values against R (Figure 7.4) appear to indicate that as R increases, there is an increase in rate of  $^{29}\text{Si}$  longitudinal relaxation.

### 7.3.2 $^{23}\text{Na}$ NMR STUDIES OF A COLLOIDAL SILICA

Efforts to investigate the nature of colloidal silicas stabilised by the addition of sodium hydroxide using  $^{29}\text{Si}$  NMR solution-state techniques have proved unsuccessful, owing to the low mobility of the colloidal particles. However, the nature of the interaction between the sodium ions and the silica surface may be examined using  $^{23}\text{Na}$  NMR spectroscopy.

One may assume that in colloidal silicas, the sodium ions are either in the bulk aqueous phase (state A) or bound to the surface of the colloidal particles by Si-O-Na bonds (state B).

For an integral half spin quadrupolar nucleus, it has been shown that the time dependence of the magnetisation cannot generally be described by a single exponential time constant for the longitudinal or transverse magnetisation if relaxation is dominated by quadrupolar interactions. For rapid two site exchange, the time behaviour of the transverse magnetisation in a coordinate system rotating at the resonance frequency is given as (36)

$$(7.4) \quad M(t) = M(0) [0.6 \exp(-b_1 t) + 0.4 \exp(-b_2 t)]$$

where

$$(7.5) \quad b_1 = \frac{P_A R_A + P_B}{T_{2,\text{fast}}}$$

$$(7.6) \quad b_2 = \frac{P_A R_A + P_B}{T_{2,\text{slow}}}$$

In these equations  $P_A$  and  $P_B$  are the probabilities of finding the nucleus in the free or bound states respectively.  $R_A$  is the relaxation time of the sodium nucleus in the bulk aqueous phase. The

FIGURE 7.3

GRAPH SHOWING CHANGES IN  $[T_1(^{23}\text{Na})]^{-1}$  VALUES FOR A SODIUM SILICATE SOLUTION  
 ( $[\text{SiO}_2] = 2.0 \text{ moles kg}^{-1}$ ) AS THE Na:Si RATIO IS INCREASED

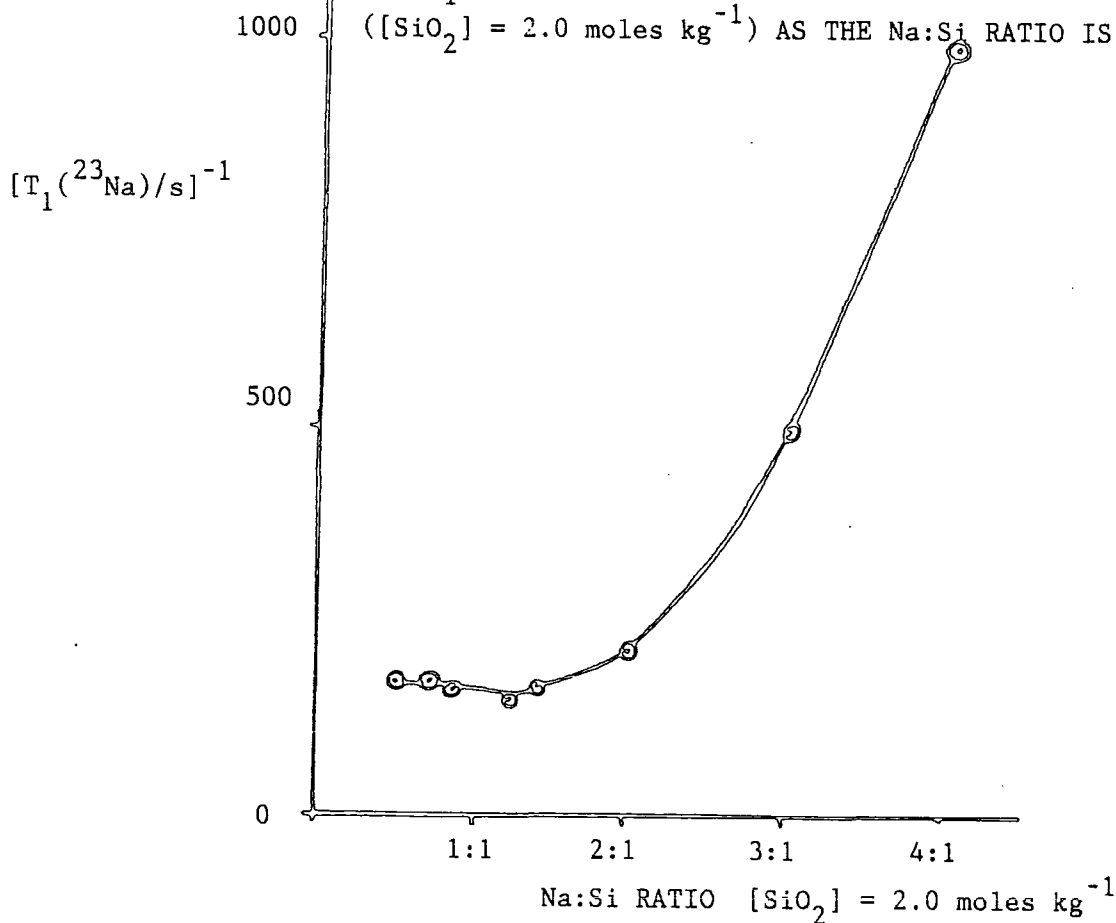
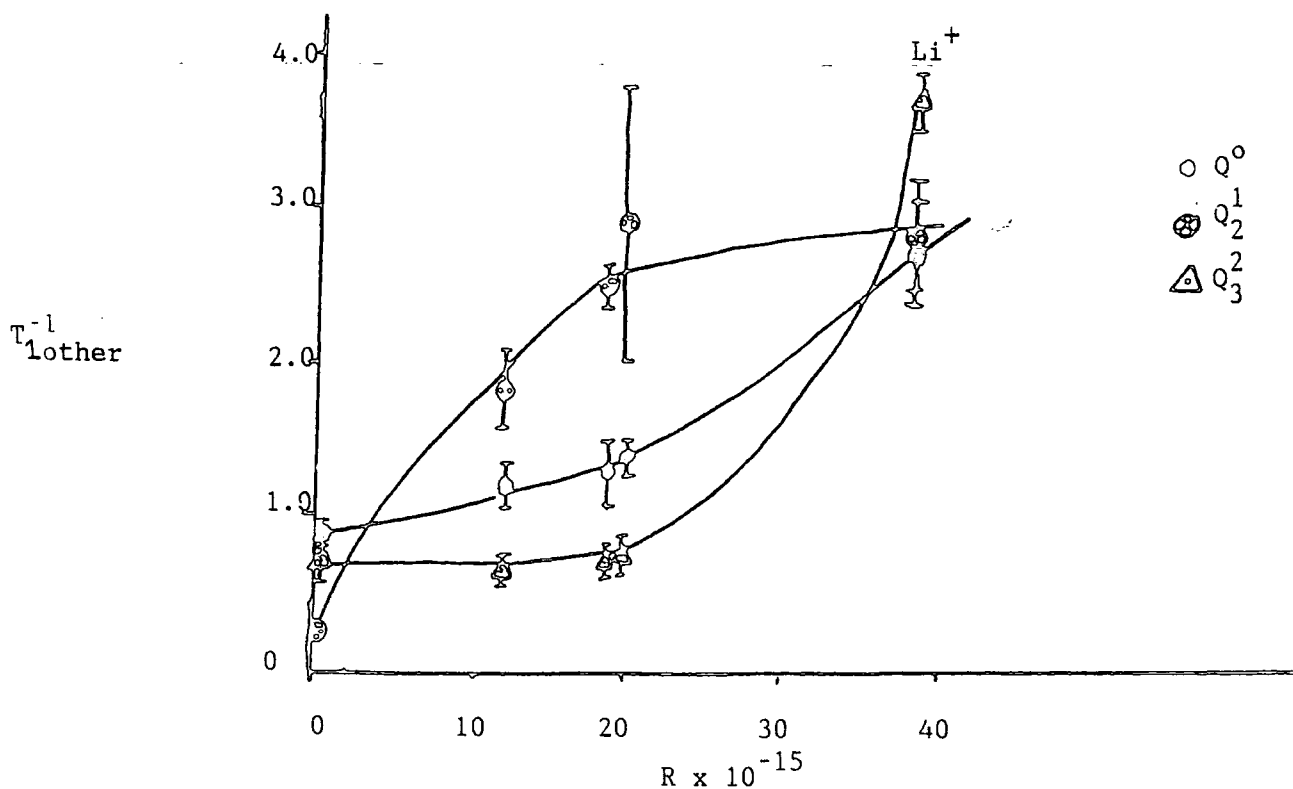


FIGURE 7.4

GRAPH SHOWING THE EFFECT OF THE COUNTER ION UPON  $[T_{\text{lother}}(^{29}\text{Si})]^{-1}$  VALUES  
 OF THREE SILICATE SPECIES IN SILICATE SOLUTIONS  
 $[\text{SiO}_2] = 1.00 \text{ moles kg}^{-1}$   $M^+:\text{Si} = 1:1$



two relaxation times  $T_{2,\text{fast}}$  and  $T_{2,\text{slow}}$  arise from the interaction of the sodium nucleus with the surface of the silica. The distortion of the electron distribution round the sodium nucleus causes quadrupolar interactions, and the electric field gradients do not fluctuate more rapidly than the Larmor frequency. As a consequence a two component  $T_2$  is observed, where the values of  $T_{2,\text{fast}}^{-1}$  and  $T_{2,\text{slow}}^{-1}$  are given as follows,

$$(7.7) \quad T_{2,\text{fast}}^{-1} = R_{\text{fast}} = \frac{\pi^2}{5} \chi^2 \tau_c [1 + 1/(1 + \omega^2 \tau_c^2)]$$

$$(7.7) \quad T_{2,\text{slow}}^{-1} = R_{\text{slow}} = \frac{\pi^2}{5} \chi^2 \tau_c [1/(1 + 4\omega^2 \tau_c^2) + 1/(1 + \omega^2 \tau_c^2)]$$

where  $\chi$  is the quadrupolar coupling constant and  $\tau_c$  is the correlation time for the bound sodium ion.  $\omega$  is the resonance frequency ( $\omega = 415.75 \times 10^6 \text{ rads}^{-1}$ ). From these equations it may be seen that if  $\omega\tau_c \ll 1$  (the extreme narrowing condition), then  $R_{\text{fast}} = R_{\text{slow}}$ , and the time dependence of the transverse magnetisation may be described in terms of a single exponential time constant. However, if  $\omega\tau_c$  is not too small, then the time dependence of the transverse magnetisation is described in terms of two time constants. Under these conditions, the high-resolution  $^{23}\text{Na}$  NMR spectrum is the superposition of two Lorentzian signals, each with the same resonance frequency, but with linewidths corresponding to the two relaxation rates  $b_1$  and  $b_2$ .

Provided  $P_A R_A$  is known, then

$$(7.9) \quad \frac{R_{\text{fast}}}{R_{\text{slow}}} = \frac{b_1 - P_A R_A}{b_2 - P_A R_A} = \frac{1 + (1 + \omega^2 \tau_c^2)^{-1}}{(1 + \omega^2 \tau_c^2)^{-1} + (1 + 4\omega^2 \tau_c^2)^{-1}}$$

Since the ratio  $R_{\text{fast}}/R_{\text{slow}}$  is a function of  $\omega\tau_c$ , from equation 7.9, the correlation time for the bound sodium ion ( $\tau_c$ ) can be determined. Once this has been done, equations 7.5, 7.6, 7.7 and 7.8 may be used to calculate the quadrupolar coupling constant.

The  $^{23}\text{Na}$  solution-state NMR spectrum of Ludox HS-30

monodisperse colloidal silica (30% $\frac{w}{w}$ ) = SiO<sub>2</sub>, 0.58% $\frac{w}{w}$ Na<sub>2</sub>O) is shown in Figure 7.5a. The signal observed is the superposition of two Lorentzian line shapes, that appear to have the same resonance frequency. From fitting the observed spectrum to two Lorentzians lineshapes, using the fitting routine LINESIM,<sup>(38)</sup> values of b<sub>1</sub> and b<sub>2</sub> may be calculated as 5884 s<sup>-1</sup> and 650 s<sup>-1</sup> respectively (see Figure 7.5b). There are no small oligomers present which can be detected using NMR. Values of  $\omega\tau_c$  may be determined from the following quadratic equation

$$(7.10) \quad 4x^2 + (9-5\Delta)x + 2(1-\Delta) = 0$$

where  $x = \omega^2\tau_c^2$  and  $\Delta = \frac{b_1 - P_A R_A}{b_2 - P_A R_A}$

The rate of relaxation for the free sodium ion in the bulk aqueous phase was determined by measuring the <sup>23</sup>Na longitudinal relaxation time for a solution of sodium hydroxide of the same concentration as Ludox HS-30. Therefore, R<sub>A</sub> = 17.06 s<sup>-1</sup>.

Unfortunately, however, the fraction of the sodium ions that are bound to the surface of the colloidal particles (P<sub>B</sub>) is unknown. However, values of P<sub>A</sub> and P<sub>B</sub> may be estimated by the following arguments.

Yates<sup>(1)</sup> derived a formula which relates the fraction of ionized silanol groups ( $\alpha$ ), the sodium ion concentration and the pH of a colloidal silica via equation 7.11

$$(7.11) \quad \text{pH} = \text{pK} - n \log_{10} \left( \frac{1-\alpha}{\alpha} \right) - 0.74 \log_{10} (2C/R_m)$$

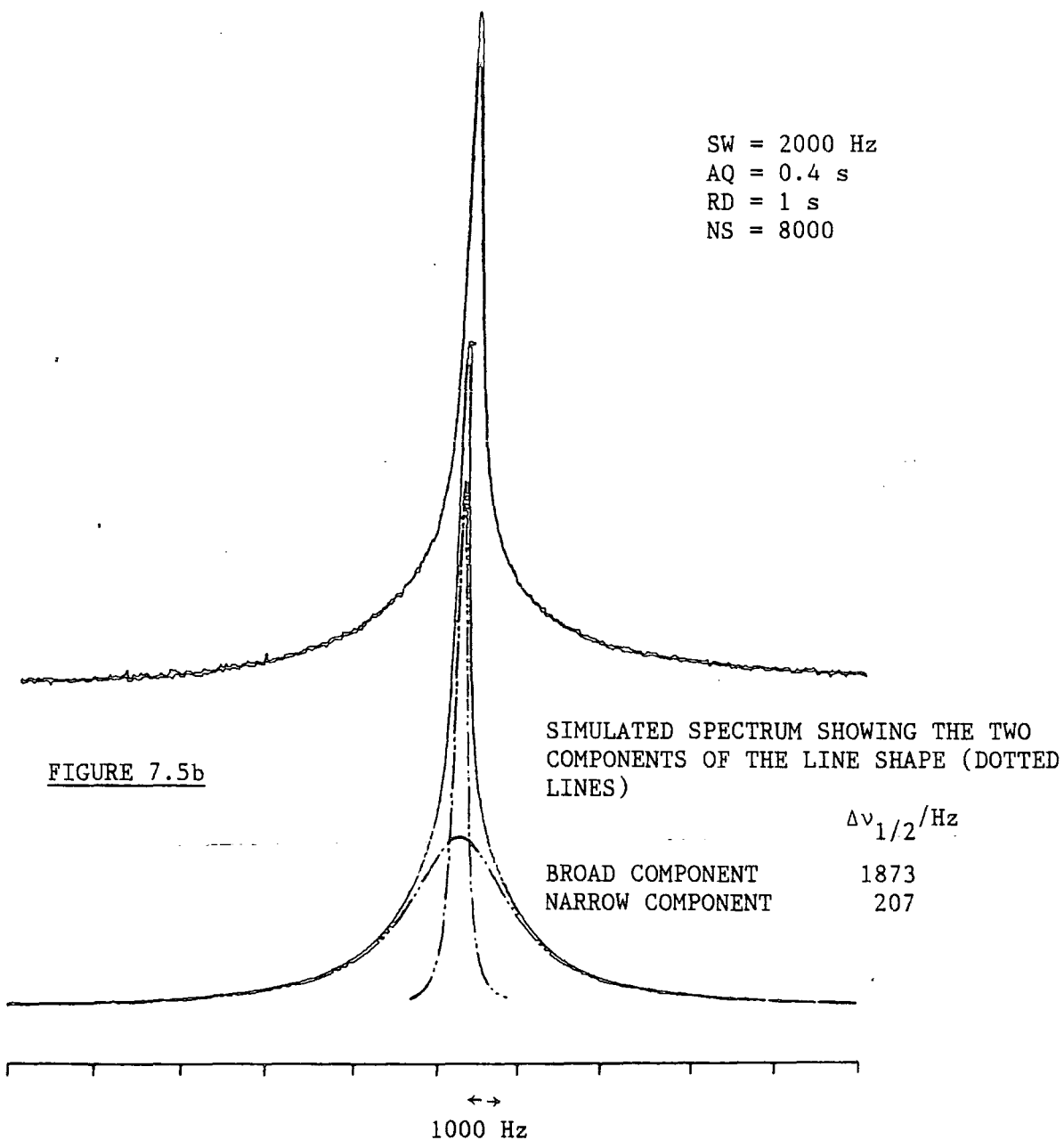
where pK = 12.08, n = 3.47, R<sub>m</sub> = [SiO<sub>2</sub>]/[Na<sub>2</sub>O] and C is the concentration of silica in solution. The fraction of surface ionized silanol groups is given as<sup>(1)</sup>

$$(7.12) \quad \alpha = \frac{2430}{AR_m}$$

where A is the specific surface area in m<sup>2</sup>g<sup>-1</sup>. From equations 7.11

FIGURE 7.5a

$^{23}\text{Na}$  SINGLE PULSE PROTON DECOUPLED SPECTRUM OF LUDOX HS-30 COLLOIDAL SILICA SOLUTION



and 7.12, the pH of the colloidal silica may be calculated as 9.8, this value is in agreement with that quoted by the manufacturers (Table 7.2). This result, therefore, suggests that the fraction of ionized silanol groups  $\alpha = 0.207$ .

Given that the average formula of a silica particle may be expressed in terms of its average degree of connectivity ( $Q$ ) as

$$(7.13) \quad H_{(4-Q)n} Si_n O_{\frac{(4-Q)n}{2}}$$

Then, assuming all particles to be spherical, composed of fully condensed silica (density =  $2.2 \text{ g cm}^{-3}$ ) and that all the <sup>surface</sup> silicon sites are  $Q^3$  units, then the total number of silanol groups in 1 kg of solution may be estimated via equation <sup>7.14</sup> as  $0.725 \text{ moles SiOH kg}^{-1}$  (37)

$$(7.14) \quad \text{moles SiOH kg}^{-1} = \frac{\%SiO_2(w/w) \times 10 \times (n_s/n_T)}{96.114 - 9.0075 \left[ \frac{4-n_s}{n_T} \right]}$$

$$\text{where } \frac{n_s}{n_T} = \frac{(\rho AC) - (\rho AC) + (\rho AC)}{3 \quad 27}^3$$

$C = 0.313 \text{ nm}$ , (37) is the average separation between silicon atoms of adjacent silicon-oxygen tetrahedra. Similarly, the number of moles  $Na^+ \text{ kg}^{-1}$  of the colloidal silica may be calculated as  $0.187 \text{ moles kg}^{-1}$ . However, there are only  $0.150 \text{ moles}$  of ionized silanol groups  $\text{kg}^{-1}$ . Assuming that for each ionized silanol group there is a  $SiO^- Na^+$  bond, then values of  $P_A$  and  $P_B$  may be estimated as  $0.2$  and  $0.8$  respectively. On the basis of these arguments the correlation time for the bound sodium ion is calculated as ca  $\tau_c = 30 \text{ ns}$ , and the quadrupolar coupling constant  $\chi$  as ca  $340 \text{ KHz}$ .

#### 7.4 CONCLUSIONS

The results outlined in this chapter are consistent with the hypothesis that the principal mechanism of  $^{29}\text{Si}$  longitudinal relaxation in aqueous alkaline silicate solutions is the dipole-dipole interaction involving the counter ion  $M^+$  through an intramolecular

process owing to the formation of a silicate anion- $M^+$  ion pair which is long-lived on the NMR timescale. Furthermore, although  $^{29}\text{Si}$  NMR techniques provide little information about the nature of colloidal silica solutions, the arguments suggest that information concerning the interaction between sodium ions and silica surfaces may be obtained using  $^{23}\text{Na}$  NMR techniques.

## 8.0 CHAPTER EIGHT

### 8.1 CONCLUSIONS AND SUGGESTIONS FOR FUTURE INVESTIGATIONS

In this thesis a number of  $^{29}\text{Si}$  solid-state NMR techniques have been demonstrated to yield information concerning the structure, and properties of a number of crystalline and amorphous silicon-containing materials. Many of the experiments reported in Chapters Five and Six have relied upon the  $^{29}\text{Si}$ - $^1\text{H}$  cross-polarisation technique. In Chapters Two and Four the theoretical and experimental aspects of the cross-polarisation experiment have been discussed. Two compounds have been investigated as potential replacements for  $\text{Q}_8^3\text{M}_8$  for setting the Hartmann-Hahn matching condition. The results of these investigations reveal that the sodium salt of trimethylsilyl-1-propanesulphonic acid exhibits a similar sensitivity as  $\text{Q}_8^3\text{M}_8$  to the matching condition and cross-polarisation efficiency. The use of this compound for setting up the cross-polarisation experiment also offers the advantage that it is cheaper and more readily obtained than  $\text{Q}_8^3\text{M}_8$ .

In Chapter Five, attention has been focused upon the use of slow-spinning  $^{29}\text{Si}$  NMR techniques to measure the principal components of the  $^{29}\text{Si}$  shielding tensors, for a variety of silicate minerals and organosilicon compounds. The theoretical aspects of the calculation of these parameters are discussed, together with the advantages to be gained by performing these measurements. Measurements of  $^{29}\text{Si}$  shielding tensors are demonstrated to be a valuable tool for investigating the structure of crystalline silicon-containing materials. The results reported are generally consistent with the published crystal structures, where these are known. In situations where the crystal structures are unknown, the results yield valuable information concerning the local symmetry at silicon sites within the compound. Following work of Grimmer, measurements of the principal components of  $^{29}\text{Si}$  shielding tensors, and Si-C and Si-H scalar

coupling constants, provide further evidence that the shielding along a given silicon-ligand bond axis depends upon the fractional s-character of the hybrid orbitals involved, relative to those of the remaining bonds in some of the organosilicon compounds studied here. It would be interesting to extend these studies to other organosilicon compounds of the type  $R_3SiX$ , in order to examine the relationship between the sign and magnitude of the anisotropy of the shielding tensor, ligand electronegativities and the net charge on the silicon atom, in order to gain a greater understanding of the factors which influence  $^{21}Si$  isotropic chemical shifts.

In Chapter Six,  $^{29}Si$  NMR techniques have been shown to yield information concerning the bulk and surface structural properties of silica xerogels. The results obtained from these studies are consistent with a corpuscular model for the xerogel structure. However, the surface structure of xerogels cannot be accounted for in terms of structural models analogous to crystalline silica phases. The quality of the data reported did not warrant the development of more sophisticated structural models. However, with more accurate surface area and porosity measurements, it may be possible to construct sophisticated models that take into account coordination numbers, and the distribution of particle sizes. Unfortunately, it was not possible to gain reliable quantitative information concerning the structure of silica hydrogels, since during the course of  $^{29}Si$  MAS NMR experiments water was "spun out", and changes in the hydrogel structure occurred.

The principal mechanism for  $^{29}Si$  longitudinal relaxation in these systems is shown to be the  $^{29}Si$ - $^1H$  dipolar interaction, and  $T_1(^{29}Si)$  and  $T_1(^1H)$  values are very sensitive to the degree of hydration. The hydration and dehydration of silica xerogels has also been investigated using a suite of  $^1H$  CRAMPS techniques, to provide

information concerning the existence of various proton environments upon the silica xerogel surfaces, and spin exchange dynamics. Unfortunately, owing to limitations of the pulse programmer, it was not possible to perform any 2D- $^1\text{H}$  CRAMPS experiments, which would have provided further information concerning spin exchange. In addition, it would be very interesting to perform a number of 2D heteronuclear ( $^{29}\text{Si}$ - $^1\text{H}$ ) chemical shift correlation experiments upon samples of a silica xerogel with differing degrees of hydration, in order to investigate the process of rehydration or dehydration more fully. Chapter Six ends by demonstrating how  $^{29}\text{Si}$  single-pulse and CP MAS NMR techniques may be employed to investigate the structural changes that occur when silica xerogels are prepared, or treated in different ways.

Finally, in Chapter Seven, measurements of  $^{29}\text{Si}$  longitudinal relaxation times for a variety of anionic species present in aqueous alkaline silicate solutions provide evidence consistent with the hypothesis that, in these systems, the principal mechanism for longitudinal relaxation is a dipole-dipole interaction. This involves the counter ion  $\text{M}^+$ , through an intra-molecular process resulting from the formation of a silicate-anion- $\text{M}^+$  ion pair which is long-lived on the NMR timescale. Furthermore, although  $^{29}\text{Si}$  NMR techniques provided little information concerning the nature of colloidal silicas, it is suggested that,  $^{23}\text{Na}$  NMR techniques may give data concerning the interaction of sodium ions with the silica surface.

In summary, in this thesis various NMR techniques have been demonstrated which yield structural information complementary to that obtained using other physical and chemical techniques. In certain silicon-containing systems where structural information is difficult or impossible to obtain using other techniques NMR is a powerful tool which may be used to gain a new insight into the structural properties of these materials.

CHAPTER TWOREFERENCES

- 1 W. Pauli, Naturwiss 1924, 12, 741
- 2 Fourier Transform NMR Spectroscopy (2nd Edition)  
D.Shaw. Elsevier, Amsterdam, 1984
- 3 Transient Techniques in NMR of Solids  
B.C. Gerstein, C.R. Dybowski. Academic Press Inc., 1985
- 4 Nuclear Magnetic Resonance Spectroscopy  
R.K. Harris. Longman Scientific and Technical, 1986
- 5 High Resolution NMR in Solids. Selective Averaging  
U. Haeberlen. Academic Press, New York, 1976
- 6 Practical NMR Spectroscopy  
M.L. Martin, J.J. Delpuech, G.L. Martin. Heyden & Son Ltd.,  
1980
- 6a P. Wilkes, Personal Communications
- 7 P. Jackson, Ph.D. Thesis  
Durham University, 1987
- 8 E.R. Andrew, L.F. Farnell, M. Firth, T.D. Gledhill  
J. Magn Reson, 1969, 1, 27
- 9 J.E. Demco, J. Tegenfeld, J.S. Waugh  
Phys. Rev. B, 1975, 11, 4413
- 10 J.S. Waugh, L.M. Huber, U. Haeberlen  
Phys. Rev. Lett., 1968, 20, 180
- 11 W.K. Rhin, D.D. Elleman, R.W. Vaughan  
J. Chem. Phys., 1973, 58, 1772
- 12 D. Burum, W.K. Rhin  
J. Chem. Phys., 1979, 71, 944
- 13 The Multinuclear Approach to NMR Spectroscopy  
Eds. J.B. Lambert, F.G. Riddell  
D. Reidel Publishing Company, 1982
- 14 A. Pines, M.S. Gibby, J.S. Waugh  
J. Chem. Phys., 1973, 59, 569
- 15 S. Hartman, E.L. Hahn  
Phys. Rev., 1962, 128, 2042
- 16 Principles of High Resolution in NMR in Solids  
M. Mehring  
Springer Verlag, Berlin, 2nd Edition, 1983
- 17 R.H. Newman

- J. Magn Reson, 1987, 72, 337
- 18 E.O. Stejskal, J. Schaefer, J.S. Waugh  
J. Magn Reson, 1977, 28, 105
- 19 E.O. Stejskal, J. Schaefer  
J. Magn Reson, 1975, 18, 560
- 20 J. Tangenfeldt, U. Haeberlen  
J. Magn Reson, 1979, 36, 453

CHAPTER THREEREFERENCES

- 1 Pulsed NMR Spectrometer CXP Instruction Manual  
Bruker Spectrospin Ltd
- 2 G.J. Nesbitt Ph.D. Thesis  
Durham University, 1986
- 3 P. Jackson Ph.D. Thesis  
Durham University, 1987
- 4 J.S. Frye, G.E. Maciel  
J. Magn Reson, 1982, 48, 125
- 5 Bruker Applications Note BII-1  
D.P. Burum
- 6 Pulsed NMR Spectrometer AC Instruction Manual  
Bruker Spectrospin Ltd.
- 7 The Chemistry of Silica  
R.K. Iler  
John Wiley and Sons, 1979
- 8 Sorpty 1750 Surface Area Analyser  
Instruction Manual
- 9 Micrometrics 9200 Mercury Porosimeter  
Instruction Manual
- 10 Unilever Research  
Personal Communications
- 11 Practical NMR Spectroscopy  
M.L. Martin, J.J. Delpuech, G.L. Martin  
Heyden and Sons ltd., 1980
- 12 M.S. Cacei, W.P. Cacheris  
BYTE, 1985, 340
- 13 Physical Chemistry. Third edition.  
P.W. Atkins  
Oxford University Press. 1986

CHAPTER FOURREFERENCES

- 1 G.R. Holzman, P.C. Lauterbur, J.H. Anderson, W. Koth  
J. Chem. Phys., 1956, 25, 172
- 2 G.C. Levy, J.D. Cargiolo, G.E. Maciel, J.J. Natterstad, E.B. Whipple, M. Ruta  
J. Magn Reson, 1973, 11, 352
- 3 R.B. Johannesen  
J. Chem. Phys., 1967, 47, 955
- 4 E. Lippmaa, M. Magi, A. Samoson, G. Englehardt, A.R. Grimmer  
J. Am. Chem. Soc., 1980, 102, 4889 (for example)
- 5 P. Jackson Ph.D. Thesis (for example)
- 6 See Section 3.3
- 7 Principles of High-resolution in NMR in Solids  
M. Mehring,  
Springer Verlag, Berlin, 2ND Edition, 1983
- 8 Transient Techniques in NMR of Solids  
B.C. Gerstein, C. R. Dybowski  
Academic Press Inc., 1985
- 9 High Resolution Solid-state NMR of Silicates and Zeolites  
G. Engelhardt, D. Michel  
John Wiley and Sons, 1987
- 10 A.R. Grimmer, F.V. Lampe, M. Magi, E. Lippmaa  
Montash. Chem., 1983, 114, 1053
- 11 J.S. Frye, G.E. Maciel  
J. Magn Reson, 1982, 48, 125-131
- 12 E.O. Stejskal, J. Schaefer, J.S. Waugh  
J. Magn Reson, 1977, 28, 105-112
- 13 Nuclear Magnetic Resonance Spectroscopy, page 87  
R.K. Harris  
Longman Scientific and Technical, 1986
- 14 W.L. Earl  
TAMU News Letter, December 22, 1983
- 15 D.A. Torchia et al  
J. Magn Reson, 1978, 30, 613-616
- 16 E.O. Stejskal, J. Schaefer  
J. Magn Reson, 1975, 18, 560

CHAPTER FIVEREFERENCES

- 1 E. Lippmaa, M. Magi, A. Samoson, G. Engelhardt, A.R. Grimmer  
J. Am. Chem. Soc., 1980, 102, 4889
- 2 E. Lippmaa, M. Magi, A. Samoson, M. Tarmak, G. Engelhardt  
J. Am. Chem. Soc., 1981, 103, 4992
- 3 E. Lippmaa, M. Magi, A. Samoson, G. Engelhardt, A.R. Grimmer  
J. Phys. Chem., 1984, 88, 1581
- 4 High-Resolution Solid-state NMR of Silicates and Zeolites  
G. Engelhardt, D. Michel  
John Wiley and Sons, 1987
- 5 G.E. Maciel, D.W. Sindorf  
J. Am. Chem. Soc., 1980, 102, 7607
- 6 B.H.W.S de Jong, Ch. M. Schramm, V.E. Parziale  
J. Am. Chem. Soc., 1984, 106, 4396
- 7 R. Durpree, D. Holland, P.W. McMillan, R.F. Pettifer  
J. Non-Cryst. Solids, 1984, 68, 399
- 8 G. Engelhardt, D. Zeigan, D. Hoebbel, A. Samoson, E. Lippmaa  
Z. Chem., 1982, 22, 314
- 9 R.K. Harris, K. Metcalf  
Polyhedron, 1985, 4, 1319
- 10 M.G. Gibby, A. Pines, J.S. Waugh  
J. Am. Chem. Soc., 1972, 94, 6231
- 11 N. Janes, E. Oldfield  
J. Am. Chem. Soc., 1985, 107, 6769  
(and references contained therein)
- 12 K.A. Smith, R.J. Kirkpatrick, E. Oldfield, D.M. Henderson  
Am. Miner. 1983, 68, 1206
- 13 J.V. Smith, C.S. Blackwell  
Nature, 1983, 303, 223
- 14 S. Ramada, J. Klinowski  
Nature, 1984, 308, 521
- 15 G. Englehardt, R. Radeaglia  
Chem. Phys. Lett., 1984, 108, 271
- 16 A.R. Grimmer, F. Von Lampe, M, Magi  
Chem. Phys. Lett., 1986, 132, 1549
- 17 J.A. Pople  
Discuss Faraday Soc., 1962, 34, 7
- 18 W.E. Lamb Jr.  
Phys. Rev. 1941, 60, 817

- 19 C.J. Jameson, H.S. Gutowsky  
J. Chem. Phys., 1964, 40, 1714
- 20 G.R. Holzman, P.C. Lauterbur, J.H. Anderson, W. Koth  
J. Chem. Phys., 1956, 25, 172
- 21 C.R. Ernst, L. Spialter, G.R. Buell, D.L. Wilhite  
J. Am. Chem. Soc., 1974, 96, 5375
- 22 G. Engelhardt, E. Lippmaa, M. Alla, T. Pehk  
J. Am. Chem. Soc., 1978, 100, 1929
- 23 K.W. Zilm, D.M. Grant, J. Michel, J.M. Fink, R. West  
Organometallics, 1983, 2, 193
- 24 B.C. Gerstein  
Anal. Chem., 1983, 55, 781a
- 25 A.R. Grimmer, R. Peter, E. Fechner, G. Molgedey  
Chem. Phys. Lett., 1981, 77, 331
- 26 A.R. Grimmer  
Spectrochim. Acta. 1978, Vol. 34A, 941
- 27 A.R. Grimmer, F. Von Lampe  
J. Chem. Soc. Chem. Commun., 1986, 3, 219
- 28 A.R. Grimmer  
Chem. Phys. Lett., 1985, 119, 416
- 29 J.S. Louisnathan, G.V. Gibbs  
Am. Miner., 1972, 57, 1643
- 30 Nuclear Magnetic Resonance Volume 16, page 16  
Senior Reporter G.A. Webb  
The Royal Society of Chemistry, London, 1987
- 31 M.M. Maricq, J.S. Waugh  
J. Chem. Phys., 1979, 70, 3300
- 32 J. Herzfeld, A.E. Berger  
J. Chem. Phys., 1980, 73, 6021
- 33 L. H. Merwin Ph.D. Thesis  
University of Durham 1987
- 34 N.J. Clayden, C.M. Dobson, L. Lian, D.J. Smith  
J. Magn Reson, 1986, 69, 476
- 35 K.H. Jost, W. Hilmer  
Acta. Cryst., 1966, 21, 583
- 36 P.B. Jamieson, L.S. Dent-Glasser  
Acta. Cryst., 1967, 22, 507
- 37 P. Gillespie, Personal Communications
- 38 An Introduction to Mossbauer Spectroscopy pg 77  
L.May, Adam Hilger. London.

- 39 A.R. Grimmer, Personal Communications
- 40 D.W.J. Cruickhank, L. Lynton, G.A Barclay  
Acta. Cryst., 1962, 15, 491
- 41 J.V. Smith  
Acta. Cryst., 1953, 6, 9
- 42 K.S. Mamedov, N.V. Belov  
Zapiski Vesenoyuznogo Mineralogichestogo Obshchestva, 1956,  
85, 13
- 43 G.J. Nesbitt Ph.D. Thesis  
Durham University, 1986
- 44 A.A. Calville, C.P. Anderson  
Am. Miner., 1971, 56, 1222
- 45 N. Kubicki, Diplomarbeit  
Karl-Marx Univeritat, Leipzig 1979
- 46 Y.I. Smolin, Y.F. Shepelev, R. Pomess, D. Hoebbel, W. Wieker  
Kristallografija, 1979, 24, 38
- 47 K.G. Sharpe, P.A. Sutor, E.A. Williams, J.D. Cargioli, T.C.  
Farrar, K. Ishibitsu  
J. Am. Chem. Soc., 1976, 98, 1977
- 48 H. Sollradl, E. Hengge  
J. Organomet Chem., 1983, 243, 257
- 49 H.C. Marsmann  
Z. Chem., 1972, 96, 288
- 50 E. Hengge  
Unpublished results, 1985
- 51 R.K. Harris, B.J. Kimber  
Adv. Mol. Relax. Proc., 1976, 8, 15
- 52 L. Parkanyi, E. Hengge  
J. Organomet. Chem., 1982, 235, 273
- 53 K.D. Summerhays, D.A. Deprez  
J. Organometal. Chem., 1976, 118, 19
- 54 R.K. Harris, B.J. Kimber  
J. Magn Reson, 1975, 17, 174
- 55 G.C. Levy, D.M. White, J.D. Cargioli  
J. Magn Reson, 1972, 8, 280
- 56 L. Parkanyi, K. Sasuari, I. Barta  
Acta. Cryst., 1978, B34, 883
- 57 C. Glidewell, D.C. Liles  
Acta. Cryst., 1978, B34, 124
- 58 J. Allemand, R. Gerdil  
Cryst. Struct. Commun., 1979, 8, 927

- 59 H.C. Marsmann  
Z. Chem., 1972, 92, 286
- 60 R.K. Harris, B.J. Kimber  
Adv. Mol. Relax. Proc., 1976, 8, 23
- 61 A. Rastelli, S.A. Pozzoli  
J. Mol. Struc., 1973, 18, 463

CHAPTER SIXREFERENCES

- 1 The Chemistry of Silica  
R.K. Iler,  
John Wiley and Sons, 1979
- 2 The Modern Inorganic Chemicals Industry  
K.R. Thompson  
The Chemical Society
- 3 Soluble Silicate  
J.G. Vail  
ACS Monograph Series, New York, 1952
- 4 S.S. Kistler, E.A. Fischer, I.R. Freeman  
J. Am. Chem. Soc., 1943, 65, 1909
- 5 C.J. Plank  
J. Colloid. Sci. 1947, 2, 413
- 6 P.B. Elkin, C.G. Shull, L.C. Roess  
Ind. Eng. Chem., 1945, 37, 327
- 7 Unilever Research  
Personal Communications
- 8 A.V. Kiselev  
Discussions Faraday Soc., 1971, 54, 14
- 9 R.S. McDonald  
J. Phys. Chem., 1958, 62, 1168
- 10 A.J. Van Roosmalen, J.C. Mol  
J. Phys. Chem., 1979, 83, 2485
- 11 V.V. Davydov, A.V. Kiselev, L.T. Zhuravlev  
Trans. Faraday Soc., 1960, 60, 2254
- 12 H.P. Boehm, M. Schneider, F. Arendt  
Z. Anorg. Allg. chem., 1963, 320, 43
- 13 J.B. Peri, A.L. Hensley  
J. Phys. Chem., 1968, 72, 2926
- 14 J.J. Fripiat, J. Uytterhoeven  
J. Phys. Chem., 1962, 66, 800
- 15 C. Naccache, B. Imelik  
Bull. Soc. Chim. Fr., 1961, 553
- 16 V.M. Chertov  
J. Phys. Chem., 1966, 40, 283
- 17 G. Wirzing  
Naturwissenschaften, 1964, 51, 211
- 18 D.W. Sindorf, G.E. Maciel

- J. Phys. Chem., 1982, 86, 5208
- 19 V.W. Bermudez  
J. Phys. Chem., 1970, 74, 4160
- 20 G. Curthoys, V.Y. Davydov, A.V. Kiselev  
J. Colloid<sup>^</sup> and Interface Sci., 1974, 48, 58
- 21 D.W. Sindorf, G.E. Maciel  
J. Am. Chem. Soc., 1983, 105, 1487
- 22 P. Hobza, J. Saver, C. Morgeneyer, J. Hurych, R. Zahradnik  
J. Phys. Chem. 1981, 85, 4061
- 23 K. Klier, A.C. Zettlemover  
J. Colloid<sup>^</sup> and Interface Sci., 1977, 58, 216
- 24 K.R. Lange  
J. Colloid<sup>^</sup> and Interface Sci., 1965, 20, 231
- 25 R.Y. Sheinfain, B.A. Lipkind, O.P. Stas, J.E. Neimark  
Kolloidnyi Zhurnal, 1964, 26(6), 734-738
- 26 V.M. Chertov, D.B. Dzhabaeva, I.E. Neimark  
Kolloidnyi Zhurnal, 1965, 27(2), 279-383
- 27 V.M. Chertov, I.E. Neimark  
Kolloidnyi Zhurnal, 1967, 29(2), 299-303
- 28 R.Y. Sheinfain, O.P. Stas, I.E. Neimark  
Kolloidnyi Zhurnal, 1965, 27(6), 916-920
- 29 A.V. Kiselev, V.M. Luklyanovich, Y.S. Nikitin, E.B. Oganessian, A.L. Scrakhov  
Kolloidnyi Zhurnal, 1969, 81, 889-893
- 30 R.L. Gorelik, L.T. Zhyravlev, A.V. Kiselev, Y.S. Nikitin, E.B. Oganessian, K.Y. Shengelya  
Kolloidnyi Zhurnal, 1970, 33(1), 51-58
- 31 R.L. Gorelik, V.Y. Davydov, L.T. Zhuravlev, G. Curthoys, A.V. Kiselev, Y.S. Nikitin,  
Kolloidnyi Zhurnal, 1973, 35(3), 45461
- 32 A.V. Kiselev, Y. S. Nikitin, E.B. Oganessian  
Kolloidnyi Zhurnal, 1969, 31(4), 525-531
- 33 J. Zimmerman, B. Holmes, J. Lasaster  
J. Phys. Chem., 1956, 60, 1157
- 34 J. Zimmerman, J. Lasaster  
J. Phys. Chem., 1958, 62, 1157
- 35 C.E. Bronnimann, I.S. Chuang, B. L. Hawkins, G.E. Maciel  
J. Am. Chem. Soc., 1987, 109, 1562-1564
- 36 C.E. Bronnimann, R.C. Zeigler, G.E. Maciel  
J. Am. Chem. Soc., 1988, 110, 2023
- 37 G.E. Maciel, D. W. Sindorf

- J. Am. Chem. Soc., 1981, 102, 7606
- 38 G.E. Maciel, D. W. Sindorf  
J. Phys. Chem., 1983 87, 5516
- 39 G.E. Maciel, D. W. Sindorf  
J. Phys. Chem., 1981, 103, 4263
- 40 G.E. Maciel, D. W. Sindorf  
J. Am. Chem. Soc., 1983, 105, 3767
- 41 J.E. De Haan, H.M. Van Den Bogaert, J.J. Ponjee, L.J.M. Van  
De Ven  
J. Colloid and Interface Sci., 1986, 110, 591
- 42 T. Bershien, P. Fink, V.M. Mastikhin, A.A. Shubin  
J. Chem. Soc. Fara. Trans. I, 1986, 82, 1879
- 43 G.E. Maciel, D. W. Sindorf  
J. Phys. Chem., 1982, 86, 5206
- 44 C.A. Fyfe, G.C. Gobbi, G.J. Kennedy  
J. Phys. Chem., 1985, 89, 277-281
- 45 J. Wang, H. Liu, R. Chen  
Huaxue Tangbao, 1986(1), 33-34
- 46 P.P. Williams, L.S. Dent-Glasser  
Acta. Cryst., 1971, B27, 2269
- 47 L.H. Merwin MSc. Thesis  
University of East Anglia, 1981
- 48 R. Freeman, H.D.W. Hill  
J. Chem. Phys., 1971, 54, 3367
- 49 T. Gerber, H. Burger,  
J. Non-Cryst. Solids, 1987, 91, 122
- 50 L.F. Gladden, T.A. Carpenter, S.N. Elliot  
Philos. Mag. B, 1986, 53(4), L81-L87
- 51 W.D. Bascom  
J. Phys. Chem., 1972, 76, 3188
- 52 W.G. Schaffer, C.R. Adams, J.N Wilson  
J. Phys. Chem., 1965, 69, 1530
- 53 B.A. Flemming  
J. Colloid and Interface Sci., 1986, 110, 40

CHAPTER SEVENREFERENCES

- 1 The Chemistry of Silica  
R.K. Iler,  
John Wiley and Sons, 1979
- 2 H. Bauman  
Naturwiss., 1956, 43, 300
- 3 C.W. Lentz  
Inorg. Chem., 1964, 4, 574
- 4 J.E. Early, D.O. Fortnum, A. Wojcicki, J.O. Edwards  
J. Am. Chem. Soc., 1959, 81, 1295
- 5 H.C. Marsmann  
Chem. Ztg., 1973, 97, 128
- 6 H.C. Marsmann  
Z. Naturforsch. Teil B, 1974, 29, 495
- 7 G. Engelhardt, H. Jancke, D. Hoebbel, W. Wieker  
Z. Chem., 1974, 14, 109
- 8 R.O. Gould, B.M. Lowe, N.A. McGlip  
J. Chem. Soc. Chem. Commun., 1974, 1720
- 9 R.K. Harris, R.H. Newman  
J. Chem. Soc. Faraday Trans. II, 1977, 73, 1204
- 10 S.D. Kinrade, T.W. Swaddle  
J. Chem. Soc. Chem. Commun., 1986, 120
- 11 C.T.G. Knight, Ph.D. Thesis  
University of East Anglia, 1982
- 12 D. Hoebbel, G. Garzo, G. Engelhardt, H. Jancke, P. Franke,  
W. Weiker  
Z. Anorg. Allg. Chem., 1976, 424, 115
- 13 R.K. Harris, R.H. Newman  
Org. Magn. Reson., 1977, 9, 426
- 14 L.S. Dent-Glasser, E.E. Lachowski, R.K. Harris, J. Jones  
J. Mol. Struct., 1979, 51, 239
- 15 E. Lippmaa, M. Magi, A. Samoson, G. Engelhardt, A.R. Grimmer  
J. Am. Chem. Soc., 1980, 102, 4889
- 16 R.K. Harris, C.T.G. Knight  
J. Chem. Soc. Faraday Trans. II, 1983, 79, 1525
- 17 R.K. Harris, C.T.G. Knight  
J. Chem. Soc. Faraday Trans. II, 1983, 79, 1539
- 18 R.K. Harris, M.J. O'Connor  
J. Magn. Reson., 1984, 57, 115

- 19 G. Engelhardt, D. Michel  
"High Resolution Solid-State NMR of Silicates and Zeolites"  
John Wiley and Sons, 1987
- 20 J. Jones, Ph.D. Thesis  
University of East Anglia, 1981
- 21 S. Sjoberg, L.O. Ohman, N, Ingri  
Acta Chem. Scand. Ser. A, 1985, 39, 93
- 22 R.K. Harris, C.J. Creswell, P.T. Jageland  
J. Chem. Soc. Chem. Commun., 1984, 1261
- 23 R.K. Harris, C.J. Cresswell, P.T. Jageland  
J. Mol. Liq., 1984, 29, 63
- 24 G. Engelhardt, D. Hoebbel  
J. Chem. Soc. Chem. Comm., 1984, 514
- 25 C.T.G. Knight, R.J. Kirkpatrick, E. Oldfield  
J. Magn Reson, 1988, 78, 31
- 26 G.A.J. Haines, Ph.D. Thesis  
University of East Anglia, 1984
- 27 I. Artaki, S. Sinha, J. Jones  
Matt. Lett., 1984, 2, 488
- 28 D. Hoebbel, G. Garzo, G. Engelhardt, A. Till  
Z. Anorg. Allg. Chem. 1979, 450, 5
- 29 G. Engelhardt  
Z. Chem., 1975, 15, 495
- 30 S.D. Kinrade, T.W. Swaddle  
J. Am. Chem. Soc., 1986, 108, 7159
- 31 A.L. Van Geet  
J. Am. Chem. Soc., 1972, 94, 5580
- 32 R.H. Newman, Ph.D. Thesis  
University of East Anglia, 1984
- 33 A.G. Sharpe  
"Inorganic Chemistry"  
Longman, 1981
- 34 L. Ando, G.A. Webb  
"Theory of NMR Parameters"  
Academic Press, 1983
- 35 S.D. Kinrade, T.W. Swaddle  
Unpublished Work
- 36 H. Gustavsson, B. Lindman, T. Bull  
J. Am. Chem. Soc., 1978, 100, 4655
- 37 SEE CHAPTER SIX
- 38 Line Sim Deconvolution Routine, Bruker Applications Note

APPENDIX 1

(A)

UNIVERSITY OF DURHAMBoard of Studies in Chemistry

## COLLOQUIA, LECTURES AND SEMINARS GIVEN BY INVITED SPEAKER:

1st AUGUST 1985 TO 31st JULY 1986

- 20.2.86 Dr. C.J.F. Barnard (Johnson Matthey Group)  
Platinum Anti-Cancer Drug Development
- 12.3.86 Dr. J.M. Brown  
Chelater Control in Homogenous Catalysis
- 28.11.85 Dr. B.A.J. Clark (Kodak Ltd.)  
Chemistry and Principles of Colour Photography
- 29.1.86 Dr. J.H. Clark (University of York)  
Novel Fluoride Ion Reagents
- 28.11.85 Dr. S.G. Davies, (University of Oxford)  
Chirality Control and Molecular Recognition
- 24.11.85\* Dr. J. Dewing (U.M.I.S.T.)  
Zeolites - Small Holes, Big Opportunities
- 7.11.85 Prof. G. Ertl (University of Munich)  
Heterogeneous Catalysis
- 13.2.86 Prof. R. Grigg (Queens University, Belfast)  
Thermal Generation of 1,3-Dipoles
- 27.2.86\* Prof. R.K. Harris (University of Durham)  
The Magic of Solid State NMR
- 5.3.86 Dr. D. Hathaway (University of Durham)  
Herbicide Selectivity
- 6.3.86 Dr. B. Iddon (University of Salford)  
The Magic of Chemistry
- 21.11.85 Prof. K.H. Jack (University of Newcastle)  
Chemistry of Si-Al-O-N Engineering Ceramics
- 14.5.86 Dr. P.P.R. Langridge-Smith (University of Edinburgh)  
Naked Metal Clusters - Synthesis, Characterisation and  
Chemistry
- 23.1.86\* Prof. Sir J. Lewis (University of Cambridge)  
Some more Recent Aspects in the Cluster Chemistry of  
Ruthenium and Osmium Carbonyls
- 17.10.85 Dr. C.J. Ludman (University of Durham)  
Some Thermochemical Aspects of Explosions
- 20.11.85 Dr. J.A.H. McBride (Sunderland Polytechnic)  
A Heterocyclic Tour on a Distorted Tricycle - Biphenylene
- 5.11.85 Prof. M.J. O'Donnell (Indiana-Purdue University)

- 13.9.85 Dr. V.S. Parmar (University of Delhi)  
Enzyme Assisted ERC Synthesis
- 30.1.86 Dr. N.J. Phillips (University of Technology, Loughborough)  
Laser Holography
- 19.2.86 Prof. G. Procter (University of Salford)  
Approaches to the Synthesis of some Natural Products
- 9.6.86 Prof. R. Schmutzler (University of Braunschweig)  
Mixed Valence Diphosphorous Compounds
- 5.3.86 Dr. M. Schroeder (University of Edinburgh)  
Studies on Macrocyclic Complexes
- 15.1.86\* Prof. N. Sheppard (University of East Anglia)  
Vibrational and Spectroscopic Determinations of the  
Structures of Molecules Chemisorbed on Metal Surfaces
- 12.2.86 Prof. O.S. Tee (Concordia University, Montreal)  
Bromination of Phenols
- 26.2.86\* Miss C. Till (University of Durham)  
ESCA and Optical Emission Studies of the Plasma  
Polymerisation of Perfluoroaromatics
- 31.10.85\* Dr. P. Timms (University of Bristol)  
Some Chemistry of Fireworks
- 28.11.85 Prof. D.J. Waddington (University of York)  
Resources for the Chemistry Teacher
- 30.10.85\* Dr. S.N. Whittleton (University of Durham)  
An investigation of a Reaction Window
- 23.6.86 Prof. R.E. Wilde (Texas Technical University)  
Molecular Dynamic Processes from Vibrational Bandshapes
- 12.2.86 Dr. J. Yarwood (University of Durham)  
The Structure of Water in Liquid Crystals

(B)

UNIVERSITY OF DURHAMBoard of Studies in ChemistryCOLLOQUIA, LECTURES AND SEMINARS GIVEN BY INVITED SPEAKERS  
1st AUGUST 1986 TO 31st JULY 1987

- 13.11.86\* Prof. Sir G. Allen (Unilever Research)  
Biothechnology and the Future of the Chemical Industry
- 6.5.87 Dr. R. Bartsch (University of Sussex)  
Low Co-ordinated Phosphorus Compounds
- 27.5.87 Dr. M. Blackburn (University of Sheffield)  
Phosphonates as Analogues of Biological Phosphate
- 9.5.87 Prof. F.G. Bordwell (Northeastern University, U.S.A.)  
Carbon Anions, Radicals, Radical Anions and Radical Cations
- 26.11.86\* Dr. N.D.S. Canning (University of Durham)  
Surface Adsorption Studies of Relevance to Heterogeneous  
Ammonia Synthesis
- 11.5.87 Dr. R.D. Cannon (University of East Anglia)  
Electron Transfer in Polynuclear Complexes
- 28.1.87 Dr. W. Clegg (University of Newcastle-upon-Tyne)  
Carboxylate Complexes of Zinc; Charting a Structural Jungle
- 5.11.86 Prof. D. Dopp<sup>II</sup> (University of Duisberg)  
Cyclo-additions and Cyclo-reversions Involving Captodative  
Alkenes
- 8.12.86 Prof. T. Dorfmueller (University of Bielefeld)  
Rotational Dynamics in Liquids and Polymers
- 12.5.87 Dr. E.M. Goodger (Cranfield Institute of Technology)  
Alternative Fuels for Transport
- 16.10.86\* Prof. N.N. Greenwood (University of Leeds)  
Glorious Gaffes in Chemistry
- 7.5.87 Dr. M. Harmer (I.C.I. Chemicals and Polymer Group)  
The Role of Organometallics in Advanced Materials
- 5.2.87 Dr. P. Hubbersley (University of Nottingham)  
Demonstration Lecture on Various Aspects of Alkali Metal  
Chemistry
- 17.3.87 Prof. R.F. Hudson (University of Kent)  
Aspects of Organophosphorus Chemistry
- 15.3.87 Prof. R.F. Hudson (University of Kent)  
Homolytic Rearrangements of Free Radical Stability
- 19.2.87 Dr. M. Jarman (Institute of Cancer Research)  
The Design of Anti Cancer Drugs

- 26.5.87 Dr. C. Krespan (E.I. Dupont de Nemours)  
Nickel(0) and Iron(0) as Reagents in Organofluorine  
Chemistry
- 23.11.86\* Prof. H.W. Kroto (University of Sussex)  
Chemistry in Stars, Between Stars and in the Laboratory
- 5.3.87\* Prof. S.V. Ley (Imperial College)  
Fact and Fantasy in Organic Synthesis
- 3.12.86 Dr. J. Miller (Dupont Central Research, U.S.A.)  
Molecular Ferromagnets; Chemistry and Physical Properties
- 20.11.86 Dr. A. Milne and Mr. S. Christie (International Paints)  
Chemical Serendipity - A Real Life Case Study
- 4.3.87\* Dr. R. Newman (University of Oxford)  
Change and Decay: A Carbon-13 CP/MAS Study of Humification  
and Coalification Processes
- 22.1.87 Prof. R.H. Ottewill (University of Bristol)  
Colloid Science a Challenging Subject
- 11.5.87 Prof. S. Pasynkiewicz (Technical University, Warsaw)  
Thermal Decomposition of Methyl Copper and its Reactions  
with Trialkylaluminium
- 24.5.87 Prof. S.M. Roberts (University of Exeter)  
Synthesis of Novel Antiviral Agents
- 12.2.87\* Dr. P.J. Rodgers (I.C.I. Billingham)  
Industrial Polymers from Bacteria
- 6.11.86 Dr. R.M. Scowston (University of Hull)  
From Myth and Magic to Modern Medicine
- 11.2.87 Dr. T. Shepherd (University of Durham)  
Pteridine Natural Products; Synthesis and Use in  
Chemotherapy
- 2.2.87 Prof. A. Thompson (University of East Anglia)  
Metalloproteins and Magneto-optics
- 27.11.86\* Prof. R.L. Williams (Metropolitan Police Forensic Science)  
Science and Crime
- 29.10.86 Prof. E.H. Wong (University of New Hampshire, U.S.A.)  
Coordination Chemistry of P-O-P Ligands
- 17.2.87\* Prof. E.H. Wong (University of New Hampshire, U.S.A.)  
Symmetrical Shapes from Molecules to Art and Nature

(C)

UNIVERSITY OF DURHAMBoard of Studies in ChemistryCOLLOQUIA, LECTURES AND SEMINARS GIVEN BY INVITED SPEAKERS  
1st AUGUST 1987 TO 31st JULY 1988

- 25.4.88 Prof. D. Birchall (I.C.I. Advanced Materials)  
Environmental Chemistry of Aluminium
- 18.2.88 Dr. K. Borer (University of Durham Industrial Research  
Labs.)  
The Brighton Bomb - A Forensic Science View
- 16.3.88 L. Bossons (Durham Chemistry Teacher's Centre)  
GCSE Practical Assesment
- 5.11.87 Dr. A.R. Butler (University of St. Andrews)  
Chinese Alchemy
- 28.1.88\* Dr. A. Cairns-Smith (Glasgow University)  
Clay Minerals and the Origin of Life
- 11.87 Dr. J. Davidson (Herriot-Watt University)  
Metal Promoted Oligomerisation Reactions of Alkynes
- 19.4.88\* Graduate Chemists (Northeast Polytechnics and Universities)  
R.S.C. Graduate Symposium
- 3.3.88 Prof. W.A.G. Graham (University of Alberta, Canada)  
Rhodium and Iridium Complexes in the Activation of  
Carbon-Hydrogen Bonds
- 22.10.87 Prof. G.W. Gray (University of Belfast)  
Liquid Crystals and their Applications
- 7.4.88 Prof. M.P. Hartshorn (University of Canterbury, New  
Zealand)  
Aspects of Ipso-Nitration
- 3.11.87 Dr. J. Howard (I.C.I. Wilton)  
Chemistry of Non-Equilibrium Processes
- 29.7.88 Dr. M.E. Jones (Durham Chemistry Teacher's Centre)  
GCSE Chemistry Post-mortem
- 6.7.88 Prof. H.F. Koch (Ithaca College, U.S.A.)  
Does the E2 Mechanism Occur in Solution?
- 7.3.88 Mr. Lacey (Durham Chemistry Teacher's Centre)  
Double Award Science
- 10.12.87 Dr. C.J. Ludman (University of Durham)  
Explosives
- 11.5.88 Dr. W.A. McDonald (I.C.I. Wilton)

## Liquid Crystal Polymers

- 8.6.88 Prof. J.-P. Majoral (Universite Paul Sabatier)  
Stabilisation by Complexation of Short-lived Phosphorus Species
- 4.11.97 Mrs. Mapletoft ((Durham Chemistry Teacher's Centre)  
Salter's Chemistry
- 18.5.88 Prof. C.A. Nieto de Castro (University of Lisbon and  
Imperial College)  
Transport Problems of Non-Polar Fluids
- 29.6.88\* Prof. G.A. Olah (University of Southern California)  
New Aspects of Hydrocarbon Chemistry
- 21.1.88\* Dr. F. Palmer (University of Nottingham)  
Luminescence (Demonstration Lecture)
- 28.4.88\* Prof. A. Pines (University of California, Berkley, U.S.A)  
Some Magnetic Moments
- 27.4.88 Dr. R. Richadson (University of Bristol)  
X-Ray Diffraction from Spread Monolayers
- 13.4.88 Mrs. E. Roberts (SASTRO Officer for Sunderland)  
Talk - Durham Chemistry Teacher's Centre - "Links Between  
Industry and Schools
- 27.4.88 Dr. J.A. Robinson (University of Southampton)  
Aspects of Antibiotic Biosynthesis
- 29.11.87 Mrs. van Rose (Geological Museum)  
Chemistry of Volcanoes
- 19.11.87 Prof. P.G. Seebach (E.T.H. Zurich)  
From Synthetic Methods to Mechanistic Insight
- 11.5.88\* Dr. J. Sodeau (University of East Anglia)  
Durham Chemistry Teacher's Centre Lecture: "Spray Cans,  
Smog and Society"
- 16.12.87 Mr. R.M. Swart (I.C.I.)  
The Interaction of Chemicals with Lipid Bilayers
- 11.2.88 Prof. J.J. Turner (University of Nottingham)  
Catching Organometallic Intermediates
- 25.2.88 Prof. A. Underhill (University of Bangor)  
Molecular Electronics
- 26.11.87 Dr. D.H. Williams (University of Cambridge)  
Molecular Recognition
- 15.10.87 Dr. M.J. Winter (University of Sheffield)  
Pyrotechnics (Demonstration Lecture)

(D)

RESEARCH CONFERENCES ATTENDED

(\* INDICATES POSTER PRESENTATION + INDICATES LECTURE)

1. NMR Discussion Group  
Royal Society of Chemistry  
London 1985
2. British Radiofrequency Society General Meeting  
Oxford 1986
- 3.\* "NMR Studies of Silica Gels" R.K. Harris, T.N. Pritchard  
NMR Conference. Royal Society of Chemistry  
London 1987
4. "Borates, Phosphates and Silicates", The Cinderella Anions  
Royal Society of Chemistry  
London 1988
- 5.+ "<sup>29</sup>Si and <sup>1</sup>H NMR Studies of Silica Xerogels", T.N. Pritchard  
NMR Discussion Group  
Manchester 1988
- 6.+ "<sup>29</sup>Si and <sup>1</sup>H NMR Studies of Silica Xerogels", T.N. Pritchard  
Graduate Symposium  
Durham 1988

(E) FIRST YEAR INDUCTION COURSE OCTOBER 1985

The course consists of a series of one hour lectures on the services available in the Department.

- (1) Departmental Organisation
- (2) Safety Matters
- (3) Electrical appliances and infra red spectroscopy
- (4) Chromotography and microanalysis
- (5) Atomic adsorptiometry and inorganic analysis
- (6) Library Facilities
- (7) Mass Spectroscopy
- (8) Nuclear Magnetic Resonance Spectroscopy
- (9) Glass blowing techniques

